



**MATERIAL
AND MECHANICAL
ENGINEERING
TECHNOLOGY**

Editorial board of the journal

Gulnara Zhetessova (Abylkas Saginov Karaganda Technical University, Kazakhstan)
Alexander Korsunsky (University of Oxford, England)
Olegas Cernasejus (Vilnius Gediminas Technical University, Lithuania)
Jaroslav Jerz (Institute of Materials & Machine Mechanics SAS, Slovakia)
Boris Moyzes (Tomsk Polytechnic University, Russia)
Nikolai Belov (National Research Technological University «Moscow Institute of Steel and Alloys», Russia)
Georgi Popov (Technical University of Sofia, Bulgaria)
Sergiy Antonyuk (University of Kaiserslautern, Germany)
Zharkynay Christian (University of Texas at Dallas Institute of Nanotechnology, USA)
Katica Simunovic (University of Slavonski Brod, Croatia)
Lesley D.Frame (School of Engineering University of Connecticut, USA)
Łukasz Gierz (Poznan University of Technology, Poland)
Łukasz Warguła (Poznan University of Technology, Poland)
Olga Zharkevich (Abylkas Saginov Karaganda Technical University, Kazakhstan)

Content

Jumaev A.A., Akhmedov Kh.I., Sayfidinov O.O., Jumaeva N.K. Analysis of The Influence of Alloying on the Performance Properties of Cast Iron Grades 280Cr29Ni and 330Cr17 with the Purpose of Increasing their Quality.....	3
Issabek T.K., Ermekov T.E., Kamarov R.K., Usenbekov M.S. Development and Creation of a Robotic Mining Complex for Selective Extraction of Coal Seams.....	11
Ali S., Al-Abbas A.H., Magid H.M. Review On Heat Sink and Efficiency Improvement of Heat Transfer In Different Applications.....	21
Antonov A.S., Struk V.A., Wan X., Zhao L., Zhang R. Nanocomposite Polymer Materials with High Performance Characteristics.....	36
Agarwal S., Singh S. Evaluation of Dry Sliding Wear Characteristics in Al5052/TiB ₂ /ZrO ₂ Composites Against EN-31 Steel Counterbody.....	44
Akhmediyev S.K., Filippova T.S., Oryntayeva G.Zh., Tazhenova G.D. Strength Calculation of Variable Bending Rigidity Rods in the Presence of Initial Cambers along Their Axes	51
Suyunbaev Sh. Modeling of Purification Process of Vehicle Exhaust Gases under the Influence of Ultrasound.....	58
Marciniak M., Świdorski A., Perz A., Kminiak R., Warguła Ł. Influence of Processing Conditions on the Particle Size Distribution of Recycled Cable Insulation.....	71
Dalavi A.M., Sarma G., Mondal A., Kukeriya L., Kamble P. Comparison of Different Types of Engineering Alloys Suitable for Automotive Industry.....	78
Buzauova T.M., Yelubaeva A.N., Toleubayeva Sh.B. Assessing the Impact of Making Adjustments to Design Documentation on the Production Process.....	84
Jasim A.H., Al-Khafaji Z., Radhi N.S. Review on Improvement the Turbine Oxidation and Hot Resistant against Corrosion by Nickel–Based Superalloy	89
Mustafin A., Sadykov N., Kabylkaiyr D., Shaimardan A., Sadykova A. Application of Ring Section Shaft in Equipment.....	105
Malyadri T., Suresh Kumar J. Investigating the Influence of Carbon Nanotubes on Basalt Fiber Nano Hybrid Composite Properties: a Dynamic Mechanical Analysis.....	110
Moyzes B.B., Kuvshinov K.A., Nizhegorodov A.I., Vavilova G.V., Vtorushina A.N. The Study of the Dynamic Characteristics of the Hydro-volume Vibration Mechanism.....	120

Analysis of The Influence of Alloying on the Performance Properties of Cast Iron Grades 280Cr29Ni and 330Cr17 with the Purpose of Increasing their Quality

Jumaev A.A., Akhmedov Kh.I., Sayfidinov O.O., Jumaeva N.K.

Navoi State University of Mining and Technologies, Navoi, Uzbekistan

*corresponding author

Abstract. The hardness and microstructure of the High chromium cast irons (HCCIs) grades 280Cr29Ni and 330Cr17, which are predominantly utilized in the production of components for mining and metallurgical equipment subject to wear conditions, have been thoroughly investigated. A thermodynamic analysis of multicomponent Fe-2.6C-Cr-alloying elements (a.e.), was conducted to investigate the crystallization processes of alloys, the development of their metallic matrix structure, and the formation and transformation of carbide phases. Based on the analysis, the optimal quantity and ratio of alloying elements (Cr, Mn, Si, and Ti) in the Fe-2.6C-Cr-a.e., system required for the formation of a metallic matrix and carbide phases that maximize the hardness of the alloy were determined. State diagrams were constructed for ternary, quaternary, and multicomponent systems, including Fe-C-Cr, Fe-C-Ni, Fe-C-Mn, Fe-C-V, Fe-C-Mo, Fe-C-Co, Fe-C-Cr-Ni, Fe-C-Cr-Mn, and Fe-C-Cr-Mn. These diagrams, along with their isothermal (at 200 °C) and polythermal sections, enriched the theory of phase diagrams, which form the foundation of HCCIs. The analysis covered a range of chromium concentrations (16-34%), nickel (0.4-3%), manganese (0.4-2%), carbon (2.4-4%), silicon (0.3-2%), titanium (0.4-5%), molybdenum (0.2-3%), and vanadium (0.01-2%). Phase equilibrium points were determined, encompassing an alloyed solid solution based on iron, multicomponent carbides, and a mixture of phases consisting of a solid solution of iron and carbides. An economical grade of HCCIs has been developed with the following composition: carbon 3.2-3.4%, manganese 0.4-0.6%, chromium 16-18%, silicon 0.4-0.6%, nickel 0.4-0.6%, molybdenum up to 0.4-0.5%, with the balance being iron.

Key words: high chromium cast iron, thermodynamic analysis, matrix, multicomponent systems, microhardness, hardness, microstructure, structure, alloying elements, phase diagrams, phase equilibrium, carbide phase.

Introduction

High chromium cast irons (HCCIs) represent a distinct class of materials characterized by an ongoing process of research and development, driven by continuous updates to their chemical compositions and structural configurations, which directly influence their operational properties. This dynamic nature underscores their unique position in materials science, where systematic investigations into alloy formulations, microstructural modifications, and corresponding performance enhancements are pivotal. Thus, the evolution of HCCIs remains a scientifically driven endeavor, perpetually refining and adapting to meet diverse industrial demands and technological advancements. [1-4]. In the realm of materials science, the evolution of HCCIs exemplifies a progressive trend marked by escalating production volumes and an expanding array of applications. This growth underscores a critical imperative within sectors such as mining and metallurgy: to enhance the economic efficiency of components crafted from HCCIs through advancements that amplify their operational performance and elevate mechanical properties. This imperative drives ongoing research and innovation aimed at refining the alloy compositions, optimizing manufacturing processes, and augmenting the structural integrity of HCCIs components. As a result, the scientific pursuit focuses on achieving superior durability, enhanced wear resistance, and heightened mechanical reliability, thereby meeting the burgeoning demands of industrial applications with improved efficacy and longevity. [5-8].

At the Navoi Machine-Building Plant in Uzbekistan, the utilization of HCCIs grade 280Cr29Ni is integral to the fabrication of components designed to endure challenging operational environments characterized by abrasive wear and impact loads. These specific cast iron alloys are selected based on their tailored properties to withstand the combined effects of abrasion and impact, reflecting a strategic approach in material selection for industrial applications. This strategic deployment underscores the plant's commitment to optimizing component longevity and reliability under demanding working conditions, aligning with stringent performance criteria essential for enhancing operational efficiency and sustaining productivity in critical sectors such as machine-building and heavy industry. The primary focus of investigation revolves around the essential quality parameters of hardness and wear resistance in HCCIs alloy 280Cr29Ni and 330Cr17. Despite exhibiting similar high levels of hardness, these alloys demonstrate varied service lives when subjected to identical operating conditions [9-13]. This discrepancy, likely attributed to differences in their chemical compositions, underscores the pivotal role of alloy structure in influencing durability and performance. The central aim of this study is to elucidate the underlying factors contributing to this observed variability, thereby providing insights into optimizing the structural integrity of these alloys for enhanced longevity and reliability in practical applications. Furthermore, in the context of alloy preparation practices, there is a pressing imperative to minimize the degree of alloying in these HCCIs. Previous research has explored the profound impact of alloying elements on the structural characteristics and functional properties of HCCIs. This ongoing scientific inquiry aims to refine alloy formulations with the goal of achieving optimal performance

efficiencies while reducing alloying costs and enhancing manufacturing feasibility. Thus, the study not only seeks to unravel the structural basis for performance disparities but also strives to advance practical methodologies for alloy optimization in industrial settings [14-18]. Currently, the establishment of definitive compositional guidelines to achieve an optimal structure that guarantees maximum hardness in HCCIs remains elusive. This unresolved challenge underscores the relevance and significance of the present study and its formulated objectives. Specifically, within the foundry operations of the Navoi Machine-Building Plant, the production volume exceeds 200 tons per month of castings made from HCCIs. The critical need to enhance understanding of alloy composition's impact on structural properties is paramount, aiming to unlock methodologies that can reliably optimize alloy formulations. By addressing this gap in knowledge, the study endeavors to pioneer insights into refining casting practices, thereby bolstering the plant's capability to consistently deliver components with superior hardness and enhanced performance characteristics. Consequently, the research not only aims to advance scientific understanding but also holds practical implications for optimizing industrial processes and maximizing the utility of HCCIs in demanding operational environments. The operational demands placed on machinery functioning in abrasive and waterjet environments are progressively intensifying each year. Consequently, there is a corresponding escalation in the standards for materials used in the fabrication of cast components for such machines and mechanisms [19-23]. This ongoing evolution highlights the unresolved challenge surrounding the selection of optimal materials for manufacturing cast parts essential to various industrial equipment. These components include centrifugal crushers, wheels, covers, and housings of dredges, sand, and slurry pumps, impellers of flotation machines, and various parts utilized in concentrating factories, grinding ball mills, and shot blasting machines.

The criticality of material selection is underscored by the need to meet stringent performance criteria in these aggressive operational settings. The quest for suitable materials is driven by the imperative to enhance durability, extend service life, and elevate operational efficiency of machinery subjected to abrasive wear and high-pressure waterjet environments. Addressing this multifaceted challenge involves advancing scientific understanding of material properties, refining alloy compositions, and developing robust manufacturing techniques. By doing so, the aim is to deliver cast components that not only withstand harsh operating conditions but also contribute to optimizing performance and reliability across diverse industrial applications. Thus, the ongoing pursuit of material innovation remains pivotal in meeting the evolving demands of modern industrial sectors.

To achieve the main goal of this study, the following tasks are delineated:

- based on an analysis of the chemical composition, structure and properties of the alloys used, simplify their composition and increase mechanical and performance properties;
- simplification of the chemical composition of three-, four- and multicomponent phase diagrams by analyzing the phase composition, equilibrium and their structure during crystallization;
- by analyzing the chemical composition, structure and properties of model alloys, simplifying the chemical composition of practically used malleable white cast irons and improving their mechanical and performance properties.

1. Methods and materials

Wear-resistant white cast irons 280Cr29Ni and 330Cr17 were chosen as the material under study, the chemical composition of which is given in Table 1.

Table 1. Compositions of the studied cast irons

Cast iron grade	Content of chemical elements,% by weight						
	C	Si	Cr	Mo	Ni	P	S
280Cr29Ni	2,55	≤ 1,5	28,0	-	0,6	≤ 0,01	≤ 0,01
330Cr17	3,40	0,6	16,5	0,5	0,6	≤ 0,01	≤ 0,01

Cast irons according to table 1 are used for castings of mining and processing equipment operating under conditions of intense abrasive wear, namely: feeding disks, substrates, plates for crushers, etc.

The thermodynamic state diagrams of the Fe-2.6C-Cr-Ni, Fe-2.6C-Cr-Mn, Fe-2.6C-Cr-Si and Fe-2.6C-Cr-Ti systems for four components were calculated using Thermo-Calc program [24-26].

To reveal the structure, the samples were etched with a reagent of the following composition: 15 ml of nitric acid, 15 ml of hydrochloric acid and 15 ml of glycerol. Etching time is 10 seconds, at a reagent temperature of 60°C.

Microsections were prepared on a NERIS grinding and polishing machine.

To measure hardness according to HRCe, a TK-2M hardness meter was used, and to measure hardness according to HV₅₀, a PMT-3M hardness meter was used.

The chemical composition of the castings was determined by the emission spectral method using a Spectro-Lab –M device.

The structures of the alloys were studied on a TESCAN VEGA4 SEM scanning electron microscope at different magnifications.

2. Results and discussion

The hardness of the samples was determined on the surface and in the core, at least at 5 points with three duplicates. The average test results are given in table. 2.

Table 2. Hardness of prototypes

Cast iron grade	330Cr17	280Cr29Ni
Surface hardness in cast state HRC	57-62	46-47
Hardness in the core in the cast state HRC	47-48	40-41

Based on the data presented in the table, it is evident that the HCCIs of the 280Cr29Ni grade exhibits a lower hardness compared to the 330Cr17 grade. This observation suggests that, in scenarios where abrasive wear is the sole mode of degradation without the presence of concurrent shock loads, the 280Cr29Ni HCCIs is likely to have a reduced service life. Furthermore, it is important to highlight that the 280Cr29Ni alloy is 1.5 times more expensive than the 330Cr17 alloy, primarily due to its alloying with costly nickel. Consequently, the use of the 280Cr29Ni alloy is economically unjustifiable for components subjected exclusively to abrasive wear conditions.

The microstructure of HCCIs 280Cr29Ni and 330Cr17 was meticulously examined under magnifications of 500, 1000, 2000, and 5000 times. This detailed analysis allowed for an in-depth investigation of the microstructural features, providing critical insights into the phase distributions, grain boundaries, and the morphology of the carbides and matrix. Such high-resolution studies are essential for understanding the intrinsic material properties and their implications on the mechanical performance and wear resistance of these alloys.

Figure 1 illustrates the microstructure of the white cast iron alloy 280Cr29Ni. The matrix of this alloy is composed predominantly of pearlite and austenite. Within this matrix, the structure features carbides of types M_3C and, to a lesser extent, M_7C_3 . The carbide phase is characterized by an average size ranging from 15 to 20 microns. This microstructural configuration is crucial for understanding the alloy's mechanical properties, wear resistance, and overall performance in various applications.

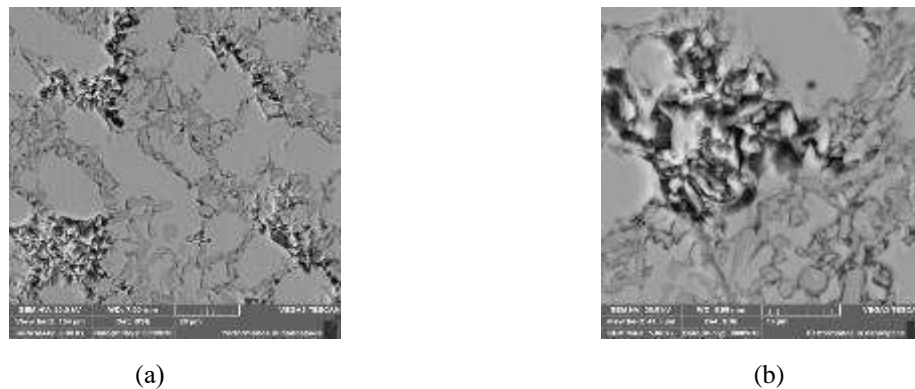


Fig. 1. Structural HCCIs brand 280Cr29Ni: a) x2000, b) x5000

Figure 2 depicts the microstructure of the HCCI grade 330Cr17. The matrix is primarily composed of austenite. The carbide phase within this matrix is represented by two distinct types of carbides: M_7C_3 and $M_{23}C_6$. The average size of these carbide particles ranges between 8 and 13 microns. This detailed structural composition is pivotal for comprehending the material's mechanical attributes and its suitability for various industrial applications, particularly those requiring enhanced wear resistance.

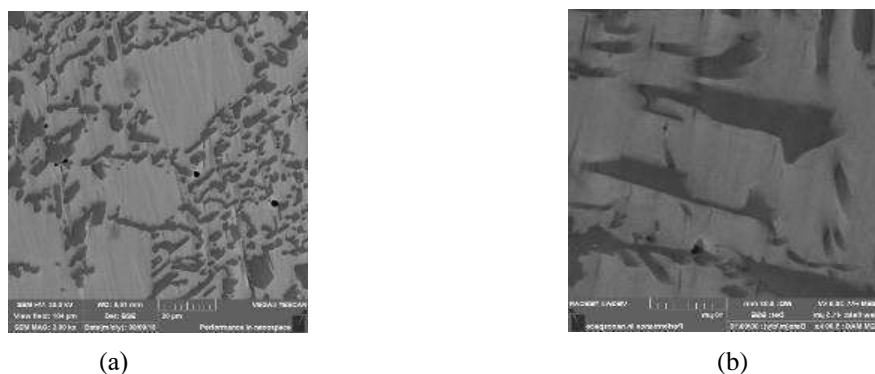


Fig. 2. Structural HCCIs brand 330Cr17: a) x2000, b) x5000

A comprehensive comparison of the structural characteristics, specifically the nature of the matrix and the carbide phase, alongside the varying dispersion of the carbide phase, elucidates the differences in hardness observed in the studied alloys. The distinct composition and distribution of the matrix - whether it is predominantly pearlite, austenite, or a combination thereof - along with the specific types and average sizes of carbides such as M_3C , M_7C_3 , and $M_{23}C_6$, play critical roles in defining the hardness of each alloy. These microstructural variations are fundamental in understanding the mechanical performance and wear resistance of the 280Cr29Ni and 330Cr17 HCCIs.

To elucidate the influence of various alloying elements on the processes of structure formation and the development of the carbide phase, a thermodynamic analysis was conducted utilizing the Thermo-Calc software. This advanced computational tool enables a detailed examination of the phase equilibria and transformations occurring within the alloy system, providing valuable insights into how different alloying elements contribute to the microstructural evolution and the stabilization of specific carbide phases. Such analysis is instrumental in optimizing the alloy design for improved mechanical properties and performance.

An isothermal section of the phase diagram for the four-component system Fe-2.6C-Cr-Ni at a temperature of 200 °C was constructed. This phase diagram elucidates the phase equilibria and stability regions for the various phases within this alloy system at the specified temperature. At 200 °C, multiple phases are observed to form, including distinct carbide phases and metallic matrices. The detailed depiction of these phases within the Fe-2.6C-Cr-Ni system provides critical insights into the microstructural evolution and phase transformations that occur during the alloying process, contributing to a deeper understanding of the material properties and their potential industrial applications. At a nickel content of 1.2% and chromium content of 16%, the alloy's microstructure includes free graphite, ferritic and austenitic structures, and M_3C_2 carbide phases. When the chromium content is increased to 16-25% and the nickel content exceeds 1.1%, the microstructure of the alloy fully develops into austenite and ferrite, with the formation of carbide phases M_3C_2 and M_7C_3 also becoming apparent. These compositional adjustments significantly influence the phase composition and distribution within the alloy, thereby affecting its overall mechanical properties and performance characteristics. It is important to note that when the chromium content reaches 26%, the metallic matrix of the alloy comprises both austenite and ferrite, while the carbide phase is exclusively represented by M_7C_3 carbides. This specific compositional threshold marks a significant shift in the microstructural configuration, influencing the alloy's mechanical properties and behavior under various operating conditions. The exclusive presence of M_7C_3 carbides at this chromium level highlights the critical role of chromium in stabilizing particular carbide phases and modifying the alloy's overall performance.

When the chromium content in the alloy exceeds 16% and the nickel content is increased to 1%, the microstructure predominantly exhibits a ferritic phase, with fully formed M_7C_3 type carbides (Fig. 3).

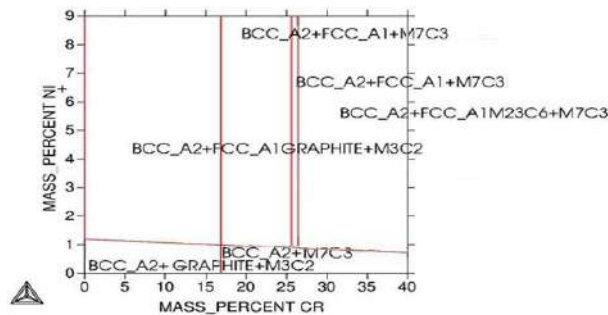


Fig. 3. Phase diagram of Fe-2.6C-Cr-Ni, T=200 °C

This compositional adjustment is crucial as it enhances the formation and stabilization of M_7C_3 carbides, significantly influencing the alloy's mechanical properties and wear resistance. The presence of these well-defined carbides within a ferritic matrix underscores the impact of chromium and nickel in determining the alloy's structural characteristics and overall performance. When the chromium content in the alloy exceeds 16% and the nickel content is increased to 1%, a microstructure characterized by a ferritic matrix and fully developed M_7C_3 type carbides is observed. This composition facilitates the stable formation of M_7C_3 carbides within the ferritic structure, influencing the alloy's mechanical properties, particularly its hardness and wear resistance. Upon further increasing the chromium content to 26% and maintaining the nickel content at 1%, the alloy's microstructure transitions to include both ferritic and austenitic phases. Additionally, this composition promotes the formation of carbides of both M_7C_3 and $M_{23}C_6$ types within the alloy's structure. This dual-phase microstructural configuration, comprising both ferrite and austenite along with distinct carbide phases, enhances the alloy's mechanical strength, corrosion resistance, and suitability for applications requiring robust performance under demanding conditions [27].

In the analysis of the Fe-2.6C-Cr-Mn system, alloys containing chromium levels up to 45% and manganese levels up to 9% exhibit a fully developed matrix structure. This structure encompasses phases such as ferrite and austenite, accompanied by the formation of carbide phases including M_3C_2 , M_7C_3 , and $M_{23}C_6$. These carbides play a critical role in determining the alloy's mechanical properties, including hardness and wear resistance. However, as the manganese content surpasses 9%, a notable transformation occurs in the alloy's microstructure. Specifically, the presence of free graphite becomes evident alongside the metallic phases. This change is indicative of manganese's influence in promoting graphite formation, altering the alloy's characteristics and potentially impacting its suitability for specific applications where graphite presence may affect performance parameters such as strength and machinability.

At manganese contents ranging from 3-4%, the alloy exhibits a fully developed ferritic structure accompanied by the formation of carbide phases M_7C_3 and $M_{23}C_6$. This composition supports the stable presence of both carbide types within the ferritic matrix, influencing the alloy's mechanical properties, particularly its hardness and wear resistance (Fig. 4).

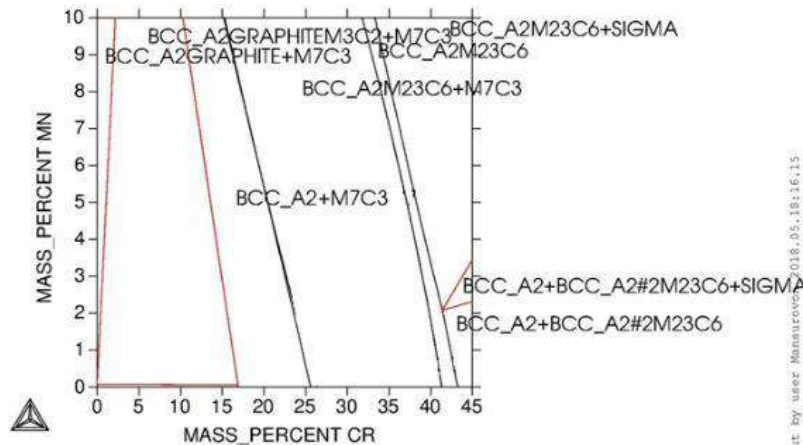


Fig. 4. Phase diagram of Fe-2.6C-Cr-Mn, T-200 °C

In contrast, at lower manganese contents of 0.7-0.8% and chromium levels spanning 16-45%, the alloy's microstructure predominantly consists of a ferritic matrix. Despite the reduced manganese content, the formation of M_7C_3 carbides is observed. This suggests that chromium plays a crucial role in facilitating the formation and stability of M_7C_3 carbides even in the absence of higher manganese levels. Such microstructural configurations are pivotal in determining the alloy's suitability for applications requiring specific mechanical and wear-resistant properties.

High manganese content in white cast iron promotes the formation of graphite within the alloy's structure. This phenomenon occurs due to manganese's tendency to favor graphite precipitation over carbide formation. Consequently, the microstructure of the alloy is characterized by the presence of ferrite, graphite, and brittle carbide phases of the M_3C_2 type. This combination of phases contributes to reduced mechanical properties, as the presence of graphite and brittle carbides diminishes the alloy's strength and toughness. Therefore, manganese's influence in promoting graphite formation and impeding carbide development significantly impacts the alloy's suitability for applications requiring high mechanical performance and wear resistance.

Based on the thermodynamic state diagram of white cast iron 280Cr29Ni of the Fe-2.6C-Cr-Mn system, it was determined that the optimal amount of manganese is 0.4-0.6%, and the optimal amount of chromium is at least 16.5%.

Thermodynamic analysis of the Fe-2.6C-Cr-Si system indicates that at silicon concentrations exceeding 4.5%, the alloy structure comprises ferrite along with free graphite. Silicon's presence promotes the formation of free graphite, which can impact the alloy's mechanical properties due to graphite's tendency to act as a stress concentration site, potentially reducing strength and ductility.

In contrast, when the chromium content exceeds 25-26%, a transformation occurs where free graphite transitions into a bound form within the alloy structure. This transformation suggests that chromium plays a crucial role in stabilizing graphite in a manner that mitigates its detrimental effects on mechanical properties. Bound graphite typically exhibits a more distributed and interconnected structure, which can enhance the alloy's mechanical strength and mitigate potential weaknesses associated with free graphite.

These thermodynamic insights are essential for understanding how variations in silicon and chromium content influence the microstructural evolution and mechanical behavior of Fe-2.6C-Cr-Si alloys, guiding their application in different industrial contexts where specific mechanical properties are required (Fig. 5).

In the phase diagram of the Fe-2.6C-Cr-Si system, the presence of silicon and chromium influences the formation of various phases, including carbides such as M_3C_2 , M_7C_3 , and $M_{23}C_6$. Additionally, chromium silicide (Cr_3Si) forms under certain silicon and chromium concentrations. Chromium silicide is undesirable in this context due to its brittle nature, which can adversely affect the alloy's mechanical properties, particularly its toughness and ductility. The formation of chromium silicide alongside carbide phases underscores the complex interplay between alloying elements and phase stability within the Fe-2.6C-Cr-Si system.

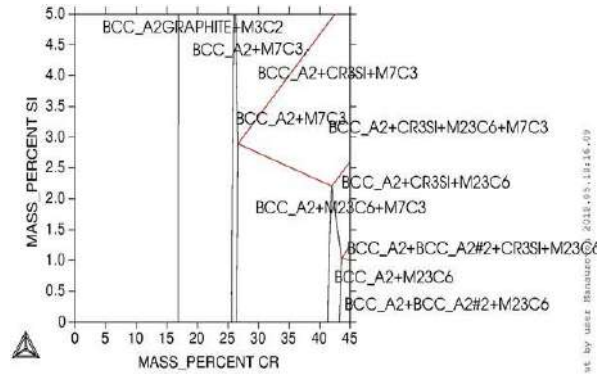


Fig. 5. Phase diagram of Fe-2.6C-Cr-Si, T-200 °C

Understanding these phase relationships is crucial for optimizing alloy compositions to minimize the formation of brittle phases like chromium silicide, thereby enhancing the alloy's suitability for applications requiring superior mechanical performance and durability.

Thus, the optimal amount of silicon in white cast iron is no more than 1%, which ensures good casting properties. The thermodynamic state diagram of the four-component Fe-2.6C-Cr-Ti alloy at 200 °C consists of several phases. Chromium content up to 16% and titanium up to 10% leads to the formation of a ferritic-austenitic structure, as well as the presence of free graphite. The carbide phase is represented by M_3C_2 type carbide.

When the chromium content falls within the range of 16-26% in the Fe-2.6C-Cr-Si system, the alloy structure does not exhibit free graphite. Instead, the carbide phase is characterized by the presence of two types of carbides: M_3C_2 and M_7C_3 . (Fig. 6).

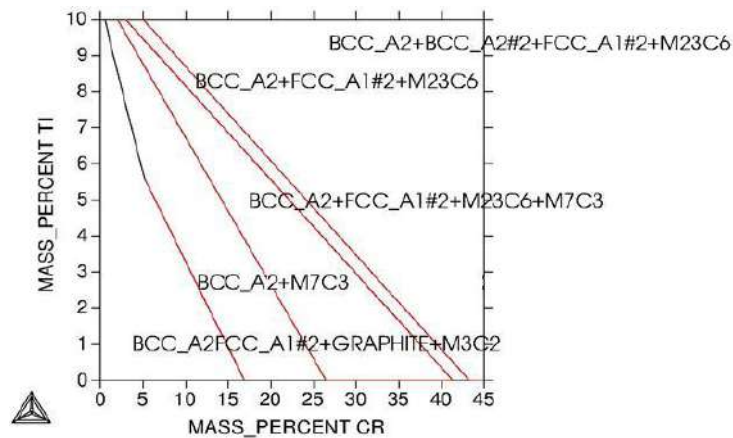


Fig. 6. Phase diagram of Fe-2.6C-Cr-Ti, T-200 °C

This compositional range supports the stable formation of these carbide phases, which play crucial roles in enhancing the alloy's hardness, wear resistance, and overall mechanical properties. The absence of free graphite is significant as it helps maintain the alloy's structural integrity and mitigates potential weaknesses associated with graphite formation, thereby optimizing its performance in demanding industrial applications. When the chromium content in the alloy is 26-42%, the structure of the alloy is represented by a ferritic-austenitic matrix, the carbide phase is represented by M_7C_3 and $M_{23}C_6$. Only when the chromium content in the alloy is more than 42%, only one type of carbides is present in the alloy structure - $M_{23}C_6$.

Conclusions

The hardness and microstructure of high-chromium cast irons (HCCIs) grades 280Cr29Ni and 330Cr17, which are commonly used in wear-resistant components for mining and metallurgical equipment, have been thoroughly studied. The investigation showed that the alloy's performance is closely linked to its metallic matrix structure and the formation of carbide phases, which are influenced by the specific alloying elements used.

A comprehensive thermodynamic analysis of the multicomponent Fe-2.6C-Cr-alloying elements system was performed to understand crystallization processes. The analysis identified the optimal ratio of alloying elements such as Cr, Mn, Si, and Ti, which are critical for the development of a metallic matrix and carbide phases that enhance the hardness of the alloy.

Ternary, quaternary, and multicomponent phase diagrams, including systems like Fe-C-Cr, Fe-C-Ni, Fe-C-Mn, and Fe-C-Cr-Ni, were developed. The resulting iso- and polythermal sections (at 200 °C) enriched the theoretical understanding of phase equilibria in high-chromium cast irons. These phase diagrams are essential for guiding the design of cast irons with tailored properties.

The research determined that the composition of 3.2-3.4% carbon, 0.4-0.6% manganese, 16-18% chromium, 0.4-0.6% silicon, 0.4-0.6% nickel, and 0.4-0.5% molybdenum (with the remainder being iron) represents an economical and high-performing grade of HCCIs. This optimized alloy composition not only improved the mechanical properties but also resulted in significant cost savings in the alloying process, particularly in reducing the consumption of ferrochrome, nickel, and other elements.

The optimized chemical composition and the use of advanced casting and heat treatment processes led to an extension of component life by at least 20% and a reduction in production costs by 30%, making the alloy highly suitable for industrial applications requiring enhanced wear resistance.

References

- [1] Journal article: Matteis P, Scavino G, Castello A, Firrao D. High temperature fatigue properties of a Si-Mo ductile cast iron. *Procedia Materials Science*. 2014 Jan 1;3: 2154-9.
- [2] Kopyciński, D., Piasny, S. Influence of tungsten and titanium on the structure of chromium cast iron // *Archives of Foundry Engineering*. 2012, No 12(1), - P 57-60.
- [3] Zhumaev A.A., Mansurov Yu.N., Mamatkulov D.D., Abdullaev K.S. Phase Transformations In Iron-Carbon Alloys Doped With Rare Earth And Transition Metals. // *"Chernye Metally"*, 2020, No. 11, pp. 22–28.
- [4] Pranav U., Agustina M., Mücklich F. A Comparative Study on the Influence of Chromium on the Phase Fraction and Elemental Distribution in As-Cast High Chromium Cast Irons: Simulation vs. Experimentation. // *Metals*. 2020, No 12, - P 4-17.
- [5] Ponomareva A. V., Ruban A. V., Mukhamedov B. O., Abrikosov I. A. Effect of multicomponent alloying with Ni, Mn and Mo on phase stability of bcc Fe-Cr alloys // *Acta Materialia*. 2018. Vol. 150. - P. 117–129.
- [6] Mukhamedov B. O., Ponomareva A. V., Abrikosov I. A. Spinodal decomposition in ternary Fe-Cr-Co-system // *Journal Alloys Compd*. 2017. Vol. 695. P. 250–256.
- [7] Ali K., Ghosh P. S., Arya A. A DFT study of structural, elastic and lattice dynamical properties of Fe₂Zr and FeZr₂ intermetallics // *Journal Alloys Compd*. 2017. Vol. 723. - P. 611–619.
- [8] Konar B., Kim J., Jung I. Critical Systematic Evaluation and Thermodynamic Optimization of the Fe-RE System: RE = La, Ce, Pr, Nd // *Journal Phase Equilibria and Diffusion*. 2016. Vol. 37, Iss. 4. - P. 438–458.
- [9] Zhumaev A.A., Mansurov Yu.N., Mamatkulov D.D., Ulugov G.U. Optimization of the composition and structure of wear-resistant white cast irons used in the mining industry. // *"Chernye Metally"*, 2020, No. 12, pp. 4–10.
- [10] Kolokoltsev V. M., Petrochenko E. V., Molochkova O. S. Influence of boron modification and cooling conditions during solidification on structural and phase state of heat- and wear-resistant white cast iron // *CIS Iron and Steel Review*. 2018. Vol. 15. - P. 11–15.
- [11] Zhumaev A.A., K. E. Baranovsky, Mansurov Yu.N., Kh. I. Akhmedov. Results of study of the structure of castings from white wear-resistant cast irons. // *"Chernye Metally"*, 2022, No. 2, pp. 4–10.
- [12] Abrikosov I. A., Ponomareva A. V., Steneteg P., Barannikova S. A., Alling B. Recent progress in simulations of the paramagnetic state of magnetic materials // *Current Opinion Solid State Materials Science*. 2016. Vol. 20. - P. 85–106.
- [13] Ahmad J. K. Melting of a new carbon-free waxed sponge iron in Electric Arc Furnace (EAF) for steelmaking // *International Journal of Materials Science and Applications*. 2015. Vol. 4. No. 1-2. - P. 1–6
- [14] Shamelkhanova N. A., Uskenbayeva A. M., Volochko A. T., Korolyov S. P. The Study of the Role of Fullerene Black Additive During the Modification of Ductile Cast Iron // *Materials Science Forum*. Switzerland. 2017. Vol. 891. - P. 235–241.
- [15] Ying Z and Hideo N. Influence of boron on ferrite formation in copper-added spheroidal graphite cast iron and its counteraction method. *China Mat Sci Tech Assoc Iron Steel Technol* 2014; 11: 409–416.
- [16] Scheidhauer N, Dommaschk C, Wolf G. Oxidation Resistant Cast Iron for High Temperature Application. In *Materials Science Forum* 2018 (Vol. 925, pp. 393-399). Trans Tech Publications Ltd.
- [17] Fava, A.; Montanari, R.; Richetta, M.; Varone, A. Analysis of Relaxation Processes in HNS Due to Interstitial-Substitutional Pairs. *Metals* 2017, 7, 246.
- [18] Zhang, Y.; Li, J.; Shi, C.; Qi, Y.; Zhu, Q. Effect of Heat Treatment on the Microstructure and Mechanical Properties of Nitrogen-Alloyed High-Mn Austenitic Hot Work Die Steel. *Metals* 2017, 7, 94.
- [19] Abdel-Aziz Kh., El-Shennawy M., Adel Omar. Microstructural characteristics and mechanical properties of heat-treated high chromium white cast iron alloys. *International Journal of Applied Engineering Research*. Vol. 12, Number 14 (2017) pp. 4675-4686.
- [20] Kim, I.W., Park, S.M.; Hong, S.I. Stress-Strain Curves and Crack Formation in an Ingot of Stainless Steel 21-4N under High-Temperature Compression. *Met. Sci Heat Treat*. 2017, 59, 24–29.
- [21] Ko, J.Y.; Hong, S.I. Microstructural evolution and mechanical performance of carbon-containing Fe-Co-Cr- Mn-Ni-C high entropy alloys. *J. Alloy. Compd*. 2018, 743, 115–125.

- [22] Lu, J.; Hultman, L.; Holmstrom, E.; Antonsson, K.H.; Grehk, M.; Li, W.; Vitos, L.; Golpayegani, A. Stacking fault energies in austenitic stainless steels. *Acta Mater.* 2016, 111, 39–46.
- [23] Pierce, D.T.; Jiménez, J.A.; Bentley, J.; Raabe, D.; Oskay, C.; Wittig, J.E. The influence of manganese content on the stacking fault and austenite/ ϵ -martensite interfacial energies in Fe–Mn–(Al–Si) steels investigated by experiment and theory. *Acta Mater.* 2014, 68, 238–253.
- [24] Xiong, R.; Peng, H.; Si, H.; Zhang, W.; Wen, Y. Thermodynamic calculation of stacking fault energy of the Fe–Mn–Si–C high manganese steels. *Mater. Sci. Eng. A* 2014, 598, 376–386.
- [25] Konca E, Tur K and Kocx E. Effects of alloying elements (Mo, Ni, and Cu) on the austemperability of GGG-60 ductile cast iron. *Metals* 2017; 7: 320.
- [26] Seidu S, Owoeye S and Owoyemi H. Assessing the effect of copper additions on the corrosion behaviour of grey cast iron. *Leonardo Electron J Pract Technol* 2015; 26: 49–58.
- [27] Zhumaev A.A., K.E. Baranovsky, Mansurov Yu.N., Kh. I. Akhmedov. Results of study of the structure of castings from white wear-resistant cast irons // “Chernye Metally”, 2022, No. 2, pp. 4–10.

Information of the authors

Jumaev Akhmadjon Abduvokhidovich, PhD, associate professor, Navoi State University of Mining and Technologies

e-mail: ahmadjon_jumaev@mail.ru

Akhmedov Khasan Islomovich, c.t.s., associate professor, Navoi State University of Mining and Technologies

e-mail: Khasan_akhmedov@mail.ru

Sayfidinov Okhunjon Odilovich, PhD, associate professor, Navoi State University of Mining and Technologies

e-mail: okhunjon_sayfidinov@mail.ru

Jumaeva Nargiza Kamoljonovna, master of science, Navoi State University of Mining and Technologies

e-mail: nargiza_jumayeva@mail.ru

Development and Creation of a Robotic Mining Complex for Selective Extraction of Coal Seams

Issabek T.K.², Ermekov T.E.¹, Kamarov R.K.^{2*}, Usenbekov M.S.²

¹L.N. Gumilyov Eurasian National University, Astana, Kazakhstan

²Abylkas Saginov Karaganda Technical University, Karaganda, Kazakhstan

*corresponding author

Abstract. The development of coal seams located in complex mining and geological conditions presents significant technical and economic challenges when using traditional high-performance mechanized complexes. In such environments, it is practical to create and employ cost-effective, yet mobile and maneuverable robotic technologies, such as mining manipulators, automated support systems, and robotic mining complexes. This paper provides a brief analysis of the mining and geological conditions of coal seams in the Karaganda basin and the current state of robotics development for coal mines. Historically, the annual coal production from 27 seam layers in the Karaganda basin suitable for selective extraction was about 15 million tons. However, losses of coal in these reserves due to traditional technology, which involves leaving coal pillars, reached approximately 9 million tons in 1998. The paper proposes a robotic technological complex for the selective extraction of coal seams under complex conditions.

Keywords: coal seam, complex mining and geological conditions, robotic mining complex, selective extraction, mining face, remote mining

Introduction

It is known that the Karaganda Basin is characterized by complex mining-geological conditions for the occurrence of coal seams and a high intensity of geological disturbances. The predominant form of discontinuous geological disturbances in the basin is faulting, which accounts for about 70% of all disturbances. The most common are tectonic disturbances with amplitudes ranging from 0.1 to 3.0 meters. Seam disturbances cause significant difficulties. About 20% of equipment relocations occur due to geological disturbances. Transition through these disturbances is associated with complications related to the need for stripping of surrounding rocks. As a result, the coal becomes contaminated with rock, and the mining machines are forced to operate under conditions that are not typical for them.

The main coal extraction in the basin is focused on flat and gently inclined seams with dip angles up to 18°, while extraction from steeply inclined and very steep seams, as well as from seams with complicated geological conditions, constitutes no more than 7%, even though their reserves exceed 30-40%. The difficulties in working these seams arise from the lack of effective technological schemes and extraction equipment. This situation leads to the detrimental practice of selectively mining the most favorable seams. As a result, not only are pillars left to support workings and in geological disturbance zones, but also significant reserves remain in localized areas characterized by various complex geological conditions. Therefore, the problem of developing localized areas with complex mining-geological conditions, including selective extraction of structurally complex and closely spaced thin seams, has been, and continues to be, particularly relevant [2, 3].

The development of unconventional technologies and specialized tools for working with various local geological formations (including formations with diverse purposes, layers exhibiting complex geometries, zones intersected by geological faults, etc.), as well as for handling complex-structured and closely spaced thin layers, has been an ongoing focus. This is particularly relevant to the selective extraction of complex-structured layers (such as k1, k, k10, k12, k13, etc.) and closely spaced thin layers separated by thin interbedded rock strata (e.g., d7-d8) [1, 2].

In the Karaganda Basin, during a certain period, the annual coal production from coal seams suitable for selective extraction reached 15 million tons using traditional technology. However, significant coal losses in the reserves, with coal packs left in place, amounted to approximately 9 million tons in 1998 [2].

It is important to note that employing the costly traditional technology using a shearer-loader within a mechanized complex was highly uneconomical under conditions that did not meet their technical specifications and performance criteria (i.e., unfavorable conditions). Serial mechanized complexes are designed based on technical parameters for operation in extended mining pillars with long mining faces. Shearers with standard screw heights are intended for complete seam extraction at a specified height, dealing with relatively soft coal masses and transporting homogeneous rock (coal) via conveyor. Selective extraction mainly targets complex-structured or closely spaced thin seams separated by thin rock interbeds. The extraction process was carried out as follows: first, the upper seam or coal pack was removed, followed by the rock interbed, and finally, the lower seam or coal pack was extracted. This selective extraction technology significantly reduces the productivity and reliability of the mining equipment, often rendering it economically unviable.

Due to the complexity of the mining conditions, there was no need to create large mining fields, which would have made the use of mechanized complexes and shearers economically unfeasible. In selective extraction

conditions, shearers were required to extract coal from closely spaced seams in two or even three passes, necessitating the undercutting of strong rock interbeds. In practice, selective extraction could also be carried out when encountering minor geological disruptions.

1. Paths to Solve the Problem

One approach to enhancing and advancing coal mining technology in complex mining-geological and mining-engineering conditions is the development of modern mechanization, automation, and robotics for extraction and tunneling operations.

Previous analysis of research and developments by leading scientists and specialists in the mining industry on robotics for coal mines indicates that the mining industry is among the foremost non-machinery sectors where the creation and implementation of industrial robots is of significant importance [3 - 5].

The primary justification for such decisions is that working conditions in mines are considered extreme for humans. As mining operations progress deeper, the number of injuries and underground explosions due to rock pressure increases. The frequency of accidents for underground workers is 4 to 5 times higher, and 8 to 9 times higher in deep mines, compared to surface operations. The complexity of mining-geological factors exacerbates the already challenging conditions of underground production. In coal mines in Russia, Ukraine, and Kazakhstan, the level of mechanization for extraction and tunneling processes is about 40%, while for auxiliary processes it is 10-15%. Given this situation, the development of mechanization and automation for various auxiliary technological operations, as well as mobile universal tools for working in localized sections of coal seams with complex geological conditions, is viewed as an alternative to specialized mechanization equipment [5 - 6].

The principles and concepts of industrial robotics and flexible automated manufacturing systems were established and began to be implemented in the former USSR and Kazakhstan by the early 1980s. During this period, the Karaganda Polytechnic Institute, under the guidance of Academician A.S. Saginov of the National Academy of Sciences of the Republic of Kazakhstan and Professor T.E. Ermekov, initiated work on developing the scientific and technical foundations and technological parameters of unconventional technology and methods for flank-front mining of seams with complex mining-geological conditions. Subsequently, these efforts focused on creating and refining the technology for seam extraction using short mining faces without the need for preparatory development works, thus reducing assembly and disassembly operations and ensuring effective extraction of localized areas and seams with challenging mining conditions. The following practical results were achieved [1 - 3]:

- parameters for technological schemes of frontal-flank selective mining using extraction manipulators—precursors to robotic technology systems - were developed and studied. These systems facilitate the effective extraction of localized areas and seams with complex geological conditions.
- a methodology was developed for selecting and justifying methods for selective face treatment and determining their advancement rates.
- various technology options were developed for transitioning geological disturbances such as normal and reverse faults with amplitudes up to 2 meters.
- technical specifications were developed for the creation and implementation of a robotic complex for selective extraction (KRS) and the "Tentekski" extraction complex with bidirectional movement of the KT-D.

In the 1990s, work on mining robotics using manipulators began in the United Kingdom, Japan, the United States, Germany, and the Czech Republic. Carnegie Mellon University (Pittsburgh, USA) developed and tested a model of an underground robot at a mine in Pennsylvania. In 1995, the United States began widely using robotic manipulators for drilling blastholes (by Fanuc) and installing concrete segmental lining in tunnels (by Daewoo). In the United Kingdom, mining robotics is being pursued as part of a government program. In Australia, a two-phase program for mining process automation was developed, consisting of:

- remote automated control of mining equipment with manipulators;
- transition to comprehensive automation of mining systems using robotic manipulators.

Existing mining and tunneling equipment cannot fully eliminate manual labor during technological operations. Several approaches could address this issue. One approach is to ensure that advanced technological schemes and corresponding equipment integrate interconnected technological operations comprehensively. However, many operations are performed discretely over time, and the overall reliability of the technological scheme is a significant factor. Another direction is the creation and implementation of equipment complexes in mining faces that mechanize and partially automate both primary and auxiliary processes. However, experience with automated mining face equipment has shown that the labor intensity of manual operations does not significantly change as a result of automation. Consequently, a new direction is emerging: a higher level of comprehensive mechanization and automation of underground operations through the application of robotics. This approach should enable manipulation operations using automated manipulators, information collection (via visual, acoustic, and other sensors) in the immediate work zone, and the creation of conditions that allow for the removal of human operators from these zones.

The future of underground mineral extraction is linked to the development and implementation of technology for unmanned mining, which is currently advancing in three main directions [3]:

- coal mining without the continuous presence of humans in the mining face, which involves only brief human visits to the face for equipment maintenance and inspection.

- coal mining using methods and tools that eliminate the need for human presence in the mining area.
- underground coal mining (or geotechnology) without human presence, involving the management of the entire process from the surface.

The first direction is based on the development of integrated and unit-based mining using microprocessor technology in long mining faces (primarily for thin and medium-thickness seams) with coal extraction by shearers or plows. Significant experience has been accumulated in this area.

The second direction focuses on creating remotely controlled units with programmable control for short mining faces (including the use of hydraulic mining) and developing technical and technological solutions using unconventional methods.

The third direction relies on technology and equipment that allows for the execution of the entire set of operations from the surface after the preliminary alteration of the coal's physical state.

To remove humans from complex mechanized mining faces during extraction, it is necessary to address the automation of core processes. For reliable operation of the equipment without constant human presence in the mining face, an automation system must be created, which includes subsystems for: drive control, roof support equipment and seam geometrics, hydraulic system control and monitoring, as well as data collection and processing about the condition of machines and equipment.

New sensors and hydraulic and optical systems have been developed and tested in mines. However, even with the creation of reliable control systems, it remains challenging to fully eliminate human presence from the mining face due to the imperfections of technology and unaccounted disturbances from the mining environment. As long as humans are responsible for monitoring equipment operation, environmental conditions, process adjustments for auxiliary operations, and resolving extreme situations in the mining face, the task of removing human operators remains difficult [3 - 5].

For complex mechanized mining faces, the problem of unmanned mining should be addressed in two stages. The goal of the first stage is to eliminate manual labor, which can be achieved by integrating a range of machines and mechanisms into the complex to perform individual work processes and auxiliary operations instead of humans. This may involve using teleoperated robotic manipulators equipped with universal manipulators, various sensor systems, and mechanisms for moving through mining faces. Only after this can the technological process be implemented without human presence in the mining faces, for which a necessary base of robotics and automation must be created.

Mining face equipment represents a higher level of development in mining technology compared to complexes, and the task of eliminating manual labor is primarily defined by technical solutions related to technology, equipment, and automation systems. Naturally, alongside traditional technical solutions, various types of robotic manipulators, such as informational and copying robots, may be used.

One of the conditions for the successful operation of underground manipulator robots is effective informational awareness of the working environment and the robot itself. This role is played by the robot's sensory system, which includes tactile (mandatory), visual, and other sensors. It is well known that through visual channels, humans receive 80-90% of all information about the environment. Therefore, a significant portion of the information needed for effective manipulation and movement of underground robots will come from visual sensors (video sensors). Since biotechnical robots controlled remotely are considered most promising for underground conditions and the final recipient of information is the human operator, the system involves "operator-visual sensor-manipulator-environment."

The use of visual sensors as informational devices, especially in non-standard underground equipment, opens up fundamentally new possibilities for assessing the state and relative positioning of objects in three-dimensional space for manipulation purposes. It allows for increased recognition and interpretation of observed objects, including tasks such as determining the boundaries of "rock-coal," diagnosing faults and hazardous conditions, and more. This should lead to improvements in traditional automation systems and the creation of robotic manipulative complexes.

The anticipated technical and economic benefits of robotizing production processes in mines include reducing manual labor and the labor intensity of operations, freeing up and more rationally utilizing workforce, creating conditions for increased productivity and machine operating time of mining and tunneling equipment, reducing injury rates by removing humans from the work zone, and relieving people from working in hazardous or hard-to-reach areas.

2. Robotic Complex for Selective Mining (KRS): Composition and Design Requirements

The KRS complex is designed for the selective (separate) extraction of coal and rock in seams located in complex mining-geological conditions, without the need for constant human presence in the mining face, while leaving rock in the mine [3 - 6]. The complex is intended for use in single seams with interburden or closely spaced coal seams with thicknesses ranging from 2.0 to 7.0 meters, with dip angles up to 55°, seam cutting resistance up to 400 kN/m, and strength of interburden layers up to 6 (according to Prof. M.M. Protodjakonov's classification). The thickness of interburden layers ranges from 0.4 to 1.5 meters. The system is designed to handle seams with hard inclusions and geological faults with amplitudes up to 1 - 2 meters.

Application Area of the KRS Complex [3]:

- development of flat, inclined, and steeply inclined seams with complex mining-geological conditions (e.g., complex seam geometrics, presence of hard inclusions, interburden layers, boulders, risk of outbursts, roof and floor instability, etc.);

- separate extraction of coal and rock;
- exploitation of blocks for various purposes;
- reworking of decommissioned reserves.

Applied Mining Systems: Pillar mining with lengths of 60 - 100 meters and short pillars with lengths of 25 - 60 meters without the creation of development workings. Roof Control: Complete collapse of the main part of the longwall and partial backfilling of the worked-out space along the conveyor drift (heading).

Complex KRS: The KRS complex consists of a screw backfilling device based on the "Start" drilling rig, the "Titan" backfilling complex, and hydro-electrical equipment with control systems and microcomputers utilizing microprocessors, specifying the quantity (set) and designation of its components (Table 1).

Table 1. Composition of the KRS Complex

№	Equipment Name	Designation	Quantity
1	Excavation Machine-Manipulator	VMF-5	2
2	Mechanized (Automated) Support (three sizes)	Based on AK-2, KPK-1 ("Pioma 25/45-03" or "Fazos 24/53")	1 (for 60-100 meters)
3	Sections of Mechanized Support (four sizes)	Based on M130*	5 - 10
4	Upper Junction Support (with ventilation drift)	T6K	1
5	Lower Junction Support (with conveyor drift)	M81SK	1
6	Face Conveyor	SKU	1
7	Screw-Feed Device	"Titan"	1
5	Reversible Drift Conveyor	SP87P	1
9	Pumping Station Group	SNU-5	2
10	Electrical Equipment	-	1
11	Automatic Control System with Microprocessor Devices and Microcomputers	-	1

* Supports, depending on technical conditions, may also be from other manufacturers.

The primary criterion for the operation of mechanized support for mining a particular seam is the correspondence of the geological conditions of the seam to its technical specifications. Key geological conditions include: the thickness of the seam being mined, the dip angle of the seam, the load-bearing capacity of the roof and floor of the seam, and the stability of the roof.

The support for the main part of the longwall, AK-2 or KPK-1, is designed to support the roof in the immediate face area, protect the working zone from roof collapse, and manage the roof of the main part of the longwall.

The support sections for the backfill area of the longwall, M130, are intended to support the roof in the immediate face area, protect the working zone from roof collapse in the backfill section, and for the suspension of backfill pipelines and ensuring the placement of waste rock in the worked-out space behind the support sections.

The junction supports T6K and M81SK are designed to secure and support the upper and lower junctions of the longwall with adjacent workings and to prevent sliding of the linear sections of the supports. Junction supports must ensure the compact arrangement of face equipment in the end parts of the longwall. Specific design modifications for the lower junction supports will be finalized during development.

The face conveyors SKU ensure the delivery of broken coal and rock. The conveyor SKU-45 includes a drive head with an electric motor, shaker sections, a chain with cantilever folding scrapers, troughs for the track chain, and hydraulic and electrical communications for control. The face conveyor on the side of the longwall's caved section must be raised relative to the seam floor to ensure the section support base fits by 130 mm with a depth of 430 mm. The length of the linear conveyor sections is 1100 mm. The spacing of the cantilever scrapers should be 1000 mm. The load on the traction chain during the transportation of coal and rock should not exceed 843 kN.

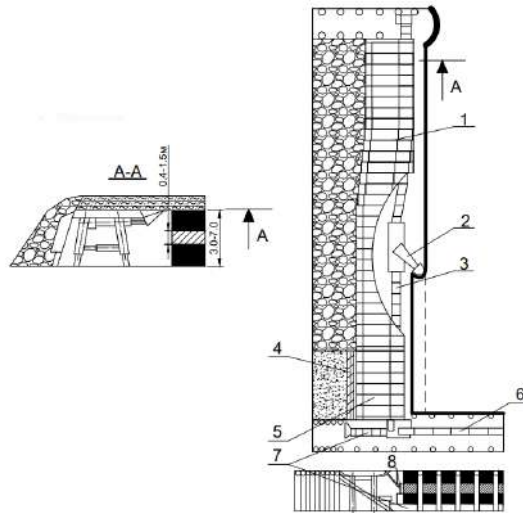
The reversible drift conveyor based on the conveyor SP87P is intended for transporting coal to subsequent drift conveyors and for loading the broken rock into the reception hopper of the backfill device during reverse operation.

The KRS complex consists of a mining manipulator VMF-5, VMF-6 with mechanized support and conveyor, electro-hydraulic equipment, and adaptive-program control equipment with diagnostic capabilities.

The application of the KRS complex allows:

- significantly reducing mineral losses during the operation of coal mines;
- mining closely spaced coal seams with a distance of (0.5 - 2 m) and a dip angle up to 55° using selective mining technology, leaving rock in the mine;
- decommissioning and mining technogenic reserves of mineral deposits, as well as developing blocks of various purposes in ore and non-ore deposits under complex geological conditions.

Figure 1 shows the general view of the complex with a single automatic mining manipulator in the longwall.



1) linear support sections AK-2, KPK-1; 2) mining manipulator VMF; 3) face conveyor SKU; 4) screw backfill machine "Titan"; 5) support sections M-130 with backfill device; 6) drift conveyor SP87P; 7) reclaimer; 8) support device

Fig. 1. - KRS Complex for Waste-Free Selective Mining (with one manipulator operating in the longwall)

According to the Figure, the KRS complex with a single mining unit includes linear sections of mechanized support 1, a mining machine in the form of a mining automatic mining manipulator 2, located on a base and supported by skis on the guide rails of the transporting conveyor 3, and a backfilling machine 4, support sections with a backfilling device 5, a drift conveyor 6, a loader 7, and a rib support device 8.

Based on the results from reviewing the indicators on the technical level and product quality card for the selective mining complex, the KRS complex should ensure full automation of clearing operations in panels with separate extraction of coal and rock without the constant presence of people in the mining face, while leaving the extracted rock in the mine for backfilling.

When developing a steeply inclined seam, a special transport base with speed dampers for coal fragmented by manipulators is used.

A brief summary of the KRS complex characteristics is presented in Table 2.

Table 2. Brief Characteristics of the KRS Complex

Indicator	Value
Productivity of one manipulator with automatic control, t/min	2,5
Number of manipulators per unit, pcs	10
Power of one manipulator's electric motor, kW	22
Number of degrees of freedom of the manipulator	5
Total power of the complex's electric motors, kW	240
Specific energy consumption of the unit, kWh/t	0,4
Weight of one manipulator, t	Up to 5.0
Total weight of the support complex for a face length up to 60 m, t	About 150
Mining system	Pillars along the strike
Roof control	Complete collapse
Soil types	Any type of support with a bearing capacity of not less than 1.0 MPa (10 kg/cm ²)
Mine gas category	Exceedingly high category
Extractable seam thickness, m	2,0-7,0
Seam dip angle, degrees	Up to 55
Face length, m	Up to 60-100
Daily load on the complex, t/day	Up to 5000
Type of support for the support complex	AK-2, KPK-1
Type of conveyor for seam dip up to 35 degrees	SKU-45

3. Description of the KRS Complex and Operating Principle

The KRS complex, consisting of several mining units, includes mechanized support (possibly of the AK-2 or KPK-1 type), M130 support sections in the backfilling part of the panel, a face conveyor SKU or a guiding transporting device, and the working organs of manipulators.

The working organs are designed as automatic manipulators, movably installed every 10 - 12 support sections, with four legs. The guides are made with movable curved sections located on the transporting device and on the base of the mechanized support sections. These curved sections are paired and connected by hydraulic cylinders, whose cavities are parallelly connected through pipelines to a distributor. The handle is positioned to interact with a cam, which is pivotally mounted on the base of the manipulator and to which the ski grips are also pivotally attached. The hydraulic cylinders are connected to the hydraulic distributor via pipelines and a check valve. At the ends of the panel, the guides have a pair of curved sections II: both on the base of the support section and in the face area, meaning that the terminal ends of the guides have a T-shaped design.

To ensure precise positioning of the manipulator under the support section at the ends of the guides installed on the base of the support section, stops are provided.

To concentrate clearing and preparatory work, the end parts of the guides are T-shaped with movable curved sections.

Figure 2a shows the general view of the KRS complex; Figure 2b shows the general plan view of the complex; Figure 3a illustrates the structural scheme of the guides and their control system; Figure 3b shows view A; Figure 4 shows the flow technology of coal extraction using several mining manipulators VMF-5, VMF-6; Figure 5 shows the control block of the KRS complex.

The KRS complex (Figures 2 and 3) includes mechanized support sections with a base 2 and a cover 1, a mining machine in the form of a manipulator 4 located on the base 5, supported by skis 6 on the guides 7 of the transporting device 8. The guides have straight sections 9, 10 located on the transporting device and movable curved sections 11 located on the base of the support sections 2. The curved and straight sections have guides 28 that interact with the grips 29 and 30 (Figure 3), controlled by hydraulic cylinders 31 and 32 (Figure 2).

On the base of the manipulator 5, control equipment 33 is installed. The hydraulic control system consists of a control hydraulic block 34 for the boom and head of the manipulator 4, pumps, a current regulator, a distributor interacting with cam-operated check valves of the lifting-lowering hydraulic cylinders, rotation, hydraulic distributor, and grip cylinders. The control hydraulic block 34 includes a pressure relief valve, a section for controlling the lifting-lowering hydraulic cylinders, and a section for controlling the rotation of the manipulator boom.

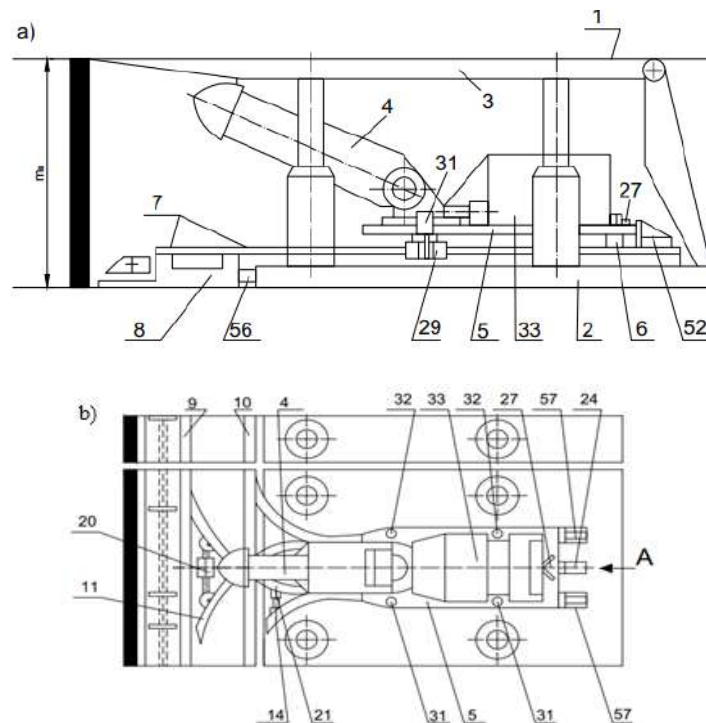


Fig. 2. – Section of mechanized support with VMF-5 manipulator: (a) general view of the KRS complex; (b) top view

The conveyor or transporting device 8 is connected to the base of the support section 2 via a hydraulic cylinder 56 (Figure 2). Fixed stops 57 are installed on the base of the support section 2. The stop 57 restricts the

manipulator's movement towards the collapse, regardless of the position of the support section, helps in accurately positioning the manipulator in the initial position, and protects the handle 25 of the distributor 24 from excessive force impacts. When positioning the manipulator in the initial position, the curved sections of the guides are automatically moved to the working position by the cam 26 of the distributor 24 through the handle 25 (Figure 3). A support-rotating device carries out the rotation of the working organ (manipulator boom) in the horizontal plane with rotation hydraulic jacks 30.

The robotic complex operates as follows. In the initial position, the manipulators are located under the support section. The handle 27 (Figure 3) is rotated to the required position, for example, for movement to the right, position "P". In this position, the cam 26, acting on the handle 25 of the distributor 24, directs the working fluid through pipeline 22 to the hydraulic cylinders 20 and 21. Under the action of the moving pistons of these hydraulic cylinders, the movable curved sections of the guides 11, 12, and 13 are tightly pressed against the straight sections of the guides 9 and 10, allowing the manipulators to move to the right, as shown in the figure.

Simultaneously, the right grips 30 are brought into the working position. For this, working fluid is supplied from the control section through pipelines via the distributor and check valve to the hydraulic cylinders 31 and 32, thus bringing the grips 30 into the working position while retracting the grips 29. At the same time, working fluid is supplied through the pipeline via the check valve to the rotation hydraulic cylinder, setting the required angle for the rotation of the manipulator boom 4 towards the face. The manipulator boom is mounted on the upper support-rotating platform, which is connected to the lower platform via hydraulic jacks for platform extension.

The preparation of manipulators I, II, III, and IV for mining operations is now complete. All preparatory work is conducted from adjacent workings: a command is given to one of the end manipulators, and the others repeat this command, as they all perform the same operation, which simplifies automation significantly.

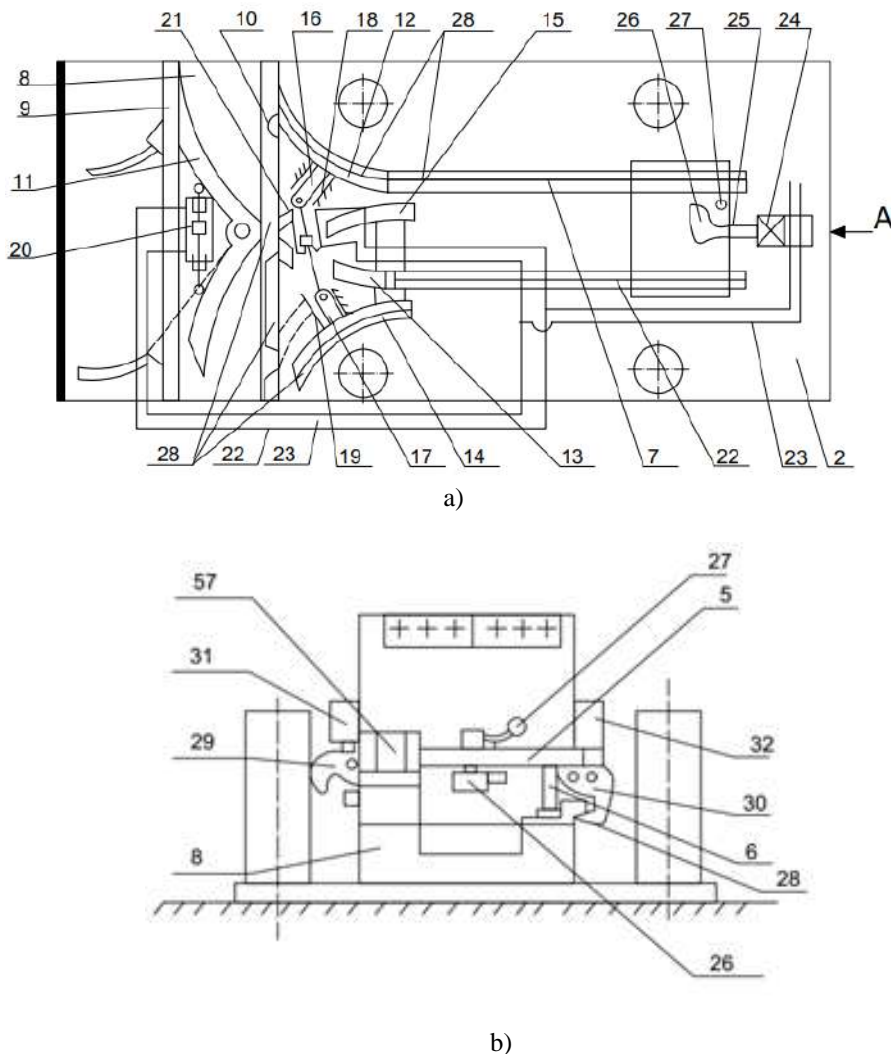


Fig. 3. - Controlled curved sections of the manipulator base: (a) structural diagram of the guides and their control system; (b) view A

Next, all manipulators gradually move onto the straight sections of the guides and start cutting. When on the straight section of the guides, each manipulator performs the excavation of valuable minerals in its section (Figure

4). After finishing the processing of their sections, manipulators I, II, and III return to the initial position under the nearest support section, the conveyor and mechanized support are moved towards the face, and manipulator IV, moving along the curved section to the guide located in the working area, performs excavation to prepare this working area to a depth equal to the unit's movement step, as shown in the figure, and then also returns to the initial position.

Excavation work in the opposite direction is performed similarly to the previous operation. In this case, the handle 27 is set to the left position "L" (Figure 2b), and working fluid is supplied through pipeline 23 to hydraulic cylinders 20 and 21. As a result, the piston of hydraulic cylinder 21 moves upward, retracting the movable curved guides 12 and 13 from the working position. These guides are moved at an angle to the straight sections of the guides, aided by the positioning of the eyelet 16 in the guiding grooves 18. At the same time, the movable curved guides 14 and 15 are brought into the working position, moving towards the positioning of the eyelet 17 in the guiding groove 19, and the curved guide II is positioned in the working state by rotating around its axis.

The grip 29 is moved to the working position by supplying working fluid through pipeline 45 (Figure 3), while grip 30 is retracted from the working position, and the manipulator boom is rotated to the opposite direction, as shown in Figure 4d. The movement of grips 29 and 30 from one position to another is necessary to ensure the stability of the manipulator base. The grips are moved in such a way that the grips on the collapse side, in this case, grips 29, are active.

If any manipulator fails, for example, the nearest manipulators that have the same movement direction, as shown in Figure 4 process manipulator 1, its section.

Upon completion of the excavation work, the transporting device is moved forward, the mechanized supports and manipulators are returned to their initial positions, and the manipulator that has entered the working area performs preparatory work (deepening the working area).



Fig. 4. – Continuous Coal Extraction Technology VMF-5, VMF-6

The continuous coal extraction technology is implemented using VMF-5 and VMF-6 manipulators. The average value of the expected current for the actuator during operation is 10 - 30 A for 6 seconds, with a variance of 4 seconds, then decreasing to 20 A and 2 A respectively, while the electric motor is loaded at 60 – 65% of its capacity.

Simultaneously, repair of the failed manipulator III is carried out, provided it does not involve accessing the electrical components, and preparation for the next cycle is undertaken (Figure 4, d).

The main advantage of the proposed unit is the ability to concentrate mining and preparatory operations within the extraction field, which provides a significant economic benefit by combining extraction and preparatory processes.

Unlike known complexes of this type, there are no issues with boom rotation, and the automation of the extraction process is facilitated since all manipulators can work simultaneously performing the same operations. The process of switching curved guide sections from one position to another is automatically handled when the machines are positioned under the support sections. If any manipulator fails, the two adjacent manipulators can replace it. During excavation work at one end, the end section of the face conveyor, conveyor line, and support sections are moved at the other end, along with other auxiliary tasks. The failed manipulator can be repaired under the support without stopping the extraction work, provided it does not involve accessing the electrical components.

Using identical manipulators for preparatory and extraction work allows mining workers to gain practical

skills in their operation more quickly. The number of curved guides exceeds the number of manipulators per unit, and these (curved guides) are spaced evenly along the length of the face.

4. Control Equipment for the Robotic Complex for Selective Extraction of Coal Seams

The creation of effective control systems for mining complexes aimed at ensuring safe working conditions requires the transition to microprocessor-based technology. The control equipment for the automated complex for selective coal seam extraction should provide a combination of manual, local, and automatic control of mechanized supports, mining manipulators, and conveyors according to a programmed schedule. Remote and automatic control of the complex for selective extraction allows for the removal of personnel from the mining face, thus increasing the productivity of both the complex and the operating staff.

At the interface preparation stage, the driver loads a microprogram (communication module) into the interface's RAM, which manages the conversion of data from the working format to a format suitable for transmission to the software module. An example of connecting the VMF-5 via the CAN bus is shown in Figure 5.

The control equipment and hydraulic drives must ensure the effective operation of the KPC complex with the help of [3 - 4]:

- boundary control sensor "Coal-Rock": according to Figure 5 (Developer - Department of Physics, KarTU);
- DMMK Sensor: A sensor for locating manipulators that operate on steeply inclined seams (used in seam development under particularly challenging conditions);
- end position sensors for combines (manipulators): Sensors for position control of the standardized DPU series. The standardized series of magneto-reed position sensors, DPU (DPU1-40, DPU2-40, DPU1-100, DPU2-100), are intended for monitoring the position of moving parts and mechanisms during various technological processes;
- upgraded sensors of the DPU series: DPG1-40, DPMG2-40, DPMG2-100, DPMG1-100, DPMG1-200, DPMG2-200 sensors are intended for controlling the movement of the monitored object (screen) perpendicular to or parallel to the working side.
- end position sensors for support sections: DPU sensors for tracking the position of the support sections during movement. The DPU-6 sensor monitors one of the end positions of the support sections; the DPU-7 sensor monitors the front position of the support sections and the stationary zone, which is equal to 60 minutes.

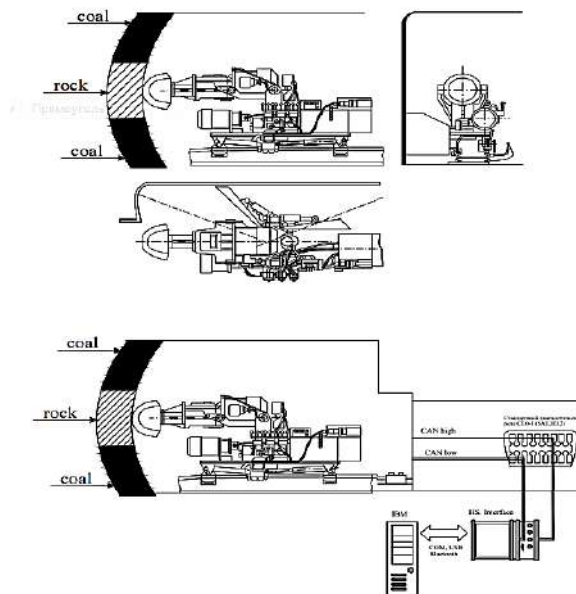


Fig. 5. - Control Block of the KPC Complex with Connection to VMF-5 via CAN Bus through "HS+Interface"

Conclusions

Based on previously conducted research and development work, a new direction for designing robotic systems and equipment using microprocessor technology for coal seam development under complex mining and geological conditions has been established. New technical solutions for creating mining complexes and equipment for the extraction of complex and closely spaced thin seams using selective mining technology are presented. These solutions are unified by the concept of using controlled mechanized supports and automated mining manipulators equipped with boundary tracking subsystems for "coal-rock" separation [7 - 10].

For the robotic complex for selective extraction (KRS), maximum use is made of standardized products based on mechanized mining supports of supporting and supporting-guard types and the actuator of the selective-action mining manipulator from serial tunneling machines. The applicability coefficient of the mining robotic complex is up to 85%.

According to the requirements for the technological and metrological support of design, production, and operation, the readiness coefficient of the KRS complex can be up to 0.8, while that of the VMF mining manipulator is up to 0.92. The service life of the SKU conveyor until the first major overhaul is 500,000 tons of transported coal.

References

- [1] Flangovo-frontal'naya vyemka plastovykh mestorozhdeniy / A.S. Saghinov, A.S. Kvon, A.G. Lazutkin, T.E. Ermekov. – Alma-Ata: Nauka, 1983. – 280 s. – (Uchastie v gl.4,5,6).
- [2] Isabekov T.K. Tekhnologiya frontal'no-flangovo-izbiratel'noy vyemki lokal'nykh uchastkov i ugol'nykh plastov so slozhnymi usloviyami zaleganiya. – Alma-Ata: KazgosINTI, 1997. – 245 s. (№ 7359-Ka97 ot 13.01.97, rus., dep).
- [3] Gornye i stroitel'nye robototekhnologicheskie komplekсы: Uchebnyk / T.E. Ermekov, T.K. Isabek, R.K. Kamarov, E.T. Isabekov. - Karaganda: Izd-vo KarGTU, 2015. – 297 s.
- [4] Ermekov T.E., Isabek T.K., Isabekov E.T. Ochistnoy kompleks robotizirovanny s avtotizirovannyim upravleniyem dlya selektivnoy vyemki ugol'nykh plastov. - Karaganda: KarGTU, Tr. universitet, KarGTU, №3, 2015. – S. 44 - 48.
- [5] Ochistnoy gorno-robototekhnologicheskiy kompleks s adaptivno-programmnyim upravleniyem: Tekhnicheskoe zadanie. / Ermekov T.E., Baymukhametov S.K., Isabek T.K., Kenzhin B.M. i dr. - Astana-Karaganda: MON RK, MIR RK, AO NATR, TOO KMK, ENU, KarGTU, 2014-2015. - 190 s.
- [6] Ermekov T.E., Isabek T.K., Kamarov R.K., Khuangan N. Ochistnoy robotizirovanny kompleks s adaptivno-programmnyim upravleniyem. - Karaganda: Tr. mezhd. nauch.-prakt. konf. «Integratsiya nauki, obrazovaniya i proizvodstva - osnova realizatsii Plana natsii», posvyashchennaya 100-letiyu akad. A.S. Saghinova (Saghinovskie chteniya №7), 10 - 11 dekabrya 2015 g., KarGTU, 2015. – S. 130 - 132.
- [7] Ermekov T.E. Nauchnye osnovy proektirovaniya i konstruirovaniya, robotizirovannogo kompleksa dlya gornoy promyshlennosti. Trudy pervoy mezhdunarodnoy nauchno-prakticheskoy konferentsii «Gornoye delo» v Kazakhstane. Sostoyanie i perspektivy: - Alma-Ata: RIO VAKRK. 2002. - S. 407 - 410;
- [8] Sozdanie i osvoenie proizvodstva gornogo ochistnogo robototekhnologicheskogo kompleksa (ORKAPU) / Ermekov T.E., Baymukhametov S.K., Isabek T.K., Kamarov R.K. i dr. - Karaganda: Tr. mezhd. nauch.-prakt. konf. «Integratsiya nauki, obrazovaniya i proizvodstva - osnova realizatsii Plana natsii», posvyashchennaya 100-letiyu akad. A.S. Saghinova (Saghinovskie chteniya №7), 10 - 11 dekabrya 2015 g., KarGTU, 2015. – S. 144 - 146.
- [9] Nauchno-prakticheskoe reshenie i obosnovanie parametrov na sozdanie i osvoenie proizvodstva gornogo ochistnogo robototekhnologicheskogo kompleksa: Monografiya / T.E. Ermekov, S.K. Baymukhametov, T.K. Isabek, E.T. Isabekov; Evraziyskiy natsional'nyy universitet imeni L.N. Gumileva, Karagandinskiy gosudarstvennyy tekhnicheskiiy universitet. – Karaganda: Izd-vo KarGTU, 2015. – 187 p.
- [10] Ochistnoy robotizirovanny kompleks s adaptivno-programmnyim upravleniyem (ORKAPU). - Dnepropetrovsk: „Nauchnyy vestnik NSU“, №4, 2016. – s.23-30. Avt. Ermekov T.E., Isabekov E.T.

Information of the authors

Issabek Tuyak Kopeevich, d.t.s., professor, Abylkas Saqinov Karaganda Technical University
e-mail: tyiak@mail.ru

Ermekov Toleukhan Ermekuly, d.t.s., professor, L.N. Gumilyov Eurasian National University
e-mail: ipk@kstu.kz

Kamarov Rymgali Kumashevich., c.t.s., professor, Abylkas Saqinov Karaganda Technical University
e-mail: kamarov_49@mail.ru

Usenbekov Meirambek Sabdenovich, c.t.s, associate professor, Abylkas Saqinov Karaganda Technical University
e-mail: meirambek1946@mail.ru

Review on Heat Sink and Efficiency Improvement of Heat Transfer in Different Applications

Ali S.*, Al-Abbas A.H., Magid H.M.

Al-Furat Al-Awsat Technical University, Technical College of Al-Mussaib, Mussaib, Iraq

*corresponding author

Abstract. Heat sinks are essential elements that disperse thermal energy from systems operating at high temperatures, including aerospace vehicles, semiconductor chips, and turbine engines. Over the last several decades, significant research has been focused on heat sinks to improve heat dissipation, reduce hot spot area temperatures, and lower components' temperature in the hot section. The enhancement of heat sink thermal performance faces several obstacles and requires the adoption of novel designs, materials, and adaptable production techniques. This study aims to provide a comprehensive review of the previous research on enhancing the thermal efficacy of heat sinks, the effect of fins arrangements on the final heat transfer efficiency and identify the improvement in the heating transfer. The effect of natural and forced convection on the heating transfer efficiency in heat sinks has been investigated in the current review with a focus on the utilization of different heat sink types of applications and uses along with the benefits and drawbacks of each type.

Keywords: heat sink, heat transfer, natural convection, forced convection, fins efficiency, fins shapes, fins arrangement.

Introduction

The temperature (Temp) rise has a detrimental impact on the functioning of several devices. For instance, a literature survey found that 55% of electronic component failures are resulting by over-temp [1], as depicted in Fig. 1. These components' failure rate doubles when the temperature rises by 10 °C. Conversely, a temperature reduction of 1 degree Celsius can result in a 4% decrease in the failure rate. Moreover, the performance of solar modules is directly influenced by the temperature of the cells [2]. It is significant to observe that only 20% of the sun rays received are transformed into electricity. The remaining surplus energy must be removed since any increase in temperature may have a detrimental influence on the system's performance. A temperature rise of 1 degree Celsius may decrease the electrical conversion efficacy of crystalline silicon cells by 0.5%. Similarly, for amorphous silicon cells, the efficacy drop is 0.25%. In general, a temperature rise of 1 degree Celsius may reduce power production by around 0.4 - 0.5% [3].

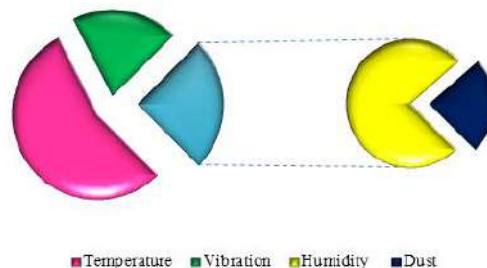


Fig. 1. The significant reasons for most electronic devices' failure [4].

Based on this data, it is evident that excessive heat or temperature rise poses a genuine issue that needs to be addressed. It is crucial to maintain the temp of various systems in the suggested limits set by producer and achieve the required performance [5]. In the last decades, there has been a dramatic transformation in microelectronic, computer, and smartphone technology, leading to their rapid dominance in the global industry [6]. The electronic business is being driven by consumer demands, leading to significant developments in device design and manufacture. In response to this need, the industry is innovating by producing more powerful and quicker goods than traditional equipment, which is considered outmoded [7]. The societal need for more advanced and efficient gadgets and the growing tendency in the electronics industry to make devices smaller but more powerful has driven significant technical progress in the engineering and design of portable electronics [8]. Tremendous progress in the thermal management of portable electronics has occurred alongside refining their power and size. Thermal management refers to the technique involved in generating, controlling, and dissipating the heat generated by electrical equipment. Insufficient thermal management may negatively impact an electronic device's reliability, performance, and power. Heat is an unavoidable consequence of all electronic devices, and due to its propensity to

negatively impact the dependability of these devices, it has become a crucial factor for designers to consider while creating advanced technology [9,10].

1. Background on Heat Sink

1.1. Fundamentals of Heat Sink

A heat sink is utilized to exchange heat and facilitate the passage of heat from a heat-producing equipment or source to a surrounding fluid. The fluid used is often air. However, it may also be any non-conductive fluid for heating transfer. The Heating sinks may be cooled passively via natural or forced convection involving a fan. Heat sinks are often fabricated using aluminum or copper [11]. A heat sink is specifically designed to efficiently disperse excess heat generated by the functioning of mechanical or electrical apparatus. If the waste heating is not effectively dissipated from the component, it might accumulate and lead to device malfunctions or decreased performance. A heat sink utilizes the principles of radiation, convective, and conductive transfer of heating to transfer heat from a higher-source temp to a lower-fluid temp [12]. Thermal energy is transferred from this source to the sink by conduction. Heat sinks are fabricated using materials with high heat capacity, meaning they can retain more heat per unit mass. Radiation and convection transfer heating from the sink to the neighboring fluid [13,14]. Increasing the surface area in contact with the heating exchange fluid enhances the heat transmission rate. Adding fins to the heat sink base material may significantly enhance the surface area. A heat sink might be either passive or active. An active heat sink utilizes forced convection generated by a fan or pump to efficiently move heat from the device, whereas a passive heat sink relies on natural convection [15].

A passive heat exchanger, a heat sink transfers thermal energy from an electrical or mechanical equipment to air or a liquid coolant [16]. This method disperses heat from the device, allowing temperature control. Computers utilize heat sinks to disperse heat from central processing units (CPUs), GPUs, chipsets, and RAM modules [17]. High-power semiconductor devices like power transistors and optoelectronics like lasers and light-emitting diodes (LEDs) need heat sinks when their natural heat dissipation capability is insufficient to maintain their temperature. Every heat sink is needed in changing applications [18]. Heat sinks are widely used for thermal management in several domains, including technology, industry, and natural systems. These components are so widespread that they may be easily disregarded, even by those knowledgeable about the technology [19]. A heat sink is specifically engineered to maximize the contact area between its surface and the surrounding cooling medium, including air, in order to enhance its cooling efficiency. The effectiveness of a heat sink is impacted by factors including airflow speed, choice of materials, design of protrusions, and treatment of the surface. The temp of integrated circuits is influenced by heat sink conduction mechanisms and thermal interface materials. Thermal paste or glue improves the efficiency of the heat sink by filling up any gaps between the heat sink and the heat spreader on the apparatus. In several engineering applications, a heat sink is often fabricated utilizing either aluminum or copper [16].

This review paper identifies and highlights the heat sinks from different perspectives including design, manufacturing, optimization, and applications. Also, the geometries and characteristics of heat sinks in previous studies are reviewed classified and summarized. It is focused on geometry design features to strengthen the impact of heating transfer and pressure drop. The correlation between geometric characteristics and heating transfer is also presented, and future research orientations are discussed. Furthermore, it provides and offers a clear vision of the majority of recent resources and contributions for many researchers in this direction and involves many analyses and evaluations about the methods of heat transfer techniques with some classification and how to conduct these techniques to be more useful and efficient. It also focuses on the methods of the design optimization process.

1.2. Temperature and Reliability

A heat sink represents a specialized apparatus that enhances the heating transfer process from a high-temperature surface, created by an electronic component, to a lower-temperature environment [13]. A fluid medium, such as oil, refrigerants, water, or surrounding air, might provide a colder atmosphere [20–23]. Cold plates, as referred to by Lee (2022), are heat sinks that use water as their fluid medium. Heat sinks primarily serve to augment the surface area of an electrical component that directly interfaces with a coolant. This design enhances the process of effectively dispersing heat, leading to a reduction in the operational temp of the device. The dependability of temp may greatly influence components such as steady-state temperature during continuous operation and temperature cycling. Within the temperature range relevant to electronical tool, it is well recognized that the dependability of electronics is significantly influenced by the temperature of their components, with a strong negative relationship that approaches exponential dependence. For every 2 degrees Celsius increase in temp, the dependability of a silicon chip decreases by around (10 percent) [24]. The standard temperature threshold for a silicon chip is 125 degrees Celsius. Nevertheless, there is sometimes a strong preference for a far lower design threshold to maintain an acceptable level of dependability, particularly in military goods. The failure rate of the component is also influenced by temperature cycling. Research funded by the U.S. Navy [25] found that equipment exposed to intentional temperature cycling of over 20 degrees Celsius had a failure rate that was eight times higher than usual.

Reliability may be assessed by examining the likelihood that a device can successfully carry out its designated tasks under specified circumstances for a particular duration. Product dependability is often regarded as

the paramount component in establishing the quality and excellence of a gadget within the industry. To guarantee the reliability of electrical equipment, it is essential to have sufficient thermal management in place [26]. Using a heat sink is the primary method of regulating thermal management in a tiny device.

2. Heating Transfer Technology

The thermal designs of electronic equipment have incorporated all three transfer of heating modes (radiation, convection, and conduction), as well as phase changes like boiling, condensation, melting, and solidification. Nevertheless, it is essential to note that electronic systems have no one-size-fits-all design approach. Several research [27–30] have reported a comprehensive overview of the advancements in the transfer of heating technology for the thermal control of electronic equipment since 1977. However, most selected techniques are based on Conduction, Convection, and Radiation. Numerous heat transfer methods are used across diverse applications. Several heat transfer methods are widely used in various applications as shown in Fig. 2 [31–36].

- heat exchangers are apparatuses that facilitate the transmission of thermal energy between two fluids. They are extensively utilized in many domains, including air conditioning systems, power generation facilities, and chemical processing plants.
- heat pipes are mechanisms for transporting heat via evaporation and condensation. These components are often used in electrical devices for heat dissipation.
- phase change materials are materials that are subject to a phase transition (changing from solid to gas or liquid) at a specific temperature. Thermal storage, cryogenics, and heat insulation are among the several applications they find useful.
- microfluidic heat transfer is a technological approach that employs diminutive channels to transmit heat. It is used in several fields, such as lab-on-a-chip technologies and medical implants.

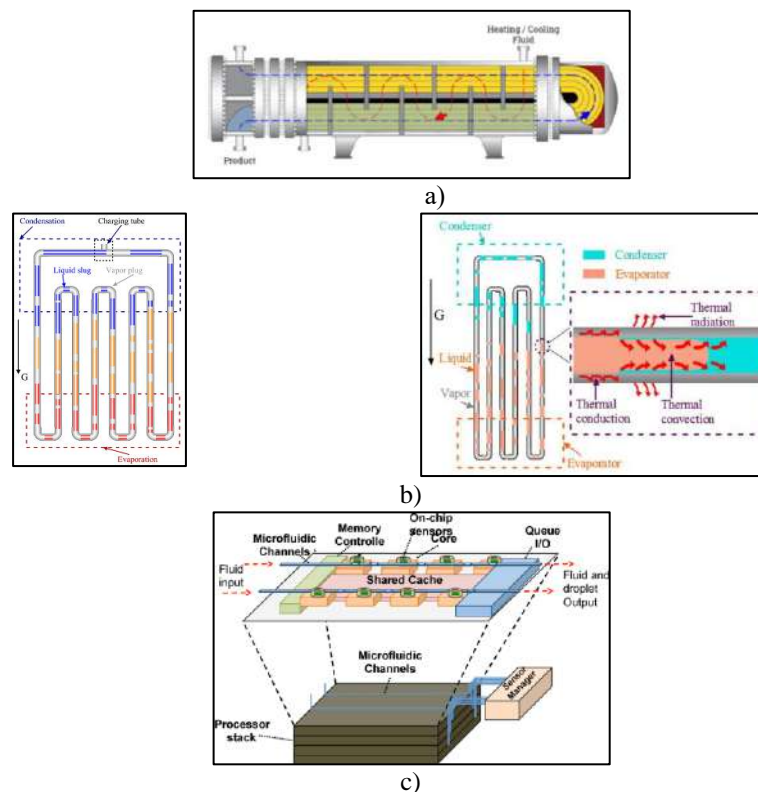


Fig. 2. - Heat transfer applications: a) heat exchanger; b) heat pipes; c) Microfluidic [37–39]

2.1.1. Principle of Heating Transfer via Heat Sink

A heat sink enables the transfer of thermal energy from a high-temperature device to a lower-temperature fluid medium. The frequently utilized fluid medium is air, however it can additionally include oil, refrigerants, or water. Once water is employed as the fluid medium, the heat sink is frequently referred to as a cold plate. In the field of thermodynamics, a heat sink refers to a reservoir that has the ability to absorb an unlimited amount of heat without experiencing a significant change in temp [40]. To efficiently conduct, radiation, and convection, heat sinks for electronic devices must maintain a temp higher than that of the surrounding environment. Electronic power supplies exhibit low efficacy, generating excess heat that may impair the device's functionality.

Consequently, the design incorporates a heat sink to dissipate heat. Utilizing the average air temperature represents an acceptable expectation for heat sinks of relatively limited duration. The logarithmic average air temperature calculates compact heat exchangers [41]. Based on Fourier's law of heat conduction, heating will flow from a location with a higher-temp to a region with a lower-temp once there is a temp difference in a system. The rate of heat conduction is directly related to the temp difference and the cross-sectional area in which heat is transmitted [42].

2.1.2. Natural and Forced Convection

Natural convection systems provide significant benefits in several disciplines and engineering scenarios because of their simplicity, low energy use, dependability, quietness, economy, and ease of maintenance. The items mentioned include heating systems, cooling systems, heat exchangers, radiators, heaters, photovoltaic panels, solar cells, condensers, evaporators, power stations, food businesses, and nuclear reactors [43].

A significant drawback of an essential natural convection system is its relatively poor transfer of heating rate compared to forced convection [44,45]. A widely used technique to enhance natural convection was to improve the transfer of the heating surface since this helps maintain relatively constant ambient temp and coefficients of thermal convection in most scenarios. Extended surfaces may be created by connecting or appending additional surfaces using components called "fins." Using fins in systems has become a prevalent technological and industrial convention. A multitude of research was performed on the transfer of heating using fins, demonstrating their significant efficacy in enhancing heat transmission [46].

Nevertheless, including a substantial quantity of comparatively large fins is likely not the favored approach owing to constraints on space efficacy and financial concerns. Furthermore, the fins' geometric characteristics will impact their transmission effectiveness favorably or unfavorably [47,48]. Hence, the fins' morphology, quantity, arrangement, altitude, and alignment are crucial factors in the study and must be considered to enhance thermal efficacy [49–52].

Over time, the designs of fins have developed to enhance the heat transmission rate within the limited area enclosed by the fins. Various considerations, including weight, construction material, and ease of manufacturing, have been considered design constraints. The fins may have a basic form, such as rectangular, triangular, elliptical, or pin-shaped, or a complicated design, such as corrugated or spiral, according to the requirements. Nevertheless, the tilt orientation has significance and warrants consideration for at least two causes. Firstly, the surface requiring cooling might not be in a vertical or horizontal position [53,54]. Secondly, a heat sink that is initially vertical or horizontal might tilt during operation.

Forced convection is a heat transmission process where the movement of external factors, including pumps, fans, suction devices, and others, influences the movement of the fluid, which is valuable for creating fluid motion as shown in Fig. 2.

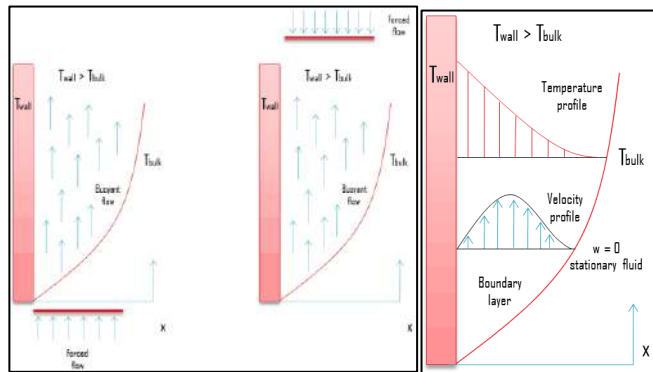


Fig. 3. - Forced and Natural convection [55].

This approach is critical due to its excellent transfer of heating capabilities from a heated item. Notable instances of this technique involve turbines, steam air conditioning, and so on [54]. Once analyzed, the forced convection process exhibits a more intricate mechanism than natural convection because, in this approach, we need to control two parameters: heat conduction and fluid velocity. These two aspects are closely linked since fluid motion could enhance heat transmission.

2.1.3. Heat Sinks Materials

Manufacturers generally use aluminum as their preferred metal since its great heat conductivity, around 235 W/(m/K). Another determinant of its appeal is its cost-effectiveness in production and exceptionally lightweight nature, which minimizes the strain exerted on a computer's motherboard. Copper is often considered optimal for creating highly efficient heat sinks due to its high thermal conductivity of around 400 W/(m/K), surpassing all other naturally occurring metals. Despite its superior heat transmission capabilities, copper is less favored by manufacturers because of its higher cost and weight than aluminum [56].

Some contemporary and practical heat sink designs are now exploring combining aluminum and copper in constructing a heat plate. This approach combines aluminum's lightweight characteristics with copper's superior thermal conductivity. The designs will combine the components mainly composed of aluminum, chosen for its reduced cost, and encased by a copper plate, selected for its excellent heat conductivity. Conceptually, these designs present a dynamic resolution to each of the metals' potential issues. Nevertheless, if the copper fails to form a

sufficiently strong bond with the aluminum (a common occurrence with low-cost heat sinks), the inclusion of a. In that case, copper plate can have a detrimental effect on the heat sink rather than a beneficial one [57].

Graphite composite materials were suggested as an alternative to copper and aluminum. However, their thermal conductivity is lower than that of copper, measuring $370\text{W}/(\text{m}\cdot\text{K})$. Graphite materials provide a significant advantage in their exceptionally lightweight nature, 70% lighter than aluminum [58]. An established principle followed by electronic designers in the industry is that the lower the cost of a heat sink, the higher the long-term expenses would be due to the need to replace components and conduct repairs. Cost-effective heat sinks often use elements like sleeve bearings in their construction, which are prone to rapid deterioration and may lead to lubrication issues. Heat sinks with ball bearings may have a higher initial cost, but they will undeniably have a longer lifespan, resulting in lower long-term expenses for the user.

2.1.4. Significance of thermal conductivity

Heat sinks are often constructed from metal because of their great thermal conductivity, enabling them to dissipate heats from the CPU and prevent overheating efficiently. Various metals may be used to construct a heat sink, each possessing distinct thermal conductivity properties [59]. The thermal conductivity of a substance may be precisely described as its capacity to transmit heat through it. Materials with greater thermal conductivity facilitate expedited and more effective heat transmission, whereas materials with lower thermal conductivity function as insulators by impeding the heat flow. Copper and aluminum are frequently utilized metals for constructing heat sinks since their exceptional thermal conductivity features.

2.1.5. Interface Thermal Resistances

Heat conduction is the main mechanism of heat transmission inside a component, which commonly necessitates transmitting thermal energy via several materials and surfaces that are layered, fastened, and joined together [60]. Using heat sinks, brackets, and circuit boards to mount components cooled using conduction is a widely used approach. A temperature gradient arises when heat is transferred across these contacts because only a small portion of points are touching each other for any two surfaces that are supposed to be flat, as seen in Fig. 3.

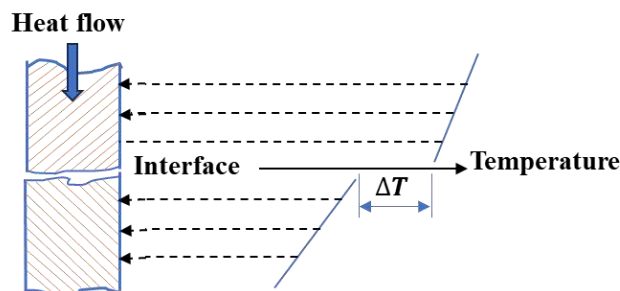


Fig. 4. - Heat flows between two faces [61].

The thermal interface resistance is a multifaceted function that depends on several aspects. The key parameters that influence thermal contact resistance are the surface qualities (such as roughness and flatness), filler materials, contact pressure, and the mechanical and thermal features of the contact solids, including hardness and thermal conductivity [62].

Several methods can be employed to reduce thermal contact resistance. These include using thermal grease, inserting a soft foil, coating surfaces with a soft metal's coating, by a low melting temp alloy between surfaces, or using the capillary actions of a filled liquid by microscopic reentrant cavities at the interface [63]. The primary factor that significantly influences the thermal contacting resistance is the filler's hardness, with a lower hardness being more favorable. It is important to emphasize that adding a filler that is harder comparison with the base substances are often increase the total contacting resistance, independent of the thickness or filler substances' thermal conductivity. Every approach to decrease contact resistance contact resistance has advantages, which vary based on varying specifics. Thermal grease, for instance, is the most affordable option. However, it presents challenges in achieving uniform application over a wide surface area and tends to evaporate in low-pressure environments and spread to neighboring surfaces. In order to be successful, metallic foils must have a thin and pliable nature, making them challenging to manipulate for practical purposes. In contrast, soft metallic coatings exhibit no wrinkling or folding and demonstrate exceptional stability, even under vacuum conditions.

Nevertheless, this strategy may incur significant costs. Molten materials' limitations in increasing interface resistance are due to their inability to hold the molten alloy at the interface and the subsequent separation of portions upon cooling. Using liquid-filled tiny holes may be impractical due to their inherent complexity.

3. Various Heat Sink Types

3.1. The generated heat source

The source in question may include any system that generates heat and necessitates removing it for proper operation. Examples include friction, nuclear, solar, chemical, electrical, and mechanical systems.


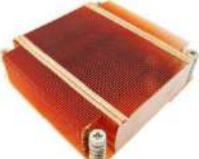
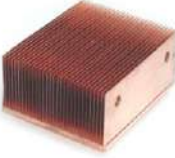



3.2. Transfer of heating




Heat pipes may also aid in facilitating this process. When the heat sink and the heat source are in direct contact, heat is transported from the source to the heat sink by natural conduction. The heat sink material's thermal conductivity directly affects this process. Copper and aluminum are frequently utilized in the production of heat sinks because of their exceptional thermal conductivity.

3.3. Heat distribution throughout the heat sink

Heat is transferred via the heat sink by conduction, moving from a location with higher temp to a region with lower temp along the thermal gradient. As a result, it is necessary for the thermal profile of the heat sink to be more uniform. Heat sinks typically display elevated temps in proximity to the heating source and decreasing temps towards the outside borders of the sink.

Table 1. Summary of different heat sink information.

Type	Ref.	Description	Applications	Performance	Pros	Cons	Photo
Extruded	[64–67]	Applicable in most situations; easy to automate production after the design is completed.	Many	Differs	Cheap	Limited to dimensions of extruded aluminum	
Stamped	[68–70]	Stamped from a single piece of metal, it is easy to automate production.	Low-power	Low	Cheap	Poor performance	
Bonded Fin	[71,72]	Produced by bonding individual fins to a base, manufacturing can be easy.	<ul style="list-style-type: none"> Uninterruptible power supplies (UPS) Variable speed motor controls Welding units Power rectification equipment Laser power supplies Traction drives 	Medium	Existing in large sizes	Expensive	
Folded Fin	[73,74]	The fin pitch is optimized for airflow; it may be plastic.	Ducted air	Exceptional	High heat-flux density	Expensive; ducting necessary	
Active	[75–77]	It includes a powered fan or blower for air movement; however, this is not a viable long-term solution, as the moving parts wear out and break down.	Emergency or quick-fix situations Used in cooling high-end graphics processors (GPUs) on graphics boards.	High	Simple, “Band-aid” solution	Poor reliability; high cost; recirculation of warm air	
Forged	[78,79]	It is manufactured by compressing aluminum or copper.	<ul style="list-style-type: none"> Cooling solutions for electric vehicle controllers. Battery pack cooling solution. Motor housing cooling. Inverter cooling. IT telecommunication 	Medium	Cheap	Limited design	

			cooling.				
Swaged	[80–82]	Like forged heat sinks, they are manufactured by forming metal into a die.	<ul style="list-style-type: none"> • Telecommunications • Computing • LED Lighting • Automotive and Transportation • Medical Devices • Aerospace and Defense 	Medium	Ideal for power devices	Heavy and unwieldy; poor flow management	
Single Fin	[83,84]	Versatile devices designed to be employed in tight spaces.	Versatile for all applications. Their performance can scale from low to high performing.	Varies	Lightweight, low-profile	Expensive	
Skived	[85,86]	Fins are cut (skived) from a single metal block (usually copper).	<ul style="list-style-type: none"> • Computers and electronic components. • Telecommunication equipment. 	Medium-High	High fin density	Thick base and high weight; directionally sensitive	

4. Fin Efficiency

The efficiency of the fins represents one of the elements that contribute to the significance of a material with greater thermal conductivity. A heat sink fin could be a flat plate with heat flowing in one end and dissipating into the fluid around it as it goes to the other end [87]. In the transfer of heating via the fin, the temp of the fin and, consequently, the transfer of heating to the fluid will drop from the base to the end of the fin, which is because the heat sink's thermal resistance impedes the flow of heat, and the heat lost due to convection will cause the temp of the fin to fall. The term "fin efficiency" refers to the ratio of the heat transmitted by the fin to the transfer of heating that would occur if the fin were isothermal (that is, if the fin had an infinite thermal conductivity).

Due to the requirements for aviation, cryogenic auxiliaries, air conditioning, gas turbines, and aerospace, there has been a particular focus on the compactness of the heat exchanger surface. This is especially true for surfaces that cause modest variations in pressure in the fluids that are cycled via them. Some of these are seen in Fig. 4. Within the context of heat exchangers, compactness is defined as the ratio of the transfer of the heating surface to the exchanger volume.

An early definition of a compact exchanger element was created by [88], who said it was defined as an element that included more than 245 square meters of exchanger per cubic meter. On the other hand, traditional heat exchangers with tubes ranging from 5/8 inches to 1 inch have a capacity of 65 to 130 square meters per cubic meter. In contrast, compact exchanger components have a capacity of approximately 4100 square meters per cubic meter. Many pieces that make up compact heat exchangers comprise main surface plates or tubes separated by spines, bars, or plates that also function as fins. By the illustration in Fig. 4d, every fin might be considered a single fin, with the fin height equal to half of the spacing between the separation plates and the separation plate serving as the primary surface. As a result, the compact heat exchanger is regarded as an additional kind of extended surface.

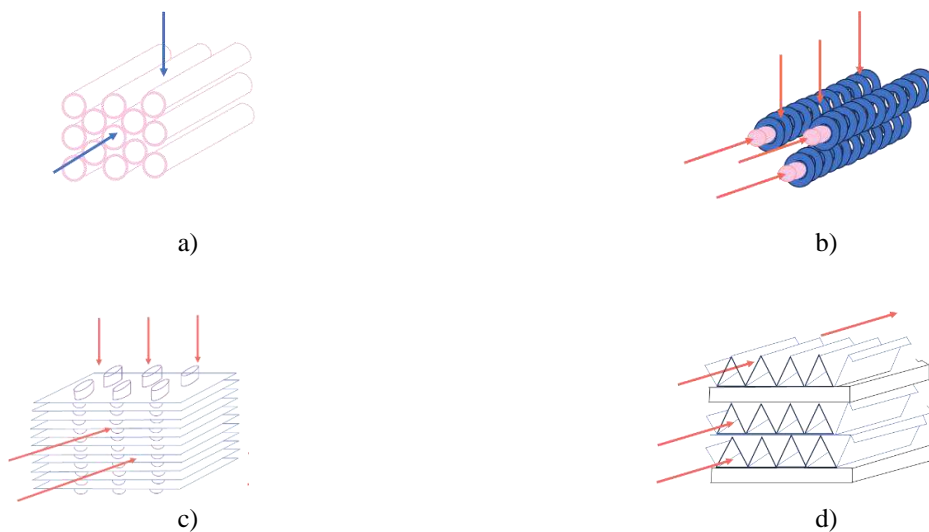


Fig. 5. - Regular instances of compact heat exchanger surfaces: (a) cylindrical tube; (b) cylindrical tube with radial fins; (c) flat tube with continuous fins; (d) plate fin.

It is easy to demonstrate that once a fin and its prime surface are subjected to a uniform thermal environment, a unit of fin surface will be less efficient than a unit of prime surface, which can be shown relatively easily. Please consider the plate in Fig. 5, which has a longitudinal fin with a rectangular cross-section. The internal plate surface should be able to extract heat from a source that has a uniform coefficient of transfer of heating and temp T1. In contrast, the outside plate and fin surfaces should be able to reject heat to cooler surrounds with a coefficient of uniform transfer of heating and temp Ts. The plate's cooler surface is at a temp somewhere in the middle, denoted by Tp, and the heat that originates from the source exits the plate due to the temp potential, which is Tp minus Ts. A similar situation occurs when the surface of the fin is at a certain temp, denoted by T, and the heat escapes the fin due to the temp potential, denoted by T-Ts. The heat can reach the fin through its base, which meets the plate and passes through it continuously through the conduction process. The temp at the base of the fin will usually be extremely close to an identical magnitude to that of Tp. When there is a temp differential inside the fin, such that Tp is more significant than T, can heat that the fin has absorbed via its base move toward its tip? Because of this circumstance, the temp T will be different from the base to the tip of the fin, which means that the temp potential T-Ts will be lower than the temp potential Tp-Ts. Additionally, a unit of fin surface will have a lower efficacy than a unit of plate or prime surface.

When compared with a unit of prime surface, the inefficacy of the fin is equivalent to the unavoidable loss of performance that occurs when a unit of fin surface is utilized. The fin efficacy is the proportion of a fin's actual heat dissipation to its ideal dissipation if the whole fin was at the same temp as its base. This definition is maintained throughout the entirety of this book. Other performance indices are utilized, including the fins' efficacy, the fins' weighted efficacy, the overall passage efficacy, the fins' resistance, and the fins' input admittance. Most of these topics are covered in subsequent chapters. Fins of a specific size, shape, and material can have varying degrees of efficacy. The efficacy of any fin will vary depending on its thermal conductivity and the manner of heat transmission to its surroundings.

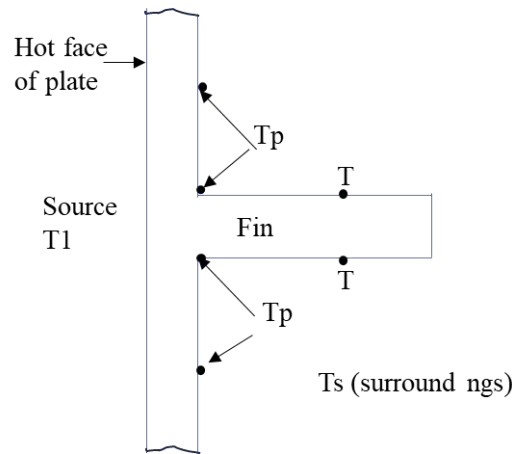


Fig. 6. Temp potential variations in fins.

5. Identify the coefficient of heating transfer

The coefficient of heating transfer needed is dependent on the flow patterns present and the velocity, V, which is utilized to calculate the Reynolds number. The evaluation of h_f for the surface of plate fins involves the use of a formula for the Nusselt number, which describes the heat transfer for developing flow between isothermal parallel plates [89]:

$$Nu = 7.55 + \frac{0.024\chi^{-1.14}}{1+0.0358\chi^{-0.64}Pr^{0.17}} \quad (1)$$

Whereas $\chi = \frac{x}{D_c \cdot Re \cdot Pr}$ and $D_c = 2\Delta$ for parallel fins plate, and h_f has been gained from formula (2):

$$Nu = \frac{h_f D_c}{K_{air}} \quad (2)$$

5.1. Overall Surface Efficiency

The efficacy of the fin and surface area based on fin geometry. Supposing that the shape of the fin is rectangular, the single fin efficacy could be stated as:

$$\eta_f = \frac{\tanh(mL)}{mL} \quad (3)$$

Whereas L refers to the length of fin, η_f is the efficacy of fin, and:

$$m = \sqrt{\frac{2h}{k_f t_f}} \quad (4)$$

Whereas t_f and k_f refer to fins' thickness and conductivity, respectively.

The efficiency of fin η_f measures the performance of an individual fin, whereas the overall surface efficacy η_0 describes the performance of a group of fins and the surface they are connected [90]:

$$\eta_0 = 1 - \frac{NA_f}{A_t} (1 - \eta_f) \quad (5)$$

Whereas N refers to the fins' number in array and each surface area A_f .

5.2. Identify the rate of heating transfer

The rate of heating transfer has been identified as following [91]:

$$Q = m_f C_p (T_{out} - T_{in}) \quad (6)$$

Whereas m_f was the rate of air flow mass, C_p provided the air-specific heating capacity, T_{in} refers to the inlet temp, and T_{out} refers to the outlet temp.

The coefficient of heating transfer was presented as following:

$$h = Q / (A \Delta T_{tm}) \quad (7)$$

In formula 7, A was the heating exchange surface area:

$$\Delta T_{tm} = \frac{(T_{t_{oull}} - T_{in}) - (T_{wall} - T_{out})}{Ln\left(\frac{(T_{wall} - T_{in})}{(T_{wall} - T_{out})}\right)} \quad (8)$$

Whereas T_{wall} provided the outer wall fins' temp.

$$Re = \rho U_m D / \mu \quad (9)$$

whereas ρ and U_m were the air density and fluid velocity at the min section of the tube row, respectively [92,93].

$$\begin{aligned} Nu &= h D_h / \lambda \\ f &= 2 \Delta p / (\rho U_m^2) \end{aligned} \quad (10)$$

The factors of heating transfer j and London goodness (JF) have been identified as following [30]:

$$\begin{aligned} j &= \frac{Nu \cdot Pr^{-1/3}}{Re} \\ JF &= j / f = \frac{Nu \cdot \rho \cdot U_m \cdot Pr^{-1/3}}{2 \Delta p \cdot Re} \end{aligned} \quad (11)$$

5.3. Fins Arrangement

A heat sink called a pin-fin heat sink has pins that grow outward from its base. The pins can be square, elliptical, or cylindrical. Pin heat sinks are among the most prevalent heat sinks now accessible in the market. The straight fin is the second form of heat-sink fin configuration that may be achieved. Throughout the whole of the heat sink, they are continuous. The cross-cut heat sink is a variant of the often- utilized straight-fin heat sink. Cuts are made at predetermined intervals on a heat sink with a straight fin-the flow of free convection around a heat sink with a pin face. In a broad sense, the larger the surface area of a heat sink, the more effectively it functions.

On the other hand, this is only sometimes the case. When designing a pin-fin heat sink, the goal is to reduce the amount of surface area contained inside a particular volume as much as feasible. In addition, it functions effectively in any orientation. Kordyban has compared the performance of a straight-fin heat sink and a pin-fin heat sink with comparable dimensions.

The temp difference between the straight-fin's heat-sink base and the ambient air was 44 degrees Celsius, 6 degrees Celsius higher than the temp difference for the pin-fin, which comes even though the straight-fin has 58 square centimeters of surface area. In contrast, the pin-fin is 194 square centimeters. Then, utilized in the application for which they were designed, the performance of pin-fin heat sinks is much superior to that of straight fins because

the fluid travels axially along the pins rather than simply tangentially across the pins. There is also the flared-fin heat sink, which has a different design. The fins of this heat sink are not parallel to each other. The flow resistance is reduced when the fins are flared, allowing more air to travel through the heat-sink fin channel. More air would pass through the channel if the fins were not flared. Changing the angle of the fins results in longer fins while maintaining the same overall proportions. They concluded that the thermal performance is at least twenty percent superior to straight-fin heat sinks when the air approach velocity is modest, generally about one meter per second. Additionally, they discovered that the flared heat sink worked better than the other heat sinks evaluated for the bypass configurations they studied.

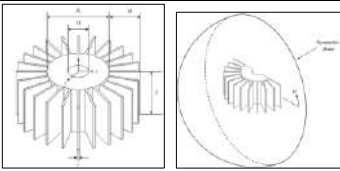
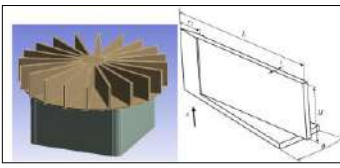
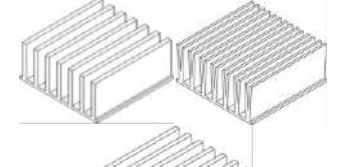
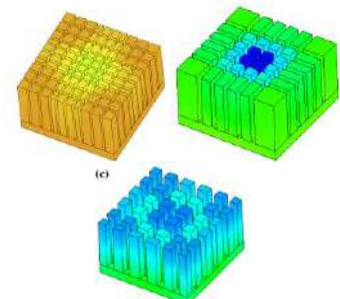
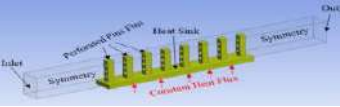
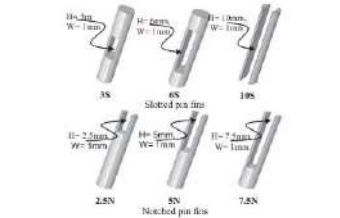
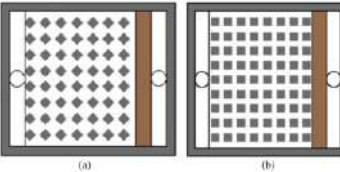
Bochicchio et al., and Giorgi et al., [94,95] have conducted considerable research on the model, which has been detailed by [96,97]. Nguyen and Aziz [97] presented a novel indicator for the efficiency of longitudinal, convecting–radiating fins to dissipate heat. This new indication assesses the dissipation, by entropy rates, of the steady state of the fin in comparison to the same dissipation of an ideal fin with the highest dissipation possible. Based on [98], there is no doubt that the efficiency of the matching fin will be greater if it is closer to the ideal fin than the actual fin. Additionally, a comparison is made about the traditional concept of efficiency for the fins, which is additionally examined. When the temp is in a steady state, the temp distribution along the fin is associated with the function that describes the profile of the longitudinal fin. The impact of altering the fin profile may result in drastically diverse temp distributions, even when the boundary conditions remain the same.

Consequently, the efficiency magnitudes are determined by the temp distributions and the boundary conditions individually, which is an old problem that has been considered by many researchers from a variety of perspectives (see, for example, [96–101]). The issue is about how the difference in the temp, the boundary conditions, and the many thermodynamic parameters that describe the system affect the efficiency magnitudes. Within this article, we offer an investigation of the concept of entropy presented in [102] and an examination of the fin profile's function in selecting an efficient method of heat dissipation. It is common knowledge that various fin profiles correlate to varied levels of efficiency in terms of the fin's ability to remove heat. Within the context of [96], it provides the efficiency of longitudinal fins simultaneously corresponding to rectangular, triangular, and parabolic profiles.

Additionally, these profiles were researched and examined in Gardner [101]. Since then, many publications have been published about the effectiveness of fins that have appropriate profiles. The performance of fins with rectangular, triangular, trapezoidal, and parabolic shapes was investigated by Nguyen and Aziz [97] to determine how well they performed at varying levels of the [103] conducted a mathematical analysis of the issue by placing limitations on the volume or perimeter of the fin and obtaining non-existent conclusions for both problems., which was done to determine whether the problem existed. The review by [104] provides an overview of the performance of finned tubes with fins with varying profiles. Another review is provided by [105], which focuses on the impact that geometrical dimensions, dimensionless numbers, and fin position play in determining the performance of the fin, particularly when it is utilized in latent heat thermal energy storage systems. Based on their findings, [106] conduct a numerical analysis of radiation's impact in conjunction with the appropriate fin profile.

Table 2. The impact of fins arrangement on the heat transfer efficiency.

Ref.	Main methodology	Images	Findings
[107]	An oblique array of flat-plate fin heat sinks has been tested to prevent flow resistance from improving as the number of fins is increased to enhance the surface area for heat transfer.		<ul style="list-style-type: none"> • Their suggested heat-sink design outperformed the one with vertical plate fins because of the increased surface area and faster flow between the fins. • By adding oblique fins, the additional cooling impact might result in a 6 °C drop in CPU case temp at high flow rates. • Their innovative design outperformed the conventional one regarding heat-dissipation performance at low flow rates.
[108]	A stationary heat sink with a spinning air jet impingement under turbulent flow conditions has been studied.		<ul style="list-style-type: none"> • They discovered that the Nu number rose with the Re number for a stationary heat sink. In a rotating heat sink with jet impingement, the average Nu number was more affected by the Re number for small Re than for stationary heat sink; however, this influence diminished as Re increased. They claimed that altering the fins' shape could maximize the heat-sink's hydrothermal performance.

[109]	The impact of the orientation on the natural convection and radiation for a cylindrical heat-sink utilized to cool an LED light bulb		<ul style="list-style-type: none"> • As the inclination angle grew, stagnation sites and flow separation developed. • The drag coefficient grew as Nu dropped. • The drag coefficient rose dramatically with the orientation angle as the fin length or number of fins increased, intensifying the orientation impact.
[110]	Improved the thermal performance of the heat-sink for a LED lamp operating under natural convection conditions.		<ul style="list-style-type: none"> • According to reports, registering the goal core temp of 65 oC included decreased fin thickness and increased fin number and height. • These geometric parameters may result in a significant drop in temp but an increase in the heat sink mass of around 24% of the starting mass. • It was shown that the optimized branched-fin heatsink's Rth dropped by as much as 30% compared to a normal heatsink. By reducing the heatsink's length and raising the pumping power, the Rth was reduced even further.
[111]	The thermal performance of a heat-sink having fins branched in the direction average to water flow.		<ul style="list-style-type: none"> • Both numerically and empirically, the Rth dropped 3.10%. Furthermore, the magnitude of Nu rose by 3.20% compared to the initial heat-sink.
[112–114]	The fin widths and heights have been adjusted to enhance the heat-sink design.		<ul style="list-style-type: none"> • The study showed that the staggered configurations of strip fins exhibited superior performance compared to the in-line configurations. Using perforated fins can enhance heat transmission while mitigating pressure loss and reducing heat sink bulk. Fig. 1 depicts a line of perforated fins arranged in an in-line configuration.
[115]	The effectiveness of the perforated pin-fins heat sink in enhancing heat transmission was established.		<ul style="list-style-type: none"> • The researchers observed a positive correlation between the size of the rectangular hole, the heat transfer rate, and the pressure reduction. The study achieved an ideal heat transfer augmentation of 10%, with a maximum decrease in fan power consumption of 30%.
[116]	The thermal efficacy of pinfin heat sinks with rectangular slotted or notched perforations was computationally evaluated.		<ul style="list-style-type: none"> • An ideal porosity was achieved, and an angle was determined to optimize thermal performance.
[117]	Improved the cooling efficacy of the micro square pin-fin heat sink by manipulating the porosity of the pinfin and the angle at which the pinfin is positioned.		

Conclusions

To satisfy the criteria for power system design, heat-sink optimization will help determine the dimensions, weight, and thermal performance. Finding the ideal number of fins is the most important step when determining the optimum solution for the temperature at the sink's base.

This endeavor aims to ascertain the ideal number of fins to gain maximum heat transmission. The thickness of the fins is the most critical metric for optimal heat-sink performance. Although smaller fins increase the optimal number of fins, they decrease the heat sink's weight and enhance its thermal performance.

Optimized heat-sink design and airflow provide a more compact cooling system with excellent heat extraction. A small power converter with high power density and a heat sink with good cooling may increase system power density.

Research is required to improve heat sink natural convection heat transmission. Agitation or pulsation flow may increase heat sink heat dissipation. Heat sink thermal design may be optimized by considering fin number, fin shape, channel form, channel aspect ratio, grooved channel, inlet/outlet location, and ribs and turbulators between channels. There is little data on enhancing spinning heat sink thermal efficiency. Filling the substrate base changed the heat sink's thermal design.

Author Contributions: All authors conducted the work equally.

Acknowledgments: The authors would like to reveal their appreciation and gratitude to the respected reviewers and editors for their constructive comments.

Conflicts of Interest: The authors declare no conflict of interest.

References

- [1] Ambreen T, Niyas H, Kanti P, Ali HM, Park C-W. Experimental investigation on the performance of RT-44HC-nickel foam-based heat sinks for thermal management of electronic gadgets. *Int J Heat Mass Transf* 2022;188:122591.
- [2] Laha SK, Sadhu PK, Ganguly A, Naskar AK. A comparative study on thermal performance of a 3-D model based solar photovoltaic panel through finite element analysis. *Ain Shams Eng J* 2022;13:101533.
- [3] He Z, Yan Y, Zhang Z. Thermal management and temperature uniformity enhancement of electronic devices by micro heat sinks: A review. *Energy* 2021;216:119223.
- [4] Ohring M, Kasprzak L. Reliability and failure of electronic materials and devices. Academic Press; 2014.
- [5] Mora C, Dousset B, Caldwell IR, Powell FE, Geronimo RC, Bielecki CR, et al. Global risk of deadly heat. *Nat Clim Chang* 2017;7:501–6.
- [6] Miller C. Chip war: the fight for the world's most critical technology. Simon and Schuster; 2022.
- [7] Koren Y. The global manufacturing revolution: product-process-business integration and reconfigurable systems. vol. 80. John Wiley & Sons; 2010.
- [8] Liang Y, Zhao C, Yuan H, Chen Y, Zhang W, Huang J, et al. A review of rechargeable batteries for portable electronic devices. *InfoMat* 2019;1:6–32.
- [9] Mathew J, Krishnan S. A review on transient thermal management of electronic devices. *J Electron Packag* 2022;144:10801.
- [10] Wang C, Hua L, Yan H, Li B, Tu Y, Wang R. A thermal management strategy for electronic devices based on moisture sorption-desorption processes. *Joule* 2020;4:435–47.
- [11] Lee H. Thermal design: heat sinks, thermoelectrics, heat pipes, compact heat exchangers, and solar cells. John Wiley & Sons; 2022.
- [12] Ahmed HE, Salman BH, Kherbeet AS, Ahmed MI. Optimization of thermal design of heat sinks: A review. *Int J Heat Mass Transf* 2018;118:129–53. <https://doi.org/10.1016/j.ijheatmasstransfer.2017.10.099>.
- [13] Radhi SS, Al-khafaji ZS, Falah MW. Sustainable heating system by infrared radiators 2022;4:42–52. <https://doi.org/10.37868/hsd.v4i1.82>.
- [14] Hussein; SA, Al-Khafaji; Z, Alfatlawi; T, Abbood; A-KN. Assessment of Surface and Subsurface Drainage from Permeable Friction Course (As A Sustainable Pavement) under Different Geometric and Hydrologic Conditions 2022.
- [15] Han X-H, Wang Q, Park Y-G, T'Joen C, Sommers A, Jacobi A. A review of metal foam and metal matrix composites for heat exchangers and heat sinks. *Heat Transf Eng* 2012;33:991–1009.
- [16] Tong XC, Tong XC. Materials and design for advanced heat spreader and air cooling heat sinks. *Adv Mater Therm Manag Electron Packag* 2011:373–420.
- [17] Brochard L, Kamath V, Corbalán J, Holland S, Mittelbach W, Ott M. Energy-efficient computing and data centers. John Wiley & Sons; 2019.
- [18] Li C. Thermal Management of Electronics and Optoelectronics: From Heat Source Characterization to Heat Mitigation at the Device and Package Levels 2019.
- [19] Sahoo SK, Rath P, Das MK. Numerical study of phase change material based orthotropic heat sink for thermal management of electronics components. *Int J Heat Mass Transf* 2016;103:855–67.
- [20] Al-Abayechi Y, Alaiwi Y, Al-Khafaji Z. Exploration of key approaches to enhance evacuated tube solar collector efficiency. *J Adv Res Numer Heat Transf* 2024;19:1–14.
- [21] Hussain AJ, Al-Khafaji ZS, Hamza WA. An investigation into the distribution of internal residual stresses of aluminum plate subjected to thermal load by using hole drilling technique. *J Mech Eng Res Dev* 2021;44:402–11.
- [22] Aljumaili A, Alaiwi Y, Al-Khafaji Z. Investigating back surface cooling system using phase change materials and heatsink on photovoltaic performance. *J Eng Sustain Dev* 2024;28:294–315.
- [23] Sharaf-eldin MA, Yaseen ZM, Elmetwalli AH, Elsayed S, Scholz M, Al-khafaji Z, et al. Modifying Walk-In Tunnels through Solar Energy , Fogging , and Evaporative Cooling to Mitigate Heat Stress on Tomato 2023.
- [24] Christou A. Reliability of high temperature electronics. RIAC; 1996.
- [25] Li M, Liu W, Yang L, Chen P, Chen C. Chip temperature optimization for dark silicon many-core systems. *IEEE Trans Comput Des Integr Circuits Syst* 2017;37:941–53.
- [26] Băjenescu TI, Băzu MI. Component reliability for electronic systems. Artech House; 2010.
- [27] Bergles AE. Some perspectives on enhanced heat transfer—second-generation heat transfer technology 1988.
- [28] Silk EA, Gollhofer EL, Selvam RP. Spray cooling heat transfer: technology overview and assessment of future challenges for micro-gravity application. *Energy Convers Manag* 2008;49:453–68.
- [29] Cabeza LF, Sole C, Castell A, Oro E, Gil A. Review of solar thermal storage techniques and associated heat transfer technologies. *Proc IEEE* 2011;100:525–38.
- [30] Meng L, Cheng KWE. Wireless power transfer technology for electric iron based on multi-coils induction heating

design. *IET Power Electron* 2019;12:2566–77.

- [31] Yang L, Jin X, Zhang Y, Du K. Recent development on heat transfer and various applications of phase-change materials. *J Clean Prod* 2021;287:124432.
- [32] Zalba B, Marin JM, Cabeza LF, Mehling H. Review on thermal energy storage with phase change: materials, heat transfer analysis and applications. *Appl Therm Eng* 2003;23:251–83.
- [33] Dutta BK. *Heat transfer: principles and applications*. PHI Learning Pvt. Ltd.; 2023.
- [34] Assael MJ, Antoniadis KD, Wakeham WA, Zhang X. Potential applications of nanofluids for heat transfer. *Int J Heat Mass Transf* 2019;138:597–607.
- [35] John B, Senthilkumar P, Sadasivan S. Applied and theoretical aspects of conjugate heat transfer analysis: A review. *Arch Comput Methods Eng* 2019;26:475–89.
- [36] Borode AO, Ahmed NA, Olubambi PA. A review of heat transfer application of carbon-based nanofluid in heat exchangers. *Nano-Structures & Nano-Objects* 2019;20:100394.
- [37] Müller-Steinhagen H, Malayeri MR, Watkinson AP. Heat exchanger fouling: mitigation and cleaning strategies. *Heat Transf Eng* 2011;32:189–96.
- [38] Zhao X, Zhu Y, Li H. Micro-Channel Oscillating Heat Pipe Energy Conversion Approach of Battery Heat Dissipation Improvement: A Review. *Energies* 2022;15:7391.
- [39] Wirdatmadja SA, Moltchanov D, Balasubramaniam S, Koucheryavy Y. Microfluidic system protocols for integrated on-chip communications and cooling. *IEEE Access* 2017;5:2417–29.
- [40] Harikrishnan S, Dhass AD, Ali HM. *Thermal Performance of Nanofluids in Miniature Heat Sinks with Conduits*. Springer; 2022.
- [41] Laloya E, Lucia O, Sarnago H, Burdio JM. Heat management in power converters: From state of the art to future ultrahigh efficiency systems. *IEEE Trans Power Electron* 2015;31:7896–908.
- [42] Narasimhan TN. Fourier's heat conduction equation: History, influence, and connections. *Rev Geophys* 1999;37:151–72.
- [43] Soleimani S, Sheikholeslami M, Ganji DD, Gorji-Bandpay M. Natural convection heat transfer in a nanofluid filled semi-annulus enclosure. *Int Commun Heat Mass Transf* 2012;39:565–74.
- [44] Razzaghpahan Z, Sarunac N. Natural convection heat transfer from a bundle of in-line heated circular cylinders immersed in molten solar salt. *Int J Heat Mass Transf* 2020;148:119032.
- [45] Unger S, Beyer M, Pietruske H, Szalinski L, Hampel U. Natural convection heat transfer performance of additively manufactured tube bundle heat exchangers with novel fin design. *Heat Mass Transf* 2021;57:1193–203.
- [46] Mendu SS, Nagaraju D. Minimization of entropy generation in natural convection using optimum isothermal heaters: CFD analysis. *Int J Environ Sci Technol* 2023;20:5629–42.
- [47] Sattar S., Alaiwi Y., Radhi N.S., Al-Khafaji Z, Al-Hashimi O., Alzahrani H., et al. Corrosion reduction in steam turbine blades using nano-composite coating. *J King Saud Univ* 2023;35:102861. <https://doi.org/10.1016/j.jksus.2023.102861>.
- [48] Sattar S., Alaiwi Y, Radhi NS, Al-khafaji Z. Numerical Simulation for Effect of Composite Coating (TiO₂ + SiO₂) Thickness on Steam Turbine Blades Thermal and Stress Distribution. *Acad J Manuf Eng* 2023;21.
- [49] Jasim A.H., Radhi N.S., Kareem N.E., Al-Khafaji Z.S., Falah M. Identification and investigation of corrosion behavior of electroless composite coating on steel substrate. *Open Eng* 2023;13:20220472.
- [50] Radhi NS, AL-Khafaji Z, Mareai B.M., Radhi S., Alsaegh A.M. Reducing oil pipes corrosion by (zn-ni) alloy coating on low carbon steel substrate by sustainable procesS. *J Eng Sci Technol* 2023;18:1624–38.
- [51] Dawood NM, Radhi NS, Al-khafaji ZS. Investigation Corrosion and Wear Behavior of Nickel-Nano Silicon Carbide on Stainless Steel 316L 2020;1002:33–43. <https://doi.org/10.4028/www.scientific.net/MSF.1002.33>.
- [52] Abed Janabi ZM, Jaber Alsalami HS, Al-Khafaji ZS, Hussien SA. Increasing of the corrosion resistance by preparing the trivalent nickel complex. *Egypt J Chem* 2021. <https://doi.org/10.21608/EJCHEM.2021.100733.4683>.
- [53] Vogel J, Johnson M. Natural convection during melting in vertical finned tube latent thermal energy storage systems. *Appl Energy* 2019;246:38–52.
- [54] Chen H-T, Lin M-C, Chang J-R. Numerical and experimental studies of natural convection in a heated cavity with a horizontal fin on a hot sidewall. *Int J Heat Mass Transf* 2018;124:1217–29.
- [55] Cengel YA. *Heat Transference a Practical Approach*. MacGraw-Hill, 2004;4:874.
- [56] Smith L. The development and processing of novel aluminum powder metallurgy alloys for heat sink applications 2013.
- [57] Li J, Yang L. Recent Development of Heat Sink and Related Design Methods. *Energies* 2023;16:7133.
- [58] Isaac B. Thermo-mechanical characterisation of low density carbon foams and composite materials for the ATLAS upgrade 2012.
- [59] Aglawe KR, Yadav RK, Thool SB. Fabrication, experimentation and numerical simulation of micro channel heat sink for enhancing thermal performance of electronic devices. *Int J Interact Des Manuf* 2023:1–16.
- [60] Fan L, Khodadadi JM. Thermal conductivity enhancement of phase change materials for thermal energy storage: a review. *Renew Sustain Energy Rev* 2011;15:24–46.
- [61] Xu J, Läger K, Möller R, Dransfeld K, Wilson IH. Heat transfer between two metallic surfaces at small distances. *J Appl Phys* 1994;76:7209–16.
- [62] Wiśniewski TS. Experimental study of contacting surfaces microgeometry and gas gap impact on thermal contact conductance of metallic joints. *Int J Heat Mass Transf* 2023;200:123511.
- [63] Wang X, Lu C, Rao W. Liquid metal-based thermal interface materials with a high thermal conductivity for electronic cooling and bioheat-transfer applications. *Appl Therm Eng* 2021;192:116937.
- [64] Dempsey BM, Eisele S, McDowell DL. Heat sink applications of extruded metal honeycombs. *Int J Heat Mass Transf* 2005;48:527–35.
- [65] Alvin C, Chu W, Cheng C-H, Teng J. Thermal analysis of extruded aluminum fin heat sink for LED cooling application. 2011 6th Int. Microsystems, Packag. Assem. Circuits Technol. Conf., IEEE; 2011, p. 397–400.
- [66] Gammeter C, Krismer F, Kolar JW. Weight optimization of a cooling system composed of fan and extruded-fin heat

- sink. *IEEE Trans Ind Appl* 2014;51:509–20.
- [67] Huttunen E, Nykänen MT, Alexandersen J. Material extrusion additive manufacturing and experimental testing of topology-optimized passive heat sinks using a thermally-conductive plastic filament. *Addit Manuf* 2022;59:103123.
- [68] Biber C. Choosing a heat sink: Some tips and recommendations. *EDN* 1995;40:125–30.
- [69] Park J, Choi D, Hong W. Millimeter-wave phased-array antenna-in-package (AiP) using stamped metal process for enhanced heat dissipation. *IEEE Antennas Wirel Propag Lett* 2019;18:2355–9.
- [70] Kim DH, Lee JM, Kim BM. Development of Stamping Technology for the Fine Pitch L/F with Heat Sink (I). *Proc. Korean Soc. Precis. Eng. Conf., Korean Society for Precision Engineering*; 2007, p. 551–2.
- [71] Loh CK, Chou B-B, Nelson D, Chou DJ. Study of thermal characteristics on solder and adhesive bonded folded fin heat sink. *ITHERM 2000. Seventh Intersoc. Conf. Therm. Thermomechanical Phenom. Electron. Syst. (Cat. No. 00CH37069)*, vol. 2, IEEE; 2000, p. 1–7.
- [72] Ahamat MA, Abidin R, Roslin EN, Zain NM, Ishak R, Kuan PC. Performance of Brazed and Adhesive Bonded Pin Fins. *Int J Appl Eng Res* 2017;12:14541–6.
- [73] Ji TH, Kim SY, Hyun JM. Pressure drop and heat transfer correlations for triangular folded fin heat sinks. *IEEE Trans Components Packag Technol* 2007;30:3–8.
- [74] Luiten G, Verhoeven M, Johannes A, Zuidema P, VREHEN J. Folded sheet metal heat sink 2018.
- [75] Vetrovec J. Active heat sink for automotive electronics. *SAE Int J Passeng Cars-Electronic Electr Syst* 2009;2:336–43.
- [76] Staats WL. Active heat transfer enhancement in integrated fan heat sinks 2012.
- [77] Tang Y, Luo Y, Du P, Wang H, Ma H, Qin Y, et al. Experimental investigation on active heat sink with heat pipe assistance for high-power automotive LED headlights. *Case Stud Therm Eng* 2021;28:101503.
- [78] Wang K, Han Y, Zhang H, Zhang L. FEM simulation for cold press forging forming of the round-fin heat sink. *AIP Conf. Proc.*, vol. 1532, American Institute of Physics; 2013, p. 857–62.
- [79] Pujol T, T’Jollyn I, Massaguer E, Massaguer A, Cózar IR, De Paepe M. Design optimization of plate-fin heat sink with forced convection for single-module thermoelectric generator. *Appl Therm Eng* 2023;221:119866.
- [80] Zaghlool A, Leonard W, Culham R. Characterization of swaged mixed metal heat sinks. *Eighteenth Annu. IEEE Appl. Power Electron. Conf. Expo. 2003. APEC’03.*, vol. 2, IEEE; 2003, p. 1037–42.
- [81] Kim JH, Ku MY, Lee GW. Evaluation of Heat Release Performance of Swaged-and Extruded-type Heat Sink Used in Industrial Inverter. *J Korea Acad Coop Soc* 2013;14:523–8.
- [82] Kim JH, Ku MY, Lee GW. Heat Release Performance of Swaged-and Extruded-Type Heat Sink Used in Industrial Inverter. *Int J Ind Manuf Eng* 2012;6:2827–30.
- [83] Naphon P, Klangchart S, Wongwiset S. Numerical investigation on the heat transfer and flow in the mini-fin heat sink for CPU. *Int Commun Heat Mass Transf* 2009;36:834–40.
- [84] Prajapati YK. Influence of fin height on heat transfer and fluid flow characteristics of rectangular microchannel heat sink. *Int J Heat Mass Transf* 2019;137:1041–52.
- [85] Yang MC. Thermal comparison of plate, extrusion heat sink, and skive heat sink. *Seventeenth Annu. IEEE Semicond. Therm. Meas. Manag. Symp. (Cat. No. 01CH37189)*, IEEE; 2001, p. 102–6.
- [86] Lin F-C, Liu C-F, Yang M-T, Lee S-W, Hsu C-H, Sung K-F, et al. Flow Boiling Heat Transfer Performance Comparison of Skived Straight and CNC Diverging Microchannels Heat Sinks. *2023 39th Semicond. Therm. Meas. Model. Manag. Symp.*, IEEE; 2023, p. 1–5.
- [87] Tariq A, Altaf K, Ahmad SW, Hussain G, Ratlamwala TAH. Comparative numerical and experimental analysis of thermal and hydraulic performance of improved plate fin heat sinks. *Appl Therm Eng* 2021;182:115949.
- [88] Kays WM, London AL. *Compact heat exchangers* 1984.
- [89] Shah RK. *Laminar Flow Forced Convection in Ducts*, Supp 1 *Adv Heat Transf* 1978:153–95.
- [90] Bergman TL, Lavine AS, Incropera FP, DeWitt DP. *Introduction to heat transfer*. John Wiley & Sons; 2011.
- [91] Gholami AA, Wahid MA, Mohammed HA. Heat transfer enhancement and pressure drop for fin-and-tube compact heat exchangers with wavy rectangular winglet-type vortex generators. *Int Commun Heat Mass Transf* 2014;54:132–40.
- [92] Wang J, Fu T, Zeng L, Lien F, Deng X. Experimental investigation and numerical investigations of heat transfer enhancement in a tube with punched winglets. *Int J Therm Sci* 2022;177:107542.
- [93] Wang J, Fu T, Zeng L, Lien F, Chen G. Thermal-hydraulic performance in a tube with punched delta winglets inserts in turbulent flow. *Int J Therm Sci* 2022;172:107326.
- [94] Boichichio I, Naso MG, Vuk E, Zullo F. Convecting–radiating fins: explicit solutions, efficiency and optimization. *Appl Math Model* 2021;89:171–87.
- [95] Giorgi C, Zullo F. Entropy Production and Efficiency in Longitudinal Convecting–Radiating Fins. *Proceedings*, vol. 58, MDPI; 2020.
- [96] Kraus AD, Aziz A, Welty JR. *Extended surface heat transfer*. 2013.
- [97] Nguyen H, Aziz A. Heat transfer from convecting-radiating fins of different profile shapes. *Wärme-Und Stoffübertragung* 1992;27:67–72.
- [98] Giorgi C, Zullo F. Entropy rates and efficiency of convecting-radiating fins. *Energies* 2021;14:1643.
- [99] Mosayebidorcheh S, Hatami M, Mosayebidorcheh T, Ganji DD. Optimization analysis of convective–radiative longitudinal fins with temperature-dependent properties and different section shapes and materials. *Energy Convers Manag* 2015;106:1286–94.
- [100] Mao Q, Hu X, Zhu Y. Numerical investigation of heat transfer performance and structural optimization of fan-shaped finned tube heat exchanger. *Energies* 2022;15:5682.
- [101] Gardner KA. Efficiency of extended surface. *Trans Am Soc Mech Eng* 1945;67:621–8.
- [102] Sciacovelli A, Verda V, Sciubba E. Entropy generation analysis as a design tool—A review. *Renew Sustain Energy Rev* 2015;43:1167–81.
- [103] Marck G, Nadin G, Privat Y. What is the optimal shape of a fin for one-dimensional heat conduction? *SIAM J Appl Math* 2014;74:1194–218.
- [104] Basavarajappa S, Manavendra G, Prakash SB. A review on performance study of finned tube heat exchanger. *J. Phys.*

Conf. Ser., vol. 1473, IOP Publishing; 2020, p. 12030.

- [105] Abdulateef AM, Mat S, Abdulateef J, Sopian K, Al-Abidi AA. Geometric and design parameters of fins employed for enhancing thermal energy storage systems: a review. *Renew Sustain Energy Rev* 2018;82:1620–35.
- [106] Mert Cuce P, Cuce E. Optimization of configurations to enhance heat transfer from a longitudinal fin exposed to natural convection and radiation. *Int J Low-Carbon Technol* 2014;9:305–10.
- [107] Lin S-C, Chuang F-S, Chou C-A. Experimental study of the heat sink assembly with oblique straight fins. *Exp Therm Fluid Sci* 2005;29:591–600.
- [108] Yang Y-T, Lin S-C, Wang Y-H, Hsu J-C. Numerical simulation and optimization of impingement cooling for rotating and stationary pin–fin heat sinks. *Int J Heat Fluid Flow* 2013;44:383–93.
- [109] Jang D, Park S-J, Yook S-J, Lee K-S. The orientation effect for cylindrical heat sinks with application to LED light bulbs. *Int J Heat Mass Transf* 2014;71:496–502.
- [110] Costa VAF, Lopes AMG. Improved radial heat sink for led lamp cooling. *Appl Therm Eng* 2014;70:131–8.
- [111] Kim D-K. Thermal optimization of branched-fin heat sinks subject to a parallel flow. *Int J Heat Mass Transf* 2014;77:278–87.
- [112] Huang C-H, Chen Y-H. An impingement heat sink module design problem in determining simultaneously the optimal non-uniform fin widths and heights. *Int J Heat Mass Transf* 2014;73:627–33.
- [113] Huang C-H, Chen Y-H. An optimal design problem in determining non-uniform fin heights and widths for an impingement heat sink module. *Appl Therm Eng* 2014;63:481–94.
- [114] Huang C-H, Chen Y-H, Li H-Y. An impingement heat sink module design problem in determining optimal non-uniform fin widths. *Int J Heat Mass Transf* 2013;67:992–1006.
- [115] Al-Sallami W, Al-Damook A, Thompson HM. A numerical investigation of thermal airflows over strip fin heat sinks. *Int Commun Heat Mass Transf* 2016;75:183–91.
- [116] Al-Damook A, Kapur N, Summers JL, Thompson HM. Computational design and optimisation of pin fin heat sinks with rectangular perforations. *Appl Therm Eng* 2016;105:691–703.
- [117] Zhao J, Huang S, Gong L, Huang Z. Numerical study and optimizing on micro square pin-fin heat sink for electronic cooling. *Appl Therm Eng* 2016;93:1347–59.

Information of the authors

Ali Sajjad , msc, lecturer ,Al-Furat Al-Awsat Technical University, Technical College of Al-Mussaib
e-mail: sajjad.ali.tcm.1@student.atu.edu.iq

Al-Abbas Audai Hussein, PhD, professor, Al-Furat Al-Awsat Technical University, Technical College of Al-Mussaib
e-mail: sajjad.ali.tcm.1@student.atu.edu.iq

Magid Hani Mizhir, PhD, professor, Al-Furat Al-Awsat Technical University, Technical College of Al-Mussaib
e-mail: sajjad.ali.tcm.1@student.atu.edu.iq

Nanocomposite Polymer Materials with High Performance Characteristics

Antonov A.S.^{1*}, Struk V.A.¹, Wan X.¹, Zhao L.¹, Zhang R.²

¹Yanka Kupala State University of Grodno, Belarus

²Zhejiang International Scientific and Technological Cooperative Base of Biomedical Materials and Technology, Zhejiang Engineering Research Center for Biomedical Materials, Laboratory of Advanced Theranostic Materials and Technology, Ningbo Institute of Materials Technology and Engineering, Chinese Academy of Sciences, Ningbo, People's Republic of China

*corresponding author

Abstract. The practical implementation of methodological approaches to the creation of nanocomposite materials for various functional purposes based on industrial thermoplastics is considered. The concept of energy and technological compliance of components is proposed, which makes it possible to provide synergistic effects in improving the parameters of the performance characteristics of nanocomposites based on thermoplastic matrices. An algorithm for the formation of a multilevel optimized structure of nanocomposites based on thermoplastics with high melt viscosity has been developed. Compositions of functional nanocomposites for the manufacture of elements with high parameters of service characteristics, the priority and novelty of which are protected by patents for inventions, are presented.

Keywords: nanocomposite materials, nanomodifier content, formation algorithm, multilevel structure, concept of energy and technological compliance, compatibilization.

Introduction

A defining feature of the development of modern mechanical engineering, chemical industry, construction industry and power engineering is wide application of composites based on high-molecular matrices as structural, tribological and sealing materials. The range of polymer functional engineering composite materials is extremely broad and permanently expanding due to the emergence of industrial products synthesized from macromolecular compounds with enhanced performance characteristics, the development of highly effective technologies for targeted filler modification, and the creation of new types of modifiers and fillers. A special place among engineering materials based on polymer binders is occupied by a new class of composite materials, in the composition of which particles with the maximum size not more than 100 nm are introduced as a functional component. Such materials are commonly referred to as nanocomposite materials and distinguish them from traditional engineering materials due to their special properties caused by the active action of a low-dimensional modifier on the structure of the polymer matrix [1-5].

The properties of polymer nanocomposite materials depend on the composition of the components and the technology used to form the material and its product. Material science and technology of polymer nanocomposite materials are largely based on traditional approaches that take into account classical ideas about the mechanisms and kinetics of interphase processes in the system "matrix-functional filler". However, in some cases experimental data cannot be described by such approaches, which do not take into account the special energy state and morphology of nanoscale particles. In this regard, comprehensive research on the physicochemical, materials science, and technological aspects of the formation and processing of composite materials with low-dimensional modifiers is necessary to develop the foundations for creating unified methodological approaches that can reliably predict the parameters of their performance characteristics, as discussed in our previous study [6].

The aim of this research is the practical implementation of methodological approaches to the creation of nanocomposite materials for various functional applications based on industrial thermoplastics.

1. Research methodology

Thermoplastic polymers and oligomers, the most common in materials science and technology of polymeric materials, were used as components for obtaining composite materials for various purposes: aliphatic polyamides (PA6 and PA6.6, produced by Branch "Khimvolokno Plant" of JSC "Grodno Azot", Belarus; PA11 (Rilsan), produced by Arkema, France), polyolefins (PP, LDPE, HDPE, produced by JSC "Polimir", Belarus), fluorine-containing compounds (polytetrafluoroethylene (PTFE) F4 and F4-M (JSC "Halogen", Russia), products of thermogasodynamic synthesis of PTFE (ultradisperse polytetrafluoroethylene UPTFE), produced by Institute of Chemistry of the Far East Branch of the Russian Academy of Sciences, Russia).

Dispersed, including nanoscale, particles of carbon-containing (carbon nanotubes (CNT), carbon fibers (CF), ultradisperse diamonds (UDA), technical carbon (TC), silicon-containing (clays) and metal-containing (Cu formates) compounds obtained by technological effects on natural and synthetic semi-finished products produced at industrial enterprises of Belarus and the Russian Federation were used to control the structure parameters and performance characteristics of composites and products made of them.

The parameters of the stress-strain characteristics of the developed materials were evaluated on standard samples according to the relevant Russian standards. Tribological characteristics were determined on universal or original friction machines according to the schemes "indenter – disk", "shaft – partial liner". Assessment of the performance of products made of developed nanomaterials in the structures of automotive units for various purposes and technological equipment was carried out on stands and in the process of virtual tests using the SKIF supercomputer and full-scale tests.

2. Results and discussion

When choosing modifiers for the production of nanocomposite materials with optimized structure that determine the expediency and efficiency of their use in systems for a given functional purpose, *the principle of energy and technological compliance of components* was used, taking into account the concept of reasonable sufficiency and technological, environmental and economic aspects. The practical implementation of the developed methodological approaches ensures the achievement of technically significant effects of increasing the parameters of stress-strain, adhesive, tribological characteristics of composites based on industrial matrices both at the doping content (0.001–1.0 wt. %) of modifiers and at their content of 20–40 wt. %. At the same time, depending on the features of the composition, structure, dispersion and shape of the modifying particles, different levels of structural organization are realized. For highly dispersed particles at a doping content (0.001–1.0 wt. %) the structure is mainly optimized at the supramolecular and intermolecular levels [7–10]; when modifying matrices with active micrometer fragments (80–150 μm) of high-modulus fibers (carbon, oxaloon, glass) at a content of 5–40 wt. % the prevailing role is played by the interfacial level [11, 12]. At the same time, modifiers can save the stability of the initial parameters of characteristics in the process of composite formation and operation of the product or metal-polymer system, or show lability due to transformation under the influence of physical and chemical processes, changing the initial structural parameters of the composite.

The mechanism of structuring action of nanosized particles (NSP) in polymer and oligomeric matrices of various structures is investigated. Based on the developed model, which assumes the formation of spherical supramolecular structures under the action of the active centers of the nanoparticle, an analytical expression was obtained to calculate the concentration of the modifier sufficient to transfer the entire matrix to an ordered state. As follows from [13, 14], the matrix will be completely modified provided that the modifier particle is active in the boundary layer with a thickness of $L = r [1 + (\rho_n/\rho_m)] ((1/C_n) - 1)^{1/3}$, where r is particle size; ρ_n, ρ_m are density of filler and polymer; C_n is filler content.

From this expression, it follows that the L is linearly related to the size of the nanoparticle and is practically independent of the ratio ρ_m / ρ_n , that suggests similar mechanisms of modifying action in particles of different composition and production technology. Even with doping content (0.001–1.0 wt.%) the ratio of $1/C_n \gg 1$ and the structuring effect of the nanoparticle on 2–3 adjacent layers of macromolecules provides a significant modification effect. Experimental studies have confirmed the adequacy of this conclusion (Fig. 1).

It has been established that the effectiveness of the modifying effect of a nanosized particle (NSP) is influenced not only by its size, composition and structure, but also by its shape. From an analytical expression that defines the size parameter of a nanoparticle characterized by a special energy state that affects the efficiency of the modifying action [15], $L_n = h \sqrt{3} \cdot \theta_D^{-1/2} / \sqrt{2m_e k}$, where h, k are Planck and Boltzmann constants, respectively, m_e is mass of electron, θ_D is Debye temperature, follows its dependence on the crystal-chemical direction. Therefore, using modifier particles with relatively large sizes, the surface layer of which contains nanoscale components that meet the calculated value of L_n , it is possible to achieve technically significant modifying effects using available technologies for obtaining and processing polymer composites.

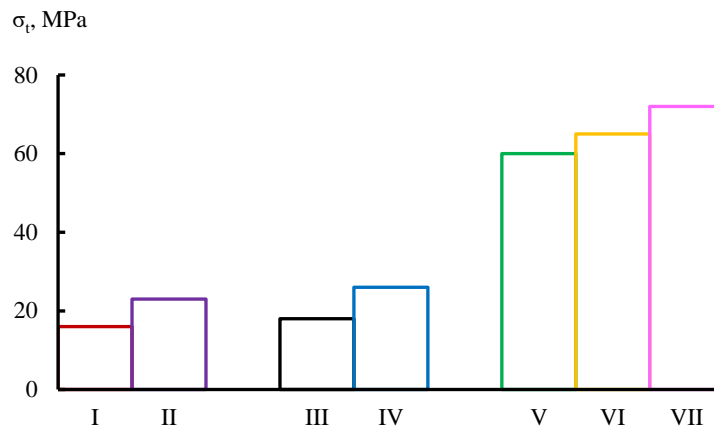


Fig. 1. – Tensile strength parameter σ_t for HDPE (I, II), PTFE (III, IV), PA 6 (V, VI, VII) initial (I, III, V) and modified by 0,05 wt. % UDD (II, VII), Cu (VI) and 0,5 wt. % UPTFE (IV)

Model concepts of the mechanisms of modification of high-molecular matrices by nanosized particles of various shapes have been developed. It is shown that when using particles of lamellar (scaly), whisker (fiber-like) and spherical shape, the degree of modification of the matrix M changes, determined by the ratio of the total modified volume to the total volume of the composite. Taking into account the different energy state of the NSP determined by the L_n parameter, and taking into account the anisotropic nature of the Debye temperature θ_D , the ratio of the degree of modification by scaly (M_{sc}), whisker (M_{wh}) and spherical (M_{sph}) particles with the same content in the composite was obtained: $M_{sc} : M_{wh} : M_{sph} = 1 : 0,4 : 0,8$.

It follows from the obtained expression that when creating poorly filled nanocomposites based on polymer matrices, it is preferable to use layered modifiers, which include natural silicates, such as clays, micas, talc, which, under certain conditions, are able to disperse to form nanosized particles of a lamellar form [7–10].

The conducted experimental and theoretical studies are based on the assumption of invariability of the structure, composition and shape of the NSP introduced into the polymer matrix. At the same time, there are classes of NSP (metallic, oxide, metal-containing), which are able to transform as a result of physical and chemical processes occurring in the boundary layers of composites under the action of operational factors (thermal, mechanical, mechanochemical, etc.) with the formation of products of a different composition and structure and with a different mechanism of structurizing effect on the matrix polymer. Therefore, the justified choice of NSP and technologies for their production for the targeted modification of a polymer or oligomeric matrix involves a system analysis of structural-phase transformations, taking into account the energy and physicochemical aspects of the formation and functioning of a metal-polymer system within the framework of the concept of synergistic structuring based on the proposed methodological principles for the implementation of the nanostate phenomenon. The developed model concepts on the effect of energy and structural parameters of NSP on the efficiency of polymer matrix modification [7–15] made it possible to determine technological approaches to obtaining effective nanomodifiers using available semi-finished products in the form of layered minerals (clay, talc, mica, tripoli, etc.), as well as technological waste from chemical industries (products of refining vegetable oils, phosphogypsum, products of metallurgical production). The essence of the developed methods for obtaining silicate-containing NSP consists in the thermal effect on the dispersed particles of the semi-finished product obtained by dispersion in impact devices (grinders) with a temperature gradient of 800–1000 K in an air medium or an oxidation-free gas flow with a density $3 \cdot 10^6$ – $8 \cdot 10^7$ W/m². Implementation of the developed methods for modification of polymer matrices of NSP in the amount of 0.1–10.0 wt. % or diffusion treatment of products made of polymer composites based on industrial thermoplastics (aliphatic polyamides PA6, PA6.6, PA11, polyolefins PP, HDPE) or their blends makes it possible to increase the strength parameters by 1.1–1.3 times, wear resistance by 1.5–2.0 times, as well as resistance to thermal-oxidative environments due to multi-level modification.

The developed principles of multi-level inoculation of composite materials, the formation of an integrated supramolecular structure by modifying the matrix by a set of nanosized particles through catalysis of interfacial interaction make it possible to implement the concept of synergistic structuring in the production of nanocomposites based on thermoplastics, including those high melt viscosity (PTFE, UHMWPE). An algorithm has been developed for the formation of compositions of high-strength wear-resistant composites based on high melt viscosity matrices (PTFE, UHMWPE), methods of their manufacture, which provides an increase in the parameters of stress-strain characteristics in comparison with analogues (Fig. 2).

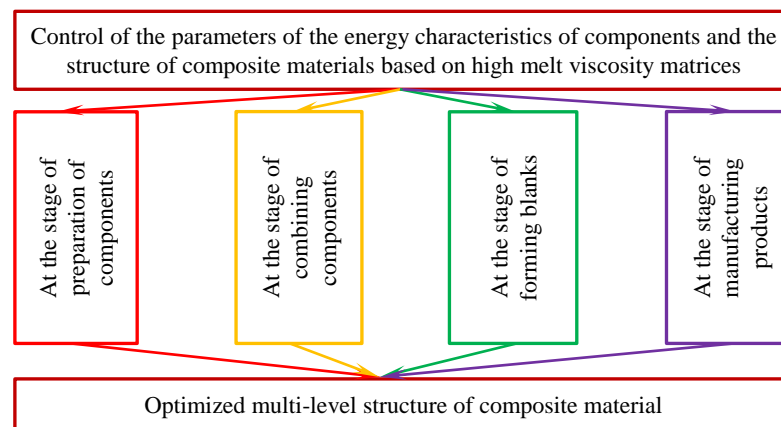


Fig. 2. – Algorithm for the formation of a multilevel optimized structure of composite materials based on thermoplastic matrices with high melt viscosity

When using nanoscale modifiers (carbon black, UPTFE, clay, talc), it is advisable to activate the components at the stages of preparation and combination using energy influences (thermal, laser). This approach has been tested in the development of technologies for the production of low-fill (0.5–5.0 wt%) nanocomposites using a combination of NSP (UPTFE, carbon black) and products of activation of layered minerals by thermal action in the temperature range 473–1373 K.

For the development of low-fill composites based on high-viscosity matrices (UHMWPE, PTFE), options for implementing the principle of multilevel modification based on a combination of components with different resistance to transformation under the influence of technological factors are proposed. Within the framework of the current technological paradigm of fluorocomposites, an imperfect structure is formed due to the absence of a pronounced viscous-fluid state of PTFE, which prevents the processes of monolithization and interfacial interaction. The proposed combination of carbon-containing particles (CNT, carbon black) and UPTFE provides a reduction in structural heterogeneity due to the polymer-oligomeric structure and special rheological characteristics, which has a favorable effect on the performance characteristics of composite (Fig. 3). When used as modifiers of dispersed particles of thermoplastics (polyamides, polyolefins, polysulfone) under the influence of molding temperatures (573–623 K) for 8–24 hours, conditions are created for the formation of carbon-containing components with high thermodynamic compatibility with PTFE, with a shape adapted to interparticle defects, and high parameters of stress-strain characteristics ($\sigma_t = 85\text{--}90\text{ MPa}$). As a result of the transformation of the initial structure of the modifier, a composite is formed with a range of characteristics close to the characteristics of composites containing carbon fiber (CF) [16].

An effective modifier of the transformable type is the dispersed particles of oligomers selected from the oligoimide group (oligomaleidoaminophenylene, oligomaleidohydroxyphenylene, tetramaleimide, N, N'-bis-maleimides of unsaturated dicarboxylic acids, etc.). Carbonization processes under the influence of technological factors lead to the formation of carbon-containing particles with a nanoscale relief of the surface layer and increased activity in the processes of interfacial interaction, as a result of which structures with high parameters of stress-strain ($\sigma_t = 36\text{--}46\text{ MPa}$) and tribological ($I \times 10^7 = 0,5\text{--}2,0\text{ mm}^3/\text{N}\cdot\text{m}$) characteristics are formed.

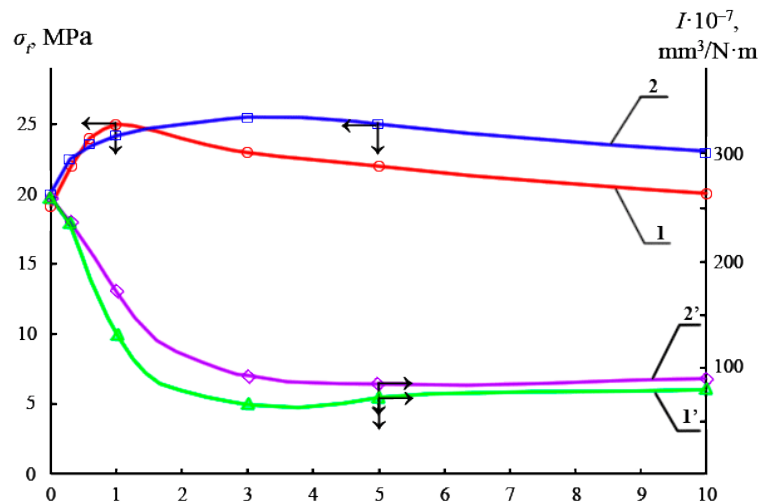


Fig. 3. – Dependence of tensile strength σ_t (1, 2) and wear intensity I (1', 2') of composite materials based on polytetrafluoroethylene modified with ultrafine polytetrafluoroethylene (UPTFE) on the content of dispersed particles of carbon black TU P324 (1, 1') and TU P803 (2, 2'). The content of UPTFE in composites is 2.0 wt. %

When developing composites with a filler with a size range of 50–150 μm and a content of 10–35 wt. % nanostate phenomenon can be realized within the framework of the concept of energy and technological compliance of components using mechanochemical activation.

Using the ideas about the mechanisms of structure formation of fluorocomposites formed using mechanically activated components developed by the scientific school of Prof. Okhlopkova A.A., methodological principles of fluorocomposite technology are proposed, in which fragments of carbon fiber (CF) are used as a modifier (Fig. 4).

Activation of components of composites based on PTFE, UHMWPE at the stage of forming blanks in accordance with patented technologies using common equipment for cold formation (LTF) with subsequent sintering made it possible to increase the tensile strength parameter for materials with a hydrocarbon content of 1–20 wt. % from 17–18 MPa to 20–35 MPa due to mechanochemical interaction at the filler-matrix interface in view of differences in thermal expansion coefficients.

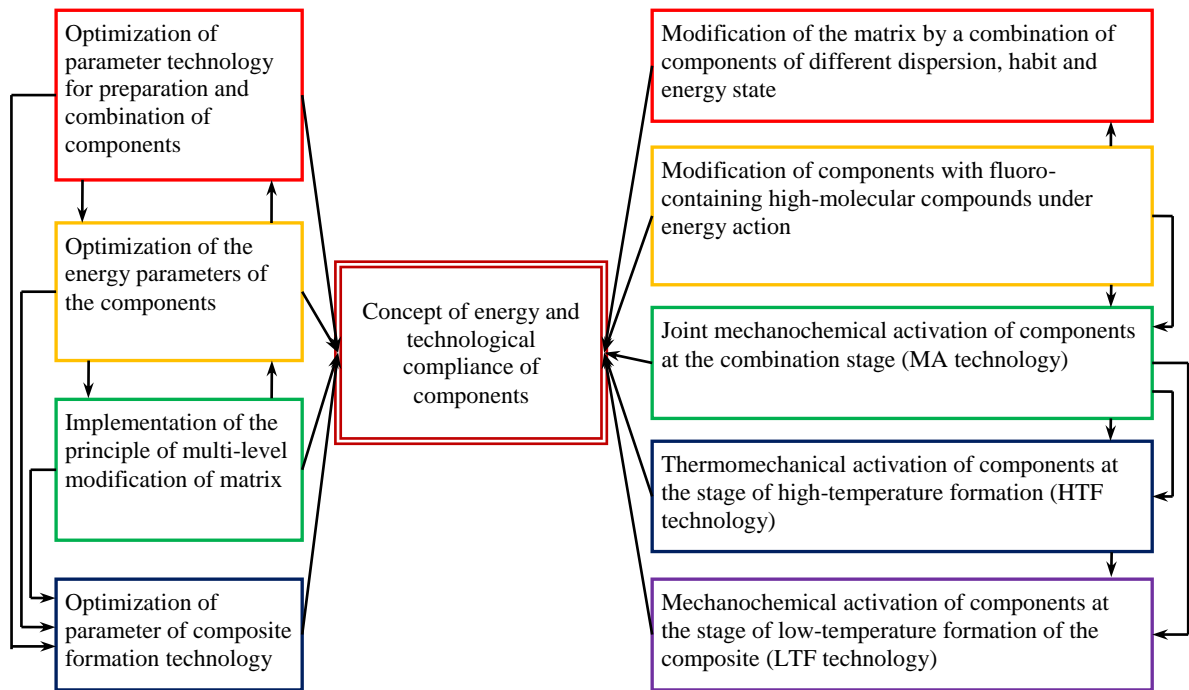


Fig. 4. – Methodological principles of technology of highly filled fluorocomposites with high performance parameters [17]

The proposed methods for achieving the nanostate of components using mechanical activation at the stages of combination (MA), high-temperature formation (HTF) and low-temperature formation (LTF) made it possible to develop a range of fluorocomposites with high performance parameters for the manufacture of elements of metal-polymer systems operated under the influence of elevated temperatures, absence or limitation of lubrication, reverse movement, exposure to active media, protected by patents of the Republic of Belarus for inventions. The combination of MA and HTF, MA and LTF technologies provides an opportunity to reduce the negative impact of the structural paradox noted in the works of A.K. Pugachev and Y.K. Mashkov (Fig. 5). The parameters of the characteristics of fluorocomposites obtained according to the proposed methodological principles in comparison with analogues are presented in [18–23]. As follows from Table 1, the developed composite compositions are superior in the main parameters of characteristics to the domestic and foreign analogues used (F4K20, Fluvis, Flubon) due to the implementation of the synergistic structuring effect, which made it possible to increase the carbon fiber content to 40–45 wt. % to increase the load characteristics of products made of such fluorocomposites.

Table 1. Comparative performance parameters of PTFE-based composite materials

Characteristic	Parameter value for composite							
	Flubon	Fluvis		Superfluvis		Composites obtained using developed technologies		
		Patent BY 9396	Patent BY 8480	Patent BY 9819				
Tensile stress, MPa	9	14	17*	18	27*	22–33	32–35	18–30
Wear intensity at friction without lubrication, $I \times 10^{-7}$, mm ³ /(N·m)	5.0	5.0	3.5*	4.5	1.5*	1.5–2.3	1.3–2.0	1.7–1.9
Filler content, wt. %	30	30	20*	30	20*	20	20–40	20–45

*Data of regulatory technical documentation for materials "Fluvis", "Superfluvis"

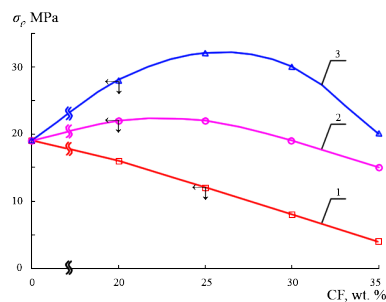


Fig. 5. – Dependence of tensile strength of PTFE-based composite materials on carbon fiber (CF) content in mechanical combination of components (1), in mechanochemical activation of components (MA) and formation in the free state (LTF) (2) and high-temperature formation (HTF) under conditions of triaxial compression (3)

Methodological principles for controlling the processes of structure formation of polymer matrices through the use of crystal-chemical parameters of nanosized particles of modifiers, the formation of an integrative supramolecular structure by modifying it with a set of nanoparticles of the same or different composition or shape are implemented in the development of composite materials based on industrial thermoplastics of the polyamide and polyolefin class.

The priority area of research was the development of composites for the manufacture of structural elements and the formation of multifunctional coatings used in the structures of automotive and tractor units (cardan shafts, brake chambers, shock absorbers) and technological equipment (belt conveyors) (Table 2).

The introduction of polyamide 11 into polyamide 6 in the presence of layered silicate nanoparticles provides an increase in adhesion and tribological characteristics [24]. The presence of nano-sized metal particles has a complex effect on the structure parameters, increasing the resistance of coatings to thermal-oxidative environments. The combined content of nanosized carbon-containing particles and fluorine-containing compounds contributes to the achievement of an optimal combination of adhesion, tribological characteristics and hydrophobicity of coatings, the parameters of which are considered in [25].

In the development of compositions of nanocomposite materials based on mixtures of polyamides, polyolefins (PA6, PA6.6, PA11, PP, HDPE, copolymer EVA), differing in thermodynamic compatibility, the established effect of physical compatibilization was used, due to the ability of nanosized particles to form intermolecular physical bonds of the adsorption type, experimentally confirmed by EPR spectroscopy and rheological studies.

Table 2. Comparative characteristics of polyamide-based composite materials

Characteristic	Parameter values for compositions				
	PA6*	Composite material			
		Patent BY 9397	Patent BY 10898	Patent BY 17434	Patent BY 21059
Tensile stress, MPa: – original	56–60	65–67	65–68	70–73	72–76
– after 1,000 h of thermal oxidation at 423 K in air	18–30	–	58–62	43–45	–
Adhesive strength (Falling indenter method), cm, not less	10–15	>50	45–51 MPa (Normal tear-off method)	28–30	50
Friction coefficient without lubrication at loads of 5–10 MPa, $v = 0,5$ m/s	0.5–0.6	0.10–0.12	–	0,08–0,11	0,08–0,09
Влагопоглощение, мас. %	9–10	–	–	3.0–3.5	2.0–3.0

*PA6 produced by JSC "Grodno Azot"

The compatibilizing effect of nanoparticles in the thermomechanical combination of components in a viscous state contributes to the formation of supramolecular and intermolecular hybrid structures. The function of a physical compatibilizer is characteristic of nano-sized particles of various composition, structure and production technology (clay, CNT, ultra-dispersed diamonds (UDD), Cu, etc.). This aspect made it possible to develop composite materials based on thermomechanically combined blends of polyamides and polyolefins with characteristics superior to analogues [26, 27].

Composites based on combined regenerated thermoplastic components are a full-fledged alternative to primary thermoplastics in the manufacture of engineering products for the construction industry (fasteners, metal-polymer rollers), including road construction (identification and restrictive elements for designating underground communications) in accordance with the developed regulatory and technical documentation – technical specifications TS BY 500037559.004-2021, TS BY 500037559.005-2021, TS BY 500037559.006-2021.

Comprehensive studies of the areas of practical implementation of the phenomenon of nanostate in materials science and technology of nanocomposites based on industrial thermoplastics have confirmed their validity and adequacy to the functioning industrial complex.

Conclusion

Based on the research, the following main results were obtained:

1) Methodological principles for the implementation of the nanostate phenomenon in materials science and technology of functional nanocomposites based on industrial thermoplastics of the polyolefin, polyamide, fluoroplastic class have been developed by optimizing the structure at the intermolecular, supramolecular and interfacial levels, ensuring the achievement of a synergistic combination of performance parameters. These principles are based on:

– established crystal-chemical prerequisites for the selection of natural and synthetic carbon-containing, metal-containing and silicon-containing semi-finished products for the directed formation of active nanosized particles with specified structural, morphological and energy parameters under optimal technological action (mechanochemical, thermal, laser);

– implementation of the conditions for the energy compliance of nanomodifiers to the prevailing mechanism for the formation of the optimal structure of polymer, oligomeric and combined matrices at various levels of organization (molecular, supramolecular and interfacial);

– providing conditions for the manifestation of the preferred mechanisms of interfacial physicochemical interactions of components with the formation of boundary layers of optimal structure, which determine the mechanisms of destruction of nanocomposites under the influence of various operational factors.

2) Based on the concepts of condensed matter physics using the wave functions of the barrier model and the Debye-Waller factor, a theoretical analysis of the prerequisites for the formation of the nanostate of material objects in the form of dispersed particles and substrates in the process of their dispersion and technological impact on semi-finished products of various composition and structure is carried out. The mechanisms of formation of dispersed particles in the active state and charge mosaic on the surface of substrates under mechanical, mechanochemical and energy effects on semi-finished products are substantiated. An analytical substantiation of the change in the parameters of energy characteristics with a decrease in the geometric dimensions of a material object is given, confirming the hypothesis of the energy equivalent.

3) Physicochemical aspects of the modifying effect of nanoparticles of various composition and structure in thermoplastic matrices are considered. Characteristic features have been established that determine the activity of low-dimensional particles in the processes of transformation of the structure of the binder composite material at the molecular, intermolecular and supramolecular levels, consisting in their special energy state due to habit, size, factor and production technology. Using the proposed analytical expression, the analysis of the dimensional factor that determines the nanostate of the NSP of mono- and polyatomic substances, which determine their transition to a nanostate with high modifying activity in relation to high-molecular matrices, is carried out.

4) Features of the mechanism of modifying action of nanoparticles of various production technologies, composition and structure are considered. It is shown that the most important criterion of activity in the processes of adsorption interaction of a nanoparticle with macromolecules of a polymer or oligomeric matrix is its energy state, characterized by the presence of an uncompensated charge with a long relaxation time.

5) The methodological principle of multi-level modification is implemented in the creation of a range of nanocomposite functional materials based on industrial thermoplastics of the polyamide, polyolefin, fluoroplastic class with the introduction of a combination of components of different composition and dispersion with high energy characteristics. It is shown that the developed compositions based on aliphatic polyamides and polyolefins (PP, HDPE, LDPE) and their mixtures are superior to the base materials and their analogues by at least 1.2–1.5 times in terms of strength, wear resistance and adhesive characteristics. Fluorine-containing nanocomposites, semi-finished products and products made of them, formed on the basis of the developed technological paradigm that ensures the formation of a low-defect structure due to the activation of interfacial interaction processes at the stages of combining components, pressing and formation, realize the synergistic effect of high parameters of stress-strain and tribological characteristics (σ , J) at least 1.5–2.6 times compared to domestic and foreign analogues formed using traditional technology.

6) Technologies for the implementation of the phenomenon of nanostate in the production of functional nanocomposite materials based on industrial thermoplastics and products from them for use in the structures of machines, mechanisms, technological equipment have been developed, providing the formation of an optimal multi-level structure to increase the service life. The technologies are based on the use of common equipment and are intended for sale at specialized enterprises for the industrial production of products from polymer and composite materials based on primary and regenerated raw materials.

Acknowledgements

The given research was carried out within the framework of integrated assignment 8.4.1.51 "The concept of multilevel modification in materials science and technology of nanocomposites based on thermoplastic blends" of R&D "Mechanisms of the influence of the energy factor in the multilevel structuring of polymer nanocomposites" and R&D "Development of compositions and technology of import-substituting nanocomposite semi-finished products based on thermoplastic blends for the production of products with high parameters of characteristics using additive technologies" included in the subprogram "Multifunctional and composite materials" of the State programs for scientific research "Materials science, new materials and technologies" in 2021–2025.

References

- [1] Ajayan P.M., Schadler L.S., Braun P.V. Nanocomposite science and technology. Weinheim: Wiley-VCH, 2003. – 230 p.
- [2] Poole Ch.P., Owens F.J. Introduction to Nanotechnology. New Jersey: John Wiley & Sons, Inc., 2003. – 399 p.
- [3] Golovin Yu.I. Introduction to nanotechnology. Moscow: Mashinostroenie, 2003. – 112 p. (In Russian).
- [4] Gusev A.I. Nanomaterials, nanostructures, nanotechnology. Moscow: Nauka, 2007. – 416 p. (In Russian).
- [5] Avdeychik S.V., Struk V.A., Antonov A.S. Nanostate factor in material science of polymer nanocomposites. Saarbrücken: LAP LAMBERT Acad. Publ., 2017. – 468 p. (in Russian).
- [6] Avdeychik S.V., Antonov A.S., Struk V.A., Prokopchuk N.R., Zhang R. Nanostate Factor in Materials Science of Functional Nanocomposite Materials // Material and Mechanical Engineering Technology, 2024, Vol. 3. – p. 69–75.

- [7] Avdeychik S.V., Ovchinnikov E.V., Liopo V.A., Struk V.A. Features of the modifying effect of natural silicates in polymer composites // Reports of the National Academy of Sciences of Belarus, 2004, T. 48, Vol. 3. – p. 113–116. (In Russian).
- [8] Avdeychik S.V., Ovchinnikov E.V., Liopo V.A., Struk V.A., Lude L., Jang X.X. On the mechanism of modifying action of nanosilicates in polymer matrices // Materials, Technologies, Tools, 2004, T. 9, Vol. 3. – p. 46–51. (In Russian).
- [9] Liopo V.A., Struk V.A., Avdeychik S.V., Kletsko V.V., Ovchinnikov E.V. Model representations on the mechanism of polymer modification by layered silicates // Reports of the National Academy of Sciences of Belarus, 2005, T. 49, Vol. 6. – p. 101–105. (In Russian).
- [10] Avdeychik S.V., Liopo V.A., Struk V.A. On the mechanism of action of doping nanoscale modifiers in polymer matrices // Plasticheskie massy, 2007, Vol. 8. – p. 36–41. (In Russian).
- [11] Struk V.A., Tsvetnikov A.K., Antonov A.S., Avdeychik S.V., Ovchinnikov E.V. Mechanochemical aspects of the technology of formation and application of fluoroplastic composites // Proceedings of the National Academy of Sciences of Belarus. Physical-technical series, 2009, Vol. 3. – p. 28–35. (In Russian).
- [12] Avdeychik S.V., Struk V.A., Voropaev V.V. Technological principles of formation of high-strength wear-resistant fluorocomposites // Plasticheskie massy, 2013. Vol. 12. – p. 3–8. (In Russian).
- [13] Avdeychik S.V., Liopo V.A., Struk V.A., Prushak V.Ya., Protaseny A.V., Dmitrochenko V.V. Polymer-silicate engineering materials: physical chemistry, technology, application. Minsk, Tekhnologiya, 2007. – 431 p. (in Russian).
- [14] Avdeychik S.V., Voropaev V.V., Skaskevich A.A., Struk V.A. Engineering fluorocomposites: structure, technology, application. Grodno, Yanka Kupala State University of Grodno, 2012. – 339 p. (in Russian).
- [15] Avdeychik S.V., Liopo V.A., Ryskulov A.A., Struk V.A. Introduction to the physics of nanocomposite engineering materials. Grodno: Grodno State Agrarian University, 2009. – 439 p. (in Russian).
- [16] Avdeychik S.V., Kostyukovich G.A., Kravchenko V.I., Lovshenko F.G., Lovshenko G.F. Nanocomposite engineering materials: experience in the development and application. Grodno, Yanka Kupala State University of Grodno, 2006. – 403 p. (In Russian).
- [17] Avdeychik S.V., Struk V.A., Antonov A.S., Lesun A.N. Nanostate factor in polymer nanocomposites technology // Plasticheskie massy, 2021, Vol. 5-6. – p. 13–17. (In Russian).
- [18] Struk V.A., Kravchenko V.I., Kostyukovich G.A., Avdeychik S.V., Ovchinnikov E.V. Composite tribological material: pat. RU 2265037. – Publ. 27.11.2005. (In Russian).
- [19] Struk V.A., Kostyukovich G.A., Kravchenko V.I., Ovchinnikov E.V., Avdeychik S.V., Gorbatshevich G.N. Method of manufacturing products from polymer-based composite materials: pat. RU 2266925. – Publ. 27.12.2005. (In Russian).
- [20] Prushak V.Ya., Ishchenko M.V., Prushak D.A., Ishchenko R.V., Avdeychik S.V., Struk V.A. Method for processing polytetrafluoroethylene and filler to produce composite materials: pat. BY 17719. – Publ. 30.12.2013. (In Russian).
- [21] Struk V.A., Gorbatshevich G.N., Prushak D.A., Barsukov V.V., Avdeychik S.V. Method for obtaining a blend for processing into products from composite materials based on polytetrafluoroethylene: pat. BY 18063. – Publ. 30.04.2014. (In Russian).
- [22] Struk V.A., Avdeychik S.V., Ovchinnikov E.V., Kostyukovich G.A., Kravchenko V.I. Composition of composite lubricant: pat. BY 18073. – Publ. 30.04.2014. (In Russian).
- [23] Struk V.A., Voropaev V.V., Gorbatshevich G.N., Avdeychik S.V., Kravchenko V.I., Ovchinnikov E.V., Kostyukovich G.A. Method for making a blank from polytetrafluoroethylene composite material: pat. BY 18089. – Publ. 30.04.2014. (In Russian).
- [24] Struk V.A., Kravchenko V.I., Kostyukovich G.A., Avdeychik S.V., Skaskevich A.A., Chekel A.V. Composite thermoplastic material: pat. BY 9820. – Publ. 30.10.2007. (In Russian).
- [25] Struk V.A., Avdeychik S.V., Ishchenko M.V., Ishchenko R.V., Prushak D.A., Prushak A.S. Method of processing carbon graphite fiber or fabric: pat. BY 17248. – Publ. 30.06.2013. (In Russian).
- [26] Struk V.A., Kravchenko V.I., Kostyukovich G.A., Ovchinnikov E.V., Lyshov D.V., Avdeychik S.V., Rogachev A.V. Sealing kit for gland seals: pat. RU 2296256. – Publ. 27.03.2007. (In Russian).
- [27] Struk V.A., Kravchenko V.I., Kostyukovich G.A., Avdeychik S.V. Composite abrasion-resistant material: pat. BY 9215. – Publ. 30.04.2007. (In Russian).

Information of the authors

Antonov Alexander Sergeevich, PhD (Engineering), Associate Professor, Associate Professor at the Department of Material Science and Resource-Saving Technologies, Yanka Kupala State University of Grodno
e-mail: antonov_as@grsu.by

Struk Vasily Alexandrovich, DSc (Engineering), Professor, Professor at the Department of Material Science and Resource-Saving Technologies, Yanka Kupala State University of Grodno
e-mail: struk@grsu.by

Wan Xuemin, MSc (Engineering), Postgraduate Student at the Department of Material Science and Resource-Saving Technologies, Yanka Kupala State University of Grodno
e-mail: w1414792871@icloud.com

Zhao Liang, MSc (Arts), Master's Student at the Department of Material Science and Resource-Saving Technologies, Yanka Kupala State University of Grodno
e-mail: leonzhao0614@gmail.com

Zhang Ruoyu, Ph.D., Professor, Zhejiang International Scientific and Technological Cooperative Base of Biomedical Materials and Technology, Zhejiang Engineering Research Center for Biomedical Materials, Laboratory of Advanced Theranostic Materials and Technology, Ningbo Institute of Materials Technology and Engineering, Chinese Academy of Sciences
e-mail: zhangruoyu@nimte.ac.cn

Evaluation of Dry Sliding Wear Characteristics in Al5052/TiB₂/ZrO₂ Composites Against EN-31 Steel Counterbody

Agarwal S. *, Singh S.

National Institute of Technology Kurukshetra, India

*corresponding author

Abstract. The current study inspected the dry sliding wear characteristics of composites with Al5052 matrix. The composites were stir-casted with nano-TiB₂ and nano-ZrO₂ as reinforcements. The test specimens were examined using a pin-on-disc device with an EN-31 steel disc under multiple loads (10 N, 20 N, and 30 N) and speeds (0.94 m/s, 1.57 m/s and 2.20 m/s). To inspect the worn surfaces, scanning electron microscopy is utilized. The wear rate increased with the load, reaching a maximum value at 30 N. The resistance to wear for Al5052-based composite with 1% TiB₂ and 1% ZrO₂ was found to be best. The wear rate was observed to increase initially at 1.57 m/s and then decrease when the speed was increased to 2.20 m/s. SEM micrographs revealed abrasion and delamination of the worn-out surfaces.

Keywords: aluminium matrix composites, titanium diboride, zirconia, stir casting, dry sliding wear.

Introduction

Aluminium matrix composites (AMCs) are evolving as a significant class of materials for advanced technical applications due to improved properties like enhanced specific strength, improved stiffness, and greater resistance to wear when compared to unreinforced Aluminium alloys [1, 2]. The applications include the components for the aerospace, automobile, marine and transportation industries [3–5]. AMCs consist of Aluminium alloy matrices reinforced with ceramic materials like Silicon carbide (SiC), Alumina (Al₂O₃), Silicon Nitride (Si₃N₄), Titanium carbide (TiC), Graphene, Titanium diboride (TiB₂), Carbon Nanotube (CNT) and Zirconia (ZrO₂) [6].

The wear characteristics of AMCs are critical for many load-bearing applications. Enhancing the wear resistance can extend the service life of components exposed to repetitive sliding conditions [7]. Factors like reinforcement content, size and distribution of particles affect the hardness and wear characteristics of AMCs [8]. The lowest wear rate was found in Al7075-AMC reinforced with 2 weight% Al₂O₃ by Baradeswaran and Perumal [9]. Shanmugaselvam et al. [10] conducted the wear test on AMCs reinforced with SiC, B₄C and graphite. Composite with 13 wt% SiC, 13 wt% B₄C and 10 wt% graphite had the lowest wear rate.

Studies have shown that factors like load, sliding speed, and distance influence the rate of wear in Aluminium-based composites [11–13]. However, there is limited understanding of the combined effects of these factors, along with the reinforcement amount, on the wear characteristics of nanoparticle-reinforced AMCs using Al5052 as matrix material. Al5052, an aluminium-magnesium alloy, provides a stable and ductile matrix for the reinforcement materials. Its combination of moderate strength, good corrosion resistance, and excellent formability makes it an ideal choice for marine, fuel tanks, automotive and aerospace applications [14–16].

The current research examines the wear attributes of Al5052-based AMCs with varying compositions of nanosized TiB₂ and ZrO₂ reinforcements, taking into account wear between cylinder liners and piston rings in automobiles and also between brake pads and discs for automobile and marine vessels. The wear characteristics will be evaluated under different loads and speeds at room temperature. The assessment of stir-cast TiB₂ and ZrO₂ nanoparticles in Al5052 alloy AMCs—a combination that is rarely studied—is what makes this research study novel.

1. Materials and Methods

1.1 Materials

A commercially available Al5052 alloy served as the matrix for this study. Table 1 shows the chemical content of Al5052 as determined by spectro analysis of the sample. TiB₂ nanoparticles of average particle size (APS) of a maximum of 80 nm size and 99.9% purity were procured from Intelligent Materials Pvt. Ltd., Punjab; whereas, ZrO₂ nanoparticles of 30-50 nm APS and 99.9% purity were obtained from Nano Research Lab, Jamshedpur.

Table 1. Chemical content (weight %) of Al5052

Elements	Si	Fe	Cu	Mn	Mg	Cr	Zn	Al
Composition	0.122	0.230	0.024	0.071	2.233	0.154	0.072	Remainder

The EDX mapping of TiB₂ and ZrO₂ powders are shown in Figs. 1a) and 1b) respectively.

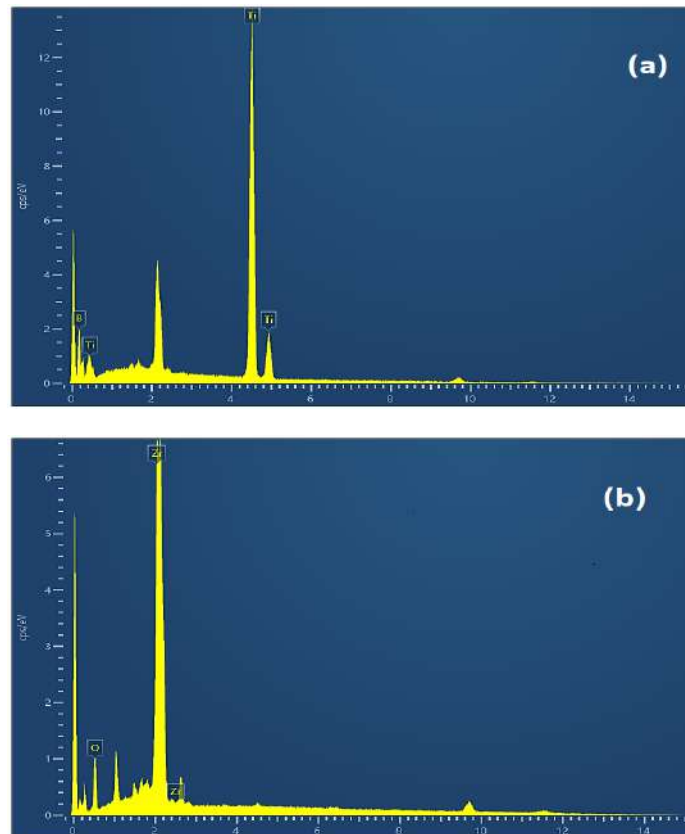


Fig. 1 - a) EDX mapping of TiB_2 and b) EDX mapping of ZrO_2

1.2 Composite fabrication

Al5052-based composite test specimens were fabricated by stir casting. In a muffle furnace, the TiB_2 and ZrO_2 nanoparticles were first preheated to $350^\circ C$ for 1 hour. This preheating step assisted in removing any moisture or gases that had been adsorbed on the nanoparticles [17].

Meanwhile, approximately 800 grams of Al5052 alloy were added to a furnace preheated to $700^\circ C$. At this temperature, the Al5052 alloy melted into a liquid state. Once the metal was fully molten, the preheated TiB_2 and ZrO_2 nanoparticles were introduced slowly into the melt. Potassium Hexafluorotitanate Powder and Mg were added to improve the wettability. The ceramic nanoparticles were distributed evenly throughout the molten aluminum alloy by agitating the composite slurry for 10 minutes with a mechanical stirrer containing high-strength steel impellers rotating within the furnace [18, 19].

Following that, the heated steel mould was filled with the composite melt and was allowed to harden into the required shape. Table 2 shows the composition of the test specimens prepared for this study.

Table 2. Specimen composition for the Al5052 composites

Specimen	Weight %		
	Al5052	TiB_2	ZrO_2
S1	99	1	0
S2	99	0	1
S3	98	1	1

2. Wear Experiment

The DUCOM pin-on-disc machine served as the primary instrument for evaluating the dry wear characteristics of Al5052-based composite samples, adhering to the ASTM G99 standard for specimen preparation. The samples, shaped as square pins, measured 25 mm in height and 10 mm in width. To evaluate the wear specimens, an EN-31 steel disc with a 200 mm diameter and a hardness of 62 HRC is employed on a pin-on-disc device. Emery sheets of grit sizes 220, 400, 600, 1000, 1500, and 2000 were employed to polish the surfaces of test specimens. The evaluations took place at 60 mm track diameter for time period of 15 minutes [20, 21]. The specimen weights were recorded using an electronic weighing machine with a resolution of 0.001 g. A scanning electron microscope analysis concluded the study, examining the worn-out surfaces of the samples. Before and after the experiment, the rotating disc and pin samples were wiped with tissue and acetone.

A total of 27 experiments were performed, with each sample subjected to nine sets of investigations. The experiments were repeated 3 times and the average wear rate was calculated. Table 3 contains the test parameters.

Table 3. Test parameters along with their respective levels

Parameters	Level 1	Level 2	Level 3
Load (N)	10	20	30
Sliding speed (m/s)	0.94	1.57	2.20
Sample	S1	S2	S3

3. Result and Discussion

3.1 Wear result

The wear attribute of the AMCs was determined using the pin-on-disc examination by finding the mass loss and calculating the specific wear rate (SWR) [22] from the Eq. 1 and Eq. 2:

$$SWR = \frac{\text{Mass loss}}{\text{Density} \times \text{Sliding Distance} \times \text{Load}} \text{ mm}^3/\text{N-m} \tag{1}$$

$$\text{Sliding Distance (m)} = \text{Sliding speed} \times \text{time} \tag{2}$$

Wear testing is conducted on composites to evaluate their resistance to wear and understand the underlying wear mechanisms. These tests help in comparing the different material compositions, predict component lifespans, and optimize material design. By simulating real-world conditions, wear tests provide crucial data for selecting appropriate materials for specific applications and ensuring manufacturing consistency.

The changes in the wear rate with respect to different loads (10N, 20N and 30N) and sliding speeds (0.94m/s, 1.57 m/s and 2.2 m/s) are shown in Figs. 2 – 5. The effect of load and sliding speed on SWR is discussed below.

3.1.1 Effect of load on wear rate of Al5052 composite

A general trend was observed from these figures that there was increase in SWR with increasing load up to 30 N which implies that wear resistance decrease with the load [23]. Minimum SWR at 0.94 m/s and 1.57 m/s was shown by S3 samples at a load of 10 N (refer to Fig. 2 and Fig.3). Low amount of SWR in any specimen means that its resistance to wear is high. The wear rate for S3 specimen spiked to $1.482 \times 10^{-4} \text{ mm}^3/\text{Nm}$ when the load was increased to 30 N at 0.94 m/s (refer to Fig. 2). It was also observed that the wear rate for S3 ($1.316 \times 10^{-4} \text{ mm}^3/\text{Nm}$) was higher than that of S2 ($1.007 \times 10^{-4} \text{ mm}^3/\text{Nm}$) when tested at 2.2 m/s under a 10 N load (refer to Fig. 4). This happened as a result of presence of void and pores (or agglomeration) within the specimens tested under those conditions.

3.1.2 Effect of sliding speed on wear rate of Al5052 composite

From the Fig. 5 it is evident that the SWR increases initially with the sliding speed at 30 N applied load but as the speed increased from 1.57 m/s to 2.2 m/s the SWR was reduced [24]. Similar trend was observed by Alidokht et. al [25], where the wear resistance of hybrid metal matrix composites was improved at higher sliding speed and sliding distance. At lower sliding speeds, adhesive wear dominates, resulting in an initial rise in wear rate. The wear mechanism changed to abrasive wear as the speed increased, resulting in a drop-in wear rate. The SWR was found minimum for sliding speed of 0.94 m/s.

The minimum SWR of $0.303 \text{ mm}^3/\text{N-m}$ was observed when Al6061 alloy was reinforced with 3% graphene nanoplatelets (GNPs) and 3% CeO₂ [20]. Mahmut et al. [22] tested Al/GNP composite for wear attribute at 10 N to 40 N load. The lowest SWR noted at 10 N and 40 N were $1.2 \times 10^{-4} \text{ mm}^3/\text{N-m}$ and $1.8 \times 10^{-4} \text{ mm}^3/\text{N-m}$ respectively. Sharma et al. [23] performed dry sliding wear test on Al6101/graphite composite and found the minimum SWR of $2 \times 10^{-4} \text{ mm}^3/\text{N-m}$ at 4% graphite.

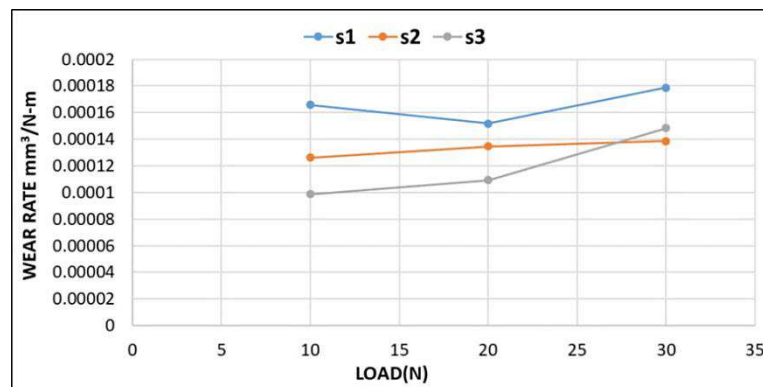


Fig. 2 - Change in SWR with load at 0.94 m/s

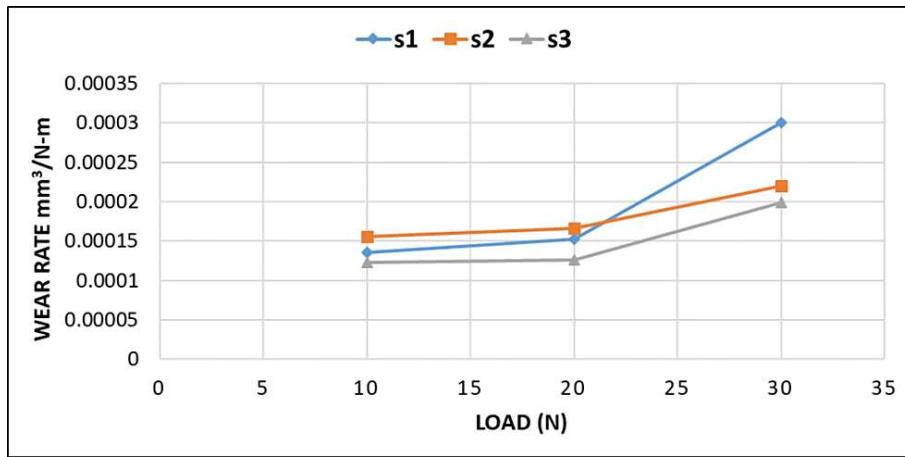


Fig. 3. - Change in SWR with load at 1.57 m/s

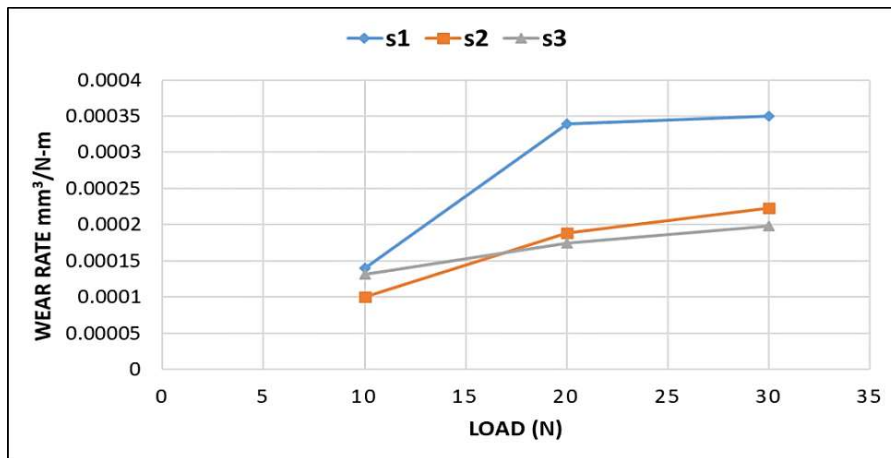


Fig. 4. - Change in SWR with load at 2.2 m/s

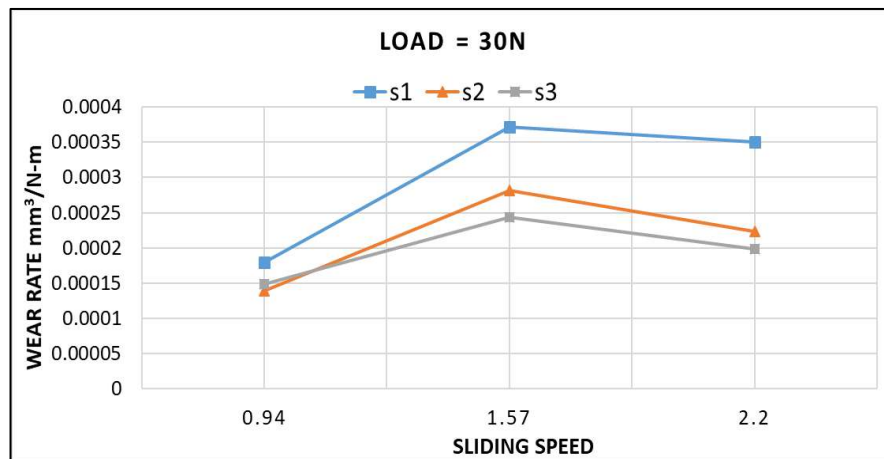


Fig. 5. - Change in SWR with speed at 30 N load with change in sliding speed (m/s)

3.2 SEM analysis of wear surfaces

The worn surfaces of Al5052-based AMCs after wear experiments were examined through SEM. The wear debris that is being formed between pin and disc were wiped off using clean cloth [26]. Fig. 6 (a-d) depict the microscopic study of the worn-out surfaces.

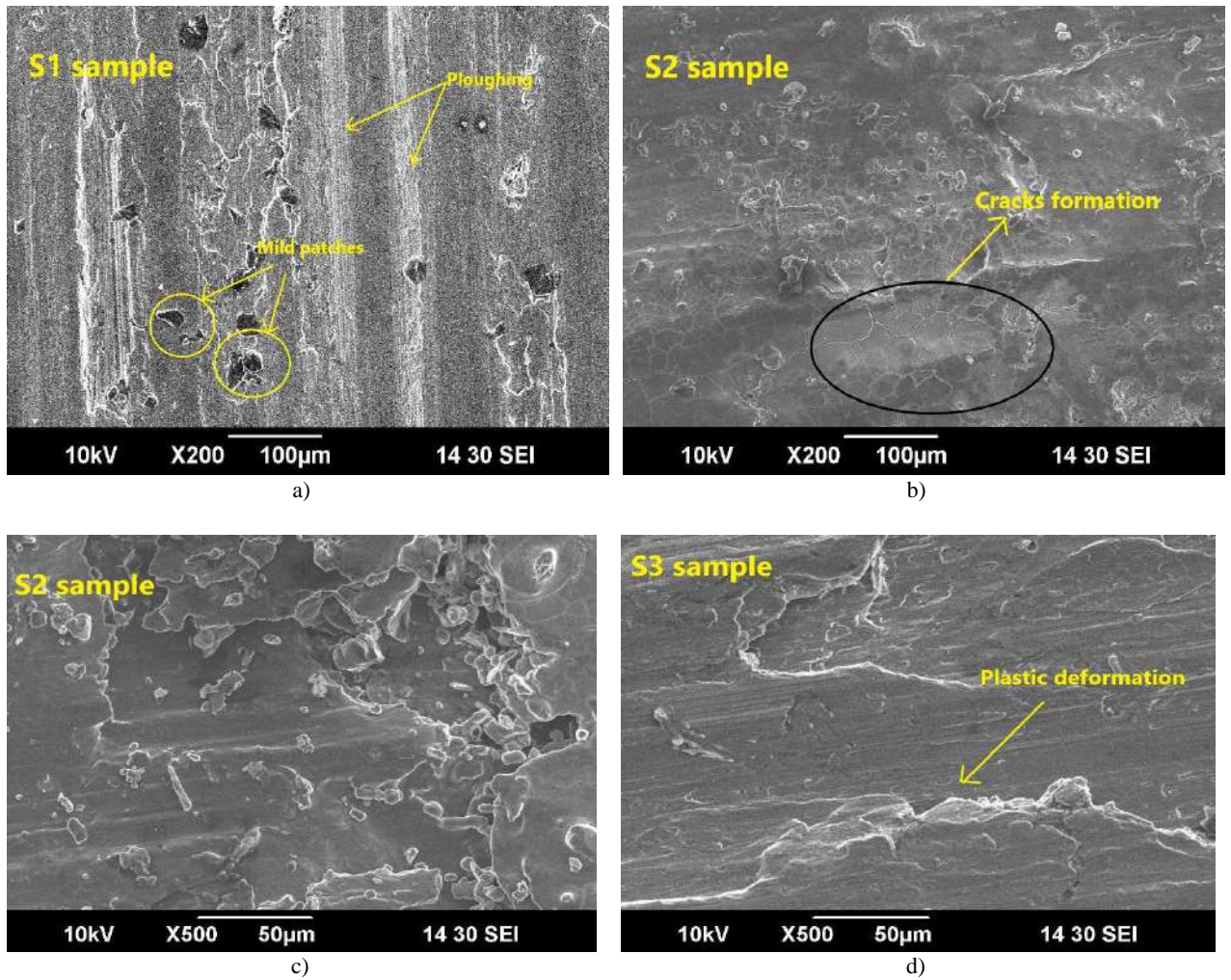


Fig. 6. - SEM images of worn surfaces at 30N load: a) S1 sample at 0.94 m/s, b) and c) S2 sample at 1.57 m/s, d) S3 sample at 1.57 m/s

In the wear test, when the composite surface touches the rotating disc, wear occurs through grooving. A lot of scratches and cracks were identified on the worn surfaces indicating abrasive wear mechanism [27]. These grooves happened because the material got pushed around by the ploughing action (refer to Fig. 6a). Delamination wear was also noticed in the composite. On the surface, the cavities and grooves are caused by delaminating and breaking of surface layer [28]. The crater formation was observed in Fig. 6b and 6c. The mild patches formed indicates towards the adhesive wear phenomena. The chipping off of the material can also be seen from the morphology. Fig. 6d shows the formation of grooves by plastic deformation.

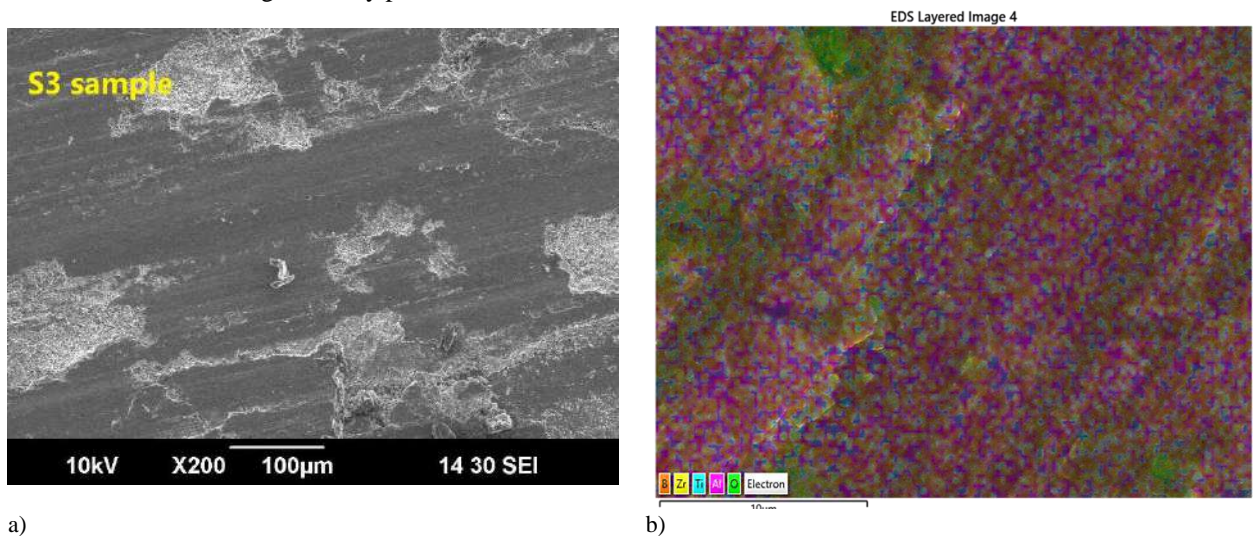


Fig. 7. - a) Morphology of S3 sample at 2.20 m/s and b) Elemental mapping of S3 sample

Oxidation formation (refer to Fig. 7a) is seen at high loads and high sliding speed [29]. The higher wear strength of S3 sample was observed as the surface was smoother compared to S1 and S2. Fig. 7b shows the element mapping of S3 sample and the existence of Al, Zr, Ti, B and O is observed.

The hybrid composite S3 specimen had the lowest SWR, while the S1 specimen had the highest SWR. The higher wear strength in S3 sample was evident as a result of adding 1% TiB_2 and 1% ZrO_2 to the matrix. The wear resistance also improved due to formation of oxides because of high temperatures during sliding. Fig. 8 displays the EDS (Energy-Dispersive X-ray Spectroscopy) examination of the S3 sample.

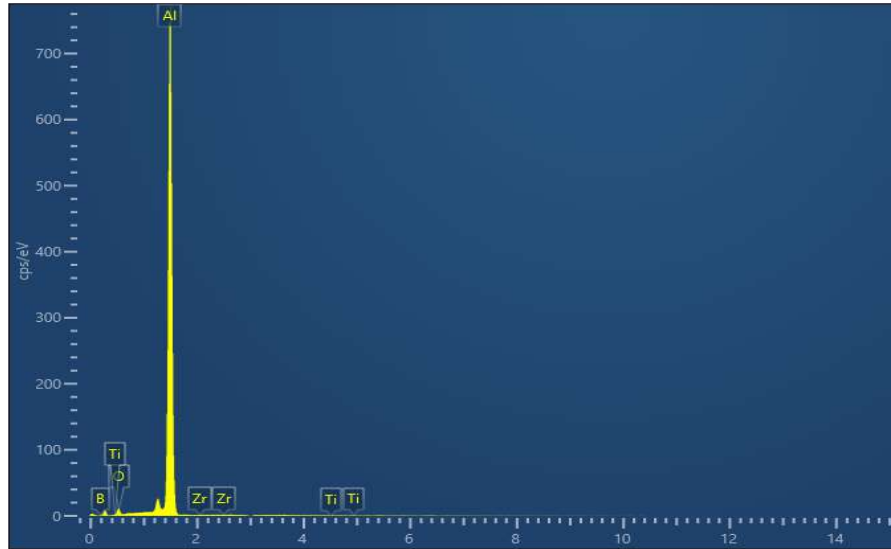


Fig. 8. - EDS analysis of S3 sample

Conclusions

The wear behaviour of Al5052-based AMCs, which were fabricated by stir casting technique, was observed using pin-on-disc device with an EN-31 steel disc at normal room condition. The investigation of experiment outcomes led to the following conclusions:

1. When Al5052-based AMCs were tested for dry sliding behavior at different loads and sliding speed.
2. The wear rate was found to be influenced by load and speed.
3. The lowest wear rate was observed for a load of 10 N and at a sliding speed of 0.94 m/s.
4. The S3 specimen exhibited good wear resistance under varying loads and speeds.
5. SEM micrographs of worn-out surfaces revealed surface faults such as ploughing, wear debris, cracks, and mild patches after dry sliding wear testing.
6. The SEM investigation revealed that some mild patches were identified as a result of material loss, as well as some places with delamination. These defects are formed as a result of the material's abrasion and adhesion during the wear test.
7. Oxidation was observed at high loads and speeds.

References

- [1] Pandiyarajan R., Maran P., Marimuthu S., Ganesh, K. C. Mechanical and tribological behavior of the metal matrix composite AA6061/ ZrO_2/C . //Journal of Mechanical Science and Technology, Vol. 31, No. 10, 2017, p. 4711–4717.
- [2] Yuan L., Han J., Liu J., Jiang Z. Mechanical properties and tribological behavior of aluminum matrix composites reinforced with in-situ AlB_2 particles. //Tribology International, Vol. 98, 2016, p. 41–47.
- [3] Suthar J., Patel K. M. Processing issues, machining, and applications of aluminum metal matrix composites. //Materials and Manufacturing Processes, Vol. 33, No. 5, 2018, p. 499–527.
- [4] Purohit R., Qureshi M. M. U., Jain A. Forming behaviour of aluminium matrix nano Al_2O_3 composites for automotive applications. //Advances in Materials and Processing Technologies, Vol. 6, No. 2, 2020, p. 324–335.
- [5] Jaber M. H., Aziz G. A., Mohammed A. J., Al-AIKawi H. J. Electrical conductivity, magnetic and fatigue properties of aluminum matrix composites reinforced with nano-titanium dioxide (TiO_2). //Nanocomposites, Vol. 6, No. 2, 2020, p. 47–55.
- [6] Kumar D., Angra S., Singh S. Mechanical Properties and Wear Behaviour of Stir Cast Aluminum Metal Matrix Composite: A Review. //International Journal of Engineering, Transactions A: Basics, Vol. 35, No. 4, 2022, p. 794–801.
- [7] Sharma S., Nanda T., Pandey O. P. Effect of particle size on dry sliding wear behaviour of sillimanite reinforced aluminium matrix composites. //Ceramics International, Vol. 44, No. 1, 2018, p. 104–114.

- [8] Reddy P. V., Prasad P. R., Krishnudu D. M., Goud E. V. An Investigation on Mechanical and Wear Characteristics of Al 6063/TiC Metal Matrix Composites Using RSM. //Journal of Bio- and Tribo-Corrosion, Vol. 5, No. 4, 2019, p. 1–10.
- [9] Baradeswaran A., Elaya Perumal A. Study on mechanical and wear properties of Al 7075/Al₂O₃/graphite hybrid composites. //Composites Part B: Engineering, Vol. 56, 2014, p. 464–471.
- [10] Shanmugaselvam P., Sasikumar R., Sivaraj S. Investigation of Hardness and Tribological Behaviour of Aluminium Alloy LM30 Reinforced with Silicon Carbide, Boron Carbide and Graphite. Advances in Manufacturing Technology. Singapore:Springer; 2019, p. 569–576.
- [11] Coyal A., Yuvaraj N., Butola R., Tyagi L. An experimental analysis of tensile, hardness and wear properties of aluminium metal matrix composite through stir casting process //SN Applied Sciences, Vol. 2, No. 5, 2020, p. 1–10.
- [12] Toptan F., Kerti I., Rocha L. A. Reciprocal dry sliding wear behaviour of B 4C p reinforced aluminium alloy matrix composites. //Wear, Vol. 290–291, 2012, p. 74–85.
- [13] Anand V. K., Aherwar A., Mia M., Elfakir O., Wang L. Influence of silicon carbide and porcelain on tribological performance of Al6061 based hybrid composites. //Tribology International, Vol. 151, 2020, p. 106514.
- [14] Dolatkah A., Golbabaei P., Besharati Givi M. K., Molaiekiya F. Investigating effects of process parameters on microstructural and mechanical properties of Al5052/SiC metal matrix composite fabricated via friction stir processing. //Materials and Design, Vol. 37, 2012, p. 458–464.
- [15] Wu J., Djevanroodi F., Shamsborhan M., Attarilar S., Ebrahimi, M. Improving Mechanical and Corrosion Behavior of 5052 Aluminum Alloy Processed by Cyclic Extrusion Compression. //Metals, Vol. 12, No. 8, 2022.
- [16] Natarajan N., Vijayarangan S., Rajendran, I. Wear behaviour of A356/25SiCp aluminium matrix composites sliding against automobile friction material. //Wear, Vol. 261, No. 7–8, 2006, p. 812–822.
- [17] Pazhouhanfar Y., Eghbali B. Microstructural characterization and mechanical properties of TiB₂ reinforced Al6061 matrix composites produced using stir casting process. //Materials Science and Engineering A, Vol. 710, 2018, p. 172–180.
- [18] Pandiyarajan R., Maran P., Marimuthu S., Prabakaran M. P. Investigation on mechanical properties of ZrO₂, C and AA6061 metal matrix composites. //Advances in Materials and Processing Technologies, Vol. 8, 2020, p. 178–186.
- [19] Singh G., Goyal S. Microstructure and mechanical behavior of AA6082-T6/SiC/B₄C-based aluminum hybrid composites. //Particulate Science and Technology, Vol. 36, No. 2, 2018, p. 154–161.
- [20] Kumar D., Singh S., Angra S. Dry sliding wear and microstructural behavior of stir-cast Al6061-based composite reinforced with cerium oxide and graphene nanoplatelets. //Wear, Vol. 516–517, 2023, p. 204615.
- [21] Canute X., Majumder M. C. Investigation of tribological and mechanical properties of aluminium boron carbide composites using response surface methodology and desirability analysis //Industrial Lubrication and Tribology, Vol. 70, No. 2, 2018, p. 301–315.
- [22] Şenel M. C., Gürbüz M., Koç E. Mechanical and tribological behaviours of aluminium matrix composites reinforced by graphene nanoplatelets. Materials Science and Technology, Vol. 34, No. 16, 2018, -p. 1980–1989.
- [23] Sharma P., Paliwal K., Garg R. K., Sharma S., Khanduja D. A study on wear behaviour of Al/6101/graphite composites. //Journal of Asian Ceramic Societies, Vol. 5, No. 1, 2017, p. 42–48.
- [24] Sreenivasan A., Paul Vizhian S., Shivakumar N. D., Muniraju M., Raguraman M. A study of microstructure and wear behaviour of TiB₂/Al metal matrix composites // Latin American Journal of Solids and Structures, Vol. 8, No. 1, 2011, p. 1–8.
- [25] Alidokht S. A., Abdollah-zadeh A., Assadi H. Effect of applied load on the dry sliding wear behaviour and the subsurface deformation on hybrid metal matrix composite //Wear, Vol. 305, No. 1–2, 2013, p. 291–298.
- [26] Lyu Y., Zhu Y., Olofsson U. Wear between wheel and rail: A pin-on-disc study of environmental conditions and iron oxides. //Wear, Vol. 328–329, 2015, p. 277–285.
- [27] Kumar H., Kumar V., Kumar D., Singh S. Wear Behavior of Friction Stir Processed Copper-Cerium Oxide Surface Composites. //Evergreen, Vol. 10, No. 1, 2023, p. 78–84.
- [28] Kuldeep B., Ravikumar K. P., Pradeep S. Effect of hexagonal boron nitrate on microstructure and mechanical behavior of Al7075 metal matrix composite producing by stir casting technique. //International Journal of Engineering, Transactions A: Basics, Vol. 32, No. 7, 2019, p. 1017–1022.
- [29] Selvam B., Marimuthu P., Narayanasamy R., Anandakrishnan V., Tun K. S., Gupta M., Kamaraj M. Dry sliding wear behaviour of zinc oxide reinforced magnesium matrix. //Materials & design, Vol. 58, 2014, p. 475–481.

Information of the authors

Agarwal Saumy, m.tech, PhD research scholar, National Institute of Technology Kurukshetra
e-mail: saumy_61900049@nitkkr.ac.in

Singh Satnam, PhD, assistant professor, National Institute of Technology Kurukshetra
e-mail: satnamsingh@nitkkr.ac.in

Strength Calculation of Variable Bending Rigidity Rods in the Presence of Initial Cambers along Their Axes

Akhmediyev S.K., Filippova T.S., Oryntayeva G.Zh., Tazhenova G.D.*

Abylkas Saginov Karaganda Technical University, Karaganda, Kazakhstan

*corresponding author

Abstract. The paper studies the stress-strain state of a rod with variable bending rigidity, compressed by an axial concentrated force in the presence of initial deflections along its axis. The initial differential equation of longitudinal bending is solved by the numerical finite difference method with the number of divisions along the axis equal to eight. Two problems are solved simultaneously: bending strength and stability under central compression. The calculated deflection diagrams are given depending on the change in the axial load value, taken as a fraction of the critical force, as well as depending on the conditions of fixing the ends of the rod. The results of the study are the formation of 7th order resolution matrices for the numerical calculation of longitudinal-transverse bending of the rod. Critical forces for various boundary conditions at the ends of the rod, and the values of the resulting deflections are determined.

Keywords: rod, bending, stability, finite difference method, deflection.

Introduction

The rod elements of various designs of transport systems, mechanisms, mobile transport [6], buildings, structures, as well as aircraft and shipbuilding structures have manufacturing and operating defects in the form of initial cambers along their longitudinal axes (transverse to the axes of linear deformations).

In these cases, the structures (technical systems) under consideration operate under conditions of the complex stress state (with flat transverse bending).

Load-bearing elements of mechanical engineering structures are in the same conditions, which require strength analysis within the limits of long-term operation [1-2].

In the process of their designing, it is necessary to identify the stress-strain state (determining linear and angular deformations, displacements, internal axial forces and bending moments in the corresponding bending plane) based on the values of which cross sections are selected according to the conditions of strength and rigidity, ensuring safe (reliable) operation of the considered systems.

For example, the study of the stress-strain state, longitudinal vibrations of rods of variable cross-section are considered in articles [7, 8, 11, 12]. In addition, impact [9, 10, 13], combined loading, dynamic stability [14, 15] of rods under various boundary conditions are often studied.

The purpose of the article is to study the stress-strain state of a complex rod system with a variable cross-sectional thickness along the length in the presence of constructive and acquired during operation "cambers" based on the numerical finite difference method taking into account longitudinal transverse bending with the determination of the resulting deflections and the value of the critical forces of central compression.

Let us consider a rod of variable bending rigidity (variable thickness) compressed by the "P" force, taking into account the given initial cambers $f_0(x)$ along the longitudinal axis with random boundary conditions at its ends (Figure 1). Here: $y=y(x)$ is a function of the desired cambers along the longitudinal axis of the rod, $f_0 = f_0(x)$ is a known function of initial cambers (linear displacements along the "y" axis); $J_i = J(x)$ is a variable axial moment of inertia of the cross section.

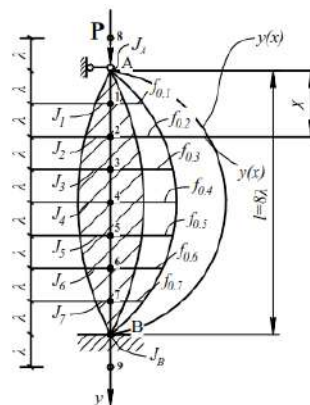


Fig. 1 – Design diagram of the rod under study

1. Methods and solutions

The initial differential equation describing the mechanical operation of the structure under study (Figure 1) has the form [1, 2, 5]:

$$(EJY^{IV} + EJ^{II}Y^{II}) + 2EJ^I Y^{III} + PY^{II} = Pf_0^{II}(x). \quad (1)$$

Both parts of equation (1) are divided by the value EJ_0 (the conditional (scale) bending rigidity of the rod), and the notation is introduced in the form of $(K = \frac{P}{EJ_0})$ as the axial load parameter.

Then, taking into account “ K ”, instead of equation (1), there is obtained the following equation:

$$\frac{EJ}{EJ_0} Y^{IV} + \frac{EJ^{II}}{EJ_0} Y^{II} + \frac{2EJ^I}{EJ_0} Y^{III} + KY^{II} = -Kf_0^{(I)}(x). \quad (2)$$

Equation (2) is implemented using the finite difference method (FDM) with a linear grid with a density equal to the “ n ” value; a fragment of such a grid is shown in Figure 2.

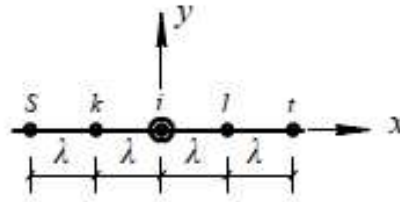


Fig. 2 – A fragment of a regular “linear grid”

Let’s write equation (2) in general form for the i -th grid node (Figure 2), using the FDM parameters known from [3÷5], taking this into account:

$$K^* = k\lambda^2 = \frac{P}{EJ_0} \lambda^2 \quad (3)$$

K^* is the grid parameter of the axial load.

$$\begin{aligned} & \frac{\alpha_i(y_t - 4y_l + 6y_i - 4y_k + y_s)}{\lambda^4} + \frac{(\alpha_l - 2\alpha_i + \alpha_k)(y_l - 2y_i + y_k)}{\lambda^4} + \\ & + \frac{0,5}{\lambda^4}(\alpha_l - \lambda_k)[y_t - 2(y_l - y_k) - y_s] + \frac{k^*}{\lambda^4}(y_l - 2y_i + y_k) = \\ & = -k^*(f_{0,l} - 2f_{0,i} + f_{0,k}), \text{ or} \\ & y_t[\alpha_i + 0,5(\alpha_l - \alpha_k)] + y_l[-4\alpha_i + (\alpha_l - 2\alpha_i + \alpha_k) - (\alpha_l - \alpha_k) + k^*] + y_i[6\alpha_i - 2(\alpha_l - 2\alpha_i + \alpha_k) - 2k^*] + \\ & y_k[-4\alpha_i + (\alpha_l - 2\alpha_i + \alpha_k) + (\alpha_l - \alpha_k) + k^*] + y_s[\alpha_i - 0,5(\alpha_l - \alpha_k)] = -k^*(f_{0,l} - 2f_{0,i} + f_{0,k}) \end{aligned}$$

Then, after reducing similar terms, there is obtained the following:

$$\begin{aligned} & y_t[\alpha_i + 0,5(\alpha_l - \alpha_k)] + y_l(-6\alpha_i + 2\alpha_k + k^*) + y_i[10\alpha_i - 2(\alpha_l + \alpha_k) - 2k^*] + y_k(-6\alpha_i + 2\alpha_l + k^*) + \\ & y_s[\alpha_i - 0,5(\alpha_l - \alpha_k)] = -k^*(f_{0,l} - 2f_{0,i} + f_{0,k}); \end{aligned} \quad (4)$$

Let’s write expression (4) in the reduced form:

$$y_t \cdot \varphi_t + y_l \cdot \varphi_l + y_i \cdot \varphi_i + y_k \cdot \varphi_k + y_s \cdot \varphi_s = -\gamma k^*(f_{0,l} - 2f_{0,i} + f_{0,k}) \quad (5)$$

where

$$\begin{aligned} & \varphi_t = \alpha_i + 0,5(\alpha_l - \alpha_k); \varphi_l = -6\alpha_i + 2\alpha_k + k^*\gamma; \\ & \varphi_i = 10\alpha_i - 2(\alpha_l + \alpha_k) - 2k^*\gamma; \varphi_k = -6\alpha_i + 2\alpha_l + k^*\gamma; \\ & \varphi_s = \alpha_i - 0,5(\alpha_l - \alpha_k). \end{aligned} \quad (6)$$

Let’s divide the length of a given rod “ l ” into 8 equal parts (the grid density $n=8$) and number the calculated nodes of the linear grid $m=1, 2, \dots, 7$ (Figure 1).

Let’s write finite-difference equations according to formula (5) for the design nodes, excluding the deflections of the contour nodes 8, 9 using the boundary conditions at the ends of the rod, i.e.

$$y_8 = \beta_1 y_1; y_9 = \beta_2 y_7, \quad (7)$$

where $(\beta_1, \beta_2) = +1$ with the fixed end of the rod,

$(\beta_1, \beta_2) = -1$ with the hinged end.

1) Node “1” ($i = 1$):

$$\beta_1 \cdot y_1[\alpha_1 + 0,5(\alpha_A - \alpha_2)] + y_1[10\alpha_1 - 2(\alpha_2 + \alpha_A) - 2k^* \cdot \gamma] + y_2(-6\alpha_1 + 2\alpha_A + k^* \cdot \gamma) + y_3[\alpha_1 - 0,5(\alpha_A - \alpha_2)] = -\gamma \cdot k^*(f_{0,2} - 2f_{0,1}),$$

or

$$y_1[-1,5\alpha_A + (10 + \beta_1)\alpha_1 - 2,5\alpha_2 - 2k^* \cdot \gamma] + y_2(2\alpha_A - 6\alpha_1 + k^* \cdot \gamma) + y_3(-0,5\alpha_A + \alpha_1 + 0,5\alpha_2) = -\gamma k^*(f_{0,2} - 2f_{0,1}) \quad (8)$$

2) Node "2" (i = 2)

$$y_1(-6\alpha_2 + 2\alpha_3 + k^* \cdot \gamma) + y_2[10\alpha_2 - 2(\alpha_A + \alpha_3) - 2k^* \cdot \gamma] + y_3(-6\alpha_2 + 2\alpha_1 + k^* \cdot \gamma) + y_4[\alpha_2 - 0,5(\alpha_1 - \alpha_3)] = -k^* \cdot \gamma(f_{0,1} - 2f_{0,2} + f_{0,3})$$

or

$$y_1(-6\alpha_2 + 2\alpha_3 + k^* \cdot \gamma) + y_2(-2\alpha_A + 10\alpha_2 - 2\alpha_3 - 2k^* \cdot \gamma) + y_3(2\alpha_1 - 6\alpha_2 + k^* \cdot \gamma) + y_4(-0,5\alpha_1 + \alpha_2 + 0,5\alpha_3) = -k^* \cdot \gamma(f_{0,1} - 2f_{0,2} + f_{0,3})$$

3) Node "3" (i = 3)

$$y_1[\alpha_3 + 0,5(\alpha_2 - \alpha_4)] + y_2(-6\alpha_3 + 2\alpha_4 + k^* \cdot \gamma) + y_3[10\alpha_3 - 2(\alpha_2 + \alpha_4) - 2k^* \cdot \gamma] + y_4(-6\alpha_3 + 2\alpha_2 + k^* \cdot \gamma) + y_5[\alpha_3 - 0,5(\alpha_2 - \alpha_4)] = -k^* \cdot \gamma(f_{0,2} - 2f_{0,3} + f_{0,4}) \quad (9)$$

or

$$y_1(0,5\alpha_2 + \alpha_3 - 0,5\alpha_4) + y_2(-6\alpha_3 + 2\alpha_4 + k^* \cdot \gamma) + y_3(-2\alpha_2 + 10\alpha_3 - 2\alpha_4 - 2k^* \cdot \gamma) + y_4(2\alpha_2 - 6\alpha_3 + k^* \cdot \gamma) + y_5(-0,5\alpha_2 + \alpha_3 + 0,5\alpha_4) = -k^* \cdot \gamma(f_{0,2} - 2f_{0,3} + f_{0,4}) \quad (10)$$

4) Node "4" (i = 4)

$$y_2[\alpha_4 + 0,5(\alpha_3 - \alpha_5)] + y_3(-6\alpha_4 + 2\alpha_5 + k^* \cdot \gamma) + y_4[10\alpha_4 - 2(\alpha_3 + \alpha_5) - 2k^* \cdot \gamma] + y_5(-6\alpha_4 + 2\alpha_3 + k^* \cdot \gamma) + y_6[\alpha_4 - 0,5(\alpha_3 - \alpha_5)] = -k^* \cdot \gamma(f_{0,3} - 2f_{0,4} + f_{0,5}),$$

or

$$y_2(0,5\alpha_3 + \alpha_4 - 0,5\alpha_5) + y_3(-6\alpha_4 + 2\alpha_5 + k^* \cdot \gamma) + y_4(-2\alpha_3 + 10\alpha_4 - 2\alpha_5 - 2k^* \cdot \gamma) + y_5(2\alpha_3 - 6\alpha_4 + k^* \cdot \gamma) + y_6(-0,5\alpha_3 + \alpha_4 + 0,5\alpha_5) = -k^* \cdot \gamma(f_{0,3} - 2f_{0,4} + f_{0,5}) \quad (11)$$

5) Node "5" (i = 5)

$$y_3[\alpha_5 + 0,5(\alpha_4 - \alpha_6)] + y_4(-6\alpha_5 + 2\alpha_6 + k^* \cdot \gamma) + y_5[10\alpha_5 - 2(\alpha_4 + \alpha_6) - 2k^* \cdot \gamma] + y_6(-6\alpha_5 + 2\alpha_4 + k^* \cdot \gamma) + y_7[\alpha_5 - 0,5(\alpha_4 - \alpha_6)] = -k^* \cdot \gamma(f_{0,4} - 2f_{0,5} + f_{0,6}),$$

or

$$y_3(0,5\alpha_4 + \alpha_5 - 0,5\alpha_6) + y_4(-6\alpha_5 + 2\alpha_6 + k^* \cdot \gamma) + y_5(-2\alpha_4 + 10\alpha_5 - 2\alpha_6 - 2k^* \cdot \gamma) + y_6(2\alpha_4 - 6\alpha_5 + k^* \cdot \gamma) + y_7(-0,5\alpha_4 + \alpha_5 + 0,5\alpha_6) = -k^* \cdot \gamma(f_{0,4} - 2f_{0,5} + f_{0,6}) \quad (12)$$

6) Node "6" (i = 6)

$$y_4[\alpha_6 + 0,5(\alpha_5 - \alpha_7)] + y_5(-6\alpha_6 + 2\alpha_7 + k^* \cdot \gamma) + y_6[10\alpha_6 - 2(\alpha_5 + \alpha_7) - 2k^* \cdot \gamma] + y_7(-6\alpha_6 + 2\alpha_5 + k^* \cdot \gamma) = -k^* \cdot \gamma(f_{0,5} - 2f_{0,6} + f_{0,7}),$$

or

$$y_4(0,5\alpha_5 + \alpha_6 - 0,5\alpha_7) + y_5(-6\alpha_6 + 2\alpha_7 + k^* \cdot \gamma) + y_6(-2\alpha_5 + 10\alpha_6 - 2\alpha_7 - 2k^* \cdot \gamma) + y_7(2\alpha_5 - 6\alpha_6 + k^* \cdot \gamma) = -k^* \cdot \gamma(f_{0,5} - 2f_{0,6} + f_{0,7}) \quad (13)$$

7) Node "7" (i = 7)

$$y_5[\alpha_7 + 0,5(\alpha_6 - \alpha_\beta)] + y_6(-6\alpha_7 + 2\alpha_\beta + k^* \cdot \gamma) + y_7[10\alpha_7 - 2(\alpha_6 + \alpha_\beta) - 2k^* \cdot \gamma] + \beta_2 y_7[\alpha_7 - 0,5(\alpha_6 - \alpha_\beta)] = k^* \gamma(f_{0,6} - 2f_{0,7}),$$

or

$$y_5(-0,5\alpha_\beta + 0,5\alpha_6 + \alpha_7) + y_6(2\alpha_\beta - 6\alpha_7 + k^* \cdot \gamma) + y_7[\alpha_\beta(-2 + 0,5\beta_2) - \alpha_6(2 + 0,5\beta_2) + \alpha_7(10 + \beta_2) - 2k^* \cdot \gamma] = -k^* \cdot \gamma(f_{0,6} - 2f_{0,7}). \quad (14)$$

Let's reduce equations (8-14) into a single system of linear algebraic equations (SLAE) of the 7th order (Table 1). By changing the initial parameters of a given rod (Figure 1), it is possible to solve various problems regarding the strength of compressed rods with different boundary conditions with variable bending rigidity in the presence of initial cambers ($f_{0,x}$).

After solving the 7th order SLAE (the rigidity structure is shown in Table 1), their transverse displacements (deflections) along the axes of the rods at the calculated grid nodes (Figure 1) are determined: y_1, y_2, \dots, y_7 . Based on the values of these deflections, the values of bending moments at the i -th grid nodes are determined (according to the template in Figure 2):

$$M_{x_i} = -EJ_i \frac{d^2 y_i}{dx^2} = -\frac{64}{l^2} (y_k - 2y_i + y_l). \quad (15)$$

In Table 1, variable alphabetic symbols (Figure 1) mean the following:

$(\alpha_A, \alpha_B, \alpha_1 \div \alpha_7)$ is the variability of the structure thickness along the length of the rod in design nodes A, 1, 2, ..., 7, B according to the law of their changing (in particular, it can be accepted according to the law of a square parabola); $(\alpha_A, \alpha_B, \alpha_1 \div \alpha_7)$ are the value of the initial losses at nodes 1, 2, ..., 7 (considered known before the start of calculations); β_1, β_2 are coefficients for specifying boundary conditions at the ends of the rod (nodes A, B); they are taken equal to "+1" when supports "A" or "B" are rigidly fixed; "-1" when they are hinged (Table 1).

Table 1. Resolving finite-difference equations

No.	y_1	y_2	y_3	y_4	y_5	y_6	y_7	Right part
1	$(0,5\beta_1 - 2)\alpha_A + (10 + \beta_1)\alpha_1 - (0,5\beta_1 + 2)\alpha_2 + 2k^* \cdot \gamma$	$2\alpha_A - 6\alpha_1 + k^* \gamma$	$-0,5\alpha_A + \alpha_1 + 0,5\alpha_2$					$-\gamma_1 k^* (f_{0,2} - 2f_{0,1})$
2	$-6\alpha_2 + 2\alpha_3 + k^* \gamma$	$-2\alpha_A + 10\alpha_2 - 2\alpha_3 - 2k^* \gamma$	$-2\alpha_1 - 6\alpha_2 + k^* \gamma$	$-0,5\alpha_1 \alpha_2 + 0,5\alpha_3$				$-\gamma_1 k^* (f_{0,1} - 2f_{0,2} + f_{0,3})$
3	$0,5\alpha_2 + \alpha_3 - 0,5\alpha_4$	$-6\alpha_3 + 2\alpha_4 + k^* \gamma$	$-2\alpha_2 + 10\alpha_3 - 2\alpha_4 - 2k^* \gamma$	$2\alpha_2 - 6\alpha_3 + k^* \gamma$	$-0,5\alpha_2 + \alpha_3 + 0,5\alpha_4$			$-\gamma_1 k^* (f_{0,2} - 2f_{0,3} + f_{0,4})$
4		$0,5\alpha_3 + \alpha_4 - 0,5\alpha_5$	$-6\alpha_4 + 2\alpha_5 + k^* \gamma$	$-2\alpha_3 + 10\alpha_4 - 2\alpha_5 - 2k^* \gamma$	$2\alpha_3 - 6\alpha_4 + k^* \gamma$	$-0,5\alpha_3 + \alpha_4 + 0,5\alpha_5$		$-\gamma_1 k^* (f_{0,3} - 2f_{0,4} + f_{0,5})$
5			$0,5\alpha_4 + \alpha_5 - 0,5\alpha_6$	$-6\alpha_5 + 2\alpha_6 + k^* \gamma$	$-2\alpha_4 + 10\alpha_5 - 2\alpha_6 - 2k^* \gamma$	$2\alpha_4 - 6\alpha_5 + k^* \gamma$	$0,5\alpha_4 + \alpha_5 + 0,5\alpha_6$	$-\gamma_1 k^* (f_{0,4} - 2f_{0,5} + f_{0,6})$
6				$0,5\alpha_5 + \alpha_6 - 0,5\alpha_7$	$-6\alpha_6 + 2\alpha_7 + k^* \gamma$	$-2\alpha_5 + 10\alpha_6 - 2\alpha_7 - 2k^* \gamma$	$2\alpha_5 - 6\alpha_6 + k^* \gamma$	$-\gamma_1 k^* (f_{0,5} - 2f_{0,6} + f_{0,7})$
7					$0,5\alpha_6 + \alpha_7 - 0,5\alpha_8$	$2\alpha_6 - 6\alpha_7 + k^* \gamma$	$\alpha_6(0,5\beta_2 - 2) + (10 + \beta_2)\alpha_7 - \alpha_6(0,5\beta_2 + 2) - 2k^* \cdot \gamma$	$-\gamma_1 k^* (f_{0,6} - 2f_{0,2})$

The calculation using the proposed numerical model is carried out in the form of the following two sequential algorithms:

1. Calculating stability of variable thickness rods without initial cambers ($f_1 = f_2 = \dots = f_7 = 0,0$) with various boundary conditions, under which the parameters of the critical force k_{min} are determined; the critical force in these cases is determined from formula (3):

$$P_{kp} = 64K_{min} \left(\frac{EJ_0}{l^2} \right). \tag{16}$$

2. Taking into account the obtained values of " k_{min} ", the calculations are performed for rods of variable bending rigidity (thickness) under various boundary conditions (a combination of hinged or rigid supports "A" and "B") in the absence and presence of initial cambers f_1, f_2, \dots, f_7 ; these calculations examine the strength of compressed-bent rods when varying the ratios (P/Pcr) that are specified by the coefficients γ, γ_1 varying in the range from 0.1 to 0.9 with a step of 0.1, while linear displacements along the axes of the rods are determined (deflections y_1, y_2, \dots, y_7), the bending moments (according to formula 15).

Then, based on the data in Table 1, the following results were obtained:

1) The calculation of a compressed rod for stability:

a) a rod of variable thickness that changes according to the law of a sinusoid: $t=y_0 \sin \left(\frac{\pi x}{l} \right)$ with three options

of boundary conditions (Figure 1):

- option "I" - hinges on supports "A" and "B";

- option "II" - rigid sealing on supports "A" and "B";

- option "III" - hinge in support "A", seal in support "B"; in this case, the thickness coefficients at the grid nodes (Figure 1) $\alpha_A = \alpha_B = 0.31$; $\alpha_1 = \alpha_7 = 0.588$; $\alpha_2 = \alpha_6 = 0.81$; $\alpha_3 = \alpha_5 = 0.952$; $\alpha_4 = 1.0$.

The results are the values of the critical load parameter “K” (in formula 2) (Table 2).

Table 2. “K” values depending on the boundary conditions at the variable thickness rod ends

Option of boundary conditions	I	II	III
“K” values (variable thickness rod)	0.078	0.135	0.106
“K” values (constant thickness rod)	0.152	0.586	0.306

According to Table 2, the graphs of changing the critical load parameter “K” are plotted (Figure 3).

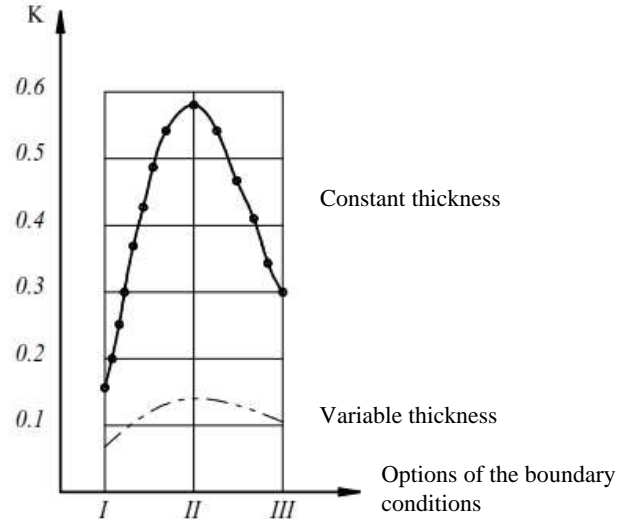


Fig. 3 – “K” dependence on the boundary conditions

2. Calculation of compressed rod strength

- rod thickness is constant ($\alpha_i = const = 1.0$);
- the initial losses, specified according to the sinusoid law, change:
 $f(x) = f_0 \sin(\frac{\pi x}{l})$ ($f_0 = 1$ cm);
- initial load step:

$$P_i = \gamma \cdot K_i \quad (K_i \rightarrow \text{according to Table 2; } \gamma = 0.1; 0.2; 0.4; 0.6; 0.8; 0.9)$$

Table 3 shows the values of deflections y_i ($i = 1, 2, 3, \dots, 7$) for three options of boundary conditions: I, II, III (rod of constant thickness). Figure 4 shows the graphical dependences of the deflections y_i ($i = 1, 2, \dots, 7$) in the design nodes of rods of constant thickness at $\gamma = 0.1; 0.2; 0.4; 0.6; 0.8; 0.9$ for three variants of boundary conditions I, II, III (according to Table 3).

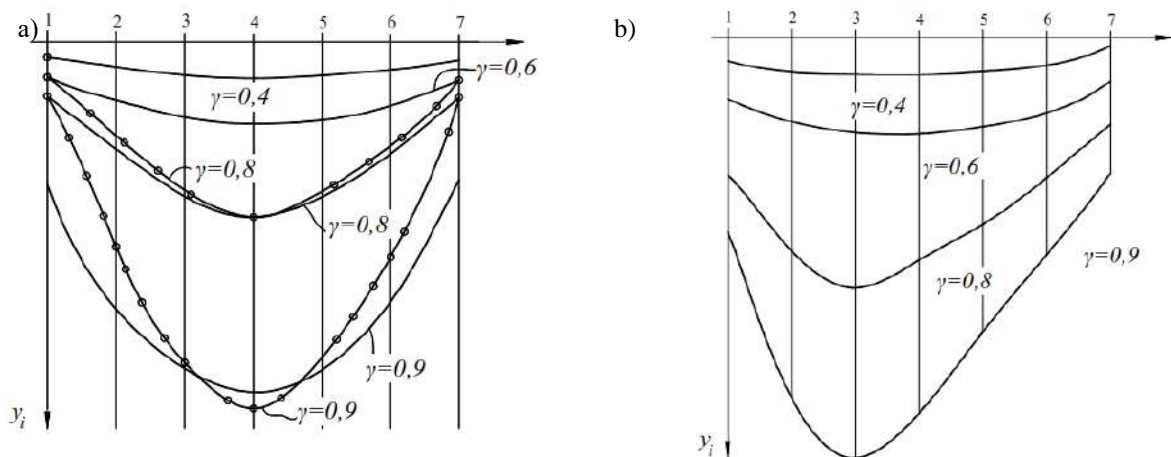


Fig. 4 – Diagrams of deflections of compressed rods of constant thickness in the presence of initial deflections for three variants of boundary conditions:
 a) options I, II; b) option III

Table 3. Deflection values in the constant thickness rod

γ value	y_i value																				
	I							II							III						
	y_1	y_2	y_3	y_4	y_5	y_6	y_7	y_1	y_2	y_3	y_4	y_5	y_6	y_7	y_1	y_2	y_3	y_4	y_5	y_6	y_7
0,1	0.034	0.064	0.085	0.093	0.085	0.064	0.034	0.016	0.049	0.081	0.097	0.081	0.049	0.016	0.035	0.065	0.083	0.085	0.066	0.038	0.012
0,2	0.077	0.143	0.190	0.209	0.190	0.143	0.077	0.036	0.109	0.183	0.219	0.183	0.109	0.036	0.080	0.146	0.186	0.190	0.148	0.085	0.027
0,4	0.205	0.383	0.507	0.554	0.507	0.383	0.205	0.093	0.290	0.487	0.580	0.487	0.290	0.093	0.217	0.394	0.496	0.498	0.385	0.219	0.069
0,6	0.465	0.865	1.14	1.242	1.14	0.865	0.465	0.202	0.649	1.095	1.297	1.095	0.649	0.202	0.500	0.899	1.114	1.096	0.839	0.473	0.145
0,8	1.248	2.314	3.037	3.298	3.037	2.314	1.248	0.520	1.719	2.918	3.438	2.918	1.719	0.520	1.373	2.438	2.964	2.851	2.154	1.195	0.358
0,9	2.818	5.215	6.830	7.406	6.830	5.215	2.818	1.148	3.845	6.561	7.709	6.561	3.845	1.148	3.139	5.539	6.661	6.321	4.736	2.603	0.769

Conclusions

1. In this work, a study was carried out of the stress-strain state (SSS) of rods of variable bending stiffness (variable thickness along the length of the rod) with various boundary conditions [a combination of hinge and pinching at the ends of the rods] in the absence and presence of initial cambers identified in the course of manufacturing or operation process.

2. The resulting calculation method was chosen to be the numerical finite difference method (FDM) using a regular linear grid of density $n=8$; The study is based on a double calculation algorithm: calculations of rods for stability in the absence of initial failures; strength calculations in the presence of initial failures of compressed-bent rods under the action of axial load (P/P_{cr}) in the 0.1; 0.2; ...; 0.9 ratios.

3. In the stability calculation algorithm, the critical force P_{kp} is determined; strength of linear displacements and bending moments at design nodes 1, 2, ..., 7 (Figure 1).

4. A number of research tasks were completed:

a) stability of compressed rods of constant and variable thickness along their length (Table 2, Figure 3);

b) strength of compressed rods of constant thickness in the presence of initial cambers varying along the length of the rod according to the sinusoidal law with increasing the axial load from 10 to 90% of the value of the corresponding critical force (Table 3, Figure 4);

5. When analyzing the results of the above studies, the following was established:

a) the value of the critical forces for all three considered options of boundary conditions I, II, III for variable thickness rods is smaller than that for the same rods of constant thickness (Figure 3);

b) deflections in the calculated grid nodes y_i ($i=1, 2, \dots, 7$) in the presence of initial cambers, with increasing the value of the corresponding load ($P_i = \gamma_i \cdot P_{kp}$) also increase monotonically; at the same time, for rods with hinged supports at the “A” and “B” nodes, option I (Figure 1), the absolute values of deflections are greater than for the other options of boundary conditions II, III (Figure 4, a, b).

6. The theoretical principles and applied results presented in this work can be used in studying the mechanics of rod systems, as well as in designing real structures used in various branches of technology.

References

[1] Kisselev V.A. Structural mechanics: Special course. Dynamics and stability of structures. M.: Stroyizdat, 1980. - 676 p.
 [2] Handbook for designers of industrial and public buildings and structures. Calculation and theory, book 2; edited by A.A. Umansky. - M.: Stroyizdat, 1972. - 600 p.
 [3] Akmehtdiyev S.K., et al. Analytical numerical methods for calculating machine-building and transport structures. - Karaganda: KTU Publishing House, 2016. - 158 p.

- [4] Varvak P.M., Varvak L.P. The grid method in problems of calculating building structures. - M.: Stroizdat, 1977. - 160 p.
- [5] Bakirov Zh.B., Zhadrassinov N.T., Akhmediyev S.K. Computational mechanics: Tutorial. Karaganda: KTU Publishing House, 2004. 102 p.
- [6] Akhmediyev S.K., Filippova T.S., Tazhenova G.D., Mikhailov V.F. Free and Forced Vibrations of the Carrier Beam of the Vehicle Chassis //Material and mechanical engineering technology. Karaganda: KSTU, 2023. Vol. 4, No. 4. P. 32-42.
- [7] Tsarenko S., Ulitin G. /Investigation of strained deformed state of variable stiffness rod// SpringerPlus, 2014. Vol 3. P. 367 DOI: 10.1186/2193-1801-3-367
- [8] Ulitin G., Tsarenko S. Longitudinal Vibrations of Elastic Rods of Variable Cross-Section //International Applied Mechanics, 2015. Vol. 51, Issue 1, P. 102 – 107.
- [9] Biturin A. A. //Calculation of the critical velocity of a stepwise rod system under a longitudinal impact// Journal of Applied Mechanics and Technical Physics. 2011. Vol. 52, Issue 4, P. 530 – 535.
- [10] Schwarz C., Fischer F. D., Werner E., Dirschmid H. J. //Impact of an elastic rod on a deformable barrier: Analytical and numerical investigations on models of a valve and a rod-shaped stamping tool// Archive of Applied Mechanics. 2009. Vol. 80, P. 3–24.
- [11] Ulitin G. //The longitudinal vibrations of an elastic rod simulating a drilling rig// International Applied Mechanics. 2000. Vol. 36, Issue 10, P. 1380 – 1384.
- [12] Werner E. A., Fischer F. D. //The stress state in a moving rod suddenly elastically fixed at its trailing end// 1995. Acta Mechanica. Vol. 111, Issue 3-4, P. 171 – 179.
- [13] Xing Yufeng, Qiao Yuansong, Zhu Dechao, Sun Guojiang //Elastic impact on finite Timoshenko beam// Acta Mechanica Sinica. 2002. Vol. 18, P. 252–263.
- [14] Cheremnykh S. Stability of the steel rod under combined loading //AIP Conference Proceedings. 2023. Vol. 2526, Issue 15.
- [15] Belyaev A. K., Ilin D. N. and Morozov N. F. //Stability of transverse vibration of rod under longitudinal step-wise loading// Journal of Physics: Conference Series. Vol. 451. DOI 10.1088/1742-6596/451/1/012023

Information of the authors

Akhmediev Serik Kabultaevich, c.t.s., docent, Abylkas Saginov Karaganda Technical University
e-mail: s.ahmediev@kstu.kz

Filippova Tatyana Silinyevna, c.t.s., professor, Abylkas Saginov Karaganda Technical University
e-mail: tsxfilippova@mail.ru

Oryntayeva Gulzhaukhar Zhunuskhanovna, senior lecturer, Abylkas Saginov Karaganda Technical University
e-mail: oryntaeva70@mail.ru

Tazhenova Gulzada Dauletkhanovna, c.t.s., docent, Abylkas Saginov Karaganda Technical University
e-mail: gulzada_2604@mail.ru

Modeling of Purification Process of Vehicle Exhaust Gases under the Influence of Ultrasound

Suyunbaev Sh.*

Tashkent State Transport University, Tashkent, Uzbekistan

*corresponding author

Abstract. Research is related to ultrasonic purification of exhaust gases of internal combustion engines of vehicles. The hypothesis of using ultrasonic radiation for purification of exhaust gases from harmful impurities and solid particles is proposed. The scheme of the ultrasonic muffler developed by the authors is presented. A mathematical model of the coagulation of exhaust gas particles in an ultrasonic muffler has been developed. Theoretical dependencies of coagulation coefficient are obtained. An experimental stand has been developed that models an ultrasonic muffler. The results of experimental studies proving possibility and efficiency of using the process of ultrasonic purification from harmful impurities and solid particles are presented. The dependencies of the content of harmful impurities in the exhaust gases were obtained, without exposure and under the influence of ultrasound at different engine revolutions. Experimental relationships of changes in toxic impurities and solid particles (exhaust carbon) are used in the calculation and design method when creating the design of an ultrasonic muffler.

Keywords: automobile, coagulation, exhaust gases, internal combustion engine, ultrasonic muffler.

Introduction

One of the main causes of air pollution is the operation of internal combustion engines of cars. The exhaust gas contains about 160 hydrocarbon derivatives, exhaust carbon and other harmful substances, which, together with salts of heavy metals, poison the atmosphere. An increase in the concentration of exhaust gases by harmful substances leads to an increase in diseases of the cardiovascular system and lungs. In this regard, the reduction of harmful emissions of exhaust gases is an important task in solving the environmental problem of pollution of the environment and modern cities [1-8].

At present time, revolutionary directions of green transport are being developed actively: electric vehicles, hydrogen fuel, etc. However, it will take a long time to completely replace internal combustion engines. Therefore, it is proposed the modernization of purification systems to reduce the harm of exhaust gases, based on ultrasonic exposure in an automobile muffler [9-19].

The exhaust gases of internal combustion engines are an aerodispersed system that is very sensitive to acoustic and electromagnetic effects. As early as the second half of the 19th century, a German physicist A. Kundt discovered that intense acoustic waves affect fine particles in gases. A visual illustration of this effect is the famous "Kundt tube" [20-22].

In 1938 the first experiments of ultrasonic purification of industrial gases were conducted by the scientist Giz, who used ultrasonic whistles and magnetostrictive emitters. At the end of the fifties of the last century "Ultrasonic Corporation" (USA) created gas purification installations with powerful ultrasonic sirens. Since this time, scientific research has been carried out on the coagulation of industrial dust in a number of countries, such as the USSR, France, Japan, Poland, etc. [23-28].

The reduction of toxic emissions of cars is carried out by installing in their mufflers various purification systems (devices), which are called neutralizers. The most common liquid, catalytic and thermal converters. These devices operate respectively on absorption, thermocatalytic and thermal afterburning methods.

Although these methods successfully perform their functions of purifying exhaust gases from nitrogen oxides, sulfur oxide, exhaust carbon and other harmful substances, they suffer from a number of disadvantages. The main disadvantages are: the high cost of chemical reagents; complexity in servicing the device; insensitivity to neutralization of carbon monoxide; difficulties at negative ambient temperatures; additional fuel consumption, etc. [29-30].

The ultrasonic method of purification is based on the ability of ultrasonic waves, a certain frequency and intensity, to accelerate the processes of coagulation and sedimentation of finely-dispersed particles. Coagulation is the physical- chemical process of adhering small particles of disperse systems to larger ones under the influence of coupling forces to form coagulation structures. There are orthokinetic and hydrodynamic coagulation of particles under the influence of ultrasound. Orthokinetic coagulation occurs as a result of the mutual collision of randomly moving particles. Hydrodynamic coagulation occurs as a result of mutual attraction of particles pulsating in the ultrasonic field, due to the Bjerknes force between them [31-33].

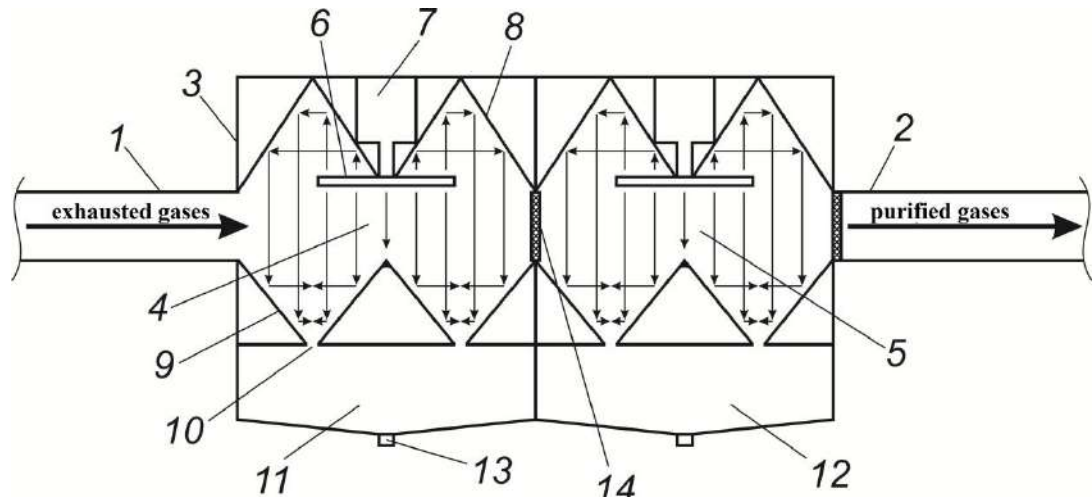
Ultrasonic purification may complement or replace the conventional methods described above. Ultrasound is widely used in geophysics, medicine, paint production, sonication, cleaning hard surfaces from paints and rust of pipes, baths, etc. Research was carried out and results were obtained on the speed of motion of ultrasonic waves in various media, the operation of standing waves and the process of reflection of waves. The works on purification air from suspension from fine particles are of particular interest due to their coagulation under the influence of

ultrasound. The principle of operation of the ultrasonic purification device is based on the ability of ultrasonic waves to intensify coagulation processes of fine solid particles of exhaust gas. Solid particles of exhaust gases enlarged as a result of coagulation processes settle at the place of intended collection and after a certain time interval are extracted and disposed.

The advantage of the ultrasonic method is that chemicals, additional equipment are not needed, as well as the ability to deposit solid exhaust gas particles at a certain place, which can then be extracted and used as recyclables. This makes it possible to use the ultrasonic method in special exhaust gas utilization systems. The disadvantage of the ultrasonic method of purification is its harmful effect on a person and the need to use special ultrasonic insulation.

A patent is known for purification exhaust gases when ultrasonic waves occur in a quarter wave resonator, but without generating waves. The disadvantage of the design is chaotic waves, with an uncontrolled frequency and amplitude [34-37].

A device for ultrasonic purification of exhaust gases is proposed, in which an emitter or several ultrasound emitters are mounted inside the muffler (Fig. 1) [36].



1 – inlet nozzle; 2 – outlet pipe; 3 – case; 4 – first coagulation cell; 5 – second coagulation cell; 6 – ultrasonic oscillation emitters; 7 – ultrasonic converters; 8 – upper reflectors; 9 – lower reflectors; 10 – holes; 11 – first storage tank; 12 – second storage vessel; 13 – holes with plug; 14 – filtration nets.

Fig. 1. – Device for ultrasonic purification of exhaust gases

The device (Fig. 1) is installed in the vehicle by mounting into a muffler or elsewhere in the exhaust system. During operation of the engine, exhaust gases enter the exhaust system, where they pass through the inlet 1 through the first 4 and second 5 coagulation cells. In upper parts of coagulation cells emitters of ultrasonic oscillations are installed 6, which are mechanically and acoustically connected to ultrasonic converters 7. Upper 8 and lower reflectors 9 of ultrasonic oscillations are also installed in coagulation cells, which make it possible to create ultrasonic fields in cells with resonance propagation of ultrasonic oscillations.

Purification of exhaust gases from solid particles is carried out due to created ultrasonic fields in coagulation cells. Oscillations in ultrasonic fields affect solid particles, which begin to move actively, collide and stick together (ultrasonic coagulation occurs). To contain coagulated particles, filtration nets 14 are installed at the outlets of the cells, which are also purified using ultrasonic fields. Removal of coagulated particles is carried out through holes 10 in lower reflectors. The particles settle in the collecting vessels 11 and 12, where some of the gases condense and merge through the holes with the plug 13. The purified gases are discharged from the nozzle 2.

Thus, the ultrasonic muffler apparatus of the present invention improves the environmental safety of vehicles when operating internal combustion engines. In addition, it has a significant advantage: it can be equipped with both new and used cars, as well as other vehicles. Patent has been obtained for the device [36].

The solutions proposed in patents have not been theoretically analyzed and have not been experimentally confirmed. Analysis of studies on the effects of ultrasound on various media gives a rich material, but cannot be applied without clarification to describe the process of operation of the ultrasonic muffler.

The importance of the environmental problem of air purification, insufficient results of theoretical and experimental studies on ultrasonic effects on gas media, a limited level of technical solutions and patents make it possible to consider the task of creating ultrasonic mufflers relevant.

The research was carried out in the laboratory of the Department of Transport Technology and Logistics Systems at the Karaganda Technical University (Karaganda, Kazakhstan) from 11/05/2020 to 30/04/2024.

2. Materials and Methods

A hypothesis was put forward about the possibility of reducing the toxicity of exhaust gases in an ultrasonic muffler and increasing the deposition of coagulated particles (soot) to the bottom of the muffler due to the influence of ultrasonic waves [38].

The exhaust gases in the muffler are coagulated continuously. Coagulation is accelerated by exposure to ultrasound, which has a dispersing effect on emulsions and liquid sols, and on aerosols (smoke, mist, dust) has a coagulating effect. This is due to the fact that in gases only longitudinal waves causing compression are possible. Transverse waves cause deformation shifts. In the longitudinal wave, the medium particles oscillate relative to their average position in the direction parallel to the wave propagation.

The efficiency of the coagulation process increases when a standing wave occurs. Standing waves are a special case of interference. They occur when the reflector (the boundary of two media) is hit and two identical waves propagate in opposite directions, since the medium and the reflector have different acoustic resistances. In this case, a standing wave zone is formed, in which coagulation occurs intensively. The gas particles, including those enlarged in size, are shifted towards the exhaust pipe at a certain speed. Coagulating particles are deposited at the bottom of the muffler, most likely closer to the exhaust hole [39-42].

The standing sound wave force \vec{F}_a is determined by the following relationship:

$$F_a = b \cos \omega \left(t - \frac{n}{c} \right), \quad (1)$$

where $b = \pi r^2 A \rho c \omega$;

r - particle radius;

A - amplitude of ultrasonic oscillations;

ρ - gas particle density;

c - is the speed of sound in the gas medium;

t - time;

n - is the phase rate;

f - oscillation frequency.

For gas particles of different sizes, a certain oscillation frequency occurs. Initially, the particles follow the movement of gas between the beams and nodes, while sticking together and increasing in size. After that, the particles increase due to chaotic fluctuations. Exhaust gas consists of particles of different sizes. Depending on their magnitude and frequency of oscillation, particles can follow sound oscillations and coagulate.

This process occurs at low oscillation frequencies. With an increase in oscillation frequency, there is an optimal frequency segment at which particles of different sizes have a different amplitude, collide with each other and coagulate. This kind of coagulation is called orthokinetic. When the frequency increases above 15000 Hz, coagulation becomes hydrodynamic and it is carried out due to friction. This process is described by hydrodynamic friction force that is the Bjerknes force \vec{F}_G :

$$F_G = 6\pi\eta r \frac{dx}{dt}, \quad (2)$$

where η - dynamic viscosity of the gas particles;

r - the average radius of the particle;

dx/dt - derivative of the difference in the speed of movement of particles during a collision.

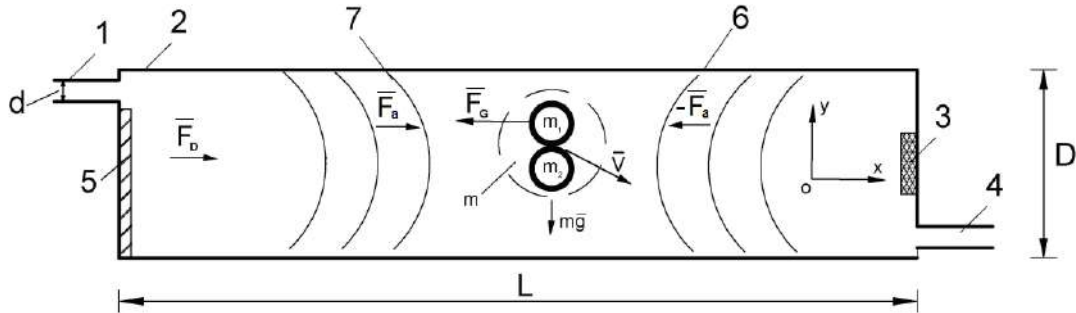
The aim of the study was to obtain theoretical and experimental dependencies describing the process of coagulation and purification from harmful impurities in a developed ultrasonic muffler. To achieve the goal, the following objectives were achieved:

- the speeds of movement of the coagulated particle are theoretically determined when moving in a muffler;
- theoretically established the mass of precipitated exhaust carbon particles and coagulation coefficient in the muffler;
- an experimental stand has been developed and tests have been carried out to reduce toxicity and establish the mass of precipitated particles;
- comparisons of theoretical and experimental results were made.

Thus, our research methods were both theoretical and experimental. The solution of the first problem consisted in modeling the movement of a gas particle m_1 under the influence of forces acting on it during its coagulation with another particle m_2 and the formation of a larger particle under the influence of ultrasound (Fig.

2). This problem is based on solving the differential equation of motion of a gas particle in a muffler under the action of forces acting on this particle. In the first approximation, a one-dimensional problem was considered. To simplify the model, one longitudinal ultrasonic emitter 3 was used (Fig. 2).

Two coagulated particles m_1 and m_2 are subjected to mass and pressure force from the engine exhaust collector \vec{F}_D , which is considered constant, the Bjerknes force \vec{F}_G , reflected alternating force of standing sound wave \vec{F}_a and gravity (Fig. 2). As a result of friction, a particle mass m is formed, moving under the pressure of the mentioned forces.



1 - exhaust gas inlet pipe; 2 - muffler case; 3 - ultrasonic emitter; 4 - outlet pipe; 5 - wave reflector; 6 and 7 - straight wave and reflected wave respectively; L and D - length and height of the muffler; d - diameter of the inlet and outlet branch pipe.

Fig. 2. – Scheme of forces acting on the coagulated gas particles

The equation of motion of the particle m along the axis Ox has the form:

$$m\ddot{x} = F_D \pm F_a - F_G. \quad (3)$$

Taking into account expressions (1), (2) and conversions:

$$m\ddot{x} - 6\pi\eta r\dot{x} = F_D \pm b \cos \omega \left(t - \frac{n}{c} \right). \quad (4)$$

The initial conditions will be as follows:

$$x_0 = 0, \quad \dot{x}_0 = v_0, \quad (5)$$

where $x_0 = 0$, $\dot{x}_0 = v_0$ – the initial position and initial speed of the particle at the entrance to the muffler. The solution of equation (4) with initial conditions (5) is given in the section “Results and discussion”. These solutions allow you to determine the speed of movement of gas particles, which are necessary for the theoretical determination of the coagulation coefficient.

It is important to establish the value of the coagulation coefficient and the regularity of its change. The coagulation coefficient K is meant as a change in the mass of precipitated particles per unit time. The coagulation coefficient in its physical essence determines the magnitude of the speed of this process and has a the dimension c^{-1} .

It is assumed that the law of exhaust carbon mass change is similar to the law of particle concentration in gas:

$$n = n_0 \exp(-Kt), \quad (6)$$

where n and n_0 – counting concentrations of gas particles in the current and initial phase, respectively. Then it turns out:

$$m = m_0 \exp(Kt), \quad (7)$$

where m and m_0 – the mass of exhaust carbon obtained when exposed to ultrasound and the mass of exhaust carbon without ultrasound effect, respectively.

It is necessary to determine the parameters on which the coagulation coefficient depends. For these purposes, experimental studies were carried out. The purpose of the experiment is to obtain dependencies determining coagulation parameters: the mass of precipitated exhaust carbon, the coagulation coefficient and its speed. As well as testing the hypothesis of purification exhaust gases from harmful impurities such as CO and CH [9-12].

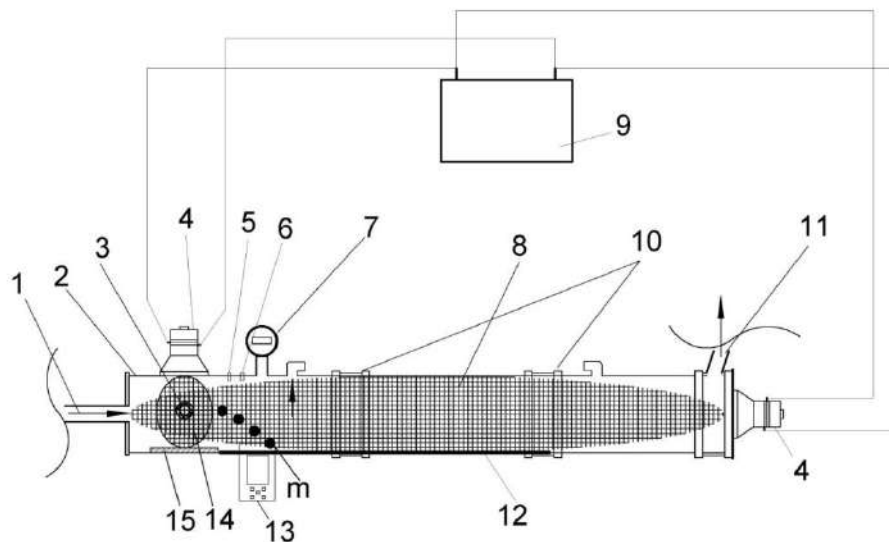
A full-size experimental stand was made for the full-scale experiment (Figures 3–5). The scheme of the experimental ultrasonic stand (muffler) is shown in Figure 4.

The experimental ultrasonic muffler (Figures 3–5) consists of a polypropylene pipe with a diameter $D=110$ mm and a length $L=3000$ mm. The following equipment is installed in the muffler case: ultrasonic generator 9; two ultrasonic emitters 4; ultrasonic wave reflector 15; digital USB-microscope MIKMED 3 with an increase coefficient from 20 to 200 with the possibility of photo and video fixation at a resolution 1920×1080 pixels; temperature sensor 5 and hygrometer 6 transmitting information to thermometer-hygrometer 13; electronic pressure gauge 7.

To determine the qualitative and quantitative composition of the exhaust gas mixture, “Meta Avtotest 01.03” gas analyzer (Russia) was used. An ultrasonic generator was used by the manufacturer “TOCOOL” (China). Input voltage of AC current 220V, with power of emitters – 50W, frequency of ultrasonic waves generation – 40 kHz. To study the internal processes of the ultrasonic muffler, a USB-microscope “MIKMED 2.0” was installed into the case, designed to check the quality and testing of industrial facilities.

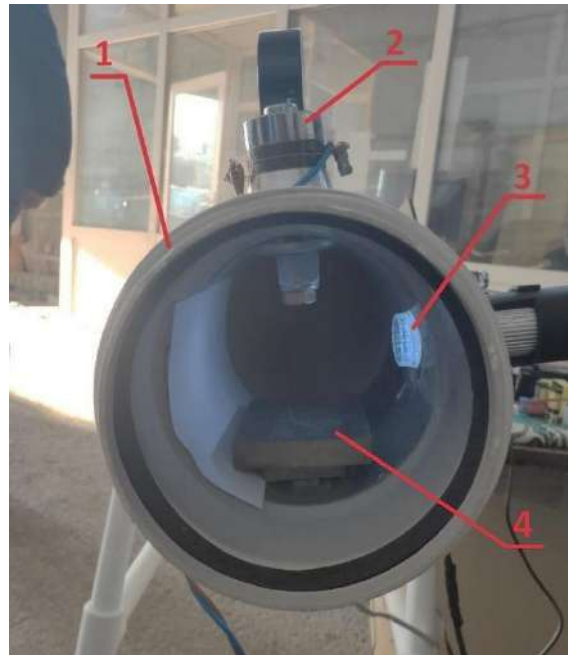


Fig. 3. – Experimental ultrasonic stand



1 – inlet nozzle; 2 – muffler case; 3 – electronic microscope MIKMED 2.0; 4 – ultrasonic emitter; 5 – temperature sensor; 6 – moisture meter; 7 – electronic pressure gauge; 8 – area of impact of longitudinal ultrasonic waves; 9 – ultrasonic generator; 10 – pipe connection coupling; 11 – outlet pipe; 12 – place of soot collection; 13 – thermometer-hygrometer; 14 – the area of impact of transverse ultrasonic waves; 15 – reflector.

Fig. 4. – Scheme of experimental ultrasonic stand



1– ultrasonic muffler case, 2 – ultrasonic radiator, 3 – digital USB microscope, 4 – reflector.

Fig. 5. – Internal design of ultrasonic muffler

During the experiment, at the first stage, the degree of purification of the exhaust gas from CO and CH was determined. At the second stage, graphs of the mass of the sediment exhaust carbon versus the length of the muffler L were established.

The experimental study was conducted as follows:

- tests were carried out without switching on and with switching on the ultrasonic equipment for 5 minutes each;
- the study was carried out at the engine crankshaft speed at idle (1000 rpm) and at 1250 rpm.

Volkswagen Passat B3 of 1991 release was used, engine capacity 1800 cc. see, fuel injection - mono engine, engine power 90 kW, fuel grade - gasoline AI-92.

To collect the settled soot, the lower part of the device was lined with five numbered sheets of paper measured 100×100 mm, with a total length of 500 mm, the mass of which was determined before testing by high-precision jewelry scales "MN-500" (Russia).

Exhaust gas from the vehicle was supplied to the ultrasonic muffler (see Fig. 4) through the inlet pipe 1 under the pressure depending on the speed of rotation of the crankshaft of the vehicle. In the muffler, when ultrasonic equipment was turned on, the exhaust gas was exposed to ultrasonic waves in the transverse and longitudinal direction. In the muffler, ultrasonic intensification of coagulation processes and purification of exhaust gases occurred due to sedimentation of enlarged exhaust gas particles at the exhaust carbon collection point 12. The purified exhaust gas was discharged through outlet 11.

During the operation of the ultrasound muffler, the readings of the gas analyzer, monometer, thermometer-hygrometer were taken. Photo and video recording were performed inside the ultrasonic muffler using a digital microscope 3. Photos are not presented due to a fuzzy image during transfer.

After each test, the numbered paper with settled soot particles was carefully removed and weighed again. Based on the difference in mass readings before and after the test, the mass of settled soot particles was determined. The sediment distance of the soot particles was determined by the location of the paper sheets (Tables 2 and 3).

Preliminary 5 repeated experiments were carried out. The coefficient of variation W is determined:

$$W = \frac{\sigma}{\bar{X}} = 0.07, \quad (8)$$

where σ – the standard deviation, \bar{X} – the arithmetic mean of the results of five measurements (experiments).

The minimum allowable value of repeated experiments with a confidence probability of 90% and a maximum relative error of the experiment of 9% was determined. The number of repeated experiments was determined from the expression:

$$n = \left(\frac{t_s W}{\varepsilon} \right)^2 = \left(\frac{2.13 \times 0.07}{0.09} \right)^2 = 2.66 \approx 3, \quad (9)$$

where t_s – the Student coefficient, ε – the ultimate relative error of the experiment. The number of repeated experiments equal to 3 was obtained.

3. Results and discussion

The analytical solution of equation (4) with initial conditions (5), for the positive direction of the standing sound wave force \vec{F}_a , made it possible to determine the following dependencies of the particle speed V_x in the projections on the Ox axis of the muffler length:

$$V_x = \frac{F_D}{a} - \left[\frac{F_D}{a} - v_0 + \frac{ba}{a^2 + m^2\omega^2} \left(\cos \frac{\omega n}{c} - \frac{m\omega}{a} \sin \frac{\omega n}{c} \right) \right] e^{-\frac{a}{m}t} + \frac{b}{a^2 + m^2\omega^2} \left[a \cos \omega \left(t - \frac{n}{c} \right) + m\omega \sin \left(t - \frac{n}{c} \right) \right], \quad (10)$$

where $a = 6\pi\eta r$ is denoted and $b = \pi^2 A\rho c\omega$ is determined from expression (1).

By logarithmizing expression (7) and performing the conversions, the dependence of the gas coagulation coefficient K on the initial concentration and time was obtained:

$$K = \ln \frac{m}{m_0} / t, \quad (11)$$

where t – the travel time of the gas particle through the muffler.

Since the average travel time of the particle through the muffler:

$$t = \frac{V_x}{L}, \quad (12)$$

then, for a specific muffler, an analytical expression was determined to determine the coagulation coefficient K :

$$K = \frac{L}{V_x} \ln \frac{m}{m_0}, \quad (13)$$

where V_x is determined by expression (10).

At the first stage of the experiment, the validity of the hypothesis about the possibility of purification exhaust gases with ultrasound in an automobile muffler was proved. Table 1 and Figures 6 and 7 show CH and CO concentrations in the muffler.

Table 1. CH and CO concentration at 1000/1250 rpm

Ultrasonic muffler operation	CH (ppm/min)	CO (%)
Without ultrasound	50/27	1.2/0.62
With ultrasound (1 transverse emitter)	31/14	1.2/0.76
With ultrasound (2 emitters)	29/12	1.6/0.9
With ultrasound (1 longitudinal emitter)	27/-	1.2/-

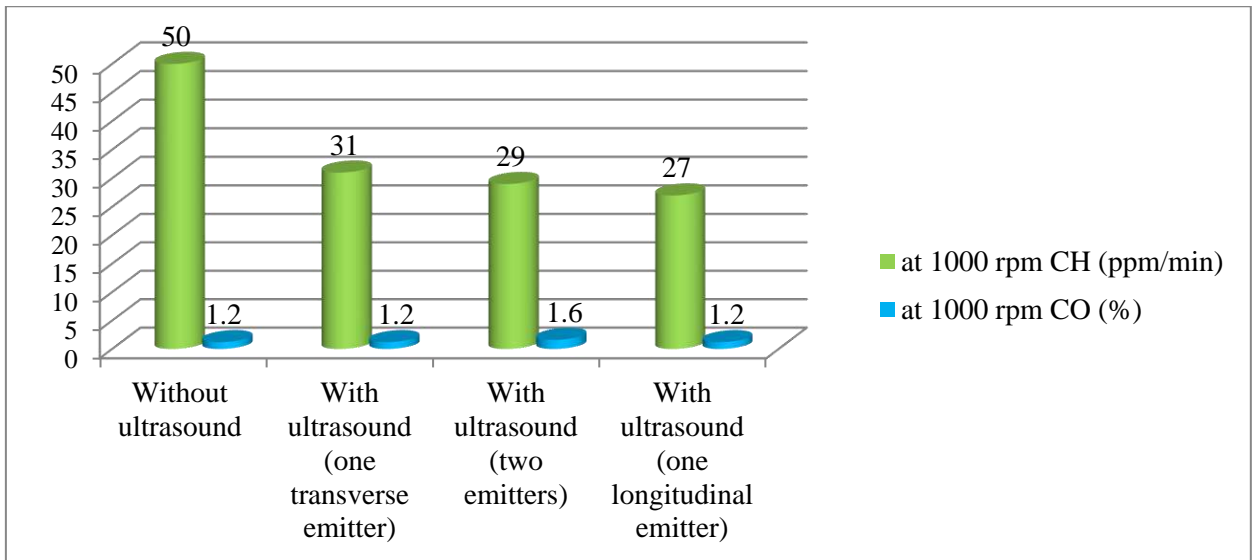


Fig. 6. – Diagram of CH and CO content in exhaust gas at 1000 rpm

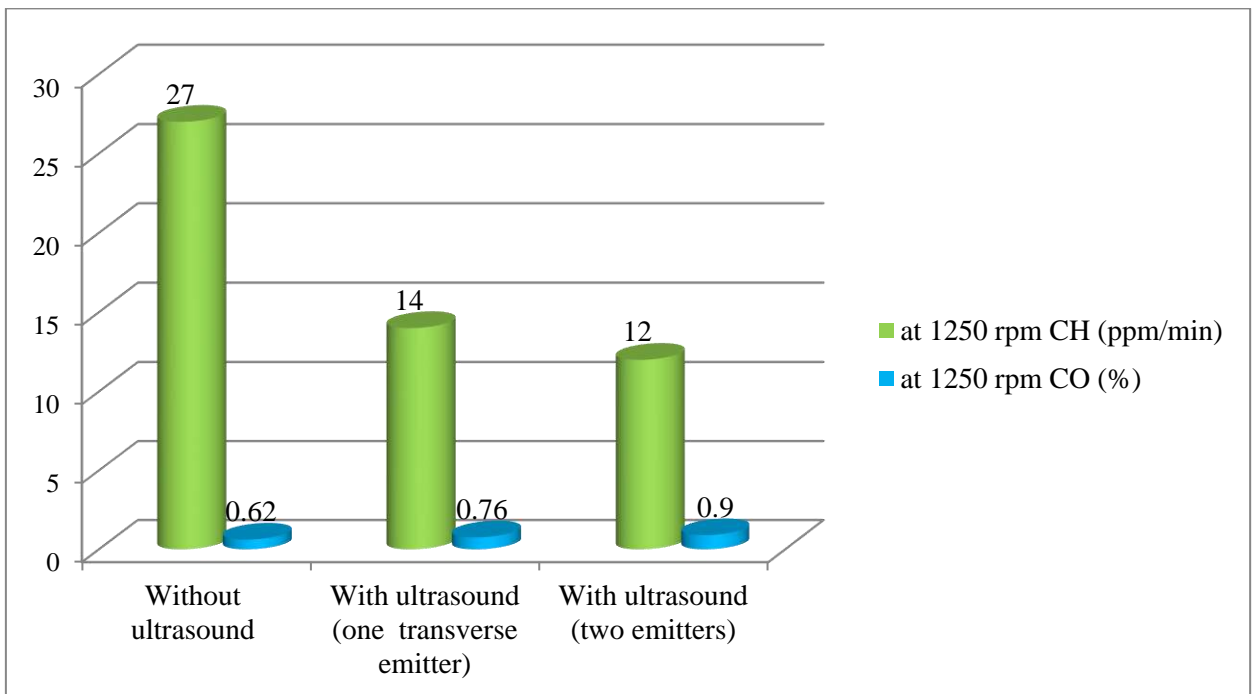


Fig. 7. – Diagram of CH and CO content in exhaust gas at 1250 rpm

The hypothesis about the possibility of reducing the toxicity of exhaust gases in an ultrasonic muffler has been confirmed. Moreover, purification is most effective when installing a muffler in the longitudinal direction of gas movement, since the friction force of particles against each other (hydrodynamic coagulation) is supplemented by gravity (Figures 6 and 7). The decrease in CH concentration shows the effectiveness of the ultrasound in purification the exhaust gas. The change in CO indicates an increase in concentration due to the effect of ultrasonic waves. At the same time, the length L on which CO molecules were to be deposited is not enough. The volatility of CO is higher than CH.

Table 2. Mass of settled exhaust carbon at 1000/1250 rpm without ultrasound

Time		Thermometer readings at 1000/1250 rpm t (°C)	Determination of exhaust carbon mass at 1000/1250 rpm			
Total time (min)	Minute		Distance (mm)	Mass of paper (g)	Mass of paper with exhaust carbon (g)	Net mass of settled exhaust carbon (g)
5	1	10.5/23.9	100	0.75/0.8	1.00/1.5	0.25/0.70
	2	11.7/26.0	200	0.84/0.79	1.00/1.18	0.16/0.39
	3	12.3/29.2	300	0.84/0.76	0.95/0.88	0.11/0.12
	4	18.5/31.7	400	0.87/0.73	0.92/1.35	0.05/0.62
	5	20.3/33.0	500	0.84/0.74	0.94/1.05	0.10/0.31
Totally:						0.67/2.14

Table 3. Mass of settled exhaust carbon at 1000/1250 rpm with ultrasound with two emitters

Time		Thermometer readings at 1000/1250 rpm t (°C)	Determination of carbon black mass at 1000/1250 rpm			
Total time (min)	Minute		Distance (mm)	Mass of paper (g)	Mass of paper with exhaust carbon (g)	Net mass of settled exhaust carbon (g)
5	1	16.1/26.4	100	0.74/0.85	1.08/1.92	0.34/1.07
	2	18.8/28.8	200	0.77/0.77	0.98/1.86	0.21/1.09
	3	23.0/31.5	300	0.74/0.76	0.88/1.51	0.14/0.75
	4	26.3/33.3	400	0.75/0.78	1.20/1.62	0.45/0.84
	5	29.2/35.4	500	0.72/0.79	1.10/1.49	0.38/0.70
Totally:						1.52/4.45

At the second stage of the experiment, the dependencies of the mass of settled exhaust carbon on the length of the settling (muffler) L were determined. Tables 2 and 3 provide the examples of the registration of experimental results.

Tables 2 and 3 show the mass of settled exhaust carbon without ultrasound and ultrasound (with two emitters) at 1000/1250 engine crankshaft rpm. The net mass of exhaust carbon was determined by subtracting the mass of paper from that of exhaust carbon.

From the tables it follows that the efficiency of solid particle sedimentation with two emitters is more than 2 times higher compared to the tests without exposure to ultrasound. Thus, gas coagulation is most effective in the longitudinal radiator, since the exposure to ultrasound extends over a longer length. Figures 8 and 9 show experimental graphs of the mass of settled soot versus the length L of the muffler. It was also established that the mass of coagulation increases significantly (2-2.5 times) with an increase in the number of engine speeds (Fig. 9). Figure 10 shows the resulting exhaust carbon from hydrodynamic coagulation.

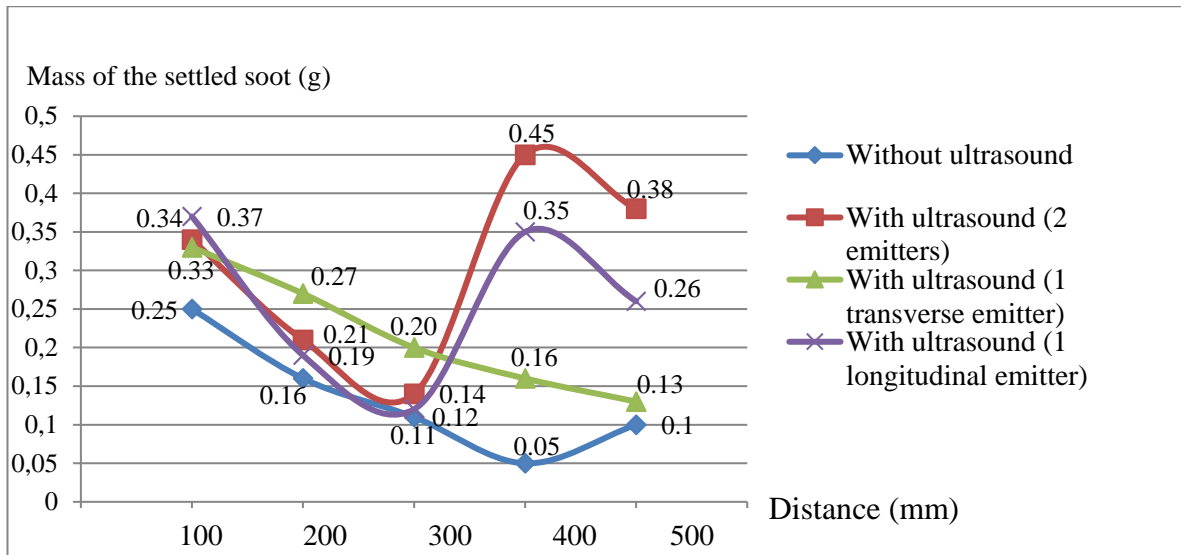


Fig. 8. – Graph of the mass of settled exhaust carbon dependence on the settling distance at 1000 rotations of the crankshaft per minute

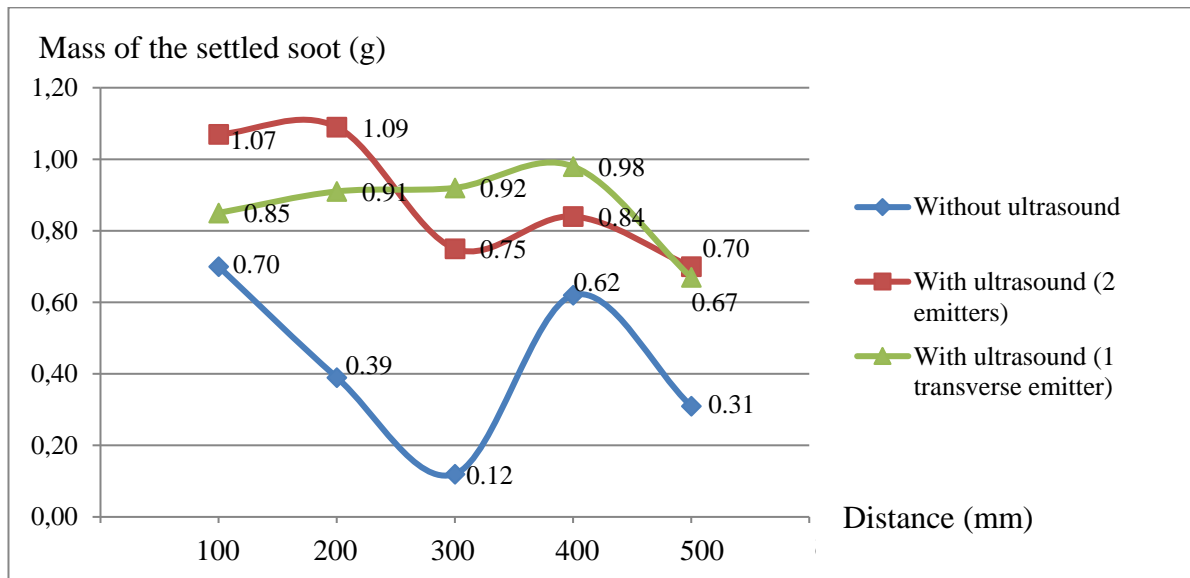


Fig. 9. – Graph of the mass of settled exhaust carbon dependence on the settling distance at 1250 rotations of the crankshaft per minute

Having determined the difference in the exhaust carbon mass under the action of ultrasound and without it, the value of the exhaust carbon mass from hydrodynamic coagulation was found (Table 4).

Table 4. Exhaust carbon mass from hydrodynamic coagulation at 1000/1250 rpm when exposed to 2 ultrasonic emitters

Determination of exhaust carbon mass			
Distance (mm)	Mass of settled exhaust carbon when exposed to ultrasound (g)	Mass of settled exhaust carbon without ultrasound (g) (effect of orthokinetic coagulation)	Mass of settled exhaust carbon when exposed to hydrodynamic coagulation (g)
100	0.34/1.07	0.25/0.70	0.9/0.37
200	0.21/1.09	0.16/0.39	0.05/0.7
300	0.14/0.75	0.11/0.12	0.03/0.63
400	0.45/0.84	0.05/0.62	0.4/0.22
500	0.38/0.70	0.10/0.31	0.28/0.39

Table 4 shows the dimension data of orthokinetic and hydrodynamic coagulation. The obtained data made it possible to quantify the mass of hydrodynamic coagulation (Fig. 10).

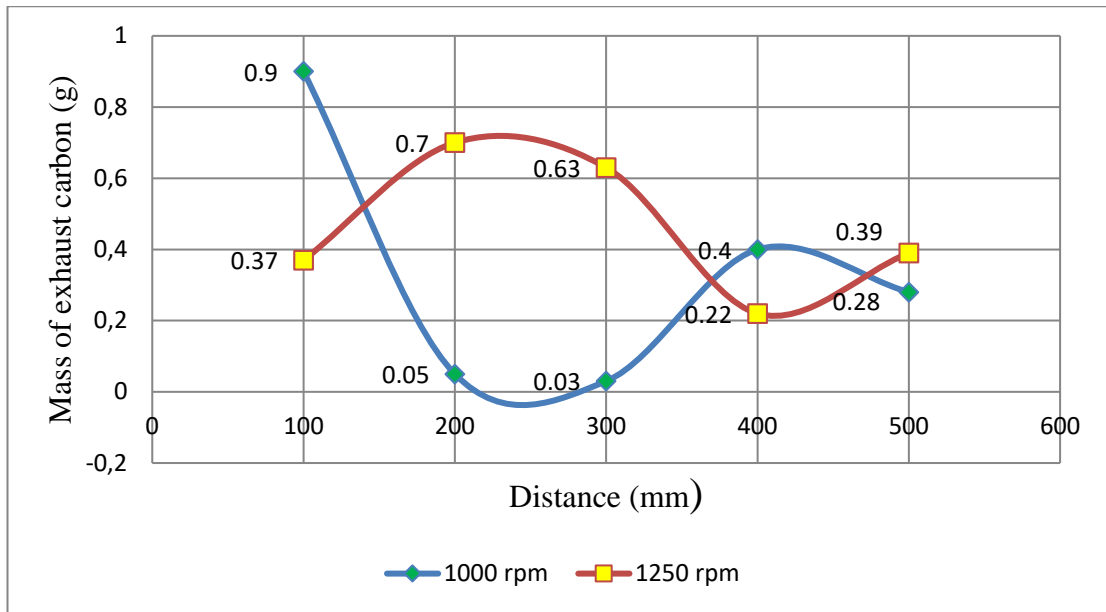


Fig. 10. – Graph of exhaust carbon mass dependence at hydrodynamic coagulation on the sedimentation distance at 1000/1250 crankshaft rotations per minute for the variant with two ultrasonic emitters

As it can be seen from the graphs, there is a local maximum of exhaust carbon deposition at the distance of 400mm from the exhaust pipe. It is true quantitatively for the stand, but the qualitative dependence will be true for polypropylene mufflers as well.

According to the formula (11), the coagulation speed coefficient K was determined for the version of operation with two ultrasound emitters in the muffler. The travel time of the gas particles through the muffler is equal to the operation time of the ultrasonic muffler $t=300$ seconds, the coagulation coefficient is obtained.

Since 5 sheets of paper measuring 100×100 mm were lined in the muffler, the total mass of the resulting exhaust carbon was calculated for all sheets of paper. According to Table 2, the sum of the obtained exhaust carbon without ultrasound at 1000/1250 rpm was 0.67/2.14 grams.

According to Table 3, the sum of the obtained exhaust carbon with ultrasound (2 emitters), at 1000/1250 rpm = 1.52/4.45 grams. Then, substituting these values into the formula, the coagulation speed coefficient K was obtained (Table 5).

Table 5. Coagulation Speed Coefficient

Engine (rpm)	Coagulation coefficient value, c^{-1}		
	With ultrasound (2 emitters)	With ultrasound (1 transverse emitter)	With ultrasound (1 longitudinal emitter)
1000/1250	$2.7 \times 10^{-3} / 2.4 \times 10^{-3}$	$1.6 \times 10^{-3} / 2.7 \times 10^{-3}$	$2.9 \times 10^{-3} / -$

Having compared the obtained data of the coagulation speed coefficient, it can be concluded that the operation of the longitudinal emitter is maximally effective, since ultrasound had an effect on the entire path of the movement of exhaust carbon particles.

Conclusions

The assumption of reducing the toxicity of exhaust gases when exposed to ultrasound is experimentally confirmed. Moreover, in this case, the longitudinal emitter is more effective. The decrease in the concentration of CH and CO was from 40% to 50%.

The hypothesis of increasing the particles of coagulated particles (exhaust carbon) to the bottom of the muffler due to the effect of ultrasonic waves on them has been proved. The physical process is explained by the increase in hydrodynamic coagulation of the gas medium, as proved by the experiment. The mass of settled exhaust carbon with ultrasonic exposure is significantly (4-5 times) higher than its mass without exposure to ultrasound.

The efficiency of solid particles sedimentation at two (transverse and longitudinal) emitters is more than twice. Working with a longitudinal emitter is more efficient, since the ultrasonic wave moves towards the movement of the gas.

The nature of the dependence graphs of the exhaust carbon mass on the distance from the collector shows that there is a local maximum (for these parameters) that equals to 400 mm.

On the basis of hypothesis on analogy of laws of concentration of particles in gas and distribution of mass by exponent, dependencies of coagulation concentration on initial mass and time of influence on medium are obtained and experimentally confirmed.

For the first time, the obtained theoretical dependence of the coagulation coefficient (13) and experimental results, the practical significance of which is the possibility of calculating and designing mufflers.

References

- [1] Shamim T. Effect of engine exhaust gas modulation on the cold start emissions. *International Journal of Automotive Technology*, Vol. 12, No. 4, 2011, pp. 475–487
- [2] Dong, S., Lipkens, B., Cameron, T.V. The effects of orthokinetic collision, acoustic wake, and gravity on acoustic agglomeration of polydisperse aerosols. *Journal of Aerosol Science*, Volume 37, Issue 4, April 2006, pp. 540-553.
- [3] Riera-Franco de Sarabia, Elvira-Segura, González-Gómez, Rodríguez-Maroto, Muñoz-Bueno, Dorronsoro-Areal. Investigation of the influence of humidity on the ultrasonic agglomeration of submicron particles in diesel exhausts, *Ultrasonics*, Volume 41, Issue 4, June 2003, Pages 277-281.
- [4] Yessenbayeva A., Apsalikov B., Massabayeva M., Kazymov M., Shakhanova A., Mussazhanova Zh., Kadyrova I., Aukenov N., Shaimardanov N. Biomarkers of immunothrombosis and polymorphisms of IL2, IL6, and IL10 genes as predictors of the severity of COVID-19 in a Kazakh population. // *PLoS ONE*, Vol. 18, Issue 6, 2023. – p. 61-67. <https://doi.org/10.1371/journal.pone.0288139>
- [5] Yegorov S., Kadyrova I., Korshukov I., Sultanbekova A., Kolesnikova Y., Barkhanskaya V., Bashirova T., Zhunusov Y., Li Y., Parakhina V., Kolesnichenko S., Baiken Y. Application of MALDI-TOF MS and machine learning for the detection of SARS-CoV-2 and non-SARS-CoV-2 respiratory infections // *Microbiology Spectrum*, Vol. 12, No. 5, 2024. <https://doi.org/10.1128/spectrum.04068-23>
- [6] Turmukhambetova A., Yegorov S., Korshukov I., Barkhanskaya V., Kolesnichenko S., Klyuyev D., Zhumadilova Z., Praliev A., Absaghit L., Belyaev R., Babenko D., Hortelano G. Miller, M., Vazemiller D., Kadyrova I. The impact of Gam-COVID-Vac, an Adv5/ Adv26 COVID-19 vaccine, on the biomarkers of endothelial function, coagulation and platelet activation // *PLoS ONE* Vol. 18, No. 10, 2023. <https://doi.org/10.1371/journal.pone.0293074>
- [7] Kadyrova I., Kolesnichenko S., Kolesnikova Ye., Korshukov I., Barkhanskaya V., Sultanbekova A., Babenko D. SARS-COV-2 detection in MALDI-TOF mass spectra by machine learning. // *AIP Conf. Proc.*, Vol. 2872, Issue 1, 2023. – p. 1-13. doi: <https://doi.org/10.1063/5.0164375>
- [8] Akhmaldinova L., Korshukov I., Kolesnikova Ye., Kolesnichenko S., Babenko D., Kadyrova I., Kabildina N., Sirota V., Zhumaliyeva V., Taizhanova D., Vazemiller D., Turmukhambetova A. Association of four genetic variants with colorectal cancer in Kazakhstan population. // *Oncotarget*, Vol.12, Issue 21, 2021. – p. 2215-2222. doi: <https://doi.org/10.18632/oncotarget.28070>
- [9] Kadyrov A., Sarsembekov B., Ganyukov A., Zhunusbekova Z., Alikarimov K. Experimental research of the coagulation process of exhaust gases under the influence of ultrasound. *Communications – Scientific Letters of the University of Žilina*, 2021, 23(4), B288-B298. <https://doi.org/10.26552/com.C.2021.4.B288-B298>
- [10] Kadyrov A., Sarsembekov B., Ganyukov A., Suyunbaev Sh., Sinelnikov K. Ultrasonic unit for reducing the toxicity of diesel vehicle exhaust gases. // *Communications - Scientific Letters of the University of Žilina*, Vol. 24, Issue 3, 2022. – p. 189-198, doi: <https://doi.org/10.26552/com>.
- [11] Kadyrov A., Ganyukov A., Pak I., Suleyev B., Balabekova K. Theoretical and experimental study of operation of the tank equipment for ultrasonic purification of the internal combustion engine exhaust gases (2021) *Communications - Scientific Letters of the University of Žilina*, 23 (3), pp. B219 - B226
- [12] Kadyrov A., Bembek M., Sarsembekov B., Kukeshva A., Nurkusheva S. The Influence of the Frequency of Ultrasound on the Exhaust Gas Purification Process in a Diesel Car Muffler. // *Appl. Sci.* Vol.14, Issue 12, 2024, – p. 1-19. doi: <https://doi.org/10.3390/app14125027>
- [13] Kadyrov A., Sarsembekov B., Kukeshva A., Sinelnikov K. Application of electric pulse and ultrasonic mufflers for increasing the degree of exhaust gas purification in car engines // *International Journal of Innovative Research and Scientific Studies*. - 2024, P.33-40. Online ISSN : 2617-6548. DOI: <https://doi.org/10.53894/ijriss.v8i1.3570>
- [14] Kadyrov A., Kukeshva A., Kryuchkov Ye., Pak I., Kurmasheva B., Kabikenov S. Development of Calculation Methodology for Optimizing the Operating Mode of an Electric Pulse Unit for Cleaning Exhaust Gases. // *Communications - Scientific Letters of the University of Žilina*, Vol. 26, Issue 1, 2024. – p. 41-53, doi: <https://doi.org/10.26552/com.C.2024.011>
- [15] Pak I., Kadyrov A., Askarov B., Suleyev B., Karsakova A. Developing and studying the method of ultrasonic purification and utilization of internal combustion engine exhaust gases (2023) *Communications - Scientific Letters of the University of Žilina*, 25 (3), pp. B245 - B258 DOI: 10.26552/com.C.2023.060
- [16] Kukeshva A., Kadyrov A., Kryuchkov Y. Establishing the parameters of the operation mode of the electric pulse automobile muffler. // *Journal of Applied Engineering Science*. Vol. 22, Issue 1, 2024. – p.89–99. doi: 10.5937/jaes0-45196
- [17] Kadyrov, A., Kryuchkov, Y., Sinelnikov, K., Ganyukov, A., Sakhapov, R., Kukeshva, A. (2022). Studying the process of the internal combustion engine exhaust gas purification by an electric pulse. // *Communications - Scientific Letters of the University of Žilina*, Vol. 24, Issue 4, 2022. – p. 275-287, doi: <https://doi.org/10.26552/com.C.2022.4.B275-B287>
- [18] Ibatov M.K., Kadyrov A.S., Pak I.A., Kadyrova I.A., Askarov B.S. The results of experimental studies of the capacitive equipment of ultrasonic cleaning of exhaust gases of vehicles. *Ugol*, 2020, (2), pp. 73–78.
- [19] Sarsembekov B.K., Kadyrov A.S., Kunayev V.A., Issabayev M.S., Kukeshva A.B. Experimental Comparison of Methods for Cleaning Car Exhaust Gas by Exposure Using Ultrasound and Laser Radiation // *Material and Mechanical Engineering Technology*, №3, 2024. ISSN 2706977X DOI: https://doi.org/10.52209/2706-977X_2024_3_44
- [20] Raj Baldev, Rajendran V., Palanichami P. Applications of ultrasound. – M.: Tekhnosfera, 2006. - 576 p.
- [21] Bergman L. Ultrasound and its application in science and technology. - Moscow: Publishing house of foreign literature, 1957. - 726 p.
- [22] Kadyrov A.S., Kunaev V.A., Georgiadi I.V. Prospects for Processing of Ferrous Metallurgical Waste Based on Arcelormittal Temirtau Experience. *Metallurgist*, 2018, 62(1-2), pp. 22–28.

- [23] Kadyrov A., Zhunusbekova Z., Ganyukov A., Kadyrova I., Kukeshva A. General characteristics for loading the working elements of drilling and milling machines when moving in the clay solution. Communications – Scientific Letters of the University of Zilina, 2021, 23(2), B97–B105.
- [24] Kadyrov A.S., Kunaev V.A., Georgiadi I.V. Ferrous metallurgy waste and waste technical fluids for obtaining the material of road bases. Ecology and Industry of Russia, 2017, 21(12), pp. 44–48.
- [25] Sherov K.T., Mardonov B.T., Kurmangaliyev T.B., Elemes D.E., Tusupova S.O., Izotova A.S., Smakova N.S., R. Gabdysalik, Buzaouva T.M. The research of micro-hardness of side surfaces of teeth cylindrical wheels processed by “shaver-rolling device”. Journal of Theoretical and Applied Mechanics, Sofia, Vol. 50, No.1 (2020), PP.50-56.
- [26] Kadyrov A., Balabekova K., Ganyukov A., Akhmediyev S. The constructive solution and calculation of elements of the unified module of the mobile bridge overcrossing. Transport Problems, 2017, 12(3), pp. 59–69.
- [27] Nasad T.G., Sherov K.T., Absadykov B.N., Tusupova S.O., Sagitov A.A. Abdugaliyeva G.B., Okimbayeva, A.E. Formation management in parts processing regenerated by surfacing. News of the National Academy of Sciences of the Republic of Kazakhstan, Series of Geology and Technical Sciences, 2019, 3(435), pp. 102–108.
- [28] Aliev S.B., Suleev B.D. Study and calculation of the disk-milling tool (2018) Ugol, (11), pp. 32 - 34 DOI: 10.18796/0041-5790-2018-11-32-34
- [29] Kadyrov A.A., Ganyukov A.A., Balabekova K.G., Zhunusbekova Z.Z., Suleev B.D. Scientific and engineering bases for development of mobile overpasses (2020) Material and Mechanical Engineering Technology, 2020 (2), pp. 7 – 13
- [30] Kyzylbaeva E.Zh., Kukeshva A.B., Kunaev V.A. Mathematical model of plate movement in thixotropic mud. // Material and Mechanical Engineering Technology, Vol. 2, Issue 2, 2020. – p. 26-30.
- [31] Kadyrov A., Sakhapov R., Ganyukov A., Sinelnikov K., Kurmasheva B., Suyunbaev Sh. Studying the process of transport equipment cooling system ultrasonic cleaning. // Communications - Scientific Letters of the University of Zilina, Vol. 24, Issue 4, 2022. – p. 288-300, doi: <https://doi.org/10.26552/com>
- [32] Menon G., Pego R.L. Approach to self-similarity in Smoluchowski's coagulation equations. // Communications on pure and applied mathematics, Vol. 57, Issue 9, 2004. – p. 1197-1232, doi: <https://doi.org/10.1002/cpa.3048>
- [33] Pak I., Burova N., Kurmasheva B., Karsakova A., Kadyrova I. Technical and Economic Efficiency of Devices for Ultrasonic Cleaning of City Bus Exhaust Gases. // Bulletin of L.N. Gumilyov Eurasian National University Technical Science and Technology Series. Vol.139, Issue 2, 2022. – p.133–142. doi: <https://doi.org/10.32523/2616-7263-2022-139-2-133-142>
- [34] Patent RU 2 373 409 C2. Device for cleaning automobile exhaust gases from particles / Savinykh Yuri Alexandrovich (RU), Logachev Viktor Grigorievich (RU), Logachev Sergey Viktorovich (RU), Vasilyeva Anastasia Yuryevna (RU); declared 10.06.2009; published 20.11.2009 Bulletin No. 32.
- [35] Patent RU 2 364 736 C2. Method for cleaning automobile exhaust gases from particles / Savinykh Yuri Alexandrovich (RU), Logachev Viktor Grigorievich (RU), Logachev Sergey Viktorovich (RU), Vasilyeva Anastasia Yuryevna (RU); declared 20.12.2008; published 20.08.2009 Bulletin No. 23.
- [36] Patent of the Republic of Kazakhstan No. 3194. Device for ultrasonic cleaning of exhaust gases / M.K. Ibatov, A.S. Kadyrov, O.T. Balabayev, B.S. Askarov, I.A. Pak; declared 20.12.2017; published 02.10.2018.
- [37] Patent of the Republic of Kazakhstan No. 9263. Ultrasonic muffler for cleaning the exhaust gases of an internal combustion engine. Kadyrov, A.S., Sarsembekov, B.K., Kadyrova, I.A.
- [38] Pak I. Experimental Study of the Ultrasonic Muffler Efficiency for Improving the Exhaust Gas Cleaning System of Internal Combustion Engines of Automobile / Material and Mechanical Engineering Technology, №2, 2024
- [39] Isagulov A., Akberdin A., Sultangaziyev R., Kim A., Kulikov V., Isagulova D. Diagram of equilibrium phase composition of Fe – C – Si – B system // Metalurgija.- 2016. Vol. 55 №3. – P. 305-308
- [40] Ilesaliev D.I. Design of Ultrasonic Technology to Improve the Efficiency of Car Exhaust Gas Cleaning System//Material and Mechanical Engineering Technology, №2, 2024
- [41] Sakhapov R. L. Method of Cleaning Internal Combustion Engine Radiator Tubes with Ultrasound//Material and Mechanical Engineering Technology, №2, 2024
- [42] Ganyukov, A.A., Sinelnikov, K.A., Kabikenov, S.Z., Karsakova, A.Z. Research and Calculation of the Deformed State of the Roadway Mobile Overpass//Material and Mechanical Engineering Technology, 3, 2024, pp.88–95.

Information of the authors

Suyunbaev Shinpolat Mansuralievich, d.t.s, professor, Tashkent State Transport University
e-mail: shinbolat_84@mail.ru

Influence of Processing Conditions on the Particle Size Distribution of Recycled Cable Insulation

Marciniak M. ¹, Świdorski A. ¹, Perz A. ¹, Kminiak R. ², Warguła L. ^{1*}

¹Poznan University of Technology, Poland

²Technical University in Zvolen, Slovakia

*corresponding author

Abstract. The particle size during the shredding process of electrical cables primarily affects the efficiency of copper separation from plastic and the energy consumption of the processes. This article aims to determine the particle fractions of plastic materials (cable sheathing) after the shredding and electrostatic separation processes. The size of these particles is significant for further material applications, such as being used as a filler in concrete instead of gravel (influencing mechanical properties). The tested granulate A was obtained during shredding in a machine equipped with a screen with 1.5 mm diameter openings, while granulate B was obtained during shredding with a machine equipped with a screen with 1 mm diameter openings. In the case of granulate A, originating from the shredding process with a 1.5 mm screen, the main fractions were: 65.5% above 1.4 mm, 27.4% between 1.4 mm and 1 mm, and 7% below 1 mm. Granulate B, derived from the shredding process of electrical cables with a 1 mm screen, showed a more diverse fraction distribution than granulate A. The dominant fraction was between 1 mm and 0.71 mm (34.1%), followed by 0.71 mm to 0.5 mm (28.2%), and 0.5 mm to 0.25 mm (28.8%). The extreme fractions - above 1 mm and below 0.25 mm - constituted 1.4% and 7.5%, respectively. A smaller screen (1 mm) leads to a more varied fraction distribution, with a higher proportion of smaller particles, resulting in higher bulk density and improved potential for applications such as concrete fillers. This knowledge can contribute to a better understanding of the mechanical properties of materials utilizing these granulates as fillers in their structure.

Keywords: shredding electrical wires, sieve analysis of fractions, particle size, Polyethylene Terephthalate (PET), Polycarbonate (PC), Polyvinyl Chloride (PVC), High-Density Polyethylene (HDPE), High Impact Polystyrene (HIPS), concrete filler

Introduction

There is an increase in the production of plastic products worldwide [1]. Due to their extensive consumption, environmentally friendly methods for their reuse are being sought [2–4]. Currently, there are three main methods for disposing of plastic waste: incineration for energy recovery [5], recycling [6–8], and landfill disposal [9]. However, incineration is associated with the emission of heavy metal pollutants, which poses a direct threat to the environment [10]. Landfill disposal, in turn, leads to issues such as soil drainage blockages and water contamination [11]. For these reasons, the search continues for methods of recycling that are both environmentally safe and cost-effective. Electrical wires and cables are subject to recycling, where the plastic insulation is stripped from the copper or aluminum core and then shredded [12]. The recycle obtained from cable insulation comprises various materials, including Polyethylene Terephthalate (PET), Polycarbonate (PC), Polyvinyl Chloride (PVC), High-Density Polyethylene (HDPE), and High Impact Polystyrene (HIPS) [13]. Due to the frequent mixing of recyclates from different cables, determining the exact composition of such agglomerates is often challenging.

Due to the various material properties crucial for proper processing during extrusion or injection molding, recycle is used as a filler in concrete. The use of plastic-derived fibers, such as Polyvinyl Alcohol (PVA) and Polypropylene (PP), as fillers in concrete mortar improves its strength properties and offers economic benefits [14]. Recycled fiberglass from water equipment can also be used as a filler in concrete. PVA and steel fibers (SE) have been incorporated into concrete mortar. These fibers act as both fillers and reinforcement for the concrete mix. They help reduce the formation of microcracks and enhance the strength properties of the material.

Developing new composites based on waste materials represents a significant research direction [15]. Studies such as those by Borawski et al. (2024) [16] and Mancel et al. (2022) [17] highlight the broad potential of recycled materials. For example, flax fibers can be used to reinforce friction composites, while waste rubber can improve the fire resistance of wooden composites. Additionally, wood-plastic composites (WPCs) from recycled wood and plastic can be used for various outdoor applications [18]. Eco-efficiency analyses, such as those conducted by Joachimiak-Lechman et al. (2019) [19], demonstrate that innovative waste utilization can contribute to environmental protection and economic sustainability. In the context of waste processing technologies, new separation methods play a crucial role, such as tribo-electrostatic separation described by Łyskawiński et al. in 2021 [20], or advanced plastic shredders that enable the production of granulate with specific particle size fractions.

Shredding of materials is an energy-intensive process; however, it provides additional advantages by facilitating transport, processing [21,22], and storage [23–25].

Depending on the type of recycle material and, most importantly, its particle size, concrete with such filler will exhibit varying mechanical properties. For this reason, an important objective has been to study the particle size fractions of granulate obtained from the recycling of electrical cables.

1. Results and discussion

The study focused on copper electrical wires from automotive harnesses (excluding fuse boxes, clamps, and plastics). The permissible range of wire diameters for shredding, determined by the design of the shredding mechanism and the limitations recommended by the shredder manufacturer, was 0.5 to 25 mm. The shredding process was carried out using a Stokkermill K750 electrical waste shredder (Udine, Italy) with a machine power of 7.5 kW. The shredder has two types of mills, each featuring three rotating blades. Changing the screens in the machine enables the separation of two particle size fractions, which were analyzed in the study. The screen opening sizes used were 1.5 mm (granulate A) and 1 mm (granulate B).

After the shredding process, a mixture of copper and plastic particles remains. To separate the copper from the wire insulation material, a HAMOS KWS 10-10 electrostatic separator (Penzberg, Germany) was used (Fig. 1). The requirements for the input material include the following: dust-free material, uniform dimensions of 0.1–8 mm, moisture content < 0.2%, free flow without sticking, a mixture of conductive and non-conductive material, and particles that are fully liberated—not adhering to each other or permanently bonded. The average throughput of the separator is 150–500 kg/h.

The study analyzed the materials constituting the insulation of the electrical wires (Fig. 2) obtained from the separator, which processed the material prepared by the shredder using screens with openings of 1.5 mm (granulate A, Fig. 2a) and 1 mm (granulate B, Fig. 2b).

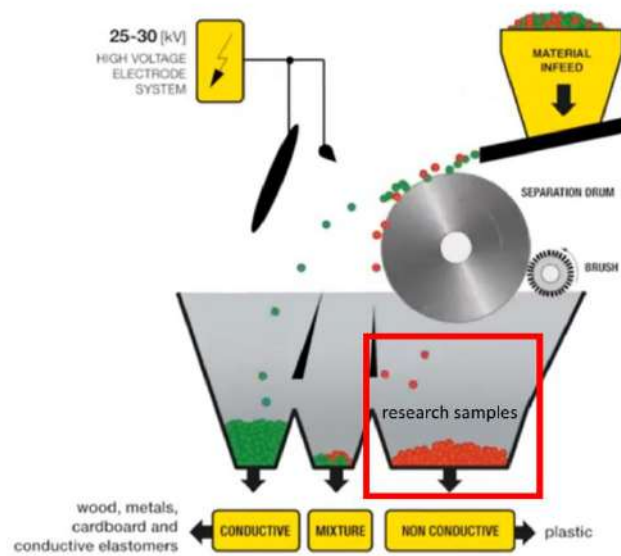


Fig. 1. – The sampling point for testing during the electrostatic separation process

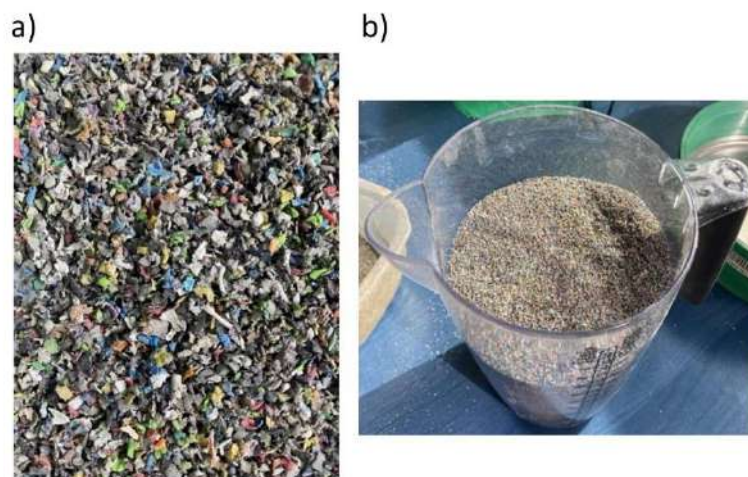


Fig. 2. – Plastic granulate constituting the insulation of electrical wiring in automobiles:
a) After the shredding process with a 1.5 mm screen; b) After the shredding process with a 1 mm screen

Granulometric composition was analyzed using a laboratory sieve shaker (model LPzE-2e, manufactured by Multiserw-Morek, Brzeźnica, Poland) [26]. Initially, the test samples were placed in a 100 ml container, and their mass was measured using a precision laboratory scale with an accuracy of 0.01 g (model 572-35, manufactured by

Kern & Sohn GmbH, Frankfurt am Main, Germany). The samples were manually compacted to avoid a loose fill. The material density for the tested volume was determined by measuring the mass with a known volume.

The material was then sieved through six sieves in the following sequence of mesh sizes: 2.5 mm, 1.4 mm, 1.0 mm, 0.71 mm, 0.50 mm, and 0.25 mm. This process resulted in seven fractions: greater than 2.5 mm, between 2.5 and 1.4 mm, between 1.4 mm and 1.0 mm, between 1.0 mm and 0.71 mm, between 0.71 mm and 0.50 mm, between 0.50 mm and 0.25 mm, and below 0.25 mm (Fig. 3). Each fraction was weighed after separation.

A total of 12 samples were prepared using granulate with finer fragmentation, and another 12 samples with coarser fragmentation. In cases where only a small quantity of particles remained on the sieves during the tests, the results from selected sieves were combined due to difficulties in accurately measuring very small masses (Fig. 4).

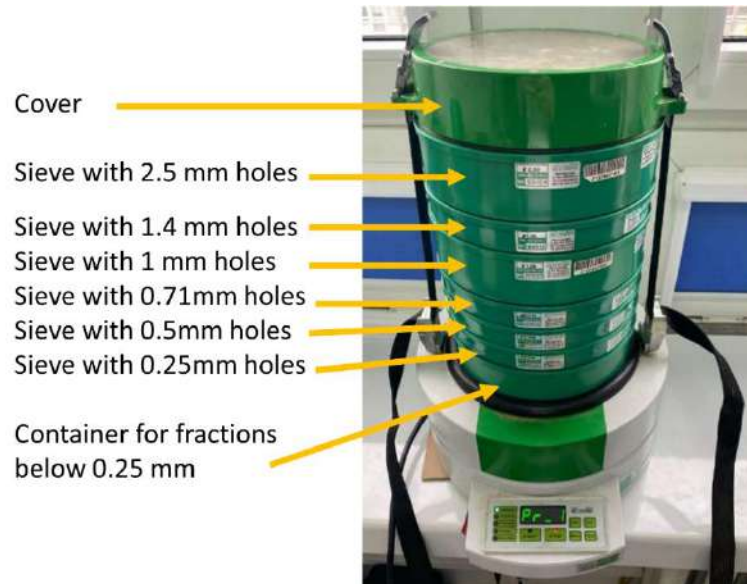


Fig. 3. – Laboratory Sieve Shaker LPzE-2e

After the process of shredding electrical wires and separating materials

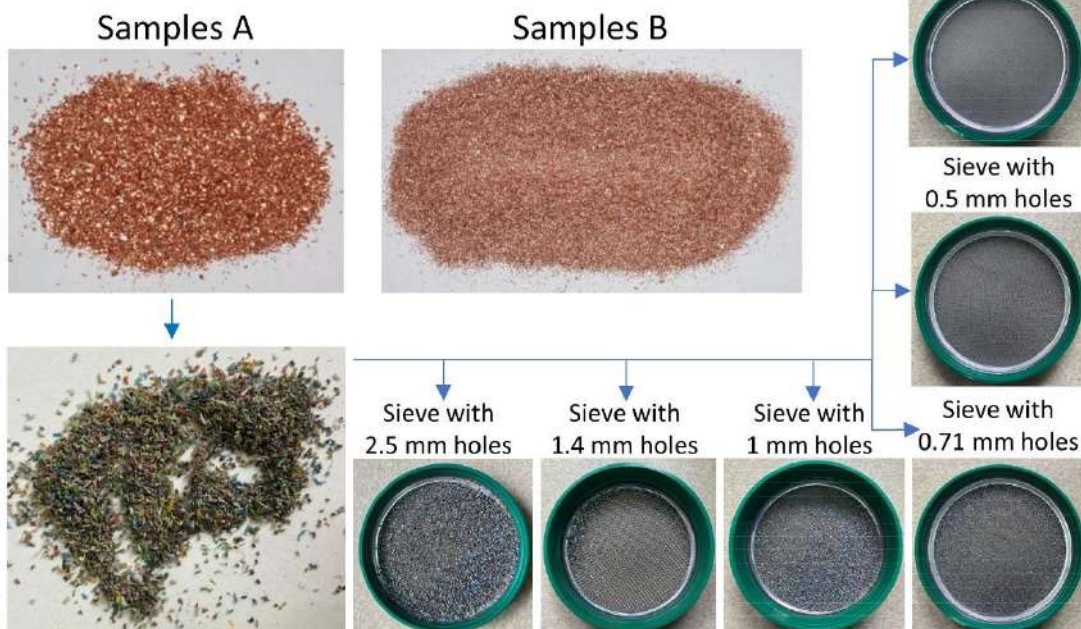


Fig. 4. – Distribution of fractions on sieves during testing

2. Methodology

The density analysis of granulate A (Fig. 5) and granulate B (Fig. 6) was conducted by measuring the mass of the granulate in a cylindrical container with a volume of 100 ml. Initially, the results were expressed in grams per 100 ml, but for consistency with the International System of Units (SI), they were converted to kilograms per cubic

meter (kg/m^3). The average density of granulate A was 444.7 kg/m^3 , while granulate B had an average density of 545.3 kg/m^3 .

The higher density of granulate B is understandable, as it consists of smaller particles that more effectively fill the available volume, reducing interparticle voids. Similar relationships between particle size and bulk density have been observed in studies on the properties of metallic powders. As noted by Otrębnik and Matula in 2010, smaller powder particles lead to higher bulk density due to better packing and reduced interparticle voids [27]. These findings align with our observations regarding granulates A and B, confirming that a reduction in particle size contributes to increased material bulk density.

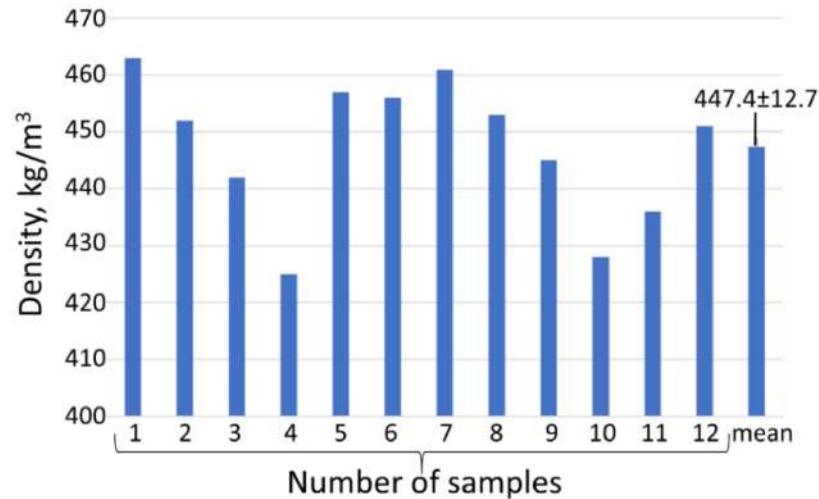


Fig. 5. – The density during the filling of the container with granulate A

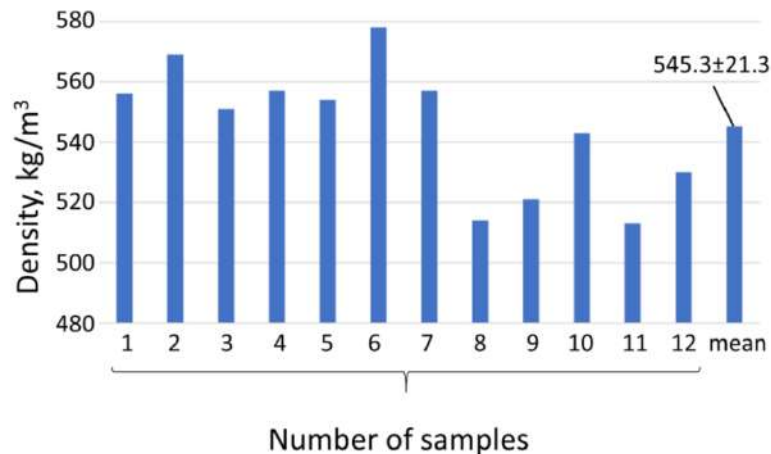


Fig. 6. – The density during the filling of the container with granulate B

The percentage contribution of specific fractions in the tested volume can be determined by knowing the total mass of the tested samples from the previous study and measuring the mass of the fractions deposited on individual sieves. The results of these studies are presented in Fig. 7 for granulate A and Fig. 8 for granulate B.

For granulate obtained from the shredding process using a machine with screens having a mesh size of 1.5 mm, the primary fractions were as follows: 65.5% above 1.4 mm, 27.4% between 1.4 mm and 1.0 mm, and 7% below 1.0 mm. While a larger number of sieves with different gradations were used during the tests, as shown in Fig. 4, some sieves collected very small amounts, which made measurements difficult. Consequently, selected fractions were grouped to increase the described range.

Granulate B, originating from the shredding process of electrical wires using a machine with a 1 mm mesh size, exhibited more dominant fractions than granulate A. The most prevalent fraction was between 1.0 mm and 0.71 mm (34.1%), followed by 0.71 mm to 0.5 mm (28.2%), and 0.5 mm to 0.25 mm (28.8%). Extreme fractions above 1 mm accounted for 1.4%, while those below 0.25 mm constituted 7.5%.

Studies conducted by other researchers, without specifying the detailed settings of the shredding machines, indicate that 85% of particles resulting from the shredding process of electrical wires are larger than 0.5 mm [28]. This is closely aligned with the results presented in this article. Wędrychowicz et al. in 2023 discussed how the granulation process influences the liberation of metallic and plastic components, noting that optimal particle sizes

are critical for effective separation techniques, such as electrostatic and density-based methods. The average particle sizes during their studies ranged from 0.34 mm to 0.59 mm. After separating the plastic material, particle sizes ranged from 0.01 mm to 0.13 mm (for copper) and 0.25 mm to 0.33 mm (for plastic material) [29]. The particles in their study were within a similar size range as those observed in this research.

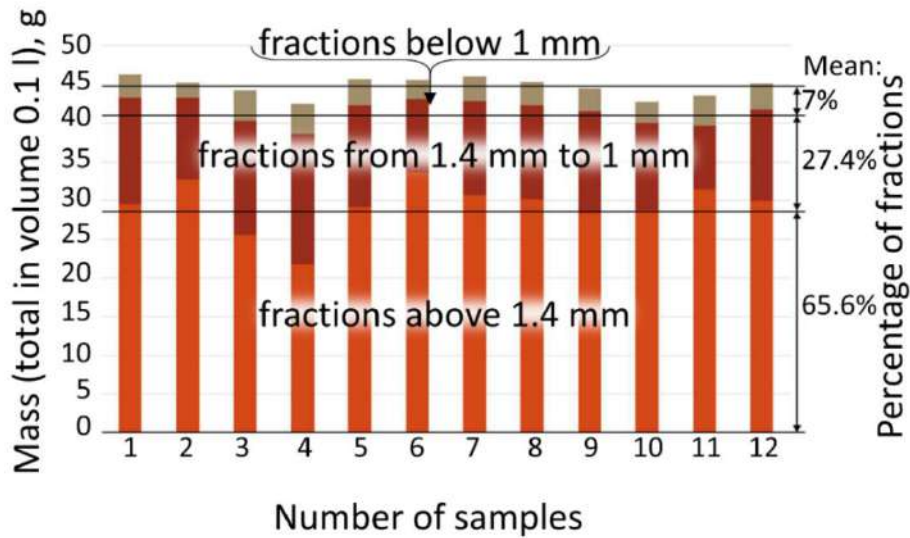


Fig. 7. – Fraction content in granulate A

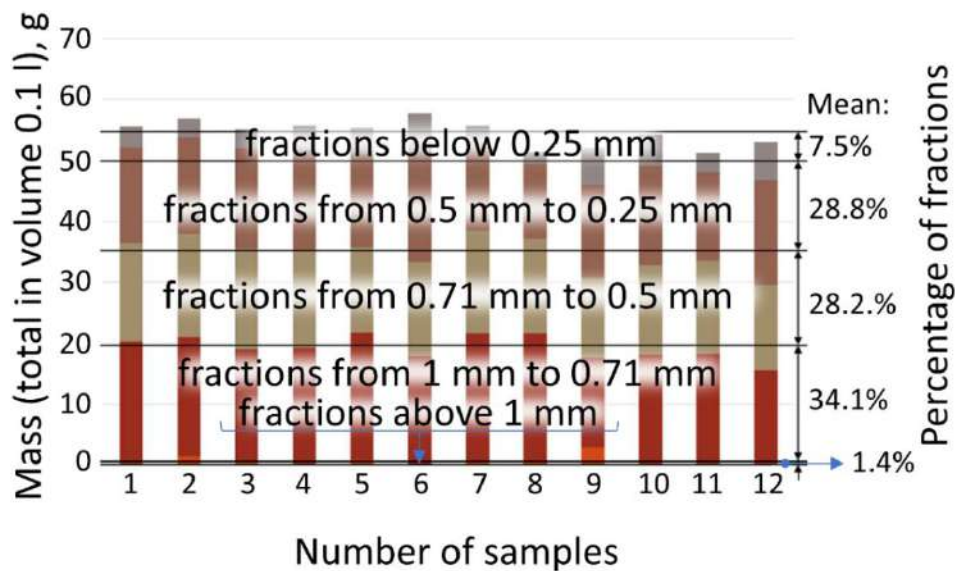


Fig. 8. – Fraction content in granulate B

The concept of using granulate derived from the recycling of electrical cable insulation presents an alternative to components made of carbon fiber in applications where dynamic loads are not significant. An example of such an application is a wheelchair [30], where a composite frame made of carbon fiber and epoxy resin can be replaced with a composite in which the carbon fiber reinforcement is substituted with polymer fractions obtained from the shredding of cable insulation. In this context, the fraction size is crucial, as its dimensions directly influence the mechanical properties of the final product. The information about the granulate fraction size is also essential for assessing slip risk on surfaces in buildings [31]. This issue becomes particularly important in modern buildings, where construction materials, such as tiles containing recycled plastic granules, are used. The fraction size affects the texture and functional properties of the surface, which directly impacts user safety. Another example of the significance of fraction size information is its application as a component in wheelchair tires. The size of the fraction used affects the mechanical properties of the tire, including rolling resistance [32]. This information is essential during the design and optimization of drive systems and structural components, as highlighted in studies on drive systems [33].

Conclusion

The study on the particle size distribution of plastics derived from the recycling of electrical cable insulation revealed a significant impact of shredding parameters on the properties of the obtained granulate. It was found that using a screen with larger openings (1.5 mm) resulted in granulate A with a coarser particle structure, where 65.5% of the particles exceeded 1.4 mm in size. Conversely, a screen with smaller openings (1 mm) produced granulate B with a finer particle distribution, dominated by fractions ranging from 1.0 mm to 0.71 mm (34.1%). The bulk density analysis showed that granulate B exhibited a higher density (545.3 kg/m³) than granulate A (444.7 kg/m³), attributed to better packing efficiency due to smaller particles filling void spaces more effectively. These results highlight the importance of particle size distribution for potential applications of recyclates, particularly as fillers in concrete, where finer particles can improve the material's mechanical properties by enhancing integration and structural reinforcement. Moreover, using a smaller screen size increases the diversity of particle fractions and optimizes the separation of conductive (copper) and non-conductive (plastic) materials during electrostatic separation. From an environmental perspective, the study emphasizes the significance of tailoring recycling process parameters to improve efficiency and minimize environmental impact. The findings provide valuable insights for optimizing recycling processes, enhancing the quality of recyclates, and expanding their applications in developing sustainable materials.

References

- [1] Oktavilia, S.; Hapsari, M.; Firmansyah; Setyadharma, A.; Wahyuningsum, I.F.S. Plastic Industry and World Environmental Problems. *E3S Web Conf.* 2020, 202, 05020, doi:10.1051/e3sconf/202020205020.
- [2] Czarnecka-Komorowska, D.; Kanciak, W.; Barczewski, M.; Barczewski, R.; Regulski, R.; Sędziak, D.; Jędrzycka, C. Recycling of Plastics from Cable Waste from Automotive Industry in Poland as an Approach to the Circular Economy. *Polymers* 2021, 13, 3845, doi:10.3390/polym13213845.
- [3] Tucki, K.; Orynycz, O.; Wasiak, A.; Gola, A.; Mieszalski, L. Potential Routes to the Sustainability of the Food Packaging Industry. *Sustainability* 2022, 14, 3924, doi:10.3390/su14073924.
- [4] Ortego, A.; Russo, S.; Iglesias-Émbil, M.; Valero, A.; Magdalena, R. Exergy Assessment of Plastic Car Parts. *Vehicles* 2023, 5, 1211–1226, doi:10.3390/vehicles5030067.
- [5] Włodarczyk, K.; Kowalczyk, J.; Ulbrich, D.; Seleh, J. A Review of Non-Destructive Evaluation Methods of Elements of Prototype Module of Drying Line Used to Receive RDF Fuel from Waste Recycling. *Procedia Eng.* 2017, 192, 959–964, doi:10.1016/j.proeng.2017.06.165.
- [5] Czarnecka-Komorowska, D.; Wiszumirska, K. Sustainability Design of Plastic Packaging for the Circular Economy/Zrownowazone Projektowanie Opakowan z Tworzyw Sztucznych w Gospodarce Cyrkularnej. *Polimery* 2020, 65, 8–18.
- [7] Čabalová, I.; Ház, A.; Krilek, J.; Bubeníková, T.; Melicherčík, J.; Kuvik, T. Recycling of Wastes Plastics and Tires from Automotive Industry. *Polymers* 2021, 13, 2210, doi:10.3390/polym13132210.
- [8] Ivanichok, N.; Kolkovskiy, P.; Ivanichok, O.; Kotsyubynsky, V.; Boychuk, V.; Rachiy, B.; Bembenek, M.; Warguła, Ł.; Abaszade, R.; Ropyak, L. Effect of Thermal Activation on the Structure and Electrochemical Properties of Carbon Material Obtained from Walnut Shells. *Materials* 2024, 17, 2514, doi:10.3390/ma17112514.
- [9] Yadav, V.; Sherly, M.A.; Ranjan, P.; Tinoco, R.O.; Boldrin, A.; Damgaard, A.; Laurent, A. Framework for Quantifying Environmental Losses of Plastics from Landfills. *Resour. Conserv. Recycl.* 2020, 161, 104914, doi:10.1016/j.resconrec.2020.104914.
- [10] Abubakar, A.; Zangina, A.S.; Maigari, A.I.; Badamasi, M.M.; Ishak, M.Y.; Abdullahi, A.S.; Haruna, J.A. Pollution of Heavy Metal Threat Posed by E-Waste Burning and Its Assessment of Human Health Risk. *Environ. Sci. Pollut. Res.* 2022, 29, 61065–61079, doi:10.1007/s11356-022-19974-6.
- [11] Fořt, J.; Kobetičová, K.; Böhm, M.; Podlesný, J.; Jelínková, V.; Vachtlová, M.; Bureš, F.; Černý, R. Environmental Consequences of Rubber Crumb Application: Soil and Water Pollution. *Polymers* 2022, 14, 1416, doi:10.3390/polym14071416.
- [12] Flizikowski, J.; Kruszelnicka, W.; Macko, M. The Development of Efficient Contaminated Polymer Materials Shredding in Recycling Processes. *Polymers* 2021, 13, 713, doi:10.3390/polym13050713.
- [13] Warguła, Ł.; Kaczmarzyk, P.; Dziechciarz, A. The Assessment of Fire Risk of Non-Road Mobile Wood Chopping Machines. *J. Res. Appl. Agric. Eng.* 2019, Vol. 64.
- [14] Shi, X.; Ning, B.; Wang, J.; Cui, T.; Zhong, M. Improving Flexural Toughness of Foamed Concrete by Mixing Polyvinyl Alcohol-Polypropylene Fibers: An Experimental Study. *Constr. Build. Mater.* 2023, 400, 132689, doi:10.1016/j.conbuildmat.2023.132689.
- [15] Bonenberg, A.; Sydor, M.; Cofta, G.; Doczekalska, B.; Grygorowicz-Kosakowska, K. Mycelium-Based Composite Materials: Study of Acceptance. *Materials* 2023, 16, 2164, doi:10.3390/ma16062164.
- [16] Borawski, A.; Szpica, D.; Mieczkowski, G. Laboratory Tests on the Possibility of Using Flax Fibers as a Plant-Origin Reinforcement Component in Composite Friction Materials for Vehicle Braking Systems. *Materials* 2024, 17, 2861, doi:10.3390/ma17122861.
- [17] Mancel, V.; Čabalová, I.; Krilek, J.; Réh, R.; Zachar, M.; Jurczykova, T. Fire Resistance Evaluation of New Wooden Composites Containing Waste Rubber from Automobiles. *Polymers* 2022, 14, 4465, doi:10.3390/polym14204465.

- [18] Sydor, M.; Wieloch, G. Construction Properties of Wood Taken into Consideration in Engineering Practice | Właściwości Konstrukcyjne Drewna Uwzględniane w Praktyce Inżynierskiej. *Drew. Pr. Nauk. Doniesienia Komun.* 2009, 52, 63–73.
- [19] Joachimiak-Lechman, K.; Selech, J.; Kasprzak, J. Eco-Efficiency Analysis of an Innovative Packaging Production: Case Study. *Clean Technol. Environ. Policy* 2019, 21, 339–350, doi:10.1007/s10098-018-1639-7.
- [20] Lyskawinski, W.; Baranski, M.; Jedryczka, C.; Mikolajewicz, J.; Regulski, R.; Sedziak, D.; Netter, K.; Rybarczyk, D.; Czarnecka-Komorowska, D.; Barczewski, M. Tribo-Electrostatic Separation Analysis of a Beneficial Solution in the Recycling of Mixed Poly(Ethylene Terephthalate) and High-Density Polyethylene. *Energies* 2021, 14, 1755, doi:10.3390/en14061755.
- [21] Nikonova, T.; Gierz, Ł.; Berg, A.; Turla, V.; Warguła, Ł.; Yurchenko, V.; Abdugaliyeva, G.; Zhunuspekov, D.; Wieczorek, B.; Robakowska, M.; et al. Comparative Analysis of Strength Fatigue Properties and Abrasive Wear Resistance for a New Composition of Polymer Concrete Coated with Metal Alloy Powders. *Coatings* 2023, 13, 586, doi:10.3390/coatings13030586.
- [22] Nikonova, T.; Zharkevich, O.; Dandybaev, E.; Baimuldin, M.; Daich, L.; Sichkarenko, A.; Kotov, E. Developing a Measuring System for Monitoring the Thickness of the 6 m Wide HDPE/LDPE Polymer Geomembrane with Its Continuous Flow Using Automation Equipment. *Appl. Sci.* 2021, 11, 10045, doi:10.3390/app112110045.
- [23] Warguła, Ł.; Lijewski, P.; Kukła, M. Effects of Changing Drive Control Method of Idling Wood Size Reduction Machines on Fuel Consumption and Exhaust Emissions. *Croat. J. For. Eng.* 2023, 44, 137–151, doi:10.5552/crojfe.2023.1700.
- [24] Warguła, Ł.; Kukła, M.; Wieczorek, B.; Krawiec, P. Energy Consumption of the Wood Size Reduction Processes with Employment of a Low-Power Machines with Various Cutting Mechanisms. *Renew. Energy* 2022, 181, 630–639, doi:10.1016/j.renene.2021.09.039.
- [25] Warguła, Ł.; Wieczorek, B.; Giedrowicz, M.; Kukła, M.; Nati, C. Wood Chippers: Influence of Feed Channel Geometry on Possibility of Musculoskeletal System Overload. *Croat. J. For. Eng.* 2025, 46, doi:10.5552/crojfe.2025.2501.
- [26] Warguła, Ł.; Wilczyński, D.; Wieczorek, B.; Palander, T.; Gierz, Ł.; Nati, C.; Sydor, M. Characterizing Sawdust Fractional Composition from Oak Parquet Woodworking for Briquette and Pellet Production. *Adv. Sci. Technol. Res. J.* 2023, 17, 236–247, doi:10.12913/22998624/172534.
- [27] Otrębniak, E.; Matuła, G. Technological Properties of Powders Original (Text in Polish: Własności Technologiczne Proszków). *Pr. Stud. Kół Nauk.* 2010.
- [28] Cansu, C.; Cuneyt, A.; Fatma, A. Recycling of Waste Electrical Cables. *Mater. Sci. Eng. Int. J.* 2019, 3, doi:10.15406/mseij.2019.03.00099.
- [29] Wędrychowicz, M.; Kurowiak, J.; Skrzekut, T.; Noga, P. Recycling of Electrical Cables—Current Challenges and Future Prospects Available online: <https://www.mdpi.com/1996-1944/16/20/6632> (accessed on 17 November 2024).
- [30] Wieczorek, B.; Warguła, Ł.; Adamiec, J.; Sowa, T.; Padjasek, M.; Padjasek, Ł.; Sydor, M. Investigating the Impact of Carbon Fiber as a Wheelchair Frame Material on Its Ability to Dissipate Kinetic Energy and Reduce Vibrations. *Materials* 2024, 17, 641, doi:10.3390/ma17030641.
- [31] Waluś, K.J.; Warguła, Ł.; Wieczorek, B.; Krawiec, P. Slip Risk Analysis on the Surface of Floors in Public Utility Buildings. *J. Build. Eng.* 2022, 54, 104643, doi:10.1016/j.jobe.2022.104643.
- [32] Wieczorek, B.; Warguła, Ł.; Kukła, M.; Rybarczyk, D.; Górecki, J.; Giedrowicz, M. The Impact of the Human Body Position Changes During Wheelchair Propelling On Motion Resistance Force. *J. Biomech. Eng.* 2021, 143, 081008-1-081008–081010.
- [33] Wieczorek, B.; Warguła, Ł.; Kukła, M. Influence of a Hybrid Manual–Electric Wheelchair Propulsion System on the User’s Muscular Effort. *Acta Mech. Autom.* 2023, 17, 28–34, doi:10.2478/ama-2023-0003.

Information of the authors

Marciniak Marcin, MSc Eng., student, Poznan University of Technology
e-mail: marcin.marciniak@student.put.poznan.pl

Świdorski Adam, MSc Eng., student, Poznan University of Technology
e-mail: adam.swidorski@student.put.poznan.pl

Perz Antoni, MSc Eng., student, Poznan University of Technology
e-mail: antoni.perz@student.put.poznan.pl

Kminiak Richard, doc. Ing. PhD., professor, Technical University in Zvolen
e-mail: richard.kminiak@tuzvo.sk

Warguła Łukasz, PhD DSc Eng., professor, Poznan University of Technology
e-mail: lukasz.wargula@put.poznan.pl

Comparison of Different Types of Engineering Alloys Suitable for Automotive Industry

Dalavi A.M.* , Sarma G., Mondal A., Kukeriya L., Kamble P.

Symbiosis Institute of Technology, Symbiosis International (Deemed) University, Gram Lavale, Mulshi, Pune, India

*corresponding author

Abstract: The automotive industry relies on a diverse array of engineering alloys to meet the rigorous demands of vehicle design and performance. This paper provides a comprehensive comparison of different types of engineering alloys suitable for the automotive industry. The alloys under consideration encompass a broad spectrum, including traditional materials such as steel and aluminum, as well as advanced options like titanium, magnesium, and composite materials. The comparison delves into key attributes such as strength, weight, corrosion resistance, and heat resistance, highlighting the advantages and applications of each alloy type. Additionally, the paper explores emerging trends and innovations in alloy development, emphasizing their implications for enhancing vehicle safety, fuel efficiency, and overall performance. By synthesizing information on the various engineering alloys, this study aims to offer valuable insights for engineers, researchers, and industry professionals involved in the design and manufacturing of automotive components.

Keywords: engineering alloys, automotive industry & materials, emerging trends, alloy development, vehicle safety

Introduction

The automotive industry, at the forefront of technological advancements, continually seeks innovative materials to address the evolving challenges of modern vehicle design. A critical aspect of this pursuit is the selection of engineering alloys, which play a pivotal role in shaping the performance, durability, and efficiency of automotive components. This paper undertakes a comprehensive exploration and comparison of various engineering alloys tailored for the automotive industry.

As the automotive landscape undergoes transformative shifts towards sustainability, safety, and enhanced performance, the demand for materials with specific properties becomes increasingly nuanced. The selection of an appropriate alloy involves a delicate balance of factors such as mechanical strength, weight considerations, corrosion resistance, and thermal stability. From the stalwart steel alloys to the lightweight and corrosion-resistant aluminum, the automotive engineer is presented with a diverse palette of materials to navigate.

This comparative study not only dissects the fundamental attributes of traditional alloys like steel and aluminum but also delves into the potential of emerging materials such as titanium, magnesium, and advanced composites. Each alloy brings its unique set of advantages and challenges to the automotive manufacturing arena, influencing decisions in component design, structural integrity, and overall vehicle performance.

Moreover, this investigation aims to provide insights into the applications of these alloys within the automotive sector, examining their roles in critical components like chassis, body panels, engine parts, and safety features. By understanding the strengths and limitations of each alloy type, engineers and researchers can make informed decisions that contribute to the development of vehicles with improved fuel efficiency, enhanced safety profiles, and reduced environmental impact.

As we embark on this comparative journey across engineering alloys, the overarching goal is to offer a valuable resource for professionals and researchers engaged in the intricate task of selecting materials that drive the automotive industry towards a future characterized by innovation, efficiency, and sustainability.

1. Literature Review

The automotive industry is prioritizing the use of lightweight constructions and high strength materials, such as high strength steels and aluminum alloys, to meet customer demands and legal requirements, resulting in thinner sheets, reduced mass, lower consumption, and increased environmental protection. However, this can also decrease formability. This paper focuses on recent material developments in the automotive industry, specifically the use of high strength steels and aluminum alloys in sheet metal forming for body-in-white manufacturing [1].

The study evaluates the corrosion performance of Al-Si automotive alloys in deep seawater using electrochemical impedance spectroscopy and potentiodynamic polarization techniques. Results show that corrosion resistance improves with increasing Si concentrations near the eutectic level, but deteriorates after. Higher Si concentrations show higher polarization resistance and open circuit potential, while corrosion current and rate values decrease. The study also reveals the presence of films after corrosion, including pits and pinholes [2].

This paper highlights the potential of chemical engineers in non-traditional technical areas in the automotive industry, such as vehicle thermal management. Chemical engineers have made significant contributions in areas like fuels, lubricants, and emission control. However, stringent emissions and fuel economy improvements have made automotive thermal management more challenging. This requires temperature management of vehicle components, systems, materials, and fluids. Chemical engineering education often focuses on chemical process industries, but

real-life examples from automotive applications can help students understand the significance of these applications. Examples include vehicle instrumentation and testing, exhaust after-treatment systems, fuel system thermal management, and kinetics of material thermal degradation. The paper also discusses the importance of thermocouple dynamics and distillation problems in the automotive industry, such as estimating fuel temperature and fuel vapour emissions. The paper recommends developing an undergraduate course in automotive thermal management, offering elective options for senior undergraduate and graduate students [3].

The study investigates the use of lightweight materials like aluminum in automotive suspension parts to achieve weight targets and reduce fuel consumption. The research uses computer-aided engineering methods, such as Abaqus and nCode, to analyze the strength and fatigue of the aluminum suspension bracket. The study also investigates the redesign of the front suspension bracket made of ductile cast iron in commercial vehicles, aiming to reduce weight and fuel consumption. The fatigue performance of the existing ductile cast iron front suspension bracket was examined using the finite element method. The design, computer analysis results, and low-pressure aluminum casting manufacturing process have been continuously improved, with a 30% weight reduction target achieved with material change [4].

Technological innovations are essential for progress in many areas, including uses of titanium alloy. Expanding the uses of titanium alloy requires new design and material applications. Biomedical devices employ metallic biomaterials such as cobalt-chromium alloys and 316L stainless steel, however the discharge of these materials from prosthetic implants might have harmful consequences. Titanium alloys provide superior corrosion resistance, a unique strength-to-weight ratio, and mechanical qualities at high temperatures. By improving the surface characteristics of titanium alloys, surface engineering techniques can reduce fuel consumption and CAFÉ penalties. Without causing surface deterioration, surface modification can raise the operating temperature [5].

Due to growing rivalry and environmental consciousness, the car industry is embracing lighter materials and energy-saving designs more and more. The low density, high strength, and corrosion resistance of aluminium alloys make them the preferable material due to their ease of recycling. This method lowers the weight, fuel consumption, and emissions of the vehicle, saving 5–10% of gasoline each km and cutting emissions. It is imperative for the environment that designs become lighter and use less energy [6].

Understanding organizational problems in the automotive industry and offering remedies for enhancements are the goals of this research project. The method collects qualitative data through semi-structured interviews and literature review. The results emphasise people skills, organizational culture, and communication and cooperation challenges. Model-Based Engineering approaches should be the main focus of future research to improve theory development and industry implementation [7].

2. Engineering Alloys classification on the basis of uses

Cast aluminium alloys are becoming increasingly popular for use in electro automotive parts due to their unique properties, such as mechanical and thermophysical properties, dimensional stability, corrosion resistance, electromagnetic compatibility, and crashworthiness. The automotive industry is shifting towards electrification due to factors like the oil crisis, air pollution, and global warming. Cast aluminium alloys like EN AC-47000, EN AC-44300, EN AC-43500, and EN AC-42100 are available for mass production using casting processes like HPDC, LPDC, and CPS. However, concerns about the addition of alloying elements and their impact on corrosion and cost may limit their use in electro automotive parts production [8].

The comparison table above encapsulates a diverse array of engineering alloys and their applications within the automotive industry, shedding light on the multifaceted landscape of material selection. As the automotive sector undergoes profound shifts towards lightweight constructions, high-strength materials, and environmental sustainability, the choice of alloys becomes a critical factor influencing vehicle design, performance, and compliance with regulatory standards.

One prominent theme emerging from the comparison is the strategic utilization of high-strength steels and aluminium alloys in body-in-white manufacturing. The automotive industry, driven by customer demands for fuel-efficient vehicles and regulatory requirements to curb carbon emissions, is increasingly favouring materials that offer a balance between strength and reduced mass. The use of high-strength steels and aluminium alloys allows for thinner sheets, contributing to lower vehicle weights and improved fuel consumption. However, the trade-off involves potential decreases in formability, a factor that demands careful consideration in the manufacturing process.

Corrosion resistance emerges as a pivotal aspect in the evaluation of Al-Si automotive alloys. The study on the corrosion performance of these alloys in deep seawater provides valuable insights into their behaviour under extreme conditions. The findings indicate a nuanced relationship between silicon concentrations and corrosion resistance, highlighting the intricate nature of alloy composition in influencing material properties. Such insights are crucial for manufacturers striving to enhance the durability and longevity of automotive components, especially those exposed to harsh environmental conditions.

The exploration of lightweight materials, specifically aluminium, in automotive suspension parts showcases a concerted effort to achieve weight reduction targets and mitigate fuel consumption. Computer-aided engineering methods, such as Abaqus and nCode, facilitate a meticulous analysis of the strength and fatigue of the aluminium suspension bracket. Additionally, the study extends to the redesign of front suspension brackets made of ductile cast

iron, exemplifying the industry's commitment to continuous improvement. The results demonstrate a significant achievement with a 30% weight reduction target through material changes, underscoring the potential for innovation in material selection to drive efficiency gains.

Beyond traditional automotive applications, the table reveals the role of titanium alloys in biomedical devices. While these alloys present unique properties ideal for load-bearing applications in implants, there are concerns about their toxic effects due to the release of nickel, chromium, and cobalt. This highlights the delicate balance required in material selection, particularly in industries where biocompatibility is paramount. The automotive sector's exploration of alternative alloys and materials signifies a broader trend in industries seeking not only performance but also environmentally conscious and health-compatible solutions.

The overarching trend in the automotive industry is a shift towards lighter materials and energy-saving designs, driven by both market competition and environmental consciousness. Aluminium alloys, with their low density, high strength, and recyclability, emerge as a preferred choice, resulting in significant fuel savings and reduced emissions. This shift aligns with global efforts to address environmental concerns and demonstrates the industry's commitment to sustainable practices.

The automotive industry is increasingly seeking materials to reduce energy consumption and air pollution. This paper discusses the application of magnesium and aluminium alloys in the automotive industry, focusing on material properties, machinability, and cost comparison. Magnesium alloys offer advantages over aluminium due to their mechanical and physical properties, making them suitable for various automotive components. The market for magnesium alloys is predicted to rise, with magnesium alloys showing potential for lightweight, environmentally friendly, safer, and cheaper cars. However, the application of magnesium profiles depends on whether established forming processes can be applied to magnesium. Further research is needed to improve processing, machinability, and mechanical properties, as magnesium has the potential to ignite if not handled properly. Cost-effective production and application technologies are crucial for making magnesium alloys an economically viable alternative to aluminium alloys [9].

The increasing demands for fuel economy improvement and greenhouse gas emission control have led to the production of lightweight automobiles. This has led to the development of lightweight yet high-performance materials as alternative solutions for conventional automotive materials like cast iron and steel. A systematic review of available lightweight materials for next-generation automobiles is provided, including light alloys, high-strength steels, composites, and advanced materials. The review discusses the entire life cycle of automotive materials, their physical/mechanical properties, characterization, manufacturing techniques, and potential applications. The advantages and drawbacks of the reviewed materials are summarized, yielding appropriate application scenarios for different lightweight materials. The review also provides general guidelines for material selection in different components and offers effective strategies for enabling extensive usage of different lightweight materials in the automotive market [10].

This study focuses on the use of a composite material with 4% WC particulates as reinforcement in an aluminium alloy matrix for a roll cage chassis of an off-road vehicle. The composite material showed improved impact resistance, high strength to weight ratio, and design safety compared to the conventional aluminium alloy. The composite material had no effect on heat treatment and showed proper distribution of WC particulates in the matrix. The CAE analysis of the composite and alloy chassis revealed that the composite material was a better choice for the roll cage chassis than the conventional A-356 alloy. The composite material also showed improved performance in front, roll over, and side impact [11].

Solid crankshafts are in growing demand since diesel engines need to operate at higher outputs while using smaller dimensions. Manufacturers are working to enhance these crankshafts' fatigue strength, quality, and dependability. New fillet hardening techniques, steel-making methods, and materials with increased strength are some of the latest developments in crankshaft production. Continuous Grain Flow (CGF) forging serves as the foundation for the design of most crankshafts. The fillets, which are the most crucial components of a solid type crankshaft, have undergone several changes to achieve greater fatigue strengths. Until around 1960, carbon steels in the 450 MPa class were in use. Low-alloy steels (≤ 800 MPa) and super-high strength steels (950 MPa class) came next. The application of additional technologies to increase fatigue strength includes cold rolling, induction hardening, nitriding, and shot-peening. The upward strength trend [12].

In order to choose and use materials in power transmission systems in the automotive industry more efficiently, researchers are developing material optimisation approaches. In order to guarantee ideal operating conditions during power transfer, engine shafts are essential. The study looks at the usage of three different types of materials: homogeneous, composite, and functionally graded materials (FGM), as well as their effects on crankshaft performance. According to research, FGM is the best material for best results. Functionally graded materials enhance the performance of stainless-steel crankshafts, according to the study, which used ANSYS to develop a finite element model of the crankshaft and perform modal and harmonic analysis. The paper proposes additional studies utilizing more traditional and functionally graded material types for modal and harmonic analysis of engine crankshafts [13].

The crankshaft is a crucial component of an Internal Combustion (I.C.) engine, responsible for rotary motion and the primary operation in automobiles. The optimal design should have low Noise Vibration and Harshness levels, as these levels determine the quality of output and affect the environment and other components of the

automobile. This paper presents a methodology for determining the best material composition for a given crankshaft, which is essential for a structure's longevity. The methodology used is a good substitute for traditional experimental methods, as it reduces time and has good accuracy. Chemical tests were performed on Tata Nano and Mahindra Maxximo crankshafts, revealing that the Tata Nano crankshaft had a chemical composition of Carbon 0.43%, Sulphur 0.024%, Phosphorous 0.021%, Manganese 1.66%, and Silicon 0.35%, while the Mahindra Maxximo crankshaft had a chemical composition of Carbon 0.38%, Sulphur 0.045%, Phosphorous 0.021%, Manganese 1.57%, and Silicon 0.60%. This methodology can be applied to design crankshafts according to specific applications, reducing time and expenses compared to traditional methods [14].

Environmental concerns have led to a rise in the need for weight reduction in crankshafts, an essential component of internal combustion engines. Existing techniques, including hot forging and drilling, have drawbacks in terms of product stiffness and manufacturing costs. It is now possible to reduce weight while maintaining enough stiffness thanks to innovative design and production techniques. In order to maintain stiffness while lowering weight, the new design has a thicker outer border and a narrower pin shoulder. The production process minimizes temperature variance during forging by increasing thickness with a bent section. Osaka Steel Works evaluated the procedure on a 5000-t press line to ensure the required stiffness and validate formability.

Conclusion

Automotive industry is looking for lightweight materials with low cost without affecting the performance requirement.

This review paper discusses about various types of engineering alloys, high strength steels, Al-Si automotive steels, and lightweight materials in automotive suspension used in automotive industry. Table 1. discusses about various aspects of materials used in automotive industry. Aspects such as application area, performance criteria, challenges if material used, Evaluation techniques, analysis or evaluation methods etc. are discussed.

Table 1. Comparison of materials with different aspects

Aspect	High Strength Steels	aluminium Alloys	Al-Si Automotive Alloys	Chemical Engineers in Automotive Industry	Lightweight Materials in Automotive Suspension
Application Area	Sheet metal forming for body-in-white manufacturing	Sheet metal forming for body-in-white manufacturing	Corrosion resistance in deep seawater	Vehicle thermal management	Automotive suspension parts
Materials Discussed	High strength steels	aluminium alloys	Al-Si automotive alloys	Lightweight materials (e.g., aluminium)	aluminium, ductile cast iron
Performance Criteria	Lightweight, high strength, environmental protection	Lightweight, high strength, environmental protection	Corrosion resistance, Si concentration effects	Thermal management, fuels, lubricants, emission control	Weight reduction, fuel consumption
Challenges	Decreased formability	Corrosion, formability challenges after increased Si concentrations	Corrosion, pit and pinhole formation	Stringent emissions, fuel economy improvements	Achieving weight targets, maintaining strength and fatigue performance

Aspect	High Strength Steels	aluminium Alloys	Al-Si Automotive Alloys	Chemical Engineers in Automotive Industry	Lightweight Materials in Automotive Suspension
Evaluation Techniques/Methods	Not specified	Electrochemical impedance spectroscopy, potentiodynamic polarization	Electrochemical impedance spectroscopy, potentiodynamic polarization	Not specified	Computer-aided engineering (Abaqus, nCode), finite element method
Recommendations/Solutions Proposed	Recent material developments in high strength steels and aluminium alloys	Optimal Si concentrations near eutectic level for improved corrosion resistance	Developing an undergraduate course in automotive thermal management	Real-life examples from automotive applications in chemical engineering education	Material change to aluminium, continuous improvement in design and manufacturing process
Targeted Goals/Achievements	Thinner sheets, reduced mass, lower consumption, increased environmental protection	Corrosion resistance improvement with optimal Si concentrations	Advancements in chemical engineering education for automotive applications	Improved understanding of automotive thermal management	30% weight reduction achieved with material change
Analysis/Methods Used for Evaluation	Not specified	Electrochemical impedance spectroscopy, potentiodynamic polarization	Electrochemical impedance spectroscopy, potentiodynamic polarization	Not specified	Computer-aided engineering (Abaqus, nCode), finite element method
Significant Findings/Results	Not specified	Corrosion resistance improves with increasing Si concentrations near eutectic level, deteriorates after	Presence of films after corrosion, including pits and pinholes	Significant contributions of chemical engineers in non-traditional technical areas	30% weight reduction achieved with material change, continuous improvement in design
Key Takeaways/Contributions to the Industry	Advancements in lightweight constructions using high strength steels and aluminium alloys	Corrosion performance insights for Al-Si alloys in deep seawater	Importance of chemical engineers in automotive thermal management	Application of chemical engineering education in automotive industry	Use of lightweight materials (e.g., aluminium) in automotive suspension for weight reduction and fuel efficiency

Use of light weight material assures over all weight reduction, less power consumption, more fuel efficiency. Use of computer aided analysis for analyzing the materials without using prototypes, thus helps in predicting the possible failure mode and stress-strain analysis. This review concludes that use of light weight materials such as aluminium and others in suitable automotive components for weight reduction and fuel efficiency.

Funding: This study was not supported by any agency or university.

Declaration of Competing Interest The authors declare that they have no known competing of interest.

References

[1] Miklos Tisza, Imre Czinege. Comparative study of the application of steels and aluminium in lightweight production of automotive parts; International Journal of Lightweight Materials and Manufacture, Vol. 1, Issue 4, 2018,-p.229-238.

- [2] A. Abdullah Khan, A. Kabir Hossain, and M. S. Kaiser, 2023. Impact of Deep Seawater on the Electrochemical Corrosion Performance of Hypoeutectic, Eutectic and Hypereutectic Al-Si Automotive Alloys, International Journal of Automotive and Mechanical Engineering vol. 20, issue 3, p.10798 – 10807.
- [3] Alaa E. El-Sharkawy, Application of Chemical Engineering Education in Automotive Thermal Management; October 2023 Conference: American Institute of Chemical Engineers (AIChE).
- [4] Volkan Nalçacıoğlu, Meral Bayraktar, aluminium suspension bracket fatigue life prediction for lightweight vehicles; - Volkan Nalçacıoğlu, Meral Bayraktar – December 2019 Conference: 5TH International Conference on Advances in Mechanical Engineeringat: Istanbul, Turkey.
- [5] G. Suresh, M. R. Ramesh, and M. S. Srinath, Surface Engineered Titanium Alloys for Biomedical, Automotive, and Aerospace Applications, 2022, In book: Advances in Processing of Lightweight Metal Alloys and Composites: p.89-102, DOI:10.1007/978-981-19-7146-4_5
- [6] Dr. Fatmagul Tolun, Use of Aluminium Alloys in Automotive Industry, 2019, Conference: International Mediterranean Natural Sciences, Health Sciences and Engineering Congress At: Budapest, Hungary.
- [7] Tommi Hakala, Organizational challenges in (model based) requirements engineering in the automotive industry, DOI: 10.13140/RG.2.2.10995.58405, Thesis, University Of Jyväskylä Faculty Of Information Technology.
- [8] Mile Djurdjevic, Srečko Manasijević, Marija Mihailović and Srečko Stopić, From Bauxite as a Critical Material to the Required Properties of Cast aluminium Alloys for Use in Electro Automotive Parts, *Metals*. 2023; Vol.13, issue 11:1796. DOI: 10.3390/met13111796.
- [9] Musfirah A.H, Jaharah A.G, Magnesium and aluminium Alloys in Automotive Industry, Journal of Applied Sciences Research, 2012, Vol.8. Issue 9: 4865-4875, 2012 ISSN 1819-544X.
- [10] Wen Zhang, Jun Xu, A review -Advanced lightweight materials for Automobiles; material and design, vol.221, 2022.
- [11] Rohith K P, Sajay Rajan E, Harilal H, Kevin Jose, Karthik V, 2018, Shankar. Study and comparison of A356-WC composite and A356 alloy for an off-road vehicle chassis; material today Proceedings, vol.5, issue 11, p. 25649-25656.
- [12] Haruyoshi KUBO, Dr. Hiroyuki MORI, Technical Developments and Recent Trends in Crankshaft Materials; Marine Engineering, 2005, Vol.40, issue 2, p-248-253 DOI: 10.5988/jime.40.2_248.
- [13] Saeed Asiri, Modeling and Analysis of Automotive Engine Crankshaft Made of Composite and Functionally Graded Materials; Advances in Materials Science and Engineering ;2022, Vol.22.DOI: 10.1155/2022/4005368.
- [14] S.N. Kurbet, V.V. Kuppast, Basavaraj Talikot, Material testing and evaluation of crankshafts for structural analysis ; Materials Today: 2021, Proceedings, Vol 34, Part 2, p- 556-562, DOI: 10.1016/j.matpr.2020.03.112.

Information of the authors

Dalavi Amol, PhD, assistant professor, Symbiosis Institute of Technology, Symbiosis International (Deemed) University

e-mail: amol.dalavi@sitpune.edu.in

Sarma Gaurab, master (pursuing), PG student, Symbiosis Institute of Technology, Symbiosis International (Deemed) University

e-mail: gaurabh.sarma.mtech2023@sitpune.edu.in

Modal Aaryaraj, master (pursuing), PG student, Symbiosis Institute of Technology, Symbiosis International (Deemed) University

e-mail: aaryaraj.mondal.mtech2023@sitpune.edu.in

Kukeriya Luv, master (pursuing), PG student, Symbiosis Institute of Technology, Symbiosis International (Deemed) University

e-mail: luv.kucheriya.mtech2023@sitpune.edu.in

Kamble Pranav, master (pursuing), PG student, Symbiosis Institute of Technology, Symbiosis International (Deemed) University

e-mail: pranav.kamble.mtech2023@sitpune.edu.in

Assessing the Impact of Making Adjustments to Design Documentation on the Production Process

Buzauova T.M.^{1*}, Yelubayeva A.N.¹, Toleubayeva Sh.B.²

¹Abylkas Saginov Karaganda Technical University, Karaganda, Kazakhstan

²L.N. Gumilyov Eurasian National University, Astana, Kazakhstan

*corresponding author

Abstract. Today's projects face rapid changes, tight deadlines, and high-quality requirements, emphasizing the importance of effective management and minimizing revisions to design documents. This article conducted a study on the impact of design documentation adjustments on the production process. It considers the main challenges arising from working with foreign design documentation and analyzes the time and resource costs associated with necessary adjustments. Based on data analysis, a mathematical model was developed that incorporates key factors such as the complexity of drawings and the experience level of employees, followed by an analysis of their influence. The results of the regression analysis can be utilized to enhance workflow and task planning within the design department. The article underscores the significance of employee experience and its effect on processing time, along with the necessity of considering task complexity levels.

Keywords: cost analysis, typical errors, adjustments to design documentation.

Introduction

In the context of globalization and intensive technological development, many enterprises engaged in repair and maintenance are faced with the need to use foreign design documentation [1, 2]. This is caused by the operation of imported equipment and machines, for which the original design documents are provided by foreign manufacturers. However, differences in standards and designations can significantly complicate the understanding and effective use of this documentation in the field [3, 4]. In order to bring these documents into compliance with the Unified system of design documentation (ESKD) requirements, significant time is required to search for information and adapt. Therefore, designers are forced to spend more time processing drawings

The aim of this study is to develop and validate a mathematical model that takes into account the degree of drawings complexity and the amount of adjustments to design documentation.

Article [3] discusses the stages of processing and factors influencing the duration of registration in accordance with the Unified system of design documentation (ESKD) requirements [4]. The work examines the main factors [5] that influence the time spent on processing design documentation, such as the drawing complexity, the number of elements, format, employee experience [6], as well as borrowings from other languages. The works [7, 8, 9] present the adaptation of design documentation to the conditions of a specific serial production of the manufacturer.

The study [10] focuses on managing changes in design documentation in engineering, procurement, and construction projects. The authors investigate the causes and consequences of such changes, including their impact on timelines, budgets, and overall work efficiency. Strategies for improvement are proposed, such as integrating project teams, involving contractors early, and enhancing collaboration.

In article [11], engineering changes are considered as a crucial part of a product's life cycle. The significant impact of these changes on productivity, cost, and quality is highlighted. The authors categorize types of changes and discuss management methods to minimize process disruptions. Design changes can trigger a chain reaction of modifications in other aspects of a product or process. The importance of analyzing the propagation of such changes and their influence on design and production is addressed in [12].

Key aspects of managing engineering changes, including their causes, impact on cost and product quality, and risk minimization methods, are described in [13].

Considering modern design approaches in the context of Industry 4.0, including digital technologies, intelligent automation, and process integration, the authors emphasize the shifts in design strategies driven by the adoption of IoT and machine learning [14]. The impact of early versus late design decisions in system development is analyzed in [15], with particular attention to how early changes can reduce costs and time expenditures in the long term.

As a rule, design documentation already takes into account the production technological capabilities of manufacturers, but the conditions of pilot and mass production have significant differences, which leads to the need for partial or even complete processing of design documentation.

1. Research methods

The literature review examined existing studies concerning the impact of various parameters on information processing within the design department. Key works on optimizing process parameters and their influence on quality and productivity were reviewed. To study the impact of different parameters, an experimental plan was developed involving four samples at two different levels of each parameter. Each experiment was repeated three times to ensure result reliability and account for potential variations. A mathematical model based on the physical principles of the processing process was constructed for numerical analysis of parameter influences. This modeling allowed prediction of parameter changes on final outcomes and process optimization. Collected data underwent statistical analysis, including variance analysis and correlation analysis. This approach assessed the statistical significance of each parameter's impact on the processing process and the reliability of the obtained results.

2. Experimental studies

To build a mathematical model from 02/01/2023 to 03/01/2023, design documentation (working drawings) received for repair by the design department of Barusan Makina LLP was selected. The conditional designations presented in the design documentation are illustrated in Figure 1.

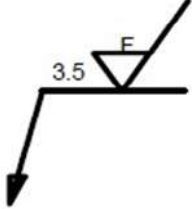

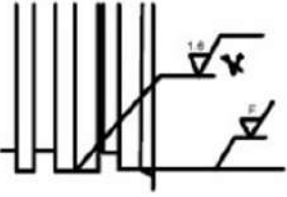
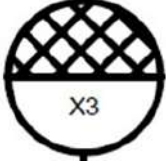
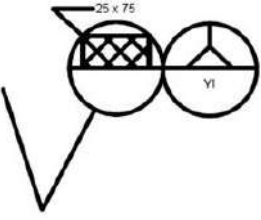
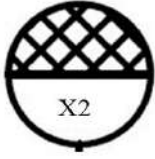
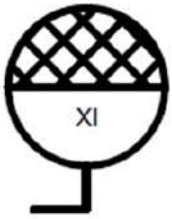
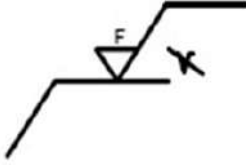
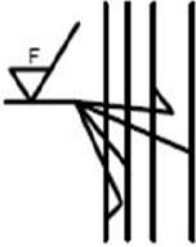
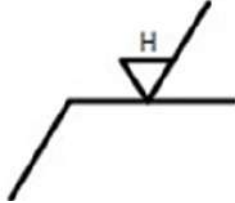
№	Sign	№	Sign
1		6	
2		7	
3		8	
4		9	
5		10	

Fig. 1. - The conditional designations in the design documentation

The independent variables influencing the amount of work performed (y) were selected:

- weighting factor z1, which takes into account the legend, dimensional lines, views and sections, etc.;
- time, taking into account the search for information, hour (Table 1).

Table 1. Initial data for experiment planning

Experiment number	Factors studied		Experimental results		
	Z ₁	Z ₂	y ₁	y ₂	y ₃
1	0,35	0,189	2	3,2	4,5
2	0,152	0,845	1,5	2,1	3
3	0,218	0,517	1	1,4	2,3
4	0,284	1,173	0,45	1,1	1,2

z₁- weight factor: $z_1^- = 0,152, z_1^+ = 0,35$.

z₂- time taking into account information search, hour: $z_2^- = 0,189, z_2^+ = 1,173$.

Table 2. Initial a full factorial experiment planning matrix 2²

Experiment number	Factors studied		Experimental results		
	Z ₁	Z ₂	y ₁	y ₂	y ₃
1	+	-	2	3,2	4,5
2	-	+	1,5	2,1	3
3	-	-	1	1,4	2,3
4	+	+	0,45	1,1	1,2

For each factor, we find the center, the range of variation, and the dependence of the encoded variable xi on the natural Zi according to formulas (1). We formalize the results in the form of a table 3.

$$x_i = \frac{z_i - z_i^0}{\lambda_i}, \tag{1}$$

where z_i^0 - is the center of the plan,
 λ_i - the variation interval.

When encoding, all new variables will take values from -1 to +1, i.e. $x_i \in [-1; +1], i = \overline{1, k}$.

Table 3. Coding of factors

Factors	Upper level z_i^+	Lower level z_i^-	Centre z_i^0	Variation interval λ_i	Dependence of the coded variable on the natural one
Z ₁	0,35	0,152	0,251	0,099	$x_1 = \frac{z_1 - 0,251}{0,099}$
Z ₂	1,173	0,189	0,681	0,492	$x_2 = \frac{z_2 - 0,681}{0,492}$

Using formula (2), we calculate the average sample results for each experiment and enter the calculation results in Table 4:

$$\bar{y}_j = \frac{1}{m} \sum_{i=1}^m y_{ij}, \quad j = \overline{1, n}. \tag{2}$$

Table 4. Planning matrix for processing results

Experiment number	Factors		Interactions x ₁ x ₂	Experimental results			Average results value \bar{y}_j
	x ₁	x ₂		y ₁	y ₂	y ₃	
1	+	-	-	2	3,2	4,5	3,23
2	-	+	-	1,5	2,1	3	2,2
3	-	-	+	1	1,4	2,3	1,57
4	+	+	+	0,45	1,1	1,2	0,92

Calculate the coefficients of the regression equation:

$$b_0 = \frac{1}{4} \sum_{i=1}^4 \bar{y}_j; \quad b_j = \frac{1}{4} \sum_{i=1}^4 x_j \bar{y}_j \tag{3}$$

Table 5. Coefficients of the regression equation

b_0	b_1	b_2	$b_{1,2}$
1,98	0,1	-0,42	0,74

The reproducibility variance $S_{\{y\}}^2$ is determined by the formula (4):

$$S_{\{y\}}^2 = \frac{1}{n} \sum_{j=1}^n S_j^2, \quad (4)$$

where S_j^2 - internal sums of sample variances of experimental results for the j-th experiment ($j=1, \dots, n$). Summing up all the elements, we get:

$$\sum_{j=1}^4 S_j^2 = 2,74255$$

From here:

$$S_{coef.} = \sqrt{\frac{S_{\{y\}}^2}{nm}} \approx 0,24 \quad (5)$$

From the Student's distribution tables [9] for the number of degrees of freedom 8 at the significance level $\alpha = 0,05$ we find $t_{cr.} = 2,31$. Consequently, $t_{cr.} \cdot S_{coef.} = 0,55$. Comparing the obtained value of 0.55 with the coefficients of the regression equation, we see that all the coefficients except b_1, b_2 are greater in absolute value than 0.55, we obtain the regression equation in the encoded variables:

$$y = 1,98 + 0,74x_{1,2} \quad (6)$$

The adequacy of the model is checked using the Fisher criterion. Table value of criterion $F_{tab.} = 4,46$. Calculated value of Fisher's criterion $F_{calc.}$ is determined by the formula (7):

$$F_{calc.} = \frac{S_{ocr.}^2}{S_{\{y\}}^2} \quad (7)$$

Since $F_{calc.} = 1,61 < F_{tab.} = 4,46$, the regression equation (6) is adequate. Let us interpret the resulting model (8):

$$y = 1,98 + 0,74x_{1,2} \quad (8)$$

Having transformed this equation, we finally obtain its form in natural variables:

$$y = 1,98 + 0,74z_1z_2 \quad (9)$$

3. Results and discussion

The constant (1.98) is the basic value of the weighting coefficients and can be interpreted as the minimum time for processing drawings without taking into account the complexity and experience of employees. The coefficient before z_1z_2 (-0.74) shows how strongly the combination of the weighting factor and processing time affects.

Conclusion

The conducted study demonstrated that adjustments to design documentation significantly impact production processes, particularly when working with foreign documentation. Based on experimental data, a mathematical model was developed that considers key factors: the complexity of drawings and the experience level of employees.

The obtained results confirm that:

- employee experience plays a crucial role in reducing the time required to process complex drawings;
- the complexity of design documentation, represented in the model by the weighting coefficient z_1 , directly increases the workload. However, this effect can be mitigated by improving employee qualifications;
- the combination of factors (z_1 and z_2) highlighted the importance of the interaction between the complexity of drawings and the time spent searching for information, allowing for more accurate predictions of time expenditures.

The practical significance of this study lies in the potential application of the developed model to optimize the processing of design documentation, including:

- 1) Reducing the time required for drawing modifications;

- 2 Improving task planning in design departments;
- 3) Enhancing the quality of work by accounting for the interrelation of key factors.

References

- [1] Locmanenko V. V., Kochegarov B.E. Design and construction (basics): Textbook. -Vladivostok: Publishing house of Far Eastern State Technical University, 2004. - P. 28-29.
- [2] Talens Ja. F. The work of the designer. - L.: Mechanical engineering. Leningr. department, 1987. – P. 255.
- [3] Semenova M.K., Rozhkova L.A., Zhanakhutdinov B.G. Making and reading drawings of mechanical engineering products: textbook / Pavlodar, 2006. – P. 358.
- [4] Reshetov A.L., Dubovikova E.P., Usmanova E.A. Working design documentation: textbook / Chelyabinsk: SUSU Publishing Center, 2015. – P. 168.
- [5] Gorodetsky R.S. International mechanical engineering drawing according to ISO standards. Differences from ESKD. Author's personal experience, 2021. - 104 p.
- [6] Borodkin N. N. Development of design documentation: a textbook for students of mechanical engineering and instrument-making specialties / [Borodkin N. N. et al.]; Ministry of Education and Science of the Russian Federation, Federal State budgetary educational institution of higher education prof. Education "Tula State University". - 2nd ed., revised. and revision - Tula: Tula State University Publishing House, 2014. - 197 p.
- [7] Medvedeva S. A. Fundamentals of technical preparation of production / Textbook. - St. Petersburg: St. Petersburg State University ITMO, 2010. – P. 69.
- [8] Typical time standards for the development of design documentation. CODE 13.01.01" (approved by the Federal State Budgetary Institution "Research Institute TSS" of the Ministry of Labor of Russia 03/07/2014 N 003).
- [9] Feoktistova O.A. Normirovanie nauchno-issledovatel'skogo truda: metodologicheskie podxody // Internet journal "SCIENCE,2014,Vol. 5 (24).
- [10] Wang R., Samarasinghe A. S., Skelton L., Bamidele J. O. A Study of Design Change Management for Infrastructure Development Projects in New Zealand. Buildings, 2022, 12(9), 1486; <https://doi.org/10.3390/buildings12091486>
- [11] Ullah I., Tang D., Yin L. Engineering Product and Process Design Changes: A Literature Overview. Procedia CIRP, 2016, Vol.56, P. 25-33. <https://doi.org/10.1016/j.procir.2016.10.010>
- [12] Brahma A., Wynn D. C. Concepts of Change Propagation Analysis in Engineering Design. Research in Engineering Design, 2023, Vol. 34, P. 117–151.
- [13] Engineering Change: An Overview and Perspective on the Literature. Research in Engineering Design, 2011, 22(2):103-124. doi:10.1007/s00163-010-0097-y.
- [14] Jiao R. J., Commuri S., Panchal J., Milisavljevic-Syed J.. Design Engineering in the Age of Industry 4.0. Journal of Mechanical Design, 2021, 143(7):1-44. doi:10.1115/1.4051041.
- [15] James T.Y., Otto K. N., Wood K. L.. Relative Impact of Early Versus Late Design Decisions in Systems Development. Design Science, 2017. doi:10.1017/dsj.2017.13.
- [16] Adler Ju. P., Markova E. V., Granovsky Ju. V. Planning an experiment when searching for optimal conditions. – M.: Nauk, 1971. – P. 282.
- [17] Gmurman V. E. Probability theory and mathematical statistics: textbook. manual for universities. – 10th ed., revised. – M.: Higher School, 2004. – P. 479.

Information of the authors

Buzauova Toty Meirbekovna, c.t.s., associate professor, Abylka Saginov Karaganda Technical University
e-mail: toty_77@mail.ru

Yelubayeva Aimereke Nassyrbaevna, master student, Abylka Saginov Karaganda Technical University
e-mail: aimereke.yelubayeva@mail.ru

Toleubayeva Shamshygaiyn Bolatkyzy, PhD, senior teacher, L.N. Gumilyov Eurasian National University
e-mail: shamshygaiyn@mail.ru

Review on Improvement the Turbine Oxidation and Hot Resistant against Corrosion by Nickel-Based Superalloy

Jasim A.H.¹, Al-Khafaji Z.^{2,3*}, Radhi N.S.⁴

¹Al-Qasim Green University, Babylon, Iraq

²Universiti Kebangsaan Malaysia, Bangi, Selangor, Malaysia

³Imam Ja'afar Al-Sadiq University, Baghdad, Iraq

⁴University of Babylon, Babylon, Iraq

*corresponding author

Abstract. High-temperature oxidation has been an important scientific and technological subject for many years since it is a life-limiting factor in most equipment operating at high temps. Turbine blades used in Iraqi electrical gas power stations frequently require expensive maintenance by traditional processes. These blades are made of nickel superalloys such as IN738LC, where this alloy was used as a substrate material in this research to repair its corroded surfaces. Currently, coatings used for high temps involve thermal barrier coatings (TBC), overlay, and diffusion. The protective properties of diffusion coatings are related to forming SiO₂, Cr₂O₃, and Al₂O₃ scales on the silicide, chromite, or aluminide at high temperatures. Diffusion coatings were first created and are the most often utilized.

Keywords: turbine oxidation, hot resistant against corrosion, superalloy.

Introduction

Protective coatings are a surface layer of materials, either metallic or ceramic or combinations thereof, which can preclude or inhibit the direct interactions between a substrate and a possibly harmful environment [1–5]. Extreme environments may lead to a loss in the material due to the processes of oxidation/corrosion along with a reduction in mechanical characteristics of the substrate because of the deleterious elements that diffuse to the substrate at high-temp protective coatings interact with oxygen in the atmosphere to form dense, adherent oxide scales inhibiting diffusion of the damaging environmental species to the substrate [6]. Protective coatings are generally rich in elements, including Al and Cr, and act as reservoirs for these elements [7–11]. A new scale is formed from this reservoir when the scale is lost due to thermal or mechanical forces. The lifespan of a protective coating is regulated by the capability of the coating to form a protective scale and retain or replace this scale [12].

The efficiency of various alloys exposed to high temps depends on their mechanical resistance and the characteristics of the corrosion/oxidation [13]. The successful applications of those alloy kinds, which are usually referred to as superalloys, are a result of their high long-time creep strength and the stability at the increased temp degrees that are combined with their exceptional resistance against corrosion (which is usually with a protective coating) in an aggressive environment that is encountered throughout the service [14]. The turbine blades have been considered critical components in stationary and aeronautical gas turbines. The engine's efficiency has been tightly associated with the material's ability to withstand higher temperatures. Stimulated with civil air transportation and military aircraft demands after 1955, the cast super alloys substituted initial wrought superalloys. Nickel-base super alloys have matrix γ phase, with a face-centred cubic (FCC) structure, which contains a dispersion of the ordered inter-metallic precipitate particles of kind γ' -Ni₃Al [14].

This review comprehensively evaluates advancements in nickel-based superalloys and coating technologies designed to enhance oxidation resistance, hot corrosion resistance, and mechanical performance in high-temperature turbine applications. By addressing the degradation challenges faced by turbine components in aggressive environments, the review identifies effective protective coatings and strategies to mitigate these issues. The primary aim of this review is to critically analyze existing literature on the development and application of nickel-based superalloys and associated protective coatings. The review focuses on understanding the mechanisms that improve oxidation and hot corrosion resistance while highlighting gaps in the research. It seeks to propose potential avenues for future investigations and provides recommendations to improve turbine component performance and durability under extreme operating conditions.

1. Superalloys

Superalloys have advanced mechanical characteristics at higher temperature degrees that approach melting point and good resistance to high-temperature corrosion. They represent the main material class utilized for high-temperature components. In fact, they are the only materials that are commercially available and retain their corrosion/oxidation-resistant and mechanical characteristics at high temperatures [15].

Superalloys, particularly Nickel-base superalloys, are a metallic material class commonly utilized as technologically significant materials in a variety of industry sectors, such as electric power generation equipment, high-temp chemical vessels, gas turbines, nuclear reactors, and thermal capacitors for the automotive industries [16,17].

Nickel-based superalloys are utilized as materials for the hot components of aero-engines, marine, and land-based gas turbines. Those superalloys have good mechanical characteristics but low resistance to oxidation at high temperatures and aggressive gas environments. To improve their lifetime, the superalloys must be protected from oxidation, heat, and corrosion degradation. An aluminide coating deposited on the Ni-based superalloy provides good corrosion and oxidation resistance to the elements [18].

The term super alloys covers a set of Co-, Ni-, and Fe-based alloys mainly designed for operating in a 500°—1100°C temp range in land-based gas turbines and jet engines. Those alloys are multi-component complex alloys, which, besides Fe, Co, or Ni, include a variety of the W, Nb, Al, Cr, Mo, Ta, Ti, Zr, B, Re, Hf, and C amounts for obtaining the required strength, besides corrosion and oxidation resistance [19].

The present study is fundamentally focused on corrosion and oxidation resistance topics. Serious results drive coating technology development through corrosion and oxidation and the way mechanisms by which they happen. Hot gas turbine components operating in aggressive environments have undergone attack modes collectively called high-temp corrosion, including sulphidising, oxidation, chlorination, carburizing, erosion, and hot corrosion induced by the molten salts. Protective coating was one remedy for the lack of high-temp surface stability for metals and alloys in harsh environments [20].

There are three basic superalloy classes: Ni-base, Co-base, and Fe-base. Superalloys are utilized in numerous high-temp fields, from the gas turbines used in aircraft to industrial and marine applications. Today, the largest consumer of superalloys is aircraft in the gas turbine engine industry [21,22].

1.1. Nickel Base Super Alloy

Ni-base superalloys have excellent efficiency, typically combining ductility, high melting point, high strength (creep, fatigue, and tensile strength), toughness, and resistance against corrosion at greater temperatures. One of the significant applications of Nickel-base superalloys is producing blades and vanes in gas turbines [23]. Figure 1 illustrates a Ni-base superalloy chart that contains different Ni and Fe amounts. The contents of the Chromium are constant at about 18-20 % [24].

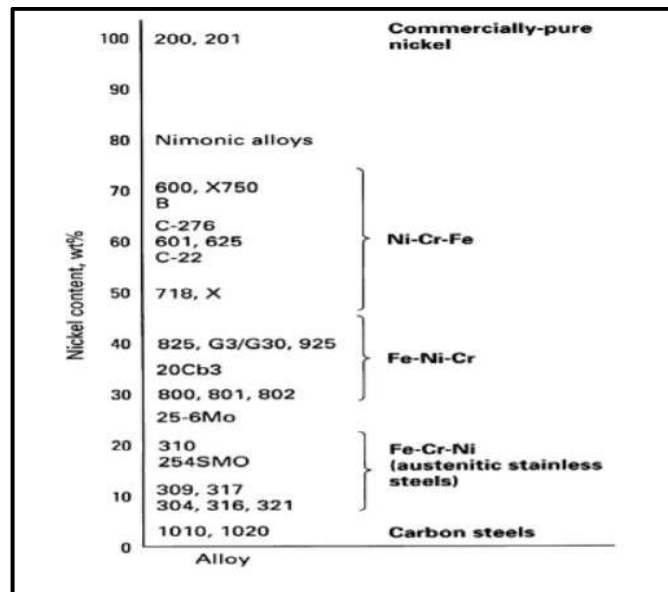


Fig.7. - Chart of Nickel-base super alloy [24].

Ni-base alloys range from simple two-component (i.e., binary) alloy systems to very complicated alloys containing up to 12 alloying elements. The main elements that are related to Ni in commercial alloys consist of Fe, Cr, Mo, and Co; however, as it has been inferred earlier, several other elements have been included in alloy kinds for imparting specific properties, such as required strength, resistant against corrosion, and ductility. For instance, Al added to the Ni alloys introduces the hardening of the precipitation through forming $AlNi_3$, or γ' phase (Figure 2). Additions of Ti and Nb also create the hardening precipitates and inter-metallic. Even non-metallic materials are sometimes added to the Ni alloys. For instance, some of the powder metallurgy alloys can be strengthened through dispersing inert particles like yttria, which are sometimes coupled with precipitation of γ' . The γ phase dissolves up to 4wt. % Al below 400°C. Solubility is increased by increasing temp. However, γ' phase has a narrower phase field, meaning that composition does not significantly depart from the $AlNi_3$. β field is quite broad, indicating that Aluminum concentration may widely depart from the stoichiometric composition $AlNi$ in this phase. In addition, β phase's melting point is considerably higher than pure Nickel's. Those β phase properties are highly preferable in coatings at high temps. The high aluminium concentration helps provide a large aluminium reservoir for protection from oxidation by forming and replenishing the Al_2O_3 scale [15,25,26].

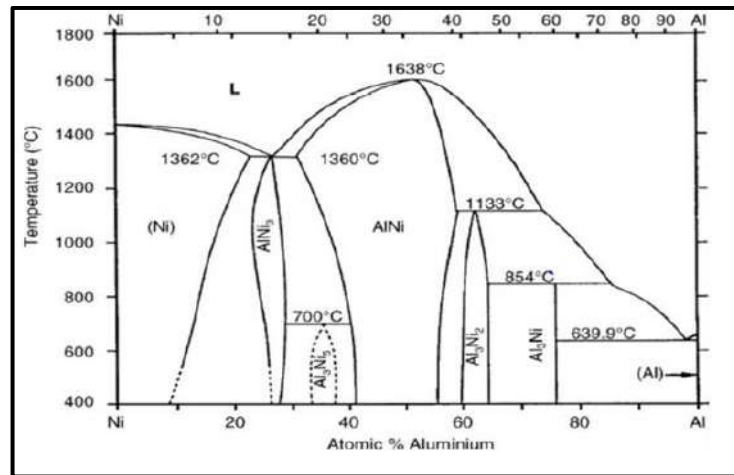


Fig. 8. - Nickel-Aluminum Phase Diagram [27].

1.2. Nickel-Cobalt Base Super Alloy

It can be defined as a unique complex alloy class based on Nickel and Cobalt, exhibiting exceptionally high strength and maintaining strength across a wide range of elevated temps called the 'super alloys.' Some alloy kinds are utilized at over 80% of the melting point in load-bearing applications. Both metals are attractive since their crystal structures and high melting points are amenable to extensive alloying. While Nickel shows an FCC crystal structure, Cobalt is a hexagonal close-packed (HCP) crystal at room temperature. The addition of an alloying element is generally utilized to stabilize the Cobalt in FCC form. Several strengthening mechanisms have produced practical alloys with Nickel and Cobalt [28].

1.3. Nickel-Iron Alloys

Which can be defined as an alloy class (Muzyka & Brown, 1987) that contains 25-60% Ni and 15-60% Fe with austenite FCC structure as a matrix and strengthened with the precipitates with extra advantages from the strengthening of the grain boundary and the solid solution. Those alloys cost less compared to the Nickel and Cobalt base superalloys. Nickel-Iron alloys may be classified into five groups:

- The first group is relatively Iron-rich, with 25-35% Nickel and < 2% Titanium. The strengthening phase is the coherent FCC (the gamma prime) precipitates. Using temp has been limited to 650°C (i.e. 1200°F).
- The second group is rich in Nickel, with more than 40% with an increased contribution from solid solution. The strengths of that alloy group exceed the ones of the affluent group. The commercial members of this alloy group are the Inco X750 and Inconel 901.
- Third group: abundant in Nickel and owes strength to the coherent BCT (i.e., the body-centered tetragonal) (referred to as the double prime gamma) precipitates. Inco706 and Inco718 are examples of this group, with Inco718 representing one of that class's most utilized alloys. Those alloys' temp capability ranges from cryogenic to 650°C (1200 F).
- Fourth group: an iron-rich Fe-Ni-Co alloy with low thermal expansion accomplished by removing Mo and Cr, stabilizing the ferrite in structure. The strength of this group of alloys is derived primarily from the coherent FCC precipitates. Commercial members of this class are Inco 903 and 909, with temp capability limited to 650 °C. Eliminating Cr makes the alloys more susceptible to oxidation and corrosion [24,26,29].
- Fifth group: The distinctive characteristic of this Nickel-rich group is the absence of coherent precipitates. Some group members derive strength from nitrides, carbides, and carbonitrides precipitates. Others (such as N-155 and Hastelloy X) have strengthened their solid-solution capabilities. The latter's application temp for the non-stressed application has been limited to 1093°C [24].

1.4. (Ni-Cr) Phase Diagram

Ni-Cr alloys grew in importance in the 1930s because of the cost of gold. Nickel-chromium alloys have sufficient characteristics to be used with ceramics. The elastic modulus and hardness of Nickel-Chromium alloys provide the ability to utilize a thinner material's cross-section, which provides more space for the porcelain veneering while remaining to offer good resistance. An additional benefit is their linear thermal expansion coefficient, like veneering porcelain. Thermal expansion similarity reduces risks of fractures and cracks throughout the processing. The sensitivity of the Ni could be a concern with those alloys (Figure 3). When choosing those alloys, a patient's sensitivity to Ni must be evaluated thoroughly and carefully. Binary Ni-Cr alloys were recognized early as having high-temperature oxidation resistance. It should be mentioned that a higher Cr is required for a temperature increase. The commercial alloys mainly include 20-30% Cr for the stabilization of a protective Cr scale and always include several minor additions for improving their chemical and mechanical characteristics: typical

'Nichrome' (UNS N-06003, EN/DIN 2.4869) includes 1% Silicon and 0.01–0.04 reactive element. In comparison, the Nimonic 75 includes 0.50% Titanium [30].

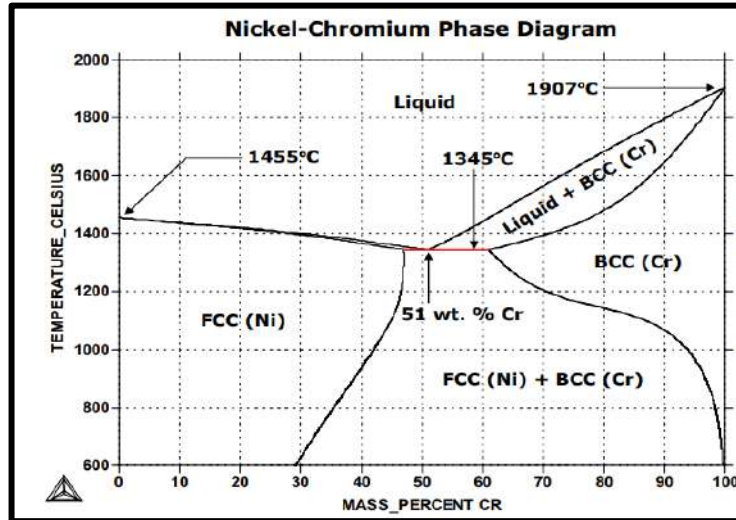


Fig. 9. Ni-Cr Phase Diagram [30].

2. Gas Turbines

Gas turbine blades must satisfy a lifetime of as high as 25000 h. Moreover, super or high-efficiency alloys are utilized to make them because they must withstand various degradation types (like thermo-mechanical fatigue, creep, corrosion, and oxidation) that occur throughout service exposure to aggressive environments. Gas turbine blades for land-based power plants are composed fundamentally of Nickel-base superalloys because Ni can retain the highest retainers at high temperatures compared to others [26,29].

The gas turbine comprises three main sections: the compressor, combustor, and turbine (even though, from the viewpoint of the material, the other main groups of components– i.e., casing, rotor, and auxiliaries – are essential as well). The combustor, turbine, and compressor sections have been represented in Figure 4. The ambient air enters the gas turbine at the inlet of the compressor. While air passes through sequential compression stages (alternating static airfoil rows referred to as the stators or the compressor vanes and rotating airfoils referred to as the compressor blades), temp and pressure increase. At the same time, the work is carried out to decrease the air volume. Then, compressed air passes to the combustion section, where air is heated further by introducing and burning the fuel. In a combustor, there is a volume increase. However, the pressure stays almost constant. Gas produced throughout the combustion expands through the turbine section (a turbine is like a compressor, which includes alternating rotating blades and static vane rows). The expanding gas performs the work because it results in the rotation of turbine blades. This rotation is driving an external generator and the compressor [31].

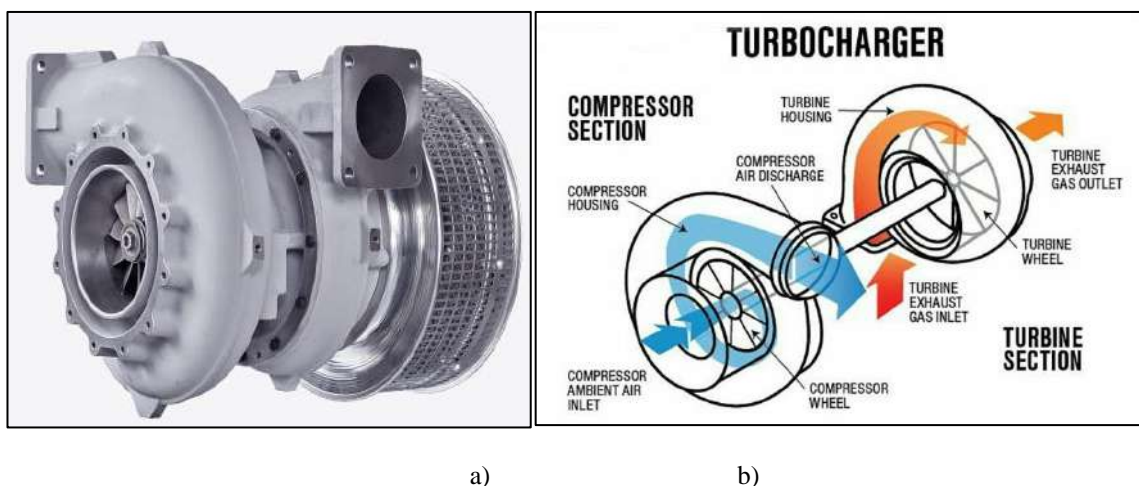


Fig. 10. - a) Turbocharger; b) Path of Exhaust Gases in Turbocharge [29,31].

Ultimately, combusted gas exits the turbine via the exhaust duct. The pressure-volume diagram in Figure 5 characterizes this cycle.

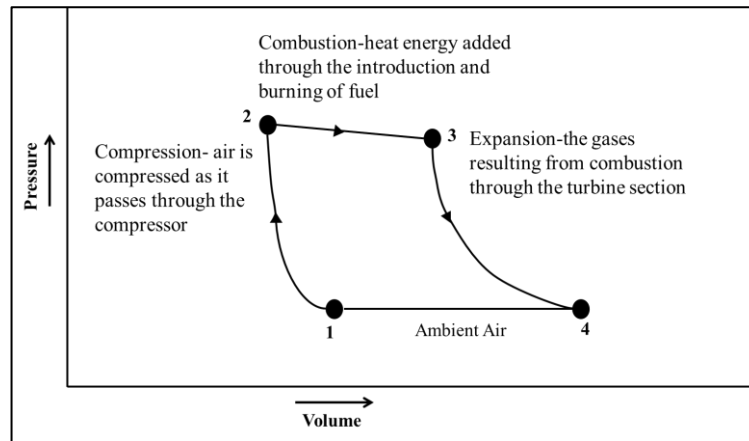


Fig.11. - Schematic pressure-volume diagram for industrial gas turbines utilized with Permission from Siemens Energy [26,29].

In general, the gas turbines use large excess air amounts for the combustion (a large air fraction is utilized as well for cooling combustor), with a typical ratio of air/fuel from approximately 40 to 1 (throughout the take-off) to 100 to 1 (at a speed of cruising) for the aircraft gas turbine engines. Those air-to-fuel ratios correspond to approximately (0.12 to 0.18) mole oxygen fractions in the combustion zone, which is why the gas atmosphere of the combustion is very oxidizing. Sulfur partial pressure in the atmosphere might be shallow, ranging between (10–40) atm and (10–26) atm over a range between (330 to 1230) °C (620 to 2240) °F. Those partial sulfur pressures are well below those required for forming the chromium sulfides, often noticed in the alloys that suffer hot corrosion attacks [32,33].

2.1. Gas Turbines Components

Demanding operating conditions for the gas turbine engines resulted in various coatings designed to protect the superalloy turbine's components from corrosion, resulting from fuel impurities, atmospheric contaminants, and increased temps. To achieve the high-temperature mechanical characteristics that are needed by the modern technology of the gas turbine, superalloys had to sacrifice hot resistance against corrosion and oxidation, which was inherent in the previously utilized heat resistance alloys with higher Chromium contents. As a result, the coatings are dependent upon for protecting the components of the superalloy, like the vanes and turbine blades, from environmental attacks. Developing and applying high-temp coatings enhanced efficiency and fuel economy in marine, aircraft, and land-based industrial turbines [34–36].

Throughout the 1st quarter of the 20th century, Chromium has been added to Co, Ni, and Fe in various amounts. The resultant products had remarkable resistance to the atmospheric (i.e., the moisture) environments and to oxidation at high degrees. By World War II, some of those alloys, which include other alloying elements, became used for applications like dental prostheses, resistance wires, cutlery, and steam turbine and furnace components. With the development of gas turbine engines throughout WWII, the need for materials resistant to corrosion to operate in the demanding conditions of the mechanical load at high temps has become apparent. At this point, the fledgling superalloy industry had begun expanding. Through the modification of stainless steels, higher levels of strength have been accomplished without a need for the particular strengthening phases at high temps. Phases like η (a Ni-Ti compound) or γ (a Ni-Al compound) were presented to Ni-Cr alloy families right before the war for producing high strength at high degrees. Increased temp degrees have forced the alloy developers to include those phases (γ & η) in Fe-base alloys to take properties of high-temp strength beyond the ones of modified stainless steels like the 19-9-DL. Alloys were first produced in Germany, and, following the modification, they reached the US as A286 or V57 and have remained used until now [37].

Nevertheless, the need for creep-rupture strength is continuously increasing. A part of this need has been met in the early years through the adaptation of Co-base corrosion-resistant alloy (i.e., the Vitallium) to be used in the superchargers of aircraft engines and, after that, in airfoils in hot sections of the gas turbines. Similar co-based superalloys remain used today. Nonetheless, the requirements of the creep-rupture for the applications of the aircraft gas turbines soon out-stripped the ones of Fe-Ni-base superalloys and Co-base superalloys, which is why Ni-base superalloys, which have been modified to provide more hardening phase γ , has become increasingly utilized [37].

2.2. Superalloys Used for Gas Turbine

The successful utilization of Ni-based superalloys in both the land-based and aero-gas turbine industries is a testament to the possible commercialization of new materials, mainly intermetallic. Power generation and air travel would not be possible as we know them if not for the superalloys developed during the last 60 years [38].

- *Inconel alloy 706* can be defined as a precipitation-hardenable alloy with properties like alloy 718, except that it has highly enhanced machinability. It has a sufficient level of resistance to corrosion and oxidation over a wide variety of temperature degrees and environments. Like alloy 718, 706 has excellent resistance to post-weld

strain-age cracking. Applications often include gas turbine components and other parts, which must have high strength, good weldability, and machinability.

- *Inconel 718* is a high-strength, age-hardenable alloy that is proper for the service at temp degrees from 253°C (i.e., 423°F) to 704°C (i.e., 1300°F). Inconel 718 has high fatigue strength and shows a high stress-rupture strength up to a temp of 704°C (1300°F) and oxidation resistance of as high as 982°C (i.e., 1800°F). It also offers good resistance against corrosion in many different environments. The exceptional property of the Inconel 718 is that it has a slow response to age hardening, which allows the material to be annealed and welded without any spontaneous hardening unless it has slowly cooled. The Inconel 718 may as well be repair-welded in entirely aged conditions. The typical applications represent jet engine components, pump parts and bodies, thrust reversers and rocket motors, and spacecraft [39].

- *Inconel X750* is an age-hardenable Ni–Cr–Fe alloy utilized because of its oxidation, resistance against corrosion, and high creep-rupture strength of 816°C (i.e., 1500°F). This alloy has been made age-hardenable by adding Al, Nb, and Ti, combined with the Ni, throughout the suitable heat treatment for forming the inter-metallic compound Ni₃(Al, Ti). X750, developed for jet engines and gas turbines, was adopted for many other utilizations due to its favorable characteristics. The exceptional relaxation resistance has made Inconel X750 suitable for springs operating at temps that might reach as high as 649°C (i.e., 1200°F). In addition, this material shows good ductility and strength at temps as low as 253°C (423°F). Inconel X750 also shows high resistance to the chloride-ion stress-corrosion cracking even in age-hardened conditions. The usual applications include gas-turbine parts (i.e., industrial and aviation), nuclear reactors, springs (i.e., steam service), vacuum envelopes, bolts, extrusion dies, heat-treating fixtures, bellows, aircraft sheets, and forming tools.

- *Inconel 617* can be defined as a solid-solution-strengthened alloy containing Co. Its perfect combination of oxidation resistance and high-temperature strength makes it a beneficial material for gas turbine aircraft engines and other areas that involve exposure to extreme temperatures, like the pressure vessels and steam generator tubing for the advanced high-temperature gas-cooled nuclear reactor [40].

- *Inconel 738*: Alloy IN-738 is a highly significant nickel-based superalloy. It is made by melting and casting it in a vacuum, and it can be hardened by precipitation. This alloy has exceptional strength against creep-rupture at high temps, and it also has better resistance to hot corrosion compared to many other superalloys with lower chromium levels. This design aims to provide the gas turbine industry with an alloy that has excellent resistance to deformation at temps up to 980°C while also being capable of enduring prolonged exposure to the high temps and corrosive conditions often seen in engines. Alloy IN-738 demonstrates improved tensile qualities compared to increased temp stress-rupture and similar capabilities to Alloy 713C, which is commonly used. Additionally, it has much greater resistance to sulfidation. There are two variations of Alloy IN-738: IN-738HC, which has a high carbon content, and IN-738LC, which has a low carbon content [39].

The hot corrosion attacks are decreased with the temp decrease to lower than 927 °C (i.e. 1700°F). At temps of less than 760°C (i.e., 1400°F), the mechanism of the hot corrosion is changed under specific conditions. The attack can start dramatically increasing with the decrease in the degree of temp; however, after that, it has decreased again with the decrease of temps to less than approximately 649°C (1200°F). In such a regime of a lower degree of temp, the province of the land-based power gas turbines, attacks are resisted optimally by producing chromium oxide on the surface. As a result, the alloys for that application and region include the IN738 designed particularly for having higher levels of the Cr in some of the faces back up higher than 20pct. (IN939 is one of the alloys in this latter category.) Other alloys have been devised to provide optimal resistance to hot corrosion in higher-temp services. Examples of those alloys are IN792 [41].

3. High-Temp Oxidation

In engineering applications, most metals and alloys have lower thermodynamic stability than their oxides, so they react with the environment to reduce their free energy. Usually, such a reaction forms a solid oxide layer on the surface, separating metal from the environment. The rate and reaction path of specific metal/gas reactions are, in turn, regulated by several parameters, like temp, gas pressure, surface morphology, and alloy composition. [42].

Generally, there are three stages of the oxidation:

- (i) The transient stage is identified by the simultaneous and temporary formation of oxide of each one of the active elements;

- (ii) Steady-state stage, which is identified by the development of a protective oxide scale;

- (iii) The break-away stage is identified by the accelerated attacks [43].

Oxidation resistance depends upon forming a defect-free, adherent oxide scale on the alloy surface. Generally, changes to protect oxidizers and exclusively protective oxides occur at higher temps and longer times. These changes involve attaining a complete external protective oxide scale, which is a steady state. The steady-state period or the time to break-away duration has been considered the most critical factor in the practical oxidation behavior. At this step, the overall reaction is regulated by the reactants' solid-state diffusion through the oxide scale, which reduces the reaction rate with the increase of time, which is a parabolic rate [44].

Thermodynamically, the oxide formation will only occur when the ambient oxygen pressure is larger than the oxide dissociation pressure in equilibrium with metal. In the case where the metals or the alloys are employed in

high-temp oxidizing environments, they are protected by oxide scale, forming and acting like a partial barrier to continuing environmental attacks, as:

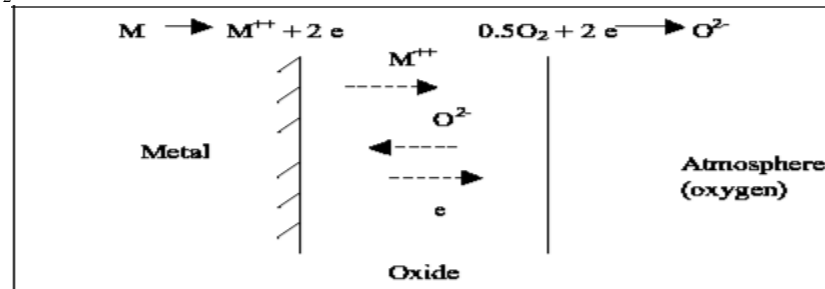


Fig. 12. - The schematic diagram for oxide scale growth in high-temperature oxidation process [44].

The oxide layer grows on metal by transporting ions, electrons, molecules, or atoms through the scale, as shown in Figure 6. The scale's capability for protecting underlying metal is acting as a mechanical barrier, and its mechanical integrity ceases inside it. Further growth behavior of the oxide scale depends upon transport mechanisms through the scale. The transport of metal ions outwards to the oxide/gas interface gives an outward-growing oxide, while the inward transport of oxygen ions gives inward growth of the oxide. In both cases, the transport rates will determine the growth rate of the oxide scale. The oxide's transport mechanisms may be divided into short-circuit and solid-state diffusion [45]. Typically, the alloys or the metals undergo oxidation at high degrees under an oxygen-containing atmosphere, which results in one oxide compound or more at the interface of gas/substrate. Such chemical species' growth can protect substrate material if this compound keeps providing a homogeneous, adherent, stable, and dense oxide layer to the surface. At the same time, it results in the reduction of oxidizing element transport to scale. Only a few oxide kinds show such properties at high temps, where all the diffusion processes are more activated.

Aluminum oxide (Al_2O_3), chromium oxide (Cr_2O_3), and silicon oxide (SiO_2) show these characteristics and possess specificities concerning the range of temp. Due to their complexity, the growth of such oxides has been of great interest. Essentially, several of the diffusion processes have been involved, in other words, diffusion in the volume and grain boundaries and anionic and cationic processes of diffusion, which may be revealed, for example, through the SIMS measurement.

The alloying elements' effect on the substrate may promote (Ti) or slow down (Zr, Y, Hf, and La) the formation of the oxide. Initial surface preparation also has an important impact on the formation of the oxide scale or, in other words, on developing the alumina layer. The chromium scale makes a good barrier that is hot-resistant against corrosion in temperatures between 950°C and 1000°C. Nevertheless, according to partial O_2 pressure at high temps, the vapor of the Chromium could be formed and volatilized. At the same time, CrO_3 was developed for high O_2 partial pressure (p_{O_2}), which resulted in the protective layer of the Cr_2O_3 being thinned down. Silica is relatively stable at high temps; however, it forms a glassy structure that is not sufficiently resistant to thermal shock. Numerous sequences of phase transformation that were impaired by starting the chemical composition of the raw material were reported in the literature. Such polymorphic transformation is also impaired by volume contraction in oxide de scale, which might be critical in establishing a protective layer of the oxide [46].

4. Hot Corrosion

Corrosion of the materials, including Nickel and Cobalt base super alloys induced by the molten salts in oxidizing gas at increased temperature, has been referred to as 'hot corrosion' to distinguish it from conventional low-temp corrosion. It results from accelerated oxidation at temperatures that are usually in the range of 700°C to 925°C, where the alloys and the metals get covered by contaminant salt films. Salts in the vapor phase are benign in general. The range of the temp within which the hot corrosion takes place is highly dependent upon gas constituents and salt chemistry, in addition to the composition of the alloy. Such corrosion was noticed in the petrochemical process equipment, coal gasifiers, boilers, internal combustion engine exhaust systems, gas turbine engines on aircraft, and industrial and marine applications. The partial pressures and temps of sulfur and oxygen in some industrial operations, even though gases separately, have no considerable corrosive effect, the overall environment in those operations results in forming molten and solid salts, which play a role in the corrosion [47,48].

Kind I hot corrosion, or high-temp corrosion, occurs at temps 800° and 950°C (i.e., 1470° and 1740°F). It has been believed that the deposit of the molten sodium sulfate is necessary to initiate the hot corrosion attacks. Usually, the morphology of Kind I hot corrosion is identified with a thick, porous oxide layer with an underlying alloy matrix depleted in Cr, which is succeeded by the internal Cr-rich sulfides. Kind II hot corrosion or low-temp generally happens in a temp range between 670° and 750°C (i.e., 1238° and 1382°F). Kind II hot corrosion has been identified through the pitting attack with little or no internal attacks underneath the pit. Co-base alloys are more susceptible to Kind II hot corrosion involving 100µm [28]. The process of hot corrosion degradation of superalloys typically includes two stages :(a) a stage of initiation, throughout which alloys are behaving much like they would have

behaved if there were no deposits, and (b) a stage of the propagation, in which deposit results in protective characteristics of oxide scales to be considerably different from the ones [49]. The low-temp hot corrosion mechanism includes forming base metal sulfates, which require a specific partial sulfur trioxide pressure to stabilize. Those sulfates react with the alkali metal sulfates to form compounds with low melting points, preventing the formation of a protective oxide [20].

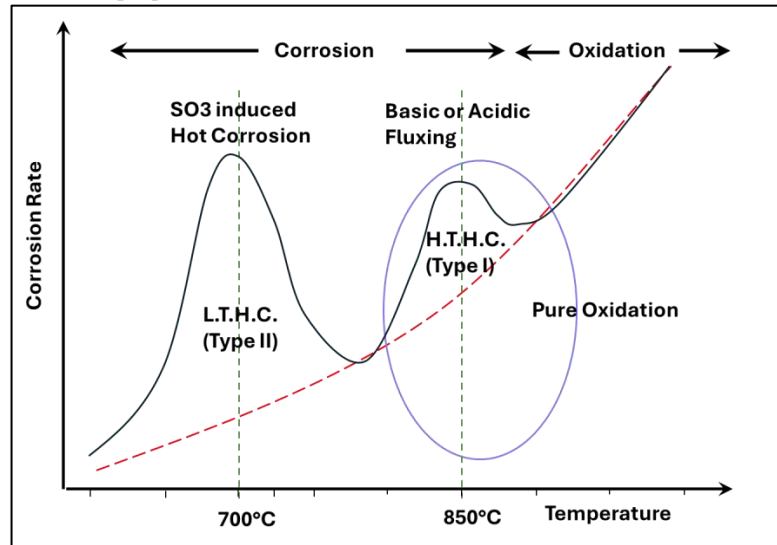
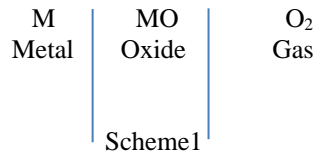


Fig. 13. - Corrosion rate vs. temp [20].

5. Oxidation Law

As can be seen from Scheme 1, the product of the solid reaction MO will separate the two reactants if we consider reaction $M(s) + 1/2 O_2(g) = MO(s)$.



For the reaction to proceed further, one reactant or both must penetrate the scale; in other words, either one of the metals has to be transported via oxide to the interface of oxide–gas. The oxygen must be transported to the oxide–metal interface and then reacted there due to mechanisms through which reactants could penetrate the oxide layer, which has been considered a significant part of the mechanism through which high-temp oxidation occurs. In particular, the same can be applied to the sulfide formation and growth and other similar products of the reaction. The p-B ratio is defined as:

$$R_{PBB} = \frac{V_{oxide}}{n \cdot V_{metal}} = \frac{M_{oxide} \cdot \rho_{metal}}{M_{metal} \cdot \rho_{oxide}} \tag{2}$$

where R_{PB} – Pilling – Bedworth ratio
 n- number of atoms of metal per molecule of the oxide
 M- atomic or molecular mass
 ρ – density
 V- Molar volume

According to the measurements, the connection below may be shown:

- R_{PB} less than 1: the layer of oxide coating is too thin, possibly broken, and does not provide any protective effects (e.g., Mg)
- R_{PB} higher than 2: oxide coating chips off and does not provide any protective effects (for instance, Fe)
- $2 > R_{PB} > 1$: oxide coating is passivating and provides a protective impact towards additional surface oxidations, such as Al, Ti, and Cr-containing steel) [50].

6. Coatings for High-Temp Applications

Most coating kinds depend upon isolation with a "barrier" of a part to be protected from environmental conditions. This barrier's role is to minimize the liquid or gaseous species' diffusion toward a component and, on the other hand, prevent the elemental diffusion from alloy toward the external surface where they would be reacting.

Most generally, a barrier is dynamic in that it is formed through coating interaction with an oxidizing environment, which is usually the coating case, whether ceramic or metallic, which results in the formation of oxides like Chromium, alumina, and silica. There is a wide range of available coating methods, and selecting the optimal process depends on functional requirements (such as substrate metallurgy, shape, and size), coating material's adaptability to the intended method, needed adhesion level, and equipment availability and cost. In general, all of the processes of the diffusion coating operations are formed due to five distinctly similar processing steps:

1. Generating vapor that contains Cr, Si, and Al.
2. Transporting that vapor to the component.
3. Vapor reaction with the substrate alloy element for the formation of various inter-metallic.
4. Diffusion in the alloy.
5. Post-processing heat treatment is used to obtain the desired composition and microstructure.

Several different manufacturing methods have been developed for diffusion coatings. Figure 8 gives an overview of the most important procedures [51].

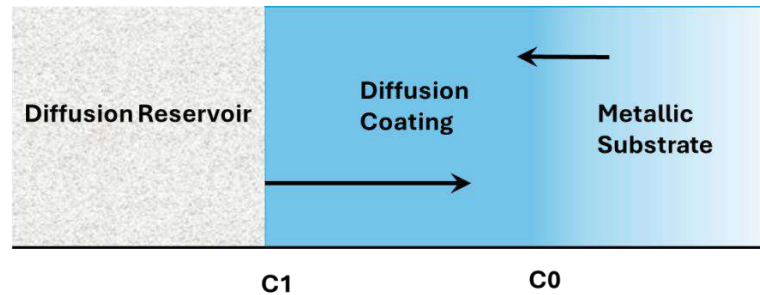


Fig. 14. - Diffusion coating manufacturing principle [51].

6.1. Pack Cementation

Pack cementation is an in situ CVD (for example, chemical vapor deposition) batch process that was utilized for producing oxidation—and corrosion-resistant coatings on inexpensive or otherwise inadequate substrates for more than 75 years [52,53].

During this procedure, the component that must be coated is submerged in a solution that contains the necessary coating material and a halide compound acting as a catalyst. The mixture and the substrate are enclosed in a sealed or partially sealed vessel and heated in a vacuum or pure argon gas at a designated temp. The halides of the material are conveyed to the surface of the material to be covered by evaporation with consistent heating. During this process, a contact occurs between the coated portion and the coating material. Novel phases or solid solutions are created inside the coating region. The significant parameters that affect the pack cementation process are [54]:

1. Chemical composition of the substrate;
2. Powder purity was utilized;
3. Time and Temp utilized in the cementation process;
4. The substrate surface state.

Figure 9 depicts the key stages of the pack cementation process. Metal halides are generated and conveyed via the gaseous phase to the component's surface for coating. At the surface, the halide reacts with the specimen and dissociates into the metal and the halogen anion.

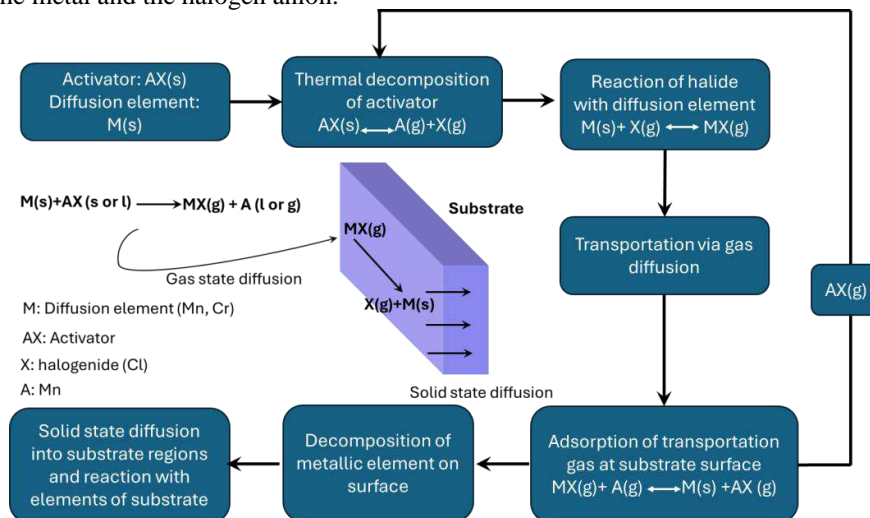


Fig. 15. - Major processes throughout back cementation operation [51].

Pack cementation can be defined as a modified vapor deposition operation performed in a closed container at increased temp degrees (typically, 1000°C). Usually, a pack includes substrates that are to be coated and inert filler powders. The master alloy is rich in elements that require deposition and activator salts (NH₄Cl, NaCl, NaF, or a combination). Activator salt reacts with master all to generate the volatile metallic halides, diffusing through materials of the porous filler (typically, α -alumina) to the surface of the subs trade. At the surface of the substrate, metallic halide vapors participate in many potential reactions [55]. The metal atom undergoes diffusion into the surface zone of the substrate. The coating development is similar to diffusion couples, and the interdiffusion is driven by the activity or concentration gradient between the environment (containing diffusing materials like Al) and the component's surface [56]. Upon being released at the surface, the halogen reacts with fresh metal atoms derived from the powder, sustaining the process in a continual manner. Halogens, such as chlorine and fluorine (although bromine or iodine may also be utilized), act as activators.

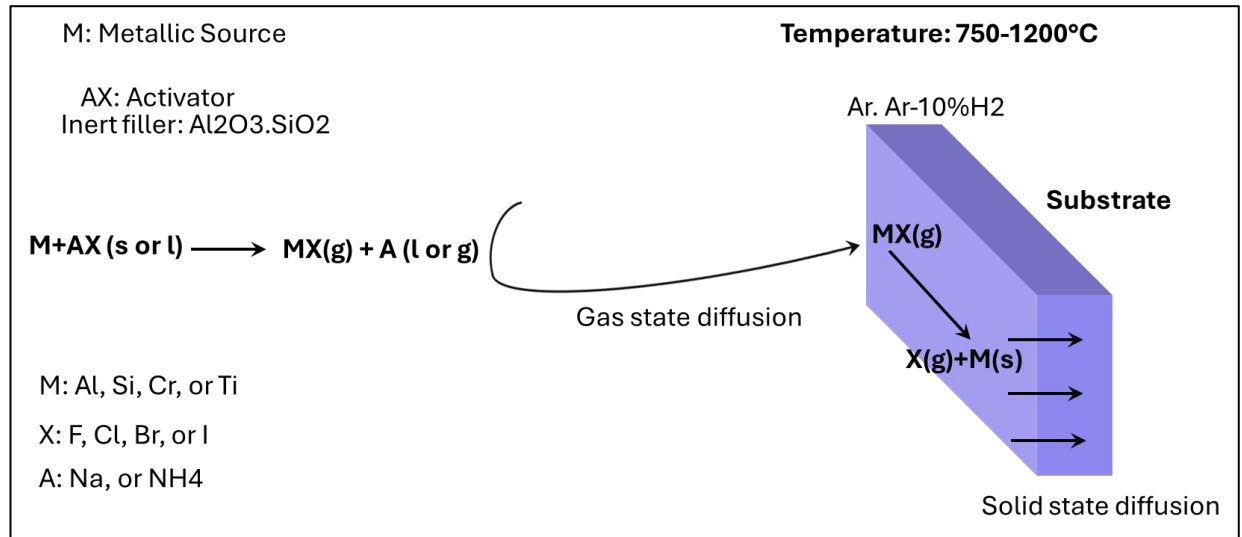


Fig. 16. - The main chemical reactions involved in the pack cementation process [57].

The pack cementation process is usually utilized to form diffusion coating coatings, which improve the oxidation resistance of various heat-resistant samples.

6.2. Physical Vapor Deposition (PVD)

Three main kinds of PVD processes involve atom-by-atom transfer mode. PVD is a group of processes where the material is converted into the vapor phase in a vacuum chamber and condensed on the surface of the substrate as a very thin film. PVD may be utilized to apply many different coating materials. Those processes include evaporation of the electron beam (EB) and sputtering, which can be combined with ion plating [58].

EB PVD: Commercial electrons beam physical vapor deposition (EB PVD) coatings are created in a vacuum environment, 10^{-2} - 10^{-4} pa, with a deposition rate usually higher than $25\mu\text{m min}^{-1}$. Generally, the components are pre-heated in a vacuum at 800° -1100°C and rotated inside the vacuum chamber during deposition. The overlay coating thickness can be much thicker, 150-300 μm , or other diffusion coatings [59].

6.3. Chemical Vapor Deposition CVD

In the CVD processes (Figure 11), the AlCl₃ is produced outside the reactor before being sent to the reaction vessel, allowing accurate activity and flow rate control due to uniform and consistent layers of aluminide being created. A particular advantage of this system is coating cleanliness, which yields enhanced resistance to oxidation and the fact that it can pass through, besides hollow components, like the turbine blades that have cooling channels so that the external and internal surfaces may be diffusion coated. On the other hand, pack aluminizing may result in causing the blockage of the cooling holes to be blocked with the particles of the diluent, requiring removal following the processing.

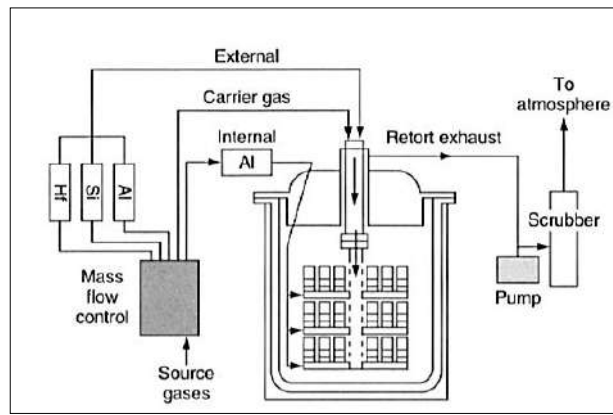


Fig. 17. - Diagram of low-activity co-deposition of Hf, Al, and Si in the CVD coatings [60].

Additional CVD advantage is that the chemistry may be regulated carefully, which enables the incorporation of additional elements like Al, Y, Hf, and Si into coating at an accurate level [60].

6.4. Plasma Thermal Spraying

Thermal plasma spraying can be defined as a procedure in which powder feedstock is injected in a high-temp plasma jet where finely divided non-metallic and metallic materials undergo deposition in semi-molten or molten states on the prepared substrate. It was utilized as one of the economical and sufficient methods for producing ceramic coatings on metallic substrates. Bulk powder production from spheroidization was fundamentally motivated by a strong drive for high-efficiency materials and the growing need for new materials processing technologies. The particles that are injected into the zone of the plasma will experience extreme rates of heating and temp degrees of up to 10000 K. Because the plasma spraying has been defined as a pretty high-temp process, injected particles with varying size distributions will melt, yielding aerosol of the molten droplets. Particles higher than the critical size range could only experience partial melting.

In contrast, small particles could have a vaporized material layer surrounding liquid droplet, so the plasma processing of the material with stringent requirements must be regulated carefully to produce the needed results because plasma technology's full potential depends on our capability to achieve an optimum match between process requirements and properties of the used plasma source and reactor designs. The plasma process has evolved into a highly flexible coating system that can be applied to many materials. One of the primary plasmas spraying applications is protecting components of aircraft engines by depositing the aerospace coating like the alumina or zirconium/ magnesium thermal barriers on the metal substrates. Lately, it has also been utilized as one of the tools for processing bio-ceramic materials like hydroxyl-apatite (HA) as both powders and coatings [14]. In the spray process, a plasma jet melts, coating feedstock in a powder form. Plasma is produced in a plasma gun. The typical gun's internal details have been illustrated in Figure 12. The process details can be summarized as follows:

A direct current between the stick-kind copper cathode (i.e., negative polarity) with the thoriated tungsten tip located along the axis of the gun and the water-cooled copper anode (i.e., positive polarity) generates electrical arcs (Figure 13). Being rigid, the thoriated tungsten tip decreases cathode wear [61].

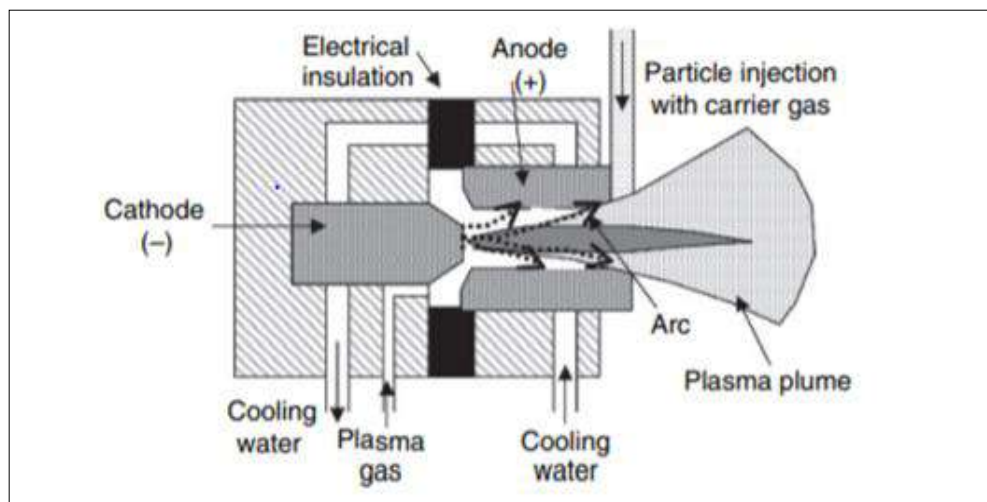


Fig. 18. - Internal Metco Plasma gun characteristics [14].

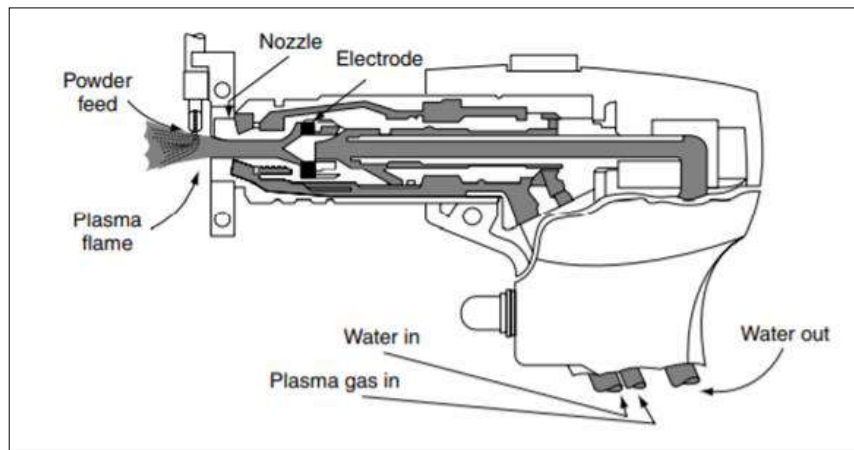


Fig. 19. - Diagram of the Plasma Spray nozzle and internal processes [14].

6.5. Slurry Coating

The slurry-based diffusion coating can be found commercially; they offer similar chemistries to those in the traditional pack cementation aluminide coating. In the slurry cementation, halide activator and coating materials are blended as a particle-loaded paint system or slurry, using a water-base emulsion or an organic binder. The system slurry/paint may be applied as part to be coated by spraying, dipping, or almost at the room's temp. After that, the slurry spray is cured onto part via low-temp thermal treatment, usually about 200°C. cured prediffusion coatings could contain only Al+Cr, Al+Al₂O₃, Si+Cr and Al+Si depending upon final service conditions. Then, the pre-coated parts are heated in the furnace to allow the Aluminum diffusion (Silicon and other additions). This step's hold temp ranges between 650° and 1100°C, according to the substrate that will be coated and its final applications. Temp is selected such that the coating material contained in the slurry reacts and inter-diffuses with a substrate to form the final inter-metallic coating [48,62]. The chemical composition evolution of slurries follows industrial normalization as well. Paints and slurries can be applied easily; nevertheless, they have not been widespread in aero domains except for repairs. In the present day, due to process flexibility, the tailoring of elements must be performed to provide a sufficient response concerning several application domains, such as aeronautics [63].

7. Summary of Literature Reviewed

Table 2.1. Summary of Literature Reviewed about increasing hot corrosion resistance and oxidation of Inconel alloys by coating

Ref.	Coating methods	Powder	Condition of hot corrosion	Temp °C	The most important conclusions
[64]	Thermal barrier coating	Ni-Cr-Al-Y	NaCl+V ₂ O ₅	1000	had studied hot corrosion in the components of gas turbines and concluded that hot corrosion represents a mechanism of failure that causes high concerns in the engines of gas turbines.
[65]	Pack cementation	Al-Cr	-	1100	Those coating kinds have very good resistance to high-temp oxidation, and their adequate temp of antioxidation may be increased to 1100° C. The phases of NiAl and Ni ₃ Al have been considered the main constituents of the aluminized coating
[66]	arc ion plating (AIP)	NiCoCrAlY	75 wt. % Na ₂ SO ₄ + 25 wt. % K ₂ SO ₄	900	Adding B and Si might enhance the coatings' resistance to hot corrosion by promoting the growth of the continuous and dense layer of α-Al ₂ O ₃ in the initial stage and enhancing the oxide scale adherence to coatings in successive processes of hot corrosion.
[67]	HVOF sprayed	NiCrBSi	Na ₂ SO ₄ -60% V ₂ O ₅	900	Formations of oxides in addition to Ni, Cr, or Co could result in all coatings' resistance to hot corrosion.
[68]	Diffusion coating	Ni-30Cr-8Al-0.5Y	75wt.% Na ₂ SO ₄ +25wt.% K ₂ SO ₄ /NaCl	900	The coating of the aluminized NiCrAlY had shown considerably superior resistance to hot corrosion in the presence of 75wt. % Na ₂ SO ₄ + K ₂ SO ₄ /NaCl films due to forming a protective and continuous scale of Al ₂ O ₃ .

Ref.	Coating methods	Powder	Condition of hot corrosion	Temp °C	The most important conclusions
[69]	pack cementation process	Al-Cr-Y	Na ₂ SO ₄ , NaCl	900	The oxidation kinetics for the uncoated IN600 alloy in the air, CO ₂ , and water vapor are almost parabolic. The values of the constant of the parabolic rate (k_p) that have been obtained at 900°C in the air, CO ₂ , and water vapor were 2.68×10^{-7} and 4.16×10^{-7} mg ² /cm ⁴ , respectively
[70]	pack cementation process	CoCrAlY	Na ₂ SO ₄	1150	the Pt+Hf-modified $\gamma'+\gamma$ and $\gamma+\beta$ -CoCrAlY coating showed the improved performance of the KindI hot corrosion compared to Platinum-modified β .
[71]	Slurry	A spray gun was applied to the Al slurry	-		Preliminary testing studies indicate that Al slurry coatings can replace Cd in aircraft components.
[72]	Slurry	Al-Al ₂ O ₃	-		Results have shown that a coated layer is created by dissolving Ni in the liquid Al at Al temperature, forming a layer of the intermetallic compound. The coated layer's main phase is Ni ₂ Al ₃ , which includes small amounts of AlCr ₂ and NiAl ₃ . AlCr ₂ mainly exists in the layer neighboring the top surface.
Ref.	Coating methods	Powder	Condition of hot corrosion	Temp °C	The most important conclusions
[73]	plasma spray	YSZ	V ₂ O ₅ and Na ₂ SO ₄	1050	Based on experimental results, the nano-structured coating showed more sufficient hot resistance against corrosion and oxidation resistance than the conventional coating.
[74]	arc ion plating	NiCrAlYSi	Na ₂ SO ₄ and NaCl	1173 k	After the NiCrAlYSi has coated K40S, a protective scale of a-Al ₂ O ₃ has been created on that coating
[75]	pack cementation process	NiAl	Na ₂ SO ₄ + NaCl	1173 K	The presence of Cobalt in a coating might promote the establishment of a protective scale of Al ₂ O ₃ on the coating and restrain internal sulfur diffusion in coatings.
[76]	Air plasma spray (APS), Low-pressure plasma spray (LPPS), and (EBPVD),		Chloride and vanadium	900 and 850	Because of the low chromium content and high tungsten content, CM 247LC is easily corroded. In comparison to IN738LC
[77]	-	-	NaCl + Na ₂ SO ₄	950	It has been discovered that the rate of sulfide corrosion is regulated with the process of high-temp Ni alloy dilution within liquid Ni sulfide eutectic
[78]	-	-	NaCl V ₂ O ₅ +Na ₂ SO ₄	550, 650	Salt mix coatings of NaCl, V ₂ O ₅ , and Na ₂ SO ₄ led to relatively slow oxidations at both temperatures. Increased salt coating thickness has been found to enhance hot corrosion rates.
[79]	Plasma	YSZ	Na ₂ SO ₄ and V ₂ O ₅	1040°C	Microstructural studies conducted with the SEM have shown that plasma coatings are sound and have no large pores or interfacial cracks.
[80]	Slurry	MoSi ₂	-	-	Max coating thickness of 60 μ m was achieved for MoSi ₂ and 5 μ m for Mo ₅ Si ₃ coating.

Ref.	Coating methods	Powder	Condition of hot corrosion	Temp °C	The most important conclusions
[81]	thermal spray	Ni-Cr	(Na ₂ SO ₄ +K ₂ SO ₄)	900	This study summarized the characteristics of the Chrome carbide nickel chrome coating types deposited by various approaches and the hot corrosion behavior of the Nano-structured as well as conventional coating types in molten salt environments.
[82]	pack cementation process	Al-Si-Y	-	-	The optimal resistance to the oxidations after 50hr at 5hrs for every one of the cycles for the addition of the Y ₂ O ₃ and yttria-doped silicon-modified aluminide hardness is approximately three times higher compared to the hardness of the uncoated alloys following the cyclic oxidation in the air at 900 °C for 50 hrs.
[83]			600 °C	40 KNO ₃ –60 NaNO ₃ (wt%).	The mass gain and oxidation rate have been increased, and the correlation between mass gain and time has been near the parabolic oxidation law.
[84]	Slurry	Al	-	-	Coating the aluminide could considerably improve the resistance to oxidation by forming a very thin scale of Al ₂ O ₃ .

Conclusion

It is apparent from the literature review summary that numerous studies have been conducted on nickel-base superalloy following thermal spray and plasma spray processes. Several works have focused on applying thermal barrier coatings with alumina and zirconia on the substrate made from IN738LC alloy. However, there is a notable research gap in the area of slurry coating at room temp for IN738LC, providing an opportunity for further investigation and serving as a key motivation for this study. The study will explore slurry coating using a mixture of (Al+Cr, Al+Si, Al+Al₂O₃, and Cr+Si) with varying percentages, which has yet to be extensively examined by other researchers.

References

- [1] Al-Khafaji Z, Kazem MA, Radhi NS, Falah M, Hadi ZM. Reducing the Issues of Implements in the Human Body by Applying HA: Review. Mater Mech Eng Technol 2024;64. <https://doi.org/10.52209/2706-977X>.
- [2] Radhi N.S., AL-Khafaji Z., Mareai B.M., Radhi S., Alsaegh A.M. Reducing oil pipes corrosion by (zn-ni) alloy coating on low carbon steel substrate by sustainable process. J Eng Sci Technol 2023;18:1624–38.
- [3] Jasim A.H., Radhi N.S., Kareem N.E., Al-Khafaji Z.S., Falah M. Identification and investigation of corrosion behavior of electroless composite coating on steel substrate. Open Eng 2023;13:20220472.
- [4] Dawood NM, Radhi NS, Al-Khafaji ZS. Investigation corrosion and wear behavior of Nickel-Nano silicon carbide on stainless steel 316L. Mater. Sci. Forum, vol. 1002, Trans Tech Publ; 2020, p. 33–43.
- [5] Abed Janabi ZM, Jaber Alsalami HS, Al-Khafaji ZS, Hussien SA. Increasing of the corrosion resistance by preparing the trivalent nickel complex. Egypt J Chem 2021. <https://doi.org/10.21608/EJCHEM.2021.100733.4683>.
- [6] Radhi NS, Al-Khafaji Z. Investigation biomedical corrosion of implant alloys in physiological environment. Int J Mech Prod Eng Res Dev 2018;8. <https://doi.org/10.24247/ijmperdaug201827>.
- [7] Radhi NS, Salman AJ, Al-Khafaji Z. Investigation of in vitro behavior of composite coating hydroxyapatite-nano silver on 316L stainless steel substrate by electrophoretic technic for biomedical tools. Open Eng 2024;14:20240017.
- [8] Radhi NS, Al-Deen HHJ, Hadi RS, Al-Khafaji Z. Investigate the applicability of coating titanium substrate by hydroxyapatite for surgical implants. Int J Integr Eng 2024;16:172–86.
- [9] Hussein EY, Al-murshdy JMS, Radhi NS, Al-khafaji Z. Surface Modification of Titanium Alloy by Titania / Silver Multilayers Coating for Biomedical Application 2024;1:66–79.
- [10] Abed KM, Radhi NS, Jasim AH, Al-Khafaji ZS, Radhi S, Hussien SA. Study the effect of adding zirconia particles to nickel–phosphorus electroless coatings as product innovation on stainless steel substrate. Open Eng 2022;12:1038–45. <https://doi.org/10.1515/eng-2022-0364>.
- [11] Jabor M, Radh NS, Al-Kinani MA, Al-Khafaji ZS. Optimization of Electro less of Nickel base coating for Cermet Cutting Tools Substrate n.d.
- [12] Rayner TJ. Development and Evaluation of Yttrium Modified Aluminide Diffusion Coatings. University of Toronto; 1998.
- [13] Pérez FJ, Pedraza F, Hierro MP, Balmain J, Bonnet G. Growth of oxide scales upon isothermal oxidation of CVD-FBR aluminide coated stainless steel. Surf Coatings Technol 2002;153:49–58.
- [14] Gessinger GH, Bomford MJ. Powder metallurgy of superalloys. Int Metall Rev 1974;19:51–76.
- [15] Davis JR. Nickel, cobalt, and their alloys. ASM international; 2000.
- [16] Reed RC. The superalloys: fundamentals and applications. Cambridge university press; 2008.
- [17] Jasim Ahmed Jasim,, Yaser A, Al-Khafaji Z. AN ANSYS SIMULATION STUDY ON THE EFFECT OF APPLYING

- TITA-NIUM ALLOY (TI-6AL-4V) COATING FOR WIND TURBINE GEAR. Acad J Manuf Eng 2024;22.
- [18] Jiang SM, Xu CZ, Li HQ, Liu SC, Gong J, Sun C. Preparation and oxidation behaviour of an AlSiY diffusion coating on a Ni-based single crystal superalloy. Corros Sci 2010;52:435–40.
- [19] Durand-Charre M. The microstructure of superalloys. Routledge; 2017.
- [20] HAN X. Diffusion coatings for high-temperature applications on Ni-base superalloys 2012.
- [21] Genova V, Paglia L, Pulci G, Bartuli C, Marra F. Diffusion aluminide coatings for hot corrosion and oxidation protection of nickel-based superalloys: Effect of fluoride-based activator salts. Coatings 2021;11:412.
- [22] Al-Hatab K. Effect of Environments on Oxidation Behavior of Inconel Alloy 600 2004.
- [23] Donachie MJ, Donachie SJ. Superalloys: a technical guide. ASM international; 2002.
- [24] Committee ASM. Properties and selection: nonferrous alloys and special-purpose materials 1990.
- [25] Council NR, Engineering D on, Sciences P, Board NMA, Engineering C on, Systems T, et al. Coatings for high-temperature structural materials: trends and opportunities. National Academies Press; 1996.
- [26] Okamoto H, Schlesinger ME, Mueller EM, Volume ASM. Alloy phase diagrams. vol. 3. Asm International Novelty, OH, USA; 2016.
- [27] Mutasa BM. Defect structures in ordered intermetallics; Grain boundaries and surfaces in FeAl, NiAl, CoAl and TiAl 1997.
- [28] Tien JK. Superalloys, supercomposites and superceramics. Elsevier; 2012.
- [29] Shirzadi A, Jackson S. Structural alloys for power plants: Operational challenges and high-temperature materials 2014.
- [30] Richardson TJA. Shreir's corrosion. Elsevier; 2009.
- [31] Raja AK, Srivastava AP. Power plant engineering. New Age International; 2006.
- [32] Capobianco M, Marelli S. Turbocharger turbine performance under steady and unsteady flow: test bed analysis and correlation criteria. 8th Int. Conf. Turbochargers Turbocharging. London, 2006, p. 17–8.
- [33] Lai GY. High-temperature corrosion and materials applications. ASM international; 2007.
- [34] Levchenko T V, Moroz VI, Buiyanova LP. Protective coatings on metals. Nauk Dumka 1971;4:158–64.
- [35] Sattar S, Alaiwi Y, Radhi NS, Al-khafaji Z. Numerical Simulation for Effect of Composite Coating (TiO₂ + SiO₂) Thickness on Steam Turbine Blades Thermal and Stress Distribution. Acad J Manuf Eng 2023;21.
- [36] Sattar S, Alaiwi Y, Radhi NS, Al-Khafaji Z, Al-Hashimi O, Alzahrani H, et al. Corrosion reduction in steam turbine blades using nano-composite coating. J King Saud Univ 2023;35:102861. <https://doi.org/10.1016/j.jksus.2023.102861>.
- [37] Alqallaf J, Ali N, Teixeira JA, Addali A. Solid particle erosion behaviour and protective coatings for gas turbine compressor blades—A review. Processes 2020;8:984.
- [38] Sagalovich O V, Sagalovich V V, Popov V V, Dudnik SF. Vacuum-plasma protective coating for turbines blades 2020.
- [39] Igumenov IK, Aksenov AN. Thermal barrier coatings on gas turbine blades: Chemical vapor deposition. Therm Eng 2017;64:865–73.
- [40] Shulov V.A., Engelko V.I., Tkachenko K.I., Mueller G., Paikin A.G., Belov A.B., et al. The effect of surface treatment with intense pulsed electron beams on the oxidation resistance of Ni-base superalloy turbine blades with NiCrAlY coating. 7th Int. Conf. Modif. Mater. with Part. Beams Plasma Flows. Tomsk. 26-29 July, vol. 2004, 2004, p. 293.
- [41] Park J-H, Kim S-Y, Lee H-S, Wi K. Influence of different metal types on the bonding strength of concrete using the arc thermal metal spraying method. Materials (Basel) 2023;16:2651.
- [42] Zhou CH, Zhang H, Guan XG, Pan RY, Sun FJ, Mao NN. High temperature oxidation of Ni-20Cr alloy under compressive stress. IOP Conf. Ser. Earth Environ. Sci., vol. 233, IOP Publishing; 2019, p. 32005.
- [43] Ahmed M, Karim AJ, Ali H. Oxidation Properties in CO₂ of Inconel Alloy 600 Coated by Simultaneous Aluminizing-Chromizing Process. Chinese J Aeronaut 2007;20:134–9.
- [44] Kiruthika P, Makineni SK, Srivastava C, Chattopadhyay K, Paul A. Growth mechanism of the interdiffusion zone between platinum modified bond coats and single crystal superalloys. Acta Mater 2016;105:438–48.
- [45] Paul B, Prakash J, Sarkar PS. Formation and characterization of uniform SiC coating on 3-D graphite substrate using halide activated pack cementation method. Surf Coatings Technol 2015;282:61–7.
- [46] Tao Z. Experimental study and modelling of mechanical features in an oxide layer under thermal loadings 2018.
- [47] Kumar S, Kumar M, Handa A. Combating hot corrosion of boiler tubes—A study. Eng Fail Anal 2018;94:379–95.
- [48] Bose S. High temperature coatings. Butterworth-Heinemann; 2017.
- [49] Thellaputta GR, Chandra PS, Rao CSP. Machinability of nickel based superalloys: a review. Mater Today Proc 2017;4:3712–21.
- [50] Birks N, Meier GH, Pettit FS. Introduction to the high temperature oxidation of metals. Cambridge university press; 2006.
- [51] Galetz MC. Coatings for superalloys. Superalloys, InTech London, UK; 2015, p. 277–98.
- [52] Cramer SD, Covino BS, Moosbrugger C. Corrosion: fundamentals, testing and protection. vol. 13. ASM international Materials Park; 2003.
- [53] Gorokhovskiy A V, Yurkov GY, Burmistrov IN, Villalpando-Reyna AF, Kuznetsov D V, Gusev AA, et al. Glass-Ceramic Protective Coatings Based on Metallurgical Slag. Coatings 2023;13:269.
- [54] Christiansen TL, Bottoli F, Dahl K V, Gammeltoft-Hansen NB, Laursen MB, Somers MAJ. Hard surface layers by pack boriding and gaseous thermo-reactive deposition and diffusion treatments. Mater Perform Charact 2017;6:475–91.
- [55] Zhu L, Zhang Y-X, Wang J-F, Luo L-M. High-performance Al–Si coatings toward enhancing oxidation resistance of tungsten by halide-activated pack cementation. Front Mater 2020;7:136.
- [56] Wang YQ, Zhang Y, Wilson DA. Formation of aluminide coatings on ferritic–martensitic steels by a low-temperature pack cementation process. Surf Coatings Technol 2010;204:2737–44.
- [57] Rohr V. Developpement de revetements pour les aciers d'échangeurs thermiques et amelioration de leur resistance a la corrosion en environnement simulant les fumees de combustion de charbon. LE TITRE DOCTEUR L'INSTITUT Natl Polytech TOULOUSE 2005.
- [58] Moosa AA, Abbas MK, Mohammed MR. Improving Oxidation Resistance of Stainless Steel (AISI 316L) by Pack Cementation. Eng Technol J, 2007, 25.

- [59] Xiang ZD, Datta PK. Pack cementation process for the formation of refractory metal modified aluminide coatings on nickel-base superalloys. *J Mater Sci* 2003;38:3721–8.
- [60] Warnes BM. Improved aluminide/MCrAlX coating systems for super alloys using CVD low activity aluminizing. *Surf Coatings Technol* 2003;163:106–11.
- [61] Gonzalez R, Ashrafizadeh H, Lopera A, Mertiny P, McDonald A. A review of thermal spray metallization of polymer-based structures. *J Therm Spray Technol* 2016;25:897–919.
- [62] Sabbir MA. Corrosion Degradation Mechanism of CBPC Coating System for Highway Bridge Steel Components 2017.
- [63] Rannou B. Slurry coatings from aluminium microparticles on Ni-based superalloys for high temperature oxidation protection 2012.
- [64] Eliaz N, Shemesh G, Latanision RM. Hot corrosion in gas turbine components. *Eng Fail Anal* 2002;9:31–43.
- [65] Bai C-Y, Luo Y-J, Koo C-H. Improvement of high temperature oxidation and corrosion resistance of superalloy IN-738LC by pack cementation. *Surf Coatings Technol* 2004;183:74–88.
- [66] Wang QM, Wu YN, Ke PL, Cao HT, Gong J, Sun C, et al. Hot corrosion behavior of AlP NiCoCrAlY (SiB) coatings on nickel base superalloys. *Surf Coatings Technol* 2004;186:389–97.
- [67] Sidhu TS, Prakash S, Agrawal RD. Hot corrosion resistance of high-velocity oxyfuel sprayed coatings on a nickel-base superalloy in molten salt environment. *J Therm Spray Technol* 2006;15:387–99.
- [68] Ren X, Wang F. High-temperature oxidation and hot-corrosion behavior of a sputtered NiCrAlY coating with and without aluminizing. *Surf Coatings Technol* 2006;201:30–7.
- [69] Haleem AH. Improvement of Inconel 600 Oxidation Resistance by Aluminizing Chromizing 2006.
- [70] Deodeshmukh V, Mu N, Li B, Gleeson B. Hot corrosion and oxidation behavior of a novel Pt+ Hf-modified γ' -Ni₃Al+ γ -Ni-based coating. *Surf Coatings Technol* 2006;201:3836–40.
- [71] Agüero A, Blanco C, Garcia M, Gutiérrez M. Al Slurry Coating for Cd Replacement for Aircraft Components. *Proceeding en X Congr. Nac. Mater. San Sebastián, 2008*, p. 1005–8.
- [72] Visuttipitukul P, Limvanutpong N, Wangyao P. Aluminizing of nickel-based superalloys grade in 738 by powder liquid coating. *Mater Trans* 2010;1004051047.
- [73] Keyvani A, Saremi M, Sohi MH. An investigation on oxidation, hot corrosion and mechanical properties of plasma-sprayed conventional and nanostructured YSZ coatings. *Surf Coatings Technol* 2011;206:208–16.
- [74] Zhang K, Liu MM, Liu SL, Sun C, Wang FH. Hot corrosion behaviour of a cobalt-base super-alloy K40S with and without NiCrAlYSi coating. *Corros Sci* 2011;53:1990–8.
- [75] Qiao M, Zhou C. Hot corrosion behavior of Co modified NiAl coating on nickel base superalloys. *Corros Sci* 2012;63:239–45.
- [76] Vadayar KS, Rani SD. Hot corrosion behaviour of nickel based superalloys. *Int J Appl Res Mech Eng(IJARME)* 2013;3:2231–5950.
- [77] Orlov MR. High-temperature corrosive damage to superalloys during operation of blades of gas-turbine engines and power plants. *Polym Sci Ser D* 2013;6:250–5.
- [78] Mahobia GS, Paulose N, Singh V. Hot corrosion behavior of superalloy IN718 at 550 and 650 C. *J Mater Eng Perform* 2013;22:2418–35.
- [79] Pakseresht AH, Javadi AH, Bahrami M, Khodabakhshi F, Simchi A. Spark plasma sintering of a multilayer thermal barrier coating on Inconel 738 superalloy: Microstructural development and hot corrosion behavior. *Ceram Int* 2016;42:2770–9.
- [80] Chakraborty SP. Development of protective coating of MoSi₂ over TZM alloy substrate by slurry coating technique. *Mater Today Proc* 2016;3:3071–6.
- [81] Saini H, Kumar D, Shukla VN. Hot corrosion behaviour of nanostructured cermet based coatings deposited by different thermal spray techniques: a review. *Mater Today Proc* 2017;4:541–5.
- [82] Jawhar MN, Abbass MK, Aziz IA, Khoshnaw F. Oxidation Behavior of Inconel 625 Alloy through Aluminide Diffusion Method Using Y₂O₃ and ZrO₂ Nanoparticles. *Eng Technol J* 2023;41:860–9.
- [83] Khorsand S, Sheikhi A, Raeissi K, Golozar MA. Hot corrosion behavior of inconel 625 superalloy in eutectic molten nitrate salts. *Oxid Met* 2018;90:169–86.
- [84] Lu J, Dang Y, Huang J, Zhou Y, Yang Z, Yan J, et al. Preparation and characterization of slurry aluminide coating on Super304H boiler tube in combination with heat-treatment process. *Surf Coatings Technol* 2019;370:97–105.

Information of the authors

Jasim Ahlam, PhD, lecturer, Al-Qasim Green University

e-mail: ahlam.hamid@wrec.uoqasim.edu.iq

Al-Khafaji Zainab, PhD, lecturer, Universiti Kebangsaan Malaysia, Imam Ja'afar Al-Sadiq University

e-mail: p123005@siswa.ukm.edu.my

Radhi Nabaa, PhD, professor, University of Babylon

e-mail: mat.nabaa.sattar@uobabylon.edu.iq

Application of Ring Section Shaft in Equipment

Mustafin A., Sadykov N.* , Kabylkaiyr D., Shaimardan A., Sadykova A.

Toraighyrov University, Pavlodar, Kazakhstan

*corresponding author

Abstract. In this bending calculation, the driven shaft of a gearbox with a gear is used. The hub of a wheel pressed onto a shaft can serve as a bushing, increasing the cross-section of the shaft. When choosing a fit for the wheel hub on the shaft, it is important to exclude rotation of the wheel on the shaft, as well as the possibility of the joint opening due to a bending moment. According to the results of the analysis, the strength of the annular shaft under the hub of the pressed wheel turned out to be quite high. Calculations have showed that the strength reserves of a hollow shaft with a pressed wheel hub for bending increase from 2.1 to 4.39, and for deflection deformation from 3.85 to 4.5. The calculation shows savings in material consumption for the manufacture of the driven shaft of the gearbox compared to a solid section. At the same time, the load from its own weight on all structural elements is reduced, and the manufacturability of the shaft is increased, since they are designed smooth, and the same range of parts is used as for a solid section shaft.

Key words: shafts, annular sections, strength, rigidity, press connection.

Introduction

Annular shafts are used in machines that mainly experience tangential stresses from torque and minor bending stresses from transverse loads. These machines include conveyors, mixing devices, mixers, etc. [1]. It is believed that hollow shafts cannot be used in power transmissions of machines for reasons of low transverse load capacity. However, as noted in [2], [3] there is currently a trend in the use of thick-walled shafts in mechanical engineering, which are able to perceive a complex stress state with a sufficient margin of safety. The relevance of the research lies in the fact that when using hollow shafts as an amplifier of dangerous cross-section, an external bandage in the form of a wheel hub pressed onto the shaft can be used. The method of designing and calculating such a connection is presented. The effectiveness of the proposed work is ensured by reducing the metal consumption of the structure. The purpose of the article is to show a possibility of use of annular shafts in high loaded equipments. The objective of the article is to design and calculate shaft with a pressed wheel hub on it. The expected results are possibility to use such annular shafts with wheel hub due to their high enough rigidity and safety factors.

1. Research methodology

The diagram of the driven shaft of a gearbox with a gear shown in Figure 1 has the following parameters: Shaft power $P_2=6$ kW; rotation speed $n=120$ min⁻¹; pitch wheel diameter $D_2=350$ mm; tooth angle $\beta=12$ mm; module $m_n=3$ mm; shaft material - steel 45 with endurance and strength limits for workpieces up to 80 mm.

Loads acting on the shaft:

- forces in wheel engagement:

$$F_t = 2T_2/D_2 = 2 \cdot 9,55P_2/D_2n_2 = 2 \cdot 9,55 \cdot 10^3 \cdot 6/350 \cdot 10^{-3} \cdot 120 = 2,72 \text{ kN} \quad (1)$$

$$F_a = 2,72 \cdot 10^3 \cdot tg12^0 = 578,2 \text{ N}, \quad (2)$$

$$F_r = 2,72 \cdot 10^3 \cdot tg20^0 / \cos 12^0 = 1,01 \text{ kN}. \quad (3)$$

Torque:

$$T = P_2/\omega = 9,55P_2/n = 9,55 \cdot 6 \cdot 10^3/120 = 477,5 \text{ N}\cdot\text{m}. \quad (4)$$

Bending moment at a point in the center of the wheel according to the calculations performed:

$$M_b = \sqrt{M_{CV}^2 + M_{CH}^2} = \sqrt{115,6^2 + 211,2^2} = 240,76 \text{ N}\cdot\text{m}. \quad (5)$$

Equivalent load moment according to strength theory:

$$M_e = \sqrt{240,76^2 + 4762^2} = 533,08 \text{ N}\cdot\text{m}. \quad (6)$$

Axial moment of resistance of the shaft:

$$W_x = 0,1d^3 . \quad (7)$$

Bending stress from equivalent load:

$$\sigma_e = M_e/W_x . \quad (8)$$

For a solid-section shaft with a keyed wheel connection experiencing alternating symmetrical cyclic bending stresses, the permissible stresses are determined by the endurance limit [4]

$$[\sigma]_{-1} = \sigma_{-1} \cdot \varepsilon_0 \cdot \beta_0 / [n] \cdot k \cdot \sigma , \quad (9)$$

where safety factors $[n]=2$; stress concentration factor for steel $\sigma_t=900 \text{ MPa}$; $k_\sigma = 1,6$ scale factor at $d=60 \text{ mm}$ $\varepsilon_0 = 0,82$; surface roughness coefficient $\beta_\sigma = 0,9 \div 0,97$

$$[\sigma]_{-1} = 410 \cdot 0,92 \cdot 0,82 / 1,6 \cdot 2 = 96,6 \text{ MPa}. \quad (10)$$

Safety factor:

$$n = [\sigma]_{-1} / \sigma_e . \quad (11)$$

The shaft is calculated for rigidity. Shaft bending force:

$$F = \sqrt{F_t^2 + F_r^2} = \sqrt{(2,72 \cdot 10^3)^2 + (1,02 \cdot 10^3)^2} = 2,91 \text{ kN}. \quad (12)$$

Shaft bending calculations are now automated, accessible and can be done online. For example, the calculation program [5] considers various design schemes of beams with common section configurations. In this case, the permissible shaft deflection:

$$[f] = (0,0001 \dots 0,0003)l = (0,0001 \dots 0,0003)(120 + 220) = 0,034 \dots 0,1 \text{ mm} \quad (13)$$

Stiffness safety factor

$$S = [f] / f_{max} , \quad (14)$$

where

$$[f] = (0,1 + 0,034) / 2 = 0,067 \text{ mm} \quad (15)$$

- average value of permissible deflection.

For tubular section:

Testing for strength and rigidity showed that the annular section with parameters $a = d_1/d = 38/60$, according to Table 1, does not provide sufficiently reliable permissible bending stress parameters and is only $n = 2,1$. According to estimates from sources [6], acceptable safety factors are in the range of $2.0 \div 3.0$. In this regard, it is necessary to strengthen the design of the tubular shaft. As shown in Figure 1, the hub of wheel, pressed onto shaft, can serve as a bushing that increases the cross-section of the shaft.

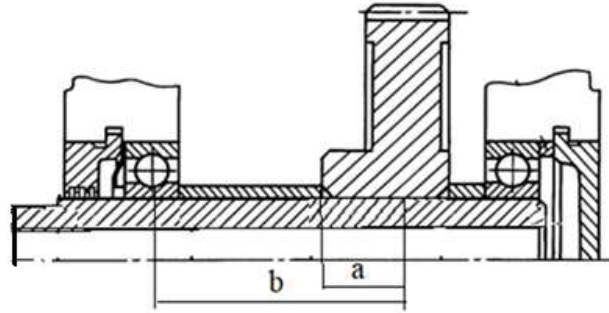


Fig. 1. - Gear pressed onto an annular shaft

When choosing the fit of the wheel hub on the shaft, you must:

- prevent the wheel from turning on the shaft;
- possibility of opening the joint from a bending moment.

For the first condition, the calculated pressure

$$p = 2kM_{cr}/d2\pi L_h f, \quad (16)$$

where f is the coefficient of friction in the shaft-hub connection; k -safety factor; L_h - the length of the landing area of the wheel on the shaft, equal to the width of the hub.

The second condition is met when sufficient pressure is created in connection with interference

$$p = 4M_b/2W_y\pi, \quad (17)$$

where $W_y = b^2(d - d_1)/6$ – moment of resistance to bending of the diametrical section of the bushing;

b - width of the area for landing the wheel hub on the shaft;

M_b - bending moment equal to the maximum moment.

To ensure that the joint does not open due to shaft bending, the tension pressure must be at least $p = p_1/0,25$ [4]. Based on this pressure, according to a method known in engineering calculations, the interference is determined and the fit is selected. The dimensions of the wheel hub for shafts recommended in technical manuals for the machine parts course [7] and foreign sources [8], [9] require clarification. In this connection, the dimensions of the parts connected with interference when the female part is heated were calculated. From the condition of ensuring maximum tension, ensuring the strength of the part and the heating temperature not exceeding the permissible values, the outer diameter of the bushing (wheel hub) is selected - $d_h = 80$ mm and its length $L_h = 50$ mm.

Allowable bending stresses for shafts experiencing alternating stresses are determined by the endurance limit. When calculating, the use of an interference fit that weakens the cross-section is taken into account by the corresponding values of the coefficients

$$[\sigma]_{-1} = \sigma_{-1} \cdot \varepsilon_0 \cdot \beta_0 / [n] \cdot k \cdot \sigma, \quad (18)$$

where safety factors $[n]=2$; the ratio of the stress concentration coefficient to the scale factor during interference fit at $\sigma_t = 900$ MPa and $d=60$ mm, pressing pressure more than 20 MPa, $k_\sigma/\varepsilon_\sigma = 3,0$; surface roughness coefficients $\beta_\sigma = 0,9 \div 0,97$;

$$[\sigma]_{-1} = 410 \cdot 0,92/3 \cdot 2 = 62,83 \text{ MPa}. \quad (19)$$

Bending stress

$$\sigma_e = 553,08 \cdot 10^3/37130 = 14,3 \text{ MPa}. \quad (20)$$

The strength of the annular shaft under the hub, the pressed-in wheel, turned out to be quite high, safety factor $n = \sigma_e/[\sigma]_{-1} = 4,39$.

The presence of a step in the form of a wheel hub pressed onto the shaft complicates calculations for deflection. To simplify it in engineering calculations, one can use the reduction of a shaft with steps to an equivalent smooth shaft [10]. At the junction of the shaft parts, additional forces ΔQ and moments ΔM are introduced, which are the difference in the internal force factors of the section, determined from the diagrams:

$$\Delta Q_1 = Q_1(\beta_2 - \beta_1); \Delta Q_2 = Q_2(\beta_2 - \beta_1);$$

$$\Delta M_1 = M_1(\beta_2 - \beta_1); \Delta M_2 = M_2(\beta_2 - \beta_1);$$

Using the reduction coefficients, the stepped shaft is replaced by an equivalent rod of constant stiffness with a moment of inertia J_0 , taking into account the moment of inertia of the middle section of the shaft J_2 with a hub and two extreme sections with moments J_1 and J_2

$$\beta_1 = J_0/J_1; \beta_2 = J_0/J_2; \beta_3 = J_0/J_3.$$

Next, the calculation is carried out using the calculation program [11] for an equivalent beam with a constant moment of inertia of the section.

To fix the wheel on the shaft, spacer bushings are installed between it and the bearings on both sides (Figure 1). They are usually installed on shafts with transitional fits. The magnitude of the equivalent moment at the end of the hub is less than in the middle section of the wheel

$$M = M_e(b - a)/b.$$

In this regard, the outer surface of the wheel hub can be sloped in the direction of the ends of the hub. To transmit rotation from the shaft to the actuators, keyed or splined connections of parts are used. To use the former, a shank with a keyway is pressed into the hole at the output end of the shaft [12], [13]. To prevent rotation of the shank in the shaft hole, it is necessary to calculate the pressure, select the required interference fit and the length of the mating part l

$$p = 2kM_{cr}/d2\pi L_h f \tag{21}$$

If the wall thickness is sufficient, spline grooves can be cut at the output end of the tubular shaft.

2. Results and discussion

The dangerous section under the wheel hub, as the main element of the power transmission, loaded with torque and bending moments, is enhanced by pressing it onto the shaft.

For example, for a hollow shaft with a diameter ratio of 38/60, when pressing a hub with an outer diameter of 74 mm, the wall thickness increased from 11 mm to 18 mm. Calculations show that the strength reserves of a hollow shaft with a pressed wheel hub for bending increase from 2.1 to 4.39, and for deflection deformation from 3.85 to 4.5. Table 1 shows the main results of the research.

Table 1. Calculation results for various cross sections of the driven shaft

S, mm	d ₁ /d, mm/mm	I _x , mm ⁴	W _x , mm ³	m, kg	f, mm	S = [f]/f	σ _e , MPa	[σ] ₋₁ , MPa	n = σ _e /[σ] ₋₁
11	38/60	158000	17790	4,5	0,0174	3,85	29,96	62,8	2,1
21	38/80	1373900	371300	4,5	0,0149	4,29	14,3	62,8	4,39
0	60	636200	21210	7,54	0,0146	4,52	25,13	96,6	3,84

The mass of a workpiece with a diameter of 60 mm and a length of 340 mm is 7.54 kg. The mass of the workpiece for the manufacture of an annular shaft with a diameter ratio of $a = d_1/d = 38/60 = 0,633$ and a length of 340 mm does not change and amounts to 4.5 kg. Savings in material consumption compared to a solid section with a diameter of 60 mm for the manufacture of the driven shaft of the gearbox - 3 kg, mass ratio - 1.675. At the same time, the load from its own weight on all structural elements is reduced, the manufacturability of the shaft is increased, since they are designed smooth, the same nomenclature of parts is the same as for a solid shaft.

Conclusions

The article has designed and calculated shaft with a pressed wheel hub on it. The expected results have been achieved as article has showed high enough rigidity and safety factors. Research has showed that the strength reserves of a hollow shaft with a pressed wheel hub for bending increase from 2.1 to 4.39, and for deflection deformation from 3.85 to 4.5. When strengthening the hollow shaft by pressing the wheel, its hub increased the cross-section of the shaft, which makes it possible to use hollow shafts instead of solid-section shafts and create sufficient safety and rigidity factors. At the same time, the load from its own weight on all structural elements has decreased. The calculation showed savings in material consumption for the manufacture of the driven shaft of the gearbox compared to a solid section, which allows the use of hollow shafts in power transmissions of critical equipment.

References

- [1] Strengthening the design of screw devices in horizontal machines / R.Tyulyubayev , A.Mustafin , A.Kuandykov Science and Technology of Kazakhstan No1-2023
- [2] Cross-sectional behaviour of cold-formed high strength steel circular hollow sections/Xin Meng . Leroy Gardner Thin-Walled Volume 154.November.2020.106822
- [3] A systematic review of stress concentration factors (SCFs) in composite reinforced circular hollow section (CHS) joints/ /Mohsin Iqbal , Saravanan Karuppanan , Veeradasan Perumal , Mark Ovinis , Muhammad Iqbal Composites Part C Open Access Volume15.October2024100515
- [4] Opredelenie dopuskaemyh napryazhenij pri simmetrichnom i pul'siruyushchem ciklah izmeneniya [Determination of permissible stresses for symmetrical and pulsating cycles of change] - https://studopedia.su/8_5464_raschet-zaklepochnih-soedineniy.html
- [5] Raschet balok iz trub, kruglogo, kvadratnogo, shestigrannogo i pryamougol'nogo prokata na izgib i progib [Calculation of beams made of pipes, round, square, hexagonal and rectangular rolled products for bending and deflection] - <https://trubanet.ru/>
- [6] Birger I. A., Shorr B. F., Iosilevich G. V. Raschety na prochnost' detalej. Spravochnik [Calculations for the strength of parts. Directory] // . – M.: Mashinostroenie. – 1993. – 702 p.
- [7] Ivanov A.S., Ermolaev M.M. Rabota soedineniya s natyagom pri peredache soedineniem izgibayushchego momenta [Interference operation during transmission bending moment connection] // Mechanical Engineering Bulletin. – 2009. – № 5. – P. 45 – 48.
- [8] Dunaev P.F., Lelikov O.P. Konstruirovaniye uzlov i detalej mashin [Design of machine components and parts] – M.: Academy, 2008. – 496 p.
- [9] Kutz M. (Ed.) Mechanical Engineers' Handbook. 3rd Edition. Four Volume Set. – John Wiley & Sons, Inc., 2005. – 4200 p.
- [10] Childs Peter, R.N. Mechanical Design Engineering Handbook. Amsterdam: Elsevier, 2014. – 817 p. – ISBN: 978-0-08-097759-1.
- [11] Raschet balok peremennogo secheniya na prochnost' i zhestkost'. Stupenchatye sterzhni [Calculation of beams of variable cross-section for strength and rigidity. Stepped rods] – raschet-balok-peremennogo-secheniya-na-prochnost-i-zhestkost' /
- [12] Grechishchev E.S., Il'yashenko A.A. Soedineniya s natyagom: Raschety, proektirovaniye, izgotovleniye [Interference connections: Calculations, design, manufacturing] // – M.: Mashinostroenie, 1981. – 247 p.
- [13] Pershin V. F., Selivanov Yu. T. Raschet na prochnost' tonkostennyh obolochek vrashcheniya i tolstostennyh cilindrov: Metodicheskoe posobie [Calculation of the strength of thin-walled shells of revolution and thick-walled cylinders: Methodical textbook] – Tambov: GTU. – 2002. – 20 p.

Information of the authors

Mustafin Adilbek, c.t.s., professor, Toraighyrov University
e-mail: mustafin-51@mail.ru

Sadykov Nursultan, senior lecturer, Toraighyrov University
e-mail: sadykov.n@teachers.tou.edu.kz

Kabylkaiyr Dauren, senior lecturer, Toraighyrov University
e-mail: kabylkair.d@teachers.tou.edu.kz

Shaimardan Aruan, lecturer (assistant), Toraighyrov University
e-mail: aruan.shaimardan97@mail.ru

Sadykova Aigerim, lecturer (assistant), Toraighyrov University
e-mail: aygerim.sadykova.86@bk.ru

Investigating the Influence of Carbon Nanotubes on Basalt Fiber Nano Hybrid Composite Properties: a Dynamic Mechanical Analysis

Malyadri T.^{1,2*}, Suresh Kumar J.³

¹Department of Mechanical Engineering, VNR VJIET, Bachupally, 500072 Hyderabad, Telangana, India

²Department of Mechanical Engineering, JNTUH, 500050, Hyderabad, Telangana, India

³Senior Professor, Department of Mechanical Engineering, Jawaharlal Nehru Technological University (JNTUH), 500050, Telangana, India

*corresponding author

Abstract. This paper investigates the structure-property relationships in basalt fiber reinforced polymer composites doped with multi-walled carbon nanotubes (CNTs). Basalt fabrics were reinforced with 0.2-0.8 wt% CNTs using hand layup and compression molding to fabricate laminated plates. The mechanical, morphological, and thermomechanical properties were characterized using tensile, flexural, impact, SEM, FTIR, XRD, and DMA testing. Results showed that increasing CNT percentage led to progressive surface decoration and eventual obscuration of the underlying basalt fibers as observed by SEM. FTIR revealed a transition from basalt-dominated to CNT-dominated spectra with higher loadings. While tensile strength improved up to 0.4% CNTs before decreasing, flexural strength declined initially up to 0.4% before consistent enhancements. However, impact energy decreased gradually with more CNTs due to embrittlement effects. An optimal CNT loading of 0.4-0.6 wt% was found to maximize the mechanical performance through uniform dispersion and interfacial adhesion. DMA showed increased stiffness but reductions in damping and degradation resistance above 0.6 wt% CNTs. Overall, CNTs can substantially reinforce basalt fiber composites within an optimal composition range contingent on controlled aggregation and processing conditions.

Keywords: basalt fibers, carbon nanotubes, multi-walled carbon nanotubes, polymer matrix composites, hand layup, compression molding, mechanical properties, tensile strength, flexural strength, impact resistance, scanning electron microscopy, fourier transform infrared spectroscopy, X-ray diffraction, dynamic mechanical analysis

Introduction

Basalt fibers have recently emerged as a promising sustainable reinforcement for polymer matrix composites for structural applications [1]. Sourced from natural volcanic rock, these inorganic fibers provide impressive strength and modulus, excellent thermal stability and chemical resistance at relatively low cost compared to conventional glass or carbon fibers [2]. The basalt composition, rich in silica, alumina and calcium oxide, forms an amorphous glassy structure during manufacturing, resulting in smooth fiber surfaces ideal for polymer matrix adhesion [3]. With tensile strength from 484 MPa to 704 MPa [4], elastic modulus of 89 GPa [5] and failure strain of 3.2%, basalt delivers mechanical performance comparable to E-glass. Additionally, basalt maintains strength and stiffness up to 750°C, significantly higher than most glass fibers. These properties have driven rising interest in basalt-reinforced composites for high-temperature environments from automotive exhaust components to aerospace structures [6].

However, the brittle nature of basalt fibers and their glassy amorphous structure leads to certain limitations in fracture toughness, impact resistance and fatigue performance of basalt composites [6]. Recent efforts have focused on hybrid basalt fiber composites, reinforced with nanomaterials such as carbon nanotubes (CNTs) to improve the toughness, damage tolerance and durability while retaining the high strength and thermal stability. In particular, CNTs can enhance energy dissipation and crack resistance through mechanisms like crack bridging, deflection, and pulling-out [7]. The high electrical and thermal conductivity provided by the CNTs also imparts multifunctionality. But realizing these benefits requires optimizing the CNT content and tailoring the microstructure. Insufficient loading leads to negligible improvements while excessive CNTs can degrade mechanical properties through poor dispersion, bundling and impaired interfacial adhesion [8].

In this work, we fabricate basalt glass fiber composite plates reinforced with varying concentrations of multi-walled CNTs. The hybrid composite constituents include basalt fabric, 10 MIL glass fibers, epoxy resin and CNTs. We comprehensively characterize the microstructure, phase composition, and thermomechanical performance using scanning electron microscopy, Fourier transform infrared spectroscopy, X-ray diffraction and dynamic mechanical analysis. Correlating the microstructure to mechanical properties will provide critical insights toward designing enhanced hybrid basalt nanocomposites. This multifunctional combination of basalt fibers and CNTs shows promise for next-generation high-performance composites ranging from automotive and wind turbine components to aerospace structures.

1. Methodology

Composite materials, combining the favorable properties of various constituents, have gained significant attention in recent years due to their exceptional mechanical and thermal characteristics. In this study, we focus on

basalt glass fiber composite plates, which have shown great potential for use in diverse industries ranging from aerospace to automotive. The key constituents of these plates, namely basalt fabric, 10 MIL glass fiber, epoxy resin, hardener, and graphene, are analyzed comprehensively to ascertain their contributions to the overall performance of the composite.

2.1 Materials

2.1.1 Basalt Fabric

Basalt fabric, derived from natural basalt rock, is a key reinforcing material employed in the composite plates. Its structure consists of densely interwoven basalt fibers, providing excellent strength and stiffness. The physical and mechanical properties of basalt fabric are evaluated using SEM imaging and tensile testing [1].



Fig. 1. - Basalt fabric

2.1.2 10 MIL Glass Fiber

The 10 MIL glass fiber serves as an additional reinforcing element in the composite plates. Its fine, high-strength fibers enhance the structural integrity and impact resistance of the material [9]. The fiber morphology and tensile properties are examined using SEM and mechanical testing methods.

2.1.3 Epoxy Resin

Epoxy resin acts as the matrix material in the composite, offering adhesion between the reinforcing fibers and providing load transfer capabilities [10]. The chemical composition and curing characteristics of the epoxy resin are investigated using XRD analysis.

2.1.4 Hardener

The hardener is a crucial component in the epoxy resin system, facilitating the cross-linking reaction and determining the final material properties. Its impact on the curing kinetics and mechanical performance of the composite is studied through rheological measurements and mechanical testing.

2.1.5 Graphene

Graphene, a two-dimensional allotrope of carbon, is incorporated into the composite to enhance its electrical and thermal conductivity [11]. The dispersion and alignment of graphene within the Composites are assessed using SEM.

2.2 Fabrication

2.2.1 Laminate Production

Four laminates, each measuring 300*300 mm in size and possessing a thickness ranging from 3 to 3.5 mm, were fabricated using the hand lay-up technique. Basalt fabric layers were interleaved with epoxy resin to create the laminates. The resin and graphene were mixed using the hand stirring method to achieve uniform dispersion [12]. The graphene weight percentage in the composite was varied from 0.2 to 0.8 to investigate its impact on the resulting properties.

2.2.2 Compression Molding

To consolidate the laminates and ensure proper bonding between the layers, compression molding was conducted using an SVS Hydraulics compression machine. Appropriate temperature and pressure conditions were maintained during the compression process to facilitate resin curing and laminate formation.

2.3 Testing and characterization

2.3.1 Tensile Test

The evaluation of maximum tensile stress is vital in determining the mechanical strength and structural integrity of composite materials. This study focuses on basalt glass fiber composite plates and their ability to withstand tension. The ASTM D638 standard test method was employed to accurately measure the maximum tensile stress experienced by the material. By adhering to the established testing standards, reliable and consistent data were obtained, facilitating meaningful comparisons with other composite materials and enabling confident engineering applications [13].

2.3.1.1 Tensile Testing Apparatus

The tensile testing apparatus used in this study complied with the specifications outlined in the ASTM D638 standard. It consisted of a universal testing machine equipped with appropriate grips to securely hold the specimens. The testing machine was capable of applying a constant and controlled load along the longitudinal axis of the specimens. Displacement and load sensors were employed to measure and record the deformation and applied load during the test [13].

2.3.1.2 Test Procedure

The tensile test was conducted following the guidelines specified in the ASTM D638 standard. The specimens were carefully mounted onto the grips, ensuring a secure and centralized grip alignment. A constant crosshead speed was applied to the specimens, gradually inducing tensile deformation until failure occurred. The load-displacement data were continuously recorded throughout the test to capture the stress-strain behavior of the material [13].

2.3.2 Flexural Test

Determining the stiffness of composite materials is crucial in assessing their structural integrity and performance. This research focuses on basalt glass fiber composite plates and aims to evaluate their stiffness characteristics through a flexural test. The ASTM D790-17 standard test method is employed to ensure accurate and reliable measurements. By adhering to the established testing standards, consistent data can be obtained, facilitating meaningful comparisons with other materials and enabling informed engineering applications [14].

2.3.2.1 Flexural Testing Apparatus

The flexural testing apparatus utilized in this study adhered to the specifications outlined in the ASTM D790-17 standard. It consisted of a universal testing machine equipped with appropriate supports and loading fixtures. The machine applied a controlled force at a specified rate to induce bending deformation in the specimens. Load and displacement sensors were employed to measure and record the applied load and corresponding deflection during the test [14].

2.3.2.2 Test Procedure

The flexural test was conducted following the guidelines specified in the ASTM D790-17 standard. The specimens were placed on the supports, ensuring proper alignment and support conditions. A controlled load was applied at the center of the specimen, inducing a three-point bending configuration. The force was gradually increased until plastic deformation occurred. The applied load and corresponding deflection were continuously recorded to capture the material's flexural behavior.

2.3.3. Impact Test

Understanding the impact resistance of composite materials is crucial in various engineering applications. This study specifically investigates basalt glass fiber composite plates and aims to evaluate their maximum impact load capacity. The impact test, performed according to the ASTM D256-10 standard, enables the measurement of impact strength and provides valuable data for characterizing the material's behavior under sudden dynamic loading. Adhering to standardized testing procedures ensures consistent and comparable results, aiding in material selection and structural design [15].

2.3.3.1 Impact Testing Apparatus

The impact testing apparatus utilized in this study complied with the specifications outlined in the ASTM D256-10 standard. It consisted of a pendulum impact tester with appropriate supports and fixtures. The pendulum was released from a specified height, striking the specimen with a controlled impact energy. The apparatus was equipped with sensors to measure and record the absorbed energy during impact [15].

2.3.3.2 Test Procedure

The impact test was conducted following the guidelines specified in the ASTM D256-10 standard. The specimens were securely mounted on the impact testing apparatus, ensuring proper alignment and support

conditions. The pendulum was released, striking the specimen and imparting a sudden dynamic load. The absorbed energy was measured and recorded by the apparatus. Multiple tests were conducted to obtain a statistically significant dataset [15]. The composites are developed with multiple Nano particle reinforced epoxy and perform a comparative analysis of the mechanical properties[16-19].

2. Results and discussion

2.1 Flexural Testing

The flexural strength of the composites exhibited an initial decline with a small increase in CNT percentage from 0.2% to 0.4%, with the average strength decreasing from 37.57 MPa to 32.29 MPa. However, further increases in the CNT percentage led to a steady improvement in flexural strength, with the average strength increasing to 36.32 MPa at 0.6% CNT and reaching an optimum value of 41.52 MPa at 0.8% CNT. This trend of an initial decline followed by consistent improvements suggests the existence of a CNT composition threshold between 0.2% and 0.6%, below which the strength decreases and above which it improves with increasing CNT content. The non-monotonic dependence of flexural strength on CNT percentage can be attributed to changes in microstructure and CNT dispersion influenced by the CNT composition. The results of the flexural test are shown in Table 1.

Table 1. Flexural testing results

S.No	Sample Details	Width (mm)	Thickness (mm)	Force(N)	Flexural Strength (MPa)
1	Sample: 0.2-1	10.34	3.21	1880	42.48
2	Sample: 0.2-2	10.74	3.35	1580	32.94
3	Sample: 0.2-3	11.05	3.77	1960	35.29
4	Sample: 0.4-1	10.37	3.13	1260	29.11
5	Sample: 0.4-2	10.02	3.01	1340	33.32
6	Sample: 0.4-3	10.26	3.06	1400	33.44
7	Sample: 0.6-1	10.78	3.26	1840	39.27
8	Sample: 0.6-2	11.22	3.34	1540	30.82
9	Sample: 0.6-3	11.06	3.28	1880	38.87
10	Sample: 0.8-1	8.69	3.28	1620	42.63
11	Sample: 0.8-2	9.07	3.36	1840	45.28
12	Sample: 0.8-3	8.66	3.26	1380	36.66

3.2 Tensile Testing

The tensile strength of the composites exhibited a non-monotonic trend with increasing CNT content, evidenced by an initial improvement from 344.40 MPa to a maximum of 396.86 MPa as the CNT percentage rose from 0.2% to 0.4%, followed by a decreasing trend down to 362.71 MPa at 0.8% CNT. This peak in strength at 0.4% CNT indicates an optimal composition, above which aggregation effects likely cause the strength to decline. Meanwhile, the elongation at break showed minimal variation with CNT percentage, hovering around 9-10% for all compositions, suggesting that the ductility was unaffected by CNT addition. The results demonstrate that the reinforcing effect of CNTs on tensile strength diminishes at high loadings beyond an optimal composition of 0.4% due to aggregation while the ductility is unaltered across compositions. The results of the tensile test are shown in Table 2.

Table 2. Tensile testing results

Sl.No	Sample details	Test Method	Tensile Strength(MPa)	Elongation (%)
1	Sample: 0.2-1	ASTM D638	350.23	9.67
2	Sample: 0.2-2		340.05	9.77
3	Sample: 0.2-3		342.91	9.22
4	Sample: 0.4-1		403.35	9.32
5	Sample: 0.4-2		389.60	8.72
6	Sample: 0.4-3		396.62	9.42
7	Sample: 0.6-1		370.02	9.41
8	Sample: 0.6-2		372.75	8.89
9	Sample: 0.6-3		376.74	9.59
10	Sample: 0.8-1		348.56	8.41
11	Sample: 0.8-2		356.47	9.27
12	Sample: 0.8-3		383.10	9.66

3.3 Impact Testing

The impact energy absorption of the composites displayed a declining trend with increasing CNT percentage, with the average impact energy decreasing progressively from 161.59 kJ/m² at 0.2% CNT to 125.92 kJ/m² at 0.8% CNT, indicating embrittlement induced by higher CNT loading. A considerable drop was observed when the CNT increased from 0.4% to 0.6%, implying the existence of a threshold composition beyond which the impact strength deterioration becomes more pronounced, likely due to constrained polymer chain mobility. The results demonstrate that CNT addition impairs the impact energy absorption capability of the composites, especially at concentrations above 0.4%, owing to an embrittlement effect that intensifies with increasing CNT content. The results of the Impact test are shown in Table 3.

Table 3. Impact testing results

S.No	Sample details	Impact Energy(KJ/m ²)
1	Sample 0.2 - 1	161.89
2	Sample 0.2 - 2	160.75
3	Sample 0.2 - 3	161.26
4	Sample 0.2 - 4	160.94
5	Sample 0.2 - 5	162.09
6	Sample 0.4 - 1	159.52
7	Sample 0.4 - 2	158.34
8	Sample 0.4 - 3	159.94
9	Sample 0.4 - 4	160.31
10	Sample 0.4 - 5	157.88

S.No	Sample details	Impact Energy(KJ/m ²)
11	Sample 0.6 - 1	135.94
12	Sample 0.6 - 2	136.22
13	Sample 0.6 - 3	134.82
14	Sample 0.6 - 4	135.71
15	Sample 0.6 - 5	135.08
16	Sample 0.8 - 1	125.88
17	Sample 0.8 - 2	127.61
18	Sample 0.8 - 3	124.77
19	Sample 0.8 - 4	125.34
20	Sample 0.8 - 5	126.79

3.4 SEM

Scanning electron microscopy (SEM) reveals carbon nanotubes (CNTs) visibly decorating the underlying smooth basalt fiber surfaces at low CNT loadings of 0.2 wt%. The nano-scale tubular CNT structures exhibit high aspect ratios. Higher magnification SEM enables detailed characterization of the CNT morphology, including hollow interiors and degree of alignment/aggregation on the basalt. Optimal CNT-basalt fiber interfacial adhesion occurs through uniform, conformal CNT coatings. However, poor dispersion or debonding at the interface indicates weak bonding.

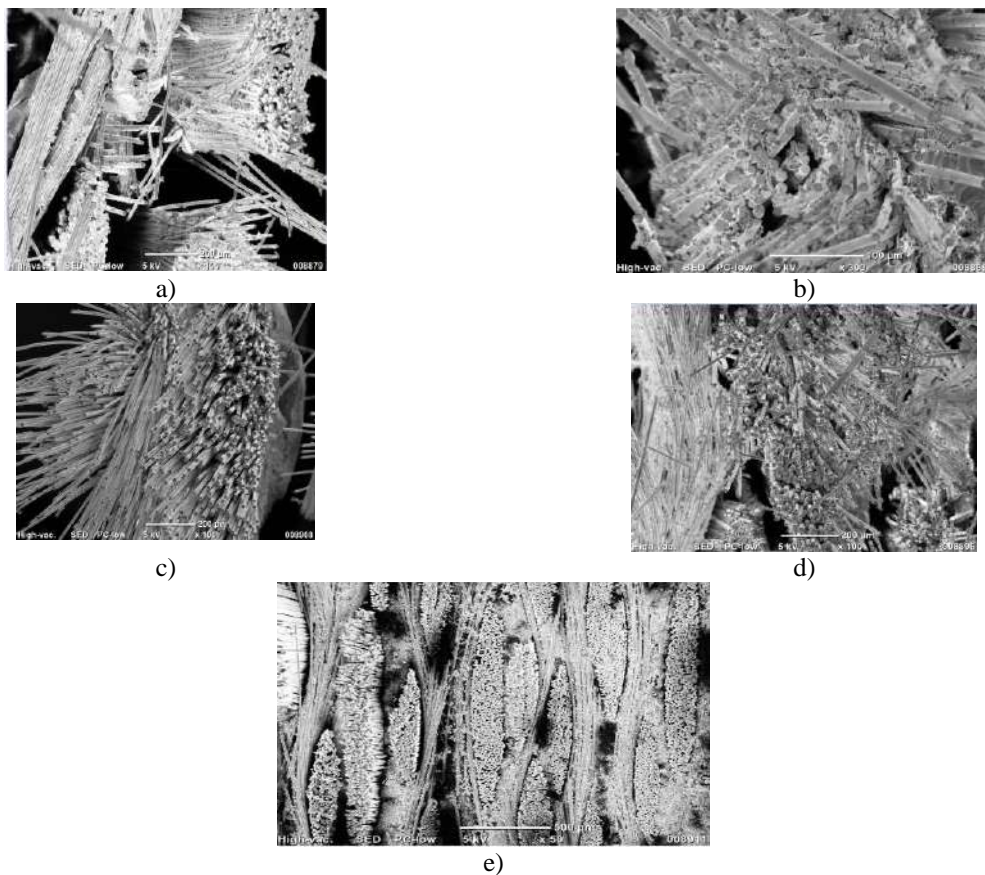


Fig. 2. - SEM images of Basalt/epoxy composite with (a)0.2% by weight CNT, (b)0.4% by weight CNT, (c)0.6% by weight CNT, (d)0.8% by weight CNT and (e) plane of the composite

As CNT concentration rises to 0.6 wt%, increased roughening of the basalt fibers is attributed to more extensive CNT surface coatings. CNT pull-out observed on fiber fracture surfaces provides evidence of mechanical interlocking and enhanced adhesion. Thicker CNT networks partially obscure the basalt morphology. At 0.8 wt% CNT loading, thick CNT coatings nearly completely obscure the underlying basalt fiber structure. Individual CNTs are no longer distinguishable. Harsher processing conditions required for these CNT loadings may damage the basalt surface with pitting, cracking, or melting. However, the CNT networks can heal defects and strengthen interfacial adhesion. Increasing CNT concentration from 0.2 to 0.8 wt% progressively modifies the basalt fiber surface morphology as detected by SEM, providing insights into CNT dispersion, interfacial bonding, and effects on the basalt reinforcement.

At 0.2 wt% CNT loading (Sample a), scanning electron microscopy reveals sparse decoration of the underlying basalt fiber surfaces with isolated carbon nanotubes (CNTs). The smooth basalt morphology remains predominantly visible. In Sample b (0.4 wt% CNTs), the number of surface-coating CNTs increases substantially, forming a more defined network while the basalt fiber shape remains discernible. Sample c (0.6 wt% CNTs) displays extensive CNT coatings that obscure the underlying basalt fibers, presenting a rough, entangled CNT mesh. Individual CNT resolution becomes challenging. With Sample d (0.8 wt% CNTs), the basalt fibers are almost completely encapsulated by thick CNT layers. The original fiber surface is heavily obscured by the dense CNT network. CNT agglomeration is likely at this high loading.

3.5 FTIR

The comparative Fourier transform infrared (FTIR) spectroscopy analysis of the epoxy resin samples with the sample integrated with CNT particles, indicates distinct modifications in the chemical composition and structure of the polymer matrix arising from the addition of the CNT particles. The pure baseline epoxy spectrum shows characteristic peaks corresponding to C-H, C=C, and C-O vibrational modes. However, the FTIR spectrum of the nanoparticle-containing epoxy sample displays lower transmittance intensities for several major epoxy peaks along with the emergence of new peaks associated with the nanoparticle inclusions. The attenuation of existing epoxy vibration intensities implies a disruption in the epoxy molecular network and reduced concentration of specific functional groups due to interactions with the nanoparticles. Furthermore, the new spectrum peaks suggest the incorporation of chemical species related to the nanoparticle composition.

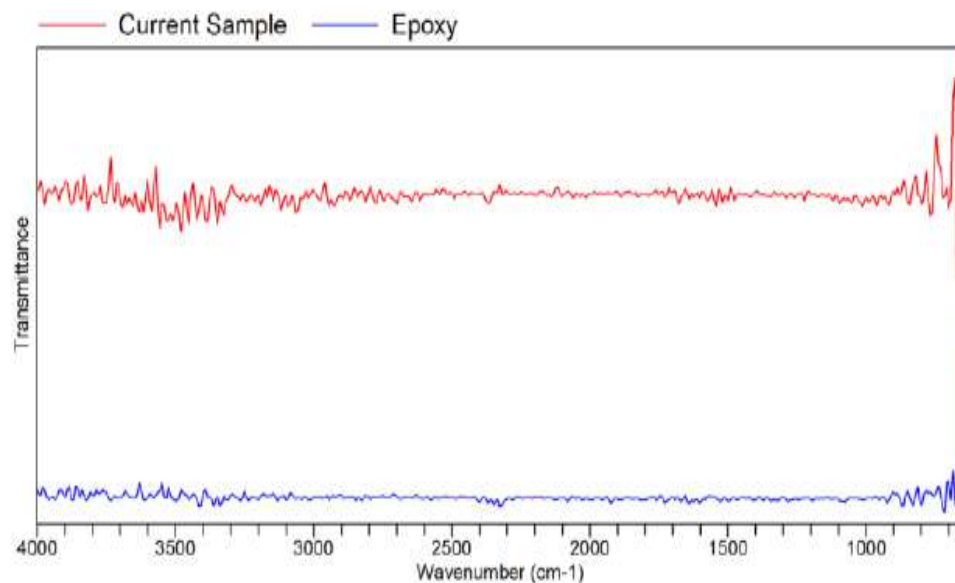


Fig. 3. - FTIR results

The comparative FTIR study verifies that the addition of the CNT particles induces measurable changes in the epoxy resin chemistry and structure based on the alterations observed in the spectral profile. Overall, the spectroscopic analysis confirms the successful integration of The CNT particles into the polymer matrix through the definitive modifications in the FTIR signature.

3.6 XRD

The X-ray diffraction (XRD) analysis of the basalt/epoxy composite sample doped with 0.8% carbon nanotubes (CNTs) by weight confirms the successful incorporation of the CNT dopant. The results show the sample contains primarily carbon, at 71.32 mass%, along with silicon oxide, aluminum oxide, and calcium oxide from the basalt and epoxy components.

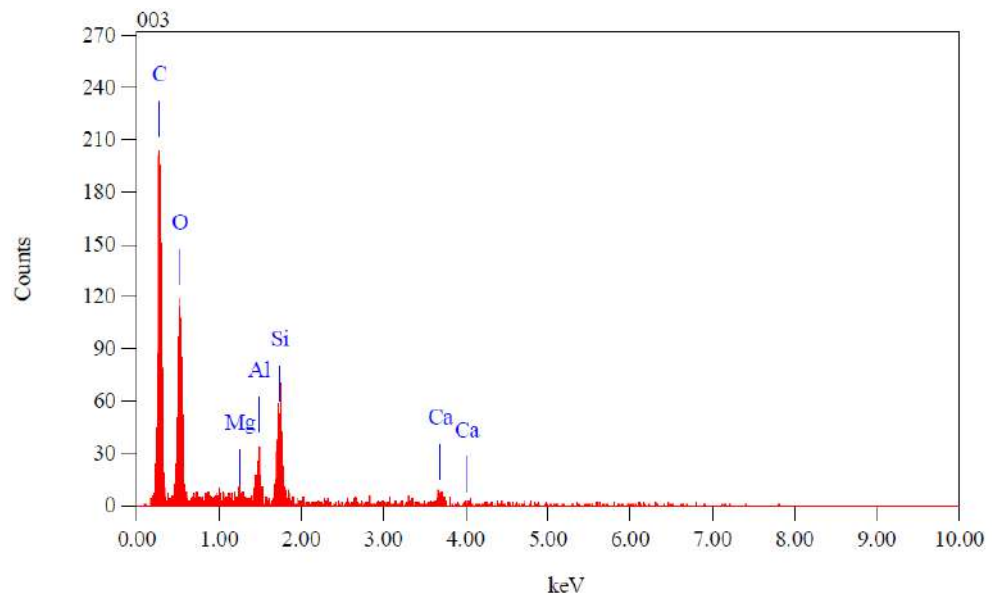


Fig. 4. - XRD of Basalt/epoxy composite with 0.8% CNT by weight

The high carbon content can be attributed to the presence of CNTs at the intended 0.8% loading. This CNT addition is significant because at this concentration, CNTs are known to enhance the mechanical, electrical, and thermal properties of composites. While further testing would be needed to quantify the magnitude of property improvements, the XRD verifies the composite contains approximately 0.8% CNTs as intended.

3.7 DMA

Dynamic mechanical analysis provides valuable insights into the viscoelastic performance and thermomechanical properties of polymeric materials. For basalt fiber composites reinforced with varying weight percentages of carbon nanotubes, the technique reveals several key trends. In particular, the addition of CNTs is shown to enhance stiffness and thermal stability up to moderate loadings, but further addition negatively impacts mobility and degradation resistance. Optimization of CNT content is required to balance reinforcing effects with retention of damping capability.

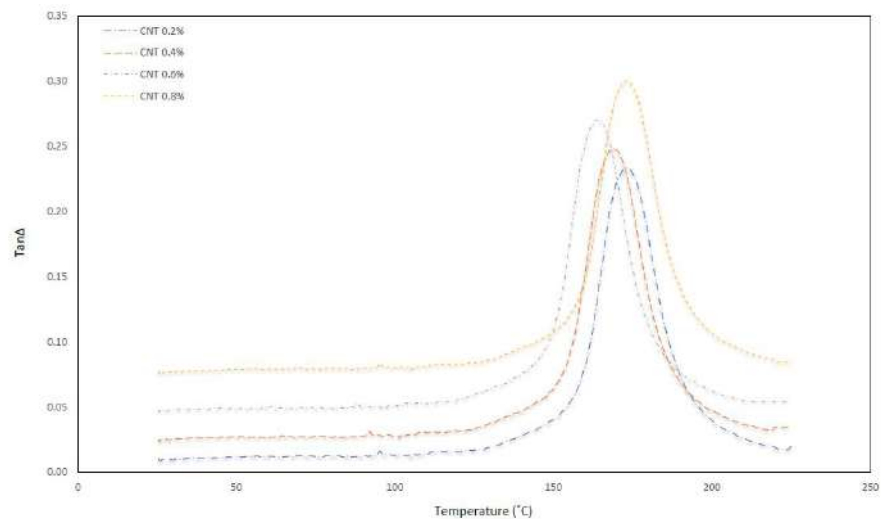


Fig. 5. – Tan Δ

Dynamic mechanical analysis reveals that the addition of carbon nanotubes (CNTs) strongly influences the viscoelastic performance of basalt fiber composites. Incorporation of CNTs from 0.2 to 0.8 wt% markedly enhances the storage modulus and stiffness across the tested temperature range, affirming the reinforcing nature of the CNT network. The glass transition temperature shifts slightly higher with increasing CNT percentages, suggesting some CNT-induced restriction of polymer chain mobility at the interface. Concurrently, the intensity of the tan delta peak progressively declines at higher CNT loadings, implying hindered damping capability due to constrained interfacial motions. The composites maintain excellent thermal stability up to 200°C for all CNT contents, however the onset of degradation emerges earlier above 0.6 wt% CNTs. Furthermore, the loss modulus peak position decreases with more CNTs, indicating altered viscoelastic energy dissipation modes.

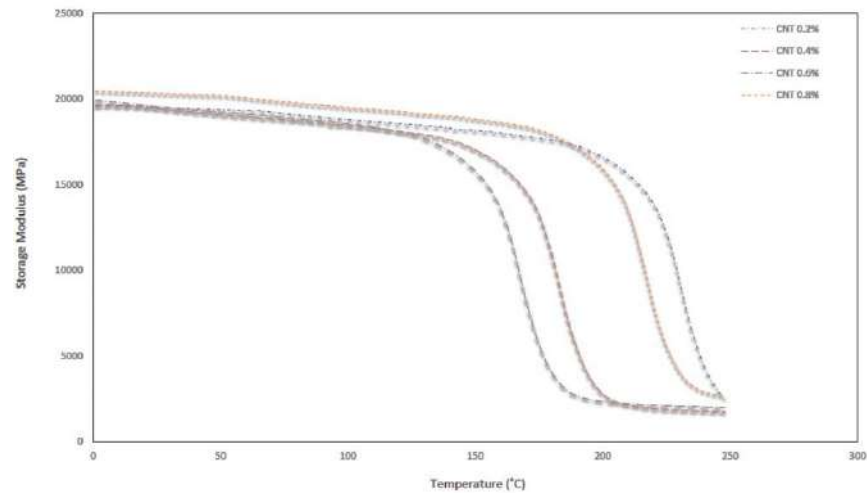


Fig. 6 - Storage Modulus

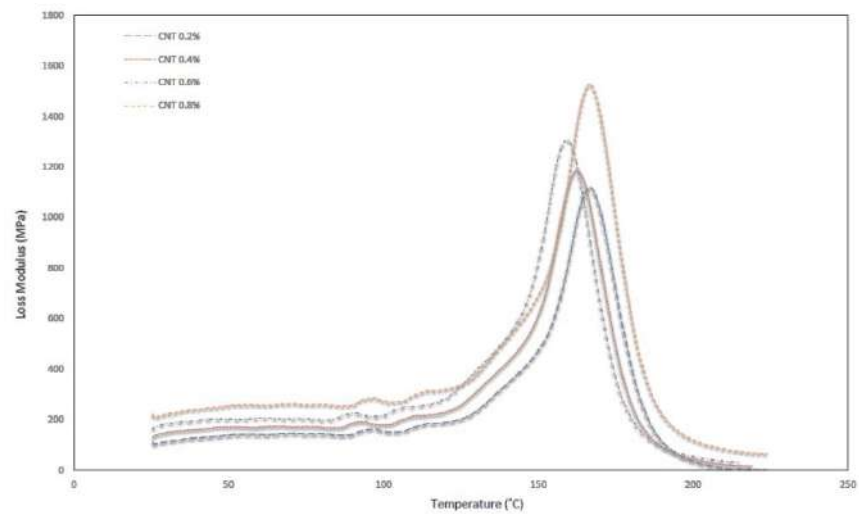


Fig. 7. - Loss modulus

In summary, CNT incorporation provides mechanical reinforcement but higher loadings begin to restrict mobility and reduce damping. An optimal CNT loading balancing stiffness, toughness, and thermal stability is estimated between 0.4-0.6 wt% for the basalt fiber composites.

Conclusion

The tensile, flexural and impact properties of the CNT-reinforced composites showed varying degrees of enhancement up to an optimal CNT percentage followed by deterioration due to aggregation effects. This comprehensive study demonstrates that augmenting basalt fiber composites with carbon nanotube reinforcements can substantially enhance certain mechanical properties when incorporated at optimal compositions between 0.4-0.6 wt%. However, detrimental effects emerge at higher CNT loadings due to aggregation issues. Scanning electron microscopy revealed increasing surface decoration and eventual obscuration of the underlying basalt fibers with rising CNT percentage. At 0.8 wt% CNTs, thick conformal coatings nearly completely encapsulated the basalt. Fourier transform infrared spectroscopy showed a transition from basalt-dominated to CNT-dominated spectra at higher CNT contents. X-ray diffraction confirmed the presence of 0.8 wt% CNTs through elevated carbon levels.

Mechanical testing exhibited noticeable property enhancements at lower CNT loadings followed by deterioration at excessive percentages where aggregation dominated. Both tensile and flexural strength improved up to 0.4-0.6 wt% CNTs before declining at 0.8 wt%, attributed to impaired interfacial adhesion. However, impact energy decreased more consistently from 0.2 to 0.8 wt% CNTs due to embrittlement effects intensifying with higher loading. Dynamic mechanical analysis revealed that increasing CNT content progressively enhanced the storage modulus, suggesting improved stiffness. But the loss modulus and damping capability diminished at higher loadings above 0.6 wt% as CNTs restricted interfacial mobility. Thermal degradation also emerged earlier above 0.6 wt%.

In summary, an optimal CNT loading between 0.4-0.6 wt% was found to maximize certain mechanical properties through uniform dispersion and strong interfacial adhesion enabling efficient stress transfer. However, concentrations above this range led to impairment from CNT aggregation. With controlled processing, CNTs can

effectively reinforce basalt fiber composites within a tailored composition range prior to the onset of negative aggregation effects.

Data Availability

The authors confirm that the data supporting the findings of this study are available within the article and its supplementary material. Raw data that support the findings of this are available from the corresponding author, upon reasonable request.

References

- [1] Dhand, V., Mittal, G., Rhee, K. Y., Park, S. J., & Hui, D. (2015, May). A short review on basalt fiber reinforced polymer composites. *Composites Part B: Engineering*, 73, 166–180 <https://doi.org/10.1016/j.compositesb.2014.12.011>
- [2] Tavadi, A. R., Naik, Y., Kumaresan, K., Jamadar, N., & Rajaravi, C. (2022, May 30). Basalt fiber and its composite manufacturing and applications: An overview. *International Journal of Engineering, Science and Technology*, 13(4), 50–56. <https://doi.org/10.4314/ijest.v13i4.6>
- [3] Xing, D., Xi, X. Y., & Ma, P. C. (2019, April). Factors governing the tensile strength of basalt fibre. *Composites Part A: Applied Science and Manufacturing*, 119, 127–133. <https://doi.org/10.1016/j.compositesa.2019.01.027>
- [4] Zhang, H., Yao, Y., Zhu, D., Mobasher, B., & Huang, L. (2016, May). Tensile mechanical properties of basalt fiber reinforced polymer composite under varying strain rates and temperatures. *Polymer Testing*, 51, 29–39. <https://doi.org/10.1016/j.polymertesting.2016.02.006>
- [5] Li, Z., Ma, J., Ma, H., & Xu, X. (2018, October 11). Properties and Applications of Basalt Fiber and Its Composites. *IOP Conference Series: Earth and Environmental Science*, 186, 012052. <https://doi.org/10.1088/1755-1315/186/2/012052>
- [6] Fiore, V., Scalici, T., Di Bella, G., & Valenza, A. (2015, June). A review on basalt fibre and its composites. *Composites Part B: Engineering*, 74, 74–94. <https://doi.org/10.1016/j.compositesb.2014.12.034>
- [7] Dlouhy, I., Tatarko, P., Bertolla, L., & Chlup, Z. (2019). Nano-fillers (nanotubes, nanosheets): do they toughen brittle matrices? *Procedia Structural Integrity*, 23, 431–438. <https://doi.org/10.1016/j.prostr.2020.01.125>
- [8] Liew, K., Kai, M., & Zhang, L. (2016, December). Carbon nanotube reinforced cementitious composites: An overview. *Composites Part A: Applied Science and Manufacturing*, 91, 301–323. <https://doi.org/10.1016/j.compositesa.2016.10.020>
- [9] Kumar, R., Sharma, S., Gulati, P., Singh, J. P., Jha, K., Li, C., Kumar, A., Eldin, S. M., & Abbas, M. (2023, July). Fabrication and characterizations of glass fiber-reinforced functional leaf spring composites with or without microcapsule-based dicyclopentadiene as self-healing agent for automobile industrial applications: comparative analysis. *Journal of Materials Research and Technology*, 25, 2797–2814. <https://doi.org/10.1016/j.jmrt.2023.06.039>
- [10] Zhao, X., Lu, S., Li, W., Zhang, S., Li, K., Nawaz, K., Wang, P., Yang, G., Ragauskas, A., Ozcan, S., & Webb, E. (2022, May 25). Epoxy as Filler or Matrix for Polymer Composites. *Epoxy-Based Composites*. <https://doi.org/10.5772/intechopen.102448>
- [11] Sang, M., Shin, J., Kim, K., & Yu, K. (2019, March 5). Electronic and Thermal Properties of Graphene and Recent Advances in Graphene Based Electronics Applications. *Nanomaterials*, 9(3), 374. <https://doi.org/10.3390/nano9030374>
- [12] Elkington, M., Bloom, D., Ward, C., Chatzimichali, A., & Potter, K. (2015, July 3). Hand layup: understanding the manual process. *Advanced Manufacturing: Polymer & Composites Science*, 1(3), 138–151. <https://doi.org/10.1080/20550340.2015.1114801>
- [13] Laureto, J. J., & Pearce, J. M. (2018, July). Anisotropic mechanical property variance between ASTM D638-14 type i and type iv fused filament fabricated specimens. *Polymer Testing*, 68, 294–301. <https://doi.org/10.1016/j.polymertesting.2018.04.029>
- [14] Raheem, Z. (2019), “Standard test methods for flexural properties of unreinforced and reinforced plastics and electrical insulating materials”, D790–03, ASTM International
- [15] ASTM, D256-10 (2018) Standard Test Methods for Determining the Izod Pendulum Impact Strength of Plastics. ASTM International, West Conshohocken <https://www.astm.org/Standards/D256>
- [16] Malyadri, T., Kumar, J.S. and Nagamathu, M., 2023. Influence of CNT Particle on Mechanical Properties of Epoxy Composites. *Journal of Mines, Metals and Fuels*, 71(11), pp.2229-2236.
- [17] Malyadri T., Kumar Dr J. S., Investigation Of Mechanical Properties For Basalt Fiber Composite With Silica Nano Particles, *International Journal of Emerging Technologies and Innovative Research*, 2022, 9, 2349– 5162.
- [18] Malyadri T., Kumar Dr J. S., Investigation Of Mechanical Properties For Basalt Fiber Composite With Graphene Nano Particles, *International Journal of Emerging Technologies and Innovative Research*, 2022, 9, 2349–5162.

Information of the authors

Malyadri T., assistant Professor, VNR VJIET, Researcher Scholar, Jawaharlal Nehru Technological University (JNTU)

e-mail: malyadri_t@vnrvjiet.in

Suresh Kumar J., PhD, senior professor, Jawaharlal Nehru Technological University (JNTU)

The Study of the Dynamic Characteristics of the Hydro-volume Vibration Mechanism

Moyzes B.B.^{1*}, Kuvshinov K.A.¹, Nizhegorodov A.I.², Vavilova G.V.¹, Vtorushina A.N.¹

¹National Research Tomsk Polytechnic University, Tomsk, Russia

²Irkutsk National Research Technical University, Irkutsk, Russia

*corresponding author

Abstract. This research reviews the study of the hydro-volume vibration mechanism of Shock Vibration Source of Seismic Signals. The developed source should have a smaller weight compared to analogs due to the fact that the source is pressed to the ground at the moment of emission of the Amplitude-Modulated Sweep Signal by a falling load. Theoretical studies were carried out on a linear mathematical model of the mechanism. A comparison of the calculated values of frequency characteristics with experimental values was the method for assessing the validity of the assumptions adopted for the mathematical model. Experimental studies of the dynamic system of the mechanism were conducted on an experimental vibration stand using frequency characteristics. To simplify the design, the fall of the load for pressing is simulated by a low-frequency generator in the vibration mechanism of the experimental stand. Thus, the vibration mechanism includes two separate drives for controlling the oscillatory system for high-frequency and low-frequency oscillations, an oscillating system and an external load. The determination of frequency characteristics of the vibration mechanism, the conditions and nature of its resonance, and finding resonant zones is the task of the research.

Keywords: sweep signal, seismic vibrations, vibration mechanism, dynamic characteristics

Introduction

Various sources of seismic vibrations are used for exploration of geological environments in modern seismic exploration. At the same time, in the research works it is noted the prospects of shock-vibration sources using [1-7].

This research is a continuation of the work “The Study of the Parameters of Amplitude-Modulated Sweep Signal of the Shock Vibration Source of Seismic Signals” [1]. The overall objective of the research is to develop a small-sized seismic shock-vibration source with an amplitude-modulated probing signal.

The article reviewed [1] the probing signals with different forms of the envelope of the amplitude of the force. The prospects of using a signal with a sinusoidal envelope are confirmed. To form such a signal, it is proposed a design scheme of the seismic signal source, including an oscillatory system with an impact unit. The force and the form of the signal envelope are formed by the process of interaction of the fallen active load with the shock absorber of the actuator.

The hydro-volume vibration mechanism [8-14] can be represented as a generalized dynamic circuit, adding additional connections to it due to the presence of a resonant circuit (Fig. 1) (regardless of the materials of the elements) [15, 16].

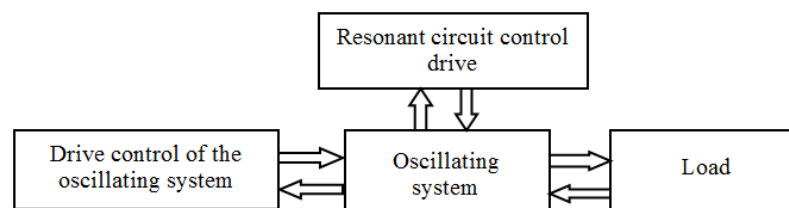


Fig 1. – Scheme of the dynamic system of the hydrovolume vibration mechanism

It is evident from the diagram of the dynamic drive system that the oscillatory system and the load acting on it represent a single system with direct and feedback connections.

The purpose of the research is to study the vibration system of the vibration mechanism that is to determine:

- its dynamic characteristics
- the parameters of the resonant mode;
- the degree of influence of high-frequency and low-frequency generators on the amplitude of oscillations.

Also it was the task to prove:

- the validity of simulating the fall of an active load by the operation of a low-frequency generator
- the possibility of the research on the formation of an amplitude-frequency modulated signal.

In the article on the base of the experiments:

- logarithmic amplitude-frequency and phase-frequency characteristics of a dynamic system are constructed;
- logarithmic amplitude-frequency and phase-frequency characteristics of a dynamic system are constructed;

- a comparison of the calculated dynamic parameters with experimental ones is given.

1. Theoretical Part

To simplify the design of the laboratory stand (Fig. 2), in laboratory conditions, the fall of a load with mass m was replaced by its rocking-oscillatory motion [1]. It was recorded, in this case, the amplitude x of the load's movement in the vertical direction.

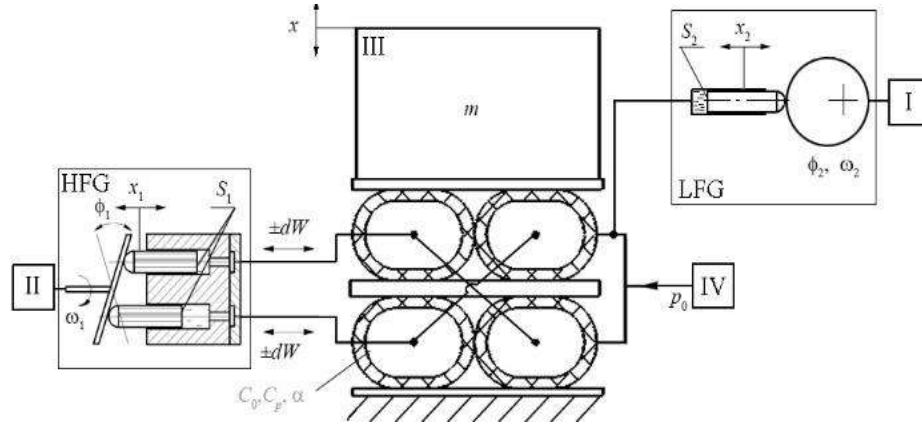


Fig 2. – Simplified schematic diagram of the experimental stand:

$S_1, S_2, x_1, x_2, \omega_1, \omega_2$ are: the area of the generators plungers and the coordinates of the plungers moving, the rotational speed of the high-frequency and low-frequency oscillation generators; ϕ_1 is the tilt angle of the high-frequency generator disk; ϕ_2 is the current position angle of the low-frequency generator shaft; p_0 is the average pressure in the system; α is coefficient of viscous losses in the vibration circuit of the mechanism; C_0 is the stiffness of the main elastic links, which includes the stiffness HPH and the stiffness due to the presence of medium pressure in the cavities; C_p is the hydraulic stiffness due to volumetric deformation; $\pm dW$ is the variable fluid flow

For this purpose, load III is placed on four cross-connected elastic shells – high-pressure hoses (HPH). The high-frequency oscillations are excited by a symmetrical generator (HFG) in them, and the shock mode is simulated by an additional low-frequency generator (LFG).

The hydrovolume vibration mechanism constructed according to this scheme consists of:

- a drive for controlling the high-frequency oscillatory system II;
- a drive for controlling the low-frequency oscillatory system I;
- an oscillating system;
- an external load III;
- medium pressure generation systems IV.

In the research [1] the general equation of displacement was obtained:

$$m \frac{d^2 x}{dt^2} + \alpha \cdot \frac{dx}{dt} + C_{\Sigma} \cdot x = C_p \cdot k_{s1} \cdot x_1 + C_p \cdot k_{s2} \cdot x_2 \quad (1)$$

where S is the operating area of the actuator;

$$k_{s1} = \frac{S_1}{S} \text{ and } k_{s2} = \frac{S_2}{S}$$

$$C_{\Sigma} = C_0 + C_p.$$

There were obtained the equations for the system of equations for subsequent computer modeling:

$$\begin{aligned} dW &= W_1 + W_2 - W_0; \\ dp &= \frac{E}{W_0} dW; \\ F_d &= S \cdot dp; \\ F_v &= \alpha \cdot V; \\ F_x &= C_0 \cdot x; \\ dF &= F_d - F_v - F_x \end{aligned} \quad (2)$$

where W_1, W_2 are liquid volumes supplied by high and low frequency generators to the HPH;

W_0, dW is the initial fluid volume in the shells and its change;

E is the fluid elasticity modulus;

S is the operating area of the actuator;

dp is the pressure drop in operating cavities;

α is the coefficient of viscous losses in the oscillatory circuit;

V is the movement speed of the movable body of the actuator.

x is the current movement of the moving body;

C_0 is the stiffness of the main elastic bonds

dF, F_d, F_x, F_V are: the force transmitted through the HPH to the "ground", the driving force, the force from the current deformation of the HPH, the force of the viscous internal resistance.

A detailed structural diagram of the mechanism (Fig. 3) is given on the based on the system of equations (2).

The first adder in this structural diagram characterizes the volume balance equation and the process of forming the deformation volume dW , the second adder describes the force balance equation.

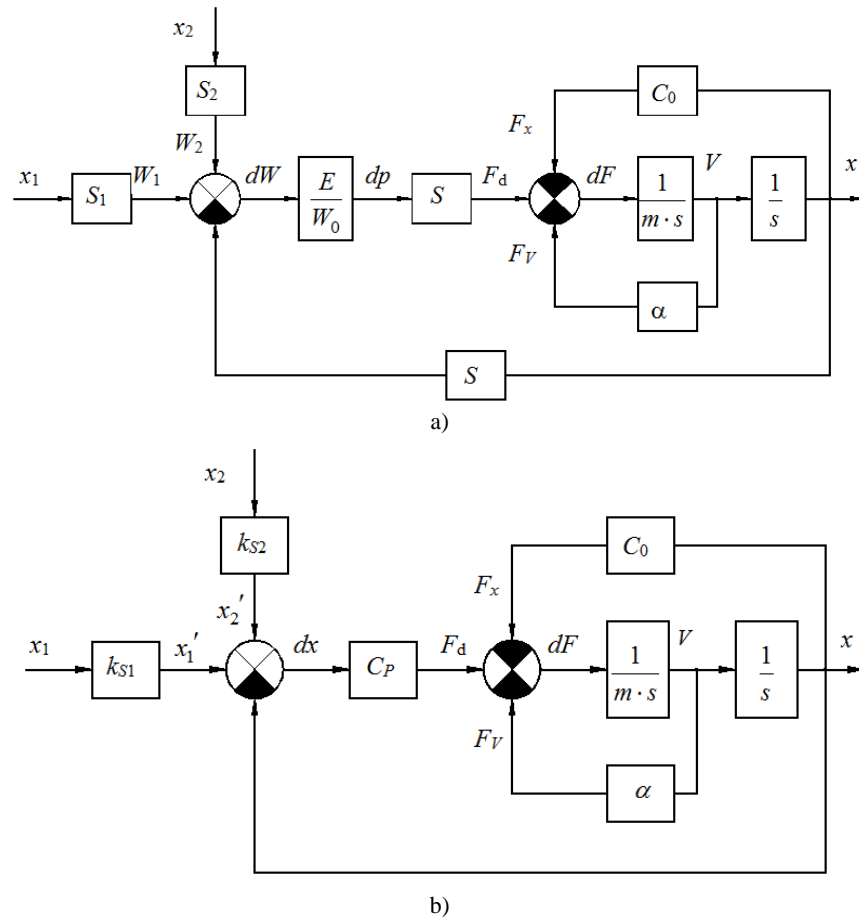


Fig 2. – Structural diagrams of a hydrovolume vibration mechanism: a) for displacement, b) for pressure drop dp is the Laplace operator

According to the assumptions made when compiling the mathematical model [1], expression (1) is linear and continuous in the frequency and time interval under consideration. This allows us to perform a transformation over expression (2) - the Laplace transform:

$$(m \cdot s^2 + \alpha \cdot s + C_{\Sigma}) \cdot X(s) = C_p \cdot k_{s1} \cdot X_1(s) + C_p \cdot k_{s2} \cdot X_2(s) \quad (3)$$

Let's rewrite expression (3):

$$(T^2 \cdot s^2 + 2 \cdot \xi \cdot T \cdot s + 1) \cdot X(s) = k_1 \cdot X_1(s) + k_2 \cdot X_2(s), \quad (4)$$

by introducing the notations:

$$k_{1(2)} = \frac{C_p \cdot k_{s1(2)}}{C_{\Sigma}};$$

$$T = \sqrt{\frac{m}{C_{\Sigma}}} = \frac{1}{\omega_*};$$

$$\alpha = 2 \cdot \xi \cdot \sqrt{\frac{m}{C_{\Sigma}}}.$$

Let us consider the operation of each of the oscillation generators separately, i.e. two variants of the system operation:

- in the first case, the input is the movement of the plunger of the high-frequency generator x_1

$$(T^2 s^2 + 2 \cdot \xi \cdot T \cdot s + 1) \cdot X(s) = k_1 \cdot X_1(s); \quad (5)$$

- in the second input is the movement of the plunger of the low-frequency generator x_2 :

$$(T^2 s^2 + 2 \cdot \xi \cdot T \cdot s + 1) \cdot X(s) = k_2 \cdot X_2(s). \quad (6)$$

We obtain two different loading schemes for the mechanical system of the vibration mechanism, differing in:

- the nature of excitation;
- the size of the excitation volume of liquid supplied by the generators into the cavities of the shells;
- stiffness parameters.

According to the assumption of linearity [1, 17, 18] in equations (5, 6), the coefficients T , ξ and k , depending on the value of the hydraulic stiffness C_p , are constant and they are input parameters.

In a real physical model, they depend both on the generator inputs and on the change in the output parameter – the displacement x , since:

$$C_p = \frac{S(x)^2 \cdot E}{W_0}, \quad (7)$$

and therefore require correction.

We obtain the transfer functions for the system from equations (6, 7):

$$W_{x1}(s) = \frac{X(s)}{X_1(s)} = \frac{k_1}{T^2 s^2 + 2 \cdot \xi \cdot T \cdot s + 1} \quad (8)$$

and

$$W_{x2}(s) = \frac{X(s)}{X_2(s)} = \frac{k_2}{T^2 s^2 + 2 \cdot \xi \cdot T \cdot s + 1}. \quad (9)$$

We obtain the frequency transfer functions by applying the Fourier transform to expressions (6, 7):

$$W_{x1}(j\omega) = \frac{X(j\omega)}{X_1(j\omega)} = \frac{k_1}{1 - T^2 \omega^2 + 2 \cdot j \cdot \xi \cdot T \cdot \omega} \quad (10)$$

and

$$W_{x2}(j\omega) = \frac{X(j\omega)}{X_2(j\omega)} = \frac{k_2}{1 - T^2 \omega^2 + 2 \cdot j \cdot \xi \cdot T \cdot \omega}. \quad (11)$$

We determine amplitude-frequency characteristics (AFC) from the expressions (10, 11)

$$W_{x1}(\omega) = \frac{k_1}{\sqrt{(1 - T^2 \omega^2)^2 + 4 \cdot \xi^2 \cdot T^2 \cdot \omega^2}} \quad (12)$$

and

$$W_{x2}(\omega) = \frac{k_2}{\sqrt{(1 - T^2 \omega^2)^2 + 4 \cdot \xi^2 \cdot T^2 \cdot \omega^2}}; \quad (13)$$

- phase-frequency characteristics (PFC)

$$\varphi_{x1(2)}(\omega) = -\arctg \frac{2 \cdot \xi \cdot T \cdot \omega}{1 - T^2 \cdot \omega^2} \quad (14)$$

To analyze the operation of the vibration mechanism in the future, we will use logarithmic frequency response (LFR):

$$L_{x1(2)}(\omega) = 20 \cdot \lg(W_{x1(2)}(\omega)). \quad (15)$$

By making structural transformations of the diagram (Fig. 2), we obtain for the pressure drop dp in the working cavities of the actuator:

- transfer functions:

$$W_{dp1}(s) = \frac{k_1 \left(T^2 s^2 + 2 \cdot \xi \cdot T \cdot s + \frac{C_0}{C_x} \right)}{T^2 s^2 + 2 \cdot \xi \cdot T \cdot s + 1} \quad (16)$$

and

$$W_{dp2}(s) = \frac{k_2 \left(T^2 s^2 + 2 \cdot \xi \cdot T \cdot s + \frac{C_0}{C_\Sigma} \right)}{T^2 s^2 + 2 \cdot \xi \cdot T \cdot s + 1} \quad (17)$$

- frequency transfer functions:

$$W_{dp1}(j\omega) = \frac{k_1 \left(\frac{C_0}{C_\Sigma} - T^2 \omega^2 + 2 \cdot j \cdot \xi \cdot T \cdot \omega \right)}{1 - T^2 \omega^2 + 2 \cdot j \cdot \xi \cdot T \cdot \omega} \quad (18)$$

and

$$W_{dp2}(j\omega) = \frac{k_1 \left(\frac{C_0}{C_\Sigma} - T^2 \omega^2 + 2 \cdot j \cdot \xi \cdot T \cdot \omega \right)}{1 - T^2 \omega^2 + 2 \cdot j \cdot \xi \cdot T \cdot \omega} \quad (19)$$

From expressions (18, 19) we obtain expressions for:

- AFC

$$W_{dp1}(\omega) = \frac{k_1 \sqrt{\left(\frac{C_0}{C_\Sigma} - T^2 \omega^2 \right)^2 + 4 \cdot \xi^2 \cdot T^2 \cdot \omega^2}}{\sqrt{(1 - T^2 \omega^2)^2 + 4 \cdot \xi^2 \cdot T^2 \cdot \omega^2}} \quad (20)$$

and

$$W_{dp2}(\omega) = \frac{k_2 \sqrt{\left(\frac{C_0}{C_\Sigma} - T^2 \omega^2 \right)^2 + 4 \cdot \xi^2 \cdot T^2 \cdot \omega^2}}{\sqrt{(1 - T^2 \omega^2)^2 + 4 \cdot \xi^2 \cdot T^2 \cdot \omega^2}} \quad (21)$$

- PFC

$$\varphi_{dp1(2)}(\omega) = -\text{arctg} \frac{2 \cdot \xi \cdot \omega \cdot C_p}{(C_\Sigma - m \cdot \omega^2) \cdot (C_0 - m \cdot \omega^2) - 4 \cdot \xi^2 \cdot T^2} \quad (22)$$

To analyze the operation of the vibration mechanism in the future, we will use logarithmic frequency response (LFR)

$$L_{dp1(2)}(\omega) = 20 \cdot W_{dp1(2)}(\omega). \quad (23)$$

2. Experimental Part

The experimental studies of the dynamic characteristics of the oscillating system of the mechanism were carried out on a stand (Fig. 1).

The stand consists of the following main elements:

- an actuating vibration element with an internal diameter of $d_{BH} = 0.01$ m and an operating pressure of $P_{work} = 24$ MPa;

- a volumetric axial-type oscillation generator with adjustment of the supplied volume $W_1 = x_1 \cdot S_1$ by changing the stroke value x_1 of pistons with an area of $S_2 = 2.6 \cdot 10^{-4}$ m²;

- a volumetric axial-type oscillation generator with adjustment of the supplied volume $W_2 = x_2 \cdot S_2$ by changing the stroke value x_2 of the piston with an area of $S_2 = 2.6 \cdot 10^{-4}$ m²;

- a generator drive adjustable in terms of rotation speed ω_1 and ω_2 ;

- a system for feeding leaks, maintaining and regulating the average pressure in the operating cavities of the hosepipes.

The mass of the moving parts of the mechanism is $m \approx 4$ κН·sec²/m.

The experiment was carried out with separate excitation of elastic shells by generators.

The purpose of the experiment is to determine the values of the resonance frequencies of the displacement x and the pressure drop dp .

The next values were determined in the result of the experiment:

- the resonance frequencies of the displacement of the “output link” x
- the main ω_x :

$$\omega_x = \sqrt{\frac{C_\Sigma}{m}} \approx \text{Hz}; \quad (23)$$

- additional $\omega_x' \approx 13 \dots 18$ Hz;

- pressure drop resonance frequencies dp :

- “positive” $\omega_{dp} = \omega_x = \omega_0$;

- “negative”

$$\omega'_{dp} = \sqrt{\frac{C_0}{m}} \approx 3.5 \text{ Hz.} \tag{24}$$

- relative damping coefficient

$$\xi = \frac{d\omega}{\omega_0} \approx 0.1 \text{ m}^2/\text{H.} \tag{25}$$

There were determined the system parameters based on the data (23-25):

- rigidity – $C_\Sigma \approx 2.5 \text{ MH/m}$, $C_p \approx 0.6 \text{ MH/m}$, $C_0 \approx 1.9 \text{ MH/m}$
- viscous loss coefficient $\alpha \approx 200 \text{ Hsec/m}$

We obtain the calculated frequency response and phase response for displacement x and pressure drop dp for both generators (Fig. 4, 5) for different values of their amplitudes X_1 and X_2 , substituting the values into expressions (12-15, 20-24).

The calculated resonance peaks coincide in frequency with the experimental ones due to the fact that the parameters determined from the experiment were substituted into the expressions. At the same time, a comparison of the nature of the asymptotes and the resonance values allows us to conclude about the admissibility of the accepted linearity.

Conclusion

The analysis of the diagrams (Fig. 4, 5) showed:

- that the slope and position of the calculated and experimental LAFC and LPFC qualitatively coincide, and the magnitude of the resonance peaks lies within the error limits of 15%;
- that the maximum LAFC for displacement x is observed in the case when the phase angle between the input $x_{1(2)}$ and the output $x_{\varphi_{x1(2)}}(2)$ is equal to $-\pi/2$;
- the resonance in pressure drop occurs at frequencies ω , ω'_{dp} with a phase shift $\varphi_{dp}(2)$ equal to $+\pi/2$;
- in the transresonant mode at $\omega \rightarrow \infty$ the magnitude of the oscillation amplitude of the “output link” tends to zero, and the pressure drop remains practically unchanged.

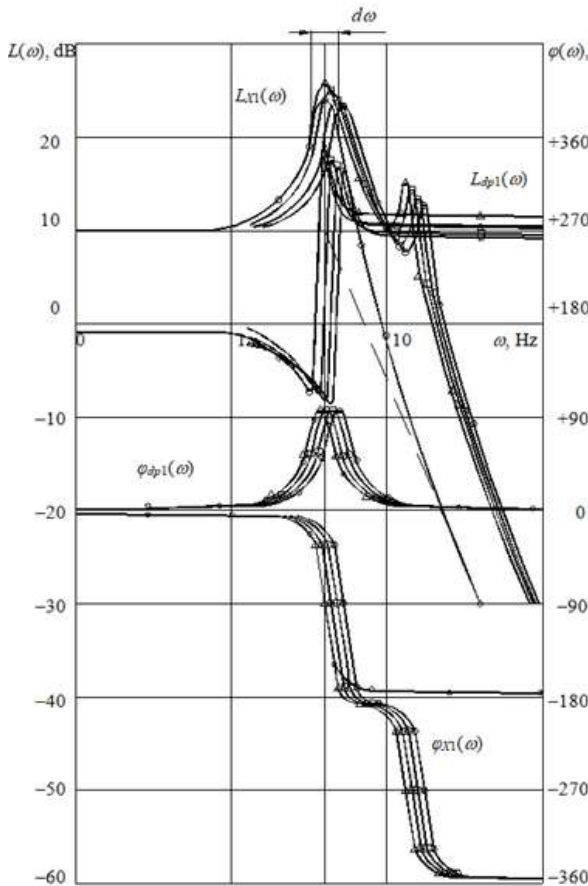


Fig. 4 – LAFH and LPFC of the high-frequency generator: o - calculated; Δ - $X_1=2 \text{ mm}$, \square - input $X_1=1.5 \text{ mm}$, \diamond - $X_1=1 \text{ mm}$, \circ - input $X_1=0.5 \text{ mm}$

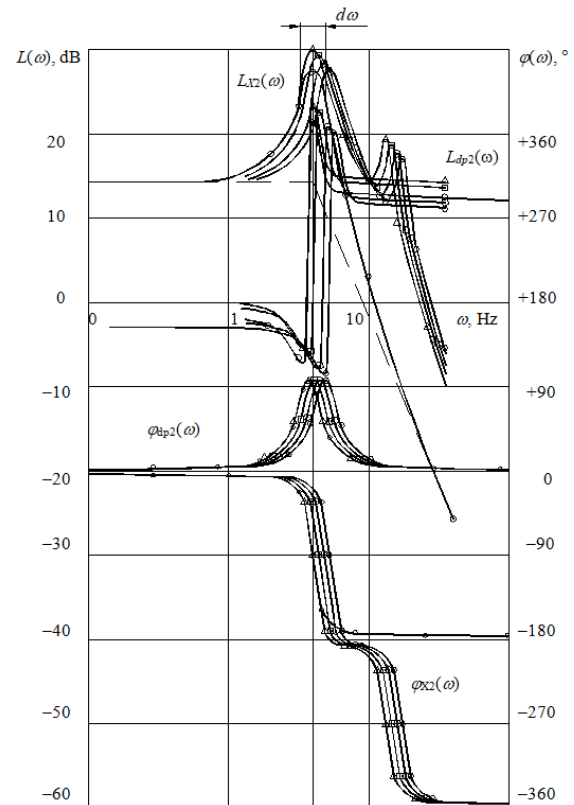


Fig. 5 LAFH and LPFC of the low-frequency generator: o - calculated; Δ - $X_1=2 \text{ mm}$, \square - input $X_1=1.5 \text{ mm}$, \diamond - $X_1=1 \text{ mm}$, \circ - input $X_1=0.5 \text{ mm}$

The experimental study method of the dynamic characteristics of the mechanism in two stationary modes (first with one high-frequency generator operating, then with a low-frequency generator) consisted of obtaining experimental amplitude-frequency and phase-frequency characteristics of the following quantities:

- output signal x ;
- pressure drop dp ;
- phase shift angles $\varphi_{x1(2)}$ and $\varphi_{dp1(2)}$.

References

- [1] Moyzes B.B., Nizhegorodov A.I. The Study of the Parameters of Amplitude-Modulated Sweep Signal of the Shock Vibration Source of Seismic Signals // Engineering Materials, 2023, Part F1222. – P. 91-128. doi: https://doi.org/10.1007/978-3-031-38964-1_7.
- [2] Verstraete J.-B., Foroozandeh M. Improved design of frequency-swept pulse sequences // Journal of Magnetic Resonance, 2022, Vol. 336. – 107146. doi: [10.1016/j.jmr.2022.107146](https://doi.org/10.1016/j.jmr.2022.107146).
- [3] Tang X., Suddarth S., Kantasaria S., Garwood M.: A frequency-swept, longitudinal detection EPR system for measuring short electron spin relaxation times at ultra-low fields // Journal of Magnetic Resonance, 2022, Vol. 342. – 107279. doi: <https://doi.org/10.1016/j.jmr.2022.107279>
- [4] Wang L., Li H.: GBO algorithm for seismic source parameters inversion // Geodesy and Geodynamics, 2022, Available online. – P.1-2. doi: <https://doi.org/10.1016/j.geog.2022.06.004>.
- [5] Poletto F., Schleifer A., Zgauc F., Meneghini F., Petronio L.: Acquisition and deconvolution of seismic signals by different methods to perform direct ground-force measurements // Journal of Applied Geophysics, 2016, Vol. 135. – P. 191-203 (2016).
- [6] Alifov A.A. On the calculation by the method of direct linearization of mixed oscillations in a system with limited power-supply // Advances in Computer Science for Engineering and Education II, 2020. – P. 23-31. doi: https://doi.org/10.1007/978-3-030-16621-2_3
- [7] Brenes A., Juillard J., Ayala J. et al. Experimental validation of a novel characterization procedure based on fast sweep measurements for linear resonators with a large time constant // Mechanical Systems and Signal Processing, 2025, Vol. 225. – 112252.
- [8] Alifov, A.A. Oscillations for delayed elastic constraint and a limited power energy source// J. Mach. Manuf. Reliabil, 2020. – Vol. 49(2). – P. 105–109.
- [9] Ahirrao N.S., Bhosle S.P., Nehete D.V. Dynamics and Vibration Measurements in Engines // Procedia Manufacturing, 2018, vol. 20, pp. 434–439.
- [10] Halit E. Acceleration, Vibration, and Shock Measurement. Abingdon, Taylor & Francis Group, CRC Press LLC. 2000. – 950 p.
- [11] Nizhegorodov A.I., Gavrilin A.N., Moyzes B.B., Kuvshinov K.A. Hydraulic drive of vibration stand for testing the robotic systems units by random vibration method // IOP Conference Series: Materials Science and Engineering, 2019, Vol. 516(1). – 012031. doi: [10.1088/1757-899X/516/1/012031](https://doi.org/10.1088/1757-899X/516/1/012031)
- [12] Plotnikova I., Vedyashkin M., Mustafina R., Plotnikov I., Tchaikovskaya O., Bastida J., Verpeta M. Optimization of the Stabilization System for Electromagnetic Suspension in Active Vibration Isolation Devices // MATEC Web of Conferences, 2016, Vol. 79. – 01019. <https://doi.org/10.1051/mateconf/20167901019>.
- [13] Nizhegorodov A I, Gavrilin A N, Moyzes B B, Cherkasov A I, Zharkevich O M, Zhetesova G S, Savelyeva N A. Radial-piston pump for drive of test machines // IOP Conf. Series: Materials Science and Engineering, 2018, Vol. 289 (1). – 012014. doi: [10.1088/1757-899X/289/1/012014](https://doi.org/10.1088/1757-899X/289/1/012014)
- [14] Sikhimbaev M.R., Sherov K.T., Zharkevich O.M., Sherov A.K., Tkachyova Y.O. Experimental studies of stabilization of boring cutter form - building top oscillation // Journal of Vibroengineering, 2012, Vol. 14, no 2. – P. 661-670
- [15] Surzhikov A.P., Lysenko E.N., Malyshev A.V., Vlasov V.A., Suslyayev V. I., Zhuravlev V.A., Korovin E.Y., Dotsenko O.A. Study of the Radio-Wave Absorbing Properties of a Lithium-Zinc Ferrite Based Composite // Russian Physics Journal, 2014, Vol. 57(5), P. 621-626 (2014). doi: [10.1007/s11182-014-0284-9](https://doi.org/10.1007/s11182-014-0284-9).
- [16] Lysenko E.N., Surzhikov A.P., Vlasov V.A., Malyshev A.V., Nikolaev E.V. Thermal analysis study of solid-phase synthesis of zinc- and titanium-substituted lithium ferrites from mechanically activated reagents // Journal of Thermal Analysis and Calorimetry, 2015, Vol. 122. – P. 1347-1353. doi: [10.1007/s10973-015-4849-9](https://doi.org/10.1007/s10973-015-4849-9).
- [17] Moyzes B., Gavrilin A., Kuvshinov K., Smyshlyayev A., Koksharova I. Using the Vibration Recorder Mobile Diagnostic Complex for Studying Vibration Processes //Material and Mechanical Engineering Technology, 2022, Vol. 3. – P. 50 – 57. doi: [10.52209/2706-977X_2022_3_50](https://doi.org/10.52209/2706-977X_2022_3_50).
- [18] Gavrilin A., Moyzes B., Cherkasov A., Mel'nov K., Zhang X. 2016 Mobile Complex for Rapid Diagnosis of the Technological System Elements //MATEC Web of Conferences, 2016, Vol. 79. – 01078 doi: [10.1051/mateconf/20167901078](https://doi.org/10.1051/mateconf/20167901078)

Information of the authors

Moyzes Boris Borisovich, c.t.s., associate professor, National Research Tomsk Polytechnic University
e-mail: mbb@tpu.ru

Kuvshinov Kirill Aleksandrovich, senior lector National Research Tomsk Polytechnic University
e-mail: kuvshinov@tpu.ru

Nizhegorodov Anatolij Ivanovich, d.t.s., professor, Irkutsk National Research Technical University
e-mail: nastromo_irkutsk@mail.ru

Vavilova Galina Vasilevna, c.t.s., associate professor, National Research Tomsk Polytechnic University
e-mail: wgw@tpu.ru

Vtorushina Anna Nikolaevna, c.t.s., associate professor, National Research Tomsk Polytechnic University
e-mail: anl@tpu.ru